UNIVERSITY COLLEGE LONDON

Faculty of Mathematics and Physical Sciences

Department of Physics & Astronomy

# THE NATURE AND STRUCTURE OF THE WINDS OF GALACTIC O STARS

Thesis submitted for the Degree of Doctor of Philosophy of University College London

by

Matthew James Austin

Supervisors:

Prof. Raman K. Prinja

Prof. Ian D. Howarth

Examiners:

Prof. Mike J. Barlow

Prof. Paul A. Crowther

June 14, 2011

*For Aileen*

I, Matthew James Austin, confirm that the work presented in this thesis is my own. Where information has been derived from other sources, I confirm that this has been indicated in the thesis.

# Abstract

O stars are highly important objects in their host galaxies due to the impact of their powerful stellar winds and strong flux output. The details of their physics and evolution as individual entities and as populations have important consequences for understanding the stars themselves and their environments. Two major issues are currently challenging the successful theory of line-driven winds; that the winds are clumped and not smooth or homogeneous, and that some objects appear to have weaker mass-loss than prescribed by theory; in the case of O supergiants by a factor of a few, and for late O dwarfs by perhaps and order of magnitude or more.

The key goal of this thesis is to exploit sophisticated model atmosphere calculations to explore the effects of wind-clumping and X-rays due to wind shocks in O stars in the Milky Way. The consequences for the spectral line profiles produced and the ionization balance are explored in detail. The level to which clumping and X-rays affect the observations of different classes of O star is further constrained.

*IUE* observations of weak-wind O stars (those at spectral types O6.5-9.5 V) are examined in light of the ion balance determinations, and comment is made about the current state of the weak-wind problem in the Galaxy. This involves empirical line-synthesis matches to CIV and NV line profiles. The influence of X-rays is found to be key in the mass-loss issue through altering the ion balance.

Finally the wind-formed sulphur line profiles of a small sample of O type supergiants are fitted using model atmospheres. Sulphur is important in these O stars since the model atmospheres predict the majority of it to be found in three adjacent ion stages that all have corresponding wind lines in the ultraviolet and far-ultraviolet. When moderate clumping in the winds is assumed, the mass-loss rates are found to be approximately in line with

estimates based on density-squared diagnostics, such as H$\alpha$.

# Acknowledgements

A good number of people deserve my thanks for helping me get to the end of my Ph.D., both for professional help (by which I mean things like supervising me and showing me how to do bits of computing, not pychological counselling or anything like that) and for being supportive. First thanks go to Raman who provided plenty of wisdom and experience, and found the perfect balance between bugging me and letting me get on with things. His continued enthusiasm for the winds of massive stars has helped keep me just as engaged with the subject now as when I was an enthusiastic, bright-eyed whippersnapper of a first year. Also regularly on hand was my second supervisor Ian, who is always ready to discuss the scarier theoretical parts of the study of massive stars, and typically with a trademark wry grin.

Further 'academic' thanks must go first to Dugan Witherick, who has helped me to master some of the trickier computing issues I have encountered. That his name appears in many a thesis acknowledgements section is testament to his skill and patience. Additionally I could not have got to grips with running CMFGEN without the help of Adam Burnley, who set me in the right direction with the code, and John Hillier, who answered some of the more obscure questions about his career's work. Fab Sidoli gets a special mention for helping me to construct this final document by way of his experience with LaTeX, and general computer-based cleverness.

I thank the various office mates that have shared in my efforts, particularly Danielle, DK and Dugan, and the many conversations we shared beyond the scope of astronomy. Both they and my newer, thesis-writing office mates Dave, Sam, Simon and Zainab have each in their own way helped to make the experience of the last few years more fun and interesting, in ways that the study of O stars could not do alone.

Thanks also go to my incredibly supportive parents, who have taken an active interest in my exploits as an astronomer beyond what one might expect. They are ever keen to lend an ear and have been relentless in phoning me to see how things are going.

Finally my deepest thanks go to my wife Aileen, who has shown such great belief in me. Her love, support and encouragement have been the main things keeping me going when work has been difficult, and she helps me to keep on seeing the things that make the world a fascinating place to be.

*"The world is a thing of utter inordinate complexity and richness and strangeness that is absolutely awesome. I mean the idea that such complexity can arise not only out of such simplicity, but probably absolutely out of nothing, is the most fabulous extraordinary idea. And once you get some kind of inkling of how that might have happened ' it's just wonderful. And . . . the opportunity to spend 70 or 80 years of your life in such a universe is time well spent as far as I am concerned"*

Douglas Adams

*"The heavens declare the glory of God, and the sky above proclaims his handiwork... Let the words of my mouth and the meditation of my heart be acceptable in your sight, O Lord, my rock and my redeemer"*

Psalm 19, verses 1 and 14

The influence of massive stars upon their environments is exemplified by open cluster Pismis-24. Some objects are still in the process of formation, and carving out space in the parent nebula via prolific winds and intense radiation.

# Contents

# List of Figures

This page is intentionally left almost blank

# List of Tables

# Chapter 1

# Introduction

*'I am always doing that which I can not do, in order that I may learn how to do it.'*

Pablo Picasso

This thesis is chiefly concerned with the stellar winds and mass-loss of some of the hottest and most luminous stars in our Galaxy. By exploiting detailed quantitative spectroscopy, the aim is to learn more about the rate at which stellar material is ejected from massive stars, and to examine effects of clumping in the outflows. It is essential to understand hot, massive and luminous stars fully since, despite their relative rarity, they are profoundly influential in their host galaxies.

In this introduction chapter a broad context for the study of massive stars is set forth, with specific attention being paid to O stars, the hottest class of objects in the MK system, which are the subject of study in this thesis. Brief discussion of their evolution and physical attributes is made, together with a more formal way of describing their powerful winds. Finally, emphasis is placed upon current and urgent issues, namely weak winds and wind clumping, setting the reasoning and context behind this work.

## 1.1 Massive stars

Stars can be broadly defined as gaseous bodies bound by self-gravity which radiate energy supplied by an internal source. They tend to be approximately spherical and they fuse

atomic nuclei in their centres to produce radiative energy. This radiative energy, in the form of electromagnetic photons, finds its way out of the star and across light years to observers on earth. Almost everything we can learn about stars must be learned through the electromagnetic radiation that stars emit and we receive through telescopes, both in broad colours (photometrically) and in specific patterns of intensity versus wavelength or frequency (spectroscopically). Indeed, the classification schemes in place for stars today are based on how they appear spectroscopically.

The scheme widely used today is that of Morgan et al. (1943), with some additions based on newly discovered object types, and is called the MK system of spectral classification. It groups stars according to features in their optical spectra and broadly runs as a function of temperature. Stars each get assigned a letter from the 'Harvard sequence' - OBAFGKM - where O denotes the hottest and bluest stars, and M refers to the coolest and reddest. These are subcategorised using the numbers 0 to 9 where 0 is the hottest sub-type and 9 is the coolest, except for O stars which begin at type O2. Each star is then assigned a Roman numeral to represent its luminosity class (this is usually constrained by determining the star's surface gravity). I is a supergiant, II, III and IV are bright, normal and sub-giants respectively, and V is a dwarf or main-sequence star. VI can be used for a star even dimmer than a regular dwarf, and the supergiant category is further subdivided into Ia, Iab and Ib from most to least luminous. Extra letters are added to symbolise peculiarities that mean the spectrum does not fit into the normal sequence, or has specific lines in emission. Much of the classification of the hottest stars has been accomplished most fully by Walborn (1990), whilst an important atlas of spectral peculiarities is presented in Walborn & Fitzpatrick (2000). Maíz-Apellániz et al. (2004) and Sota et al. (2008) present a comprehensive catalogue of O stars in the Milky Way, including a detailed list of qualifications for spectral type letters to be assigned.

Massive stars are defined chiefly by their initial mass, which must be above $\sim 8M_{\odot}$ at birth if they are to end their lives as core-collapse supernovae (see §1.1.2). The term 'massive star' can refer to any object that is thought to fulfil this criterion and can lie at any evolutionary stage. Hence OB stars on the main sequence, Wolf-Rayet (WR) stars of all types, Luminous Blue Variables (LBV) and red and yellow supergiants are all known as massive stars.

### 1.1.1 Effects of and importance of massive stars

Stars of great mass belie their rarity by acting as dominant forces in galactic dynamics and chemistry. Their prolific winds are driven to terminal velocities up to around a few thousand km $s^{-1}$, and at some evolutionary stages are thought to expel material at a rate in excess of $10^{-5} M_{\odot} yr^{-1}$. The combined effect of this copious mass-loss and the intense radiation coming from the star generally pushes out and ionizes the natal cloud in which the star was born, leaving stunning telescopic vistas and fascinating testbeds of interstellar conditions. This disruption of material is thought to constitute a 'trigger' in triggered star formation, as interstellar clouds are perturbed into contraction.

On a larger scale, the total effect of many massive stars in a cluster acting together can also trigger star formation (e.g. Lee & Chen 2007). Winds and supernova ejecta form galaxy-scale superwinds which can be observed as high-energy, high-velocity streams of material emanating from galaxies (e.g. Westmoquette et al. 2005).

Massive stars contribute enormously to the production of heavy elements through fusion in their cores, burning hydrogen via the CNO-cycle during their main-sequence lifetimes, then switching to helium-burning upon becoming a Wolf-Rayet star, then carbon, oxygen, silicon and so on until the core collapses and rebounds to produce a supernova. This supernova is energetic enough to fuse elements heavier than iron.

Cosmologically speaking, massive stars may play a very important role at early times in the Universe. They are thought to be at least partly responsible for re-ionization of the Universe at redshifts greater than z = 6. A clear relationship between their wind-momentum and their luminosity could also act as an extra-galactic distance indicator (Kudritzki et al. 1995), which would be key if type Ia supernovae are not the accurate standard candles they were once thought to be.

After the final supernova explosion, massive stars leave behind remnants in the form of either neutron stars or black holes. These exotic phenomena are laboratories in which to study relativistic physics, and physics at very high energy and density.

There is a broad context to the study of mass-loss in particular that must not be ignored. Apart from having interesting properties of their own, stellar winds have knock-on effects, and mass-loss rates are important. Models exist that simulate young populations of massive stars, which in turn are key in studying the dynamics and star formation rates and histories of clusters and galaxies. One of the key ingredients to these models is a precise

knowledge of the mass-loss rates of the massive stars. In addition, mass-loss rates from massive stars are important in determining chemical yields in galactic chemical evolution, particularly in the quest to find out exactly how much carbon is produced in the formation and evolution of the galaxy. Precise knowledge of mass-loss rates for a large sample of O stars has the potential to serve as an extragalactic distance indicator due to the existence of a Wind-momentum Luminosity Relation (WLR).

### 1.1.2 Evolution of massive stars

It may not be immediately obvious that stars are not constant in their existence. Since they live such long lives compared to the average observer (!) it is only by studying their properties in-depth that we see that they change, and they evolve. Perhaps the best way to investigate the evolution of stars is by utilising a Hertzprung-Russell diagram, named after its co-initiators Ejnar Hertzprung and Henry Norris Russell in the early part of the twentieth century. In a H-R Diagram, the derived luminosity and effective temperature of a star are plotted. An example of such a diagram for the solar neighbourhood is shown in 1.1.

**Figure 1.1.** A Hertzsprung-Russell diagram for the local neighbourhood. (Credit: Goddard Space Flight Center - http://imagine.gsfc.nasa.gov/docs/science/know_l2/stars.html)

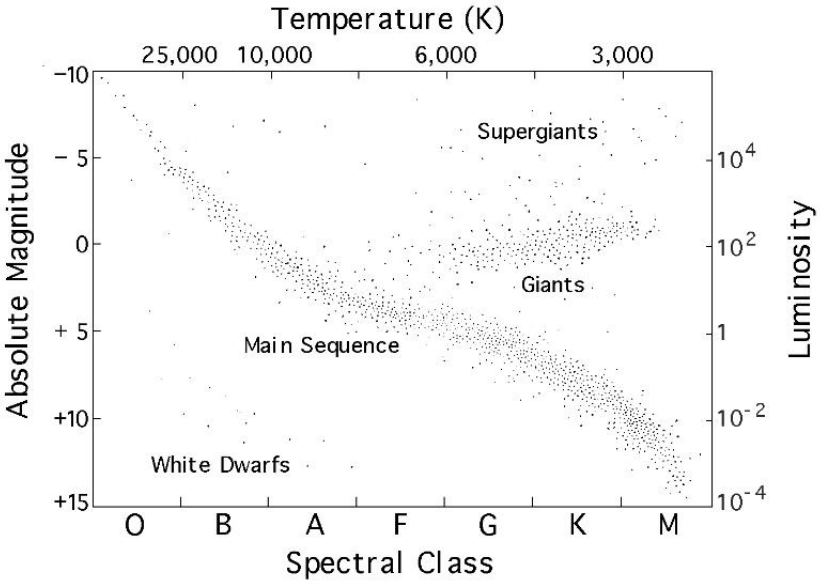


That most stars seem to lie in a diagonal band or are clustered in certain parts of the diagram indicates that not all luminosity-temperature combinations are possible. This

diagonal band is known as the main-sequence, and is where stars spend most of their lives. Because we assume that stars generally only differ in their ages or their initial mass, a star's position on this diagram must be due to one or both of these characteristics. We observe H-R diagrams for different populations of stars, and discover more objects in the upper-right (red giants) and lower-left (white dwarfs) portions of diagrams where the main sequence is comparatively depleted. In a broad sense we can hence conclude that being in the main sequence or not is dependent upon stellar age, and position on the main sequence is dependent upon initial mass.

As it turns out, stars with high initial masses appear in the upper-left part of the main sequence, whilst stars with low initial mass appear on the lower-right. As this thesis is concerned only with massive stars with initial masses greater than around $8M_{\odot}$, we will concentrate on describing the evolution of those.

The main-sequence lifetime of any star is proportional to it's mass, and inversely proportional to it's luminosity. Since the luminosity itself is inversely proportional to the cube of the mass, this means that the lifetime

$$\tau \propto M^{-2}. \tag{1.1}$$

For a $20M_{\odot}$ star, knowing the solar lifetime to be about 10 billion years, we deduce that the lifetime of this star will be about 2.5 million years.

The following picture of the evolution of a massive star (in this case one of $60M_{\odot}$) is current, but it may be in some jeopardy due to uncertainty in the mass-loss rates of some hot stars, in addition to effects such as stellar rotation and magnetism not being fully understood.

- To begin with, a cloud of mostly hydrogen begins to gravitationally collapse due to density variations. As it gets smaller and denser, so it gets hotter and eventually the core of the collapsed protostar reaches a high enough temperature for hydrogen fusion to begin. The process of converting hydrogen into helium is known as hydrogen 'burning', and it is a process that releases vast quantities of radiative energy. The pressure from this radiative flux pushes away the remnants of the natal cloud, often forming evacuated cavities in HII regions. The high energy from the star also ionizes the remaining hydrogen in the cloud (such that the presence of ionized hydrogen is a

useful indicator of star formation). The star is now said to be on the main sequence, where it will stay for most of its life. During this phase a massive star will burn hydrogen in its convective core via the CNO-cycle. During this time the star will be steadily losing mass from its outer atmosphere, and by the end of the main sequence, which generally lasts for a few million years, it will have lost a significant portion of its total mass. At this stage the H in the core is exhausted and the products of nuclear burning will be visible at the surface due to mixing by convection.

- The core is now inert and contracts, and H burning begins in a shell around the core. The star moves right across the HRD, becoming unstable and undergoing major eruptions in the Luminous Blue Variable (LBV) phase. This causes the star to contract and move back to the left on the HRD, and the greater temperature in the core due to gravitational energy ignites helium burning

- The core He-burning phase of a massive star is known as the Wolf-Rayet stage, and lasts for a few hundred thousand years. The star moves quite steadily to the left on the HRD and has a very strong stellar wind, with a much higher rate of mass-loss than on the main sequence. The star is initially classified as a nitrogen rich Wolf-Rayet star, or WN, until it has lost all evidence of H-burning due to mass-loss. As the products of He-burning are seen at the surface the star becomes a WC, or carbon-rich Wolf-Rayet star.

- The WC phase, thought to last about the same amount of time as the WN phase, ends, and the star moves on to burning other elements. It goes through a repeated sequence of core-contraction and burning a new element, first C, then O and Si and so on until it has an 'onion skin' structure around an iron core. It is no longer possible to generate energy by core-burning as Fe has the highest elemental binding energy and requires energy to be put in. These later stages are very rapid and take about a year in total.

- No longer being sustained by radiation pressure, the core contracts and heats. This causes the dissociation of iron nuclei into protons and neutrons and the core collapses further to compensate. The density becomes so high that each proton captures an electron and emits a neutrino, forming a neutron. This neutron core becomes degenerate and shock waves rebound off it transferring large quantities of energy to

the stellar envelope, ejecting the envelope in a great explosion - a supernova. The remnant left behind will be either a neutron star or a black hole, depending upon the initial mass of the star. The threshold in initial mass for yielding a black hole rather than a neutron star is thought to lie at about $25M_{\odot}$.

The exact stages a massive star passes through depend on its initial mass, for example stars that begin with less than $40M_{\odot}$ are thought to have a 'red loop' on the HRD. In other words they spend some time as a red supergiant. There is indeed some debate as to the exact nature of core-collapse supernova progenitors (see Smartt (2009) for details on the current discussion). Crowther (2007) suggests the following scheme of evolution for O stars of different initial masses:

$\geq\sim 75M_{\odot}$

$$O \rightarrow \mathrm{WN(H-rich)} \rightarrow \mathrm{LBV} \rightarrow \mathrm{WN(H-poor)} \rightarrow \mathrm{WC} \rightarrow \mathrm{SN\,Ic},$$

$\sim 40-75M_{\odot}$,

$$O \rightarrow \mathrm{LBV} \rightarrow \mathrm{WN(H-poor)} \rightarrow \mathrm{WC} \rightarrow \mathrm{SN\,Ic},$$

$25-40M_{\odot}$,

$$O \rightarrow \mathrm{LBV/RSG} \rightarrow \mathrm{WN(H-poor)} \rightarrow \mathrm{SN\,Ib}.$$

Stars of less than $25M_{\odot}$ initial mass are thought to become RSGs, and do not pass through the LBV phase. There is an observed upper boundary to the HR-diagram, where we see no very luminous RSGs, compared to BSGs. This limit is known as the Humphreys-Davidson limit and occurs at about $\log L/L_{\odot} = 5.8$ for $T_{eff} < 15kK$. Stars that are near or just inside the limit are observed to be unstable; becoming Luminous Blue Supergiants. Their position is inferred to be connected with the Eddington limit.

Figure 1.2 shows some standard evolutionary tracks showing the post main-sequence course across the HRD of stars of different masses. Rather importantly, these tracks are very sensitive to mass-loss rate of the star. Crucially, Hirschi et al. (2008) conclude that the current evolutionary models could not survive anything more than a change in estimated mass-loss rates in the post-main-sequence of a factor of $\sim$2, compared to the predictions of Vink et al. (2000). This again highlights the urgent importance of obtaining accurate

estimates of mass-loss.

Main sequence O stars, given a lifetime of 2.5 million years and an initial mass of $20M_{\odot}$, will lose around $0.25M_{\odot}$ of it's mass during this time, assuming a mass-loss rate of $10^{-7}M_{\odot}yr^{-1}$. This would be halved by reducing the main-sequence mass-loss rate by 2. This difference is not as great as reducing by 2 the mass-loss rate of a supergiant or WR star, but when the fine tuning of the mass-loss parameter determines the exact outcome of the star's life, it remains important to constrain the mass-loss rate for O dwarfs accurately too.

**Figure 1.2.** Post main sequence (PMS) evolutionary tracks from Schaller et al. (1992) for a $60M_{\odot}$ star. The black track is 'standard', and the red is for a mass-loss rate a factor 2 higher. A: beginning of PMS; B: tracks begin to diverge; C: end of evolution for standard model; D: end of evolution for high $\dot{M}$ model.

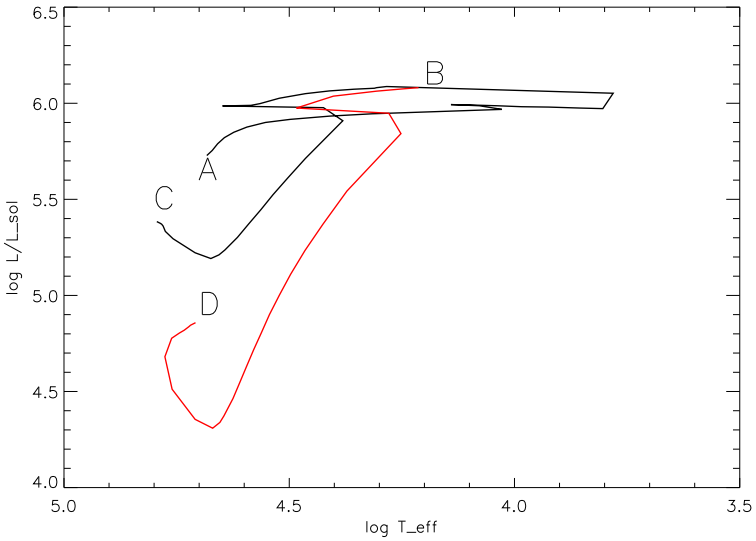


## 1.2 O stars

O stars lie at the hot end of the MK spectral classification scheme. They are blue in visible colour, and their peak intensities occur in the ultraviolet. In the Milky Way they have effective temperatures ranging from $\sim$ 30000K to $\sim$ 50000K (Martins et al. 2002), and temperatures higher by a few thousand Kelvin in the nearby Magellanic Clouds (Massey et al. 2005). This higher measured effective temperature is explained by the presence of less wind emission in temperature diagnostics, wind blanketing causing thermal backwarming, and a change in opacity in metal line blanketing due to the decreased metallicity. O stars

are classified chiefly by measuring certain optical lines. The classifications of Walborn, summarised in Walborn & Fitzpatrick (1990), follow the approximate methods of the MK classification system in using a morphological scheme to classify O stars. In this system a clear progression in morphology of lines is seen through the spectral types, and a spectral type can be assigned according to the presence and relative intensities of lines. Figure 1.3 shows how the relative strengths of HeI and HeII lines progress from type O6.5 to O8. These lines are also utilised in the quantitative scheme of Conti & Alschuler (1971), which was developed concurrently with the Walborn method. The latter scheme uses a measure of the relative equivalent widths of the two lines,

$$W' = \log W(HeI_{4471}) - \log W(HeII_{4541}), \tag{1.2}$$

to determine the spectral type that should be assigned.

We view only a portion of the flux emitted by stars, in the band of the electromagnetic spectrum through which we are observing. In order to convert a flux or luminosity in the visible band to the total flux or luminosity over the whole spectrum (the bolometric flux or luminosity), we must apply a bolometric correction. Bolometric corrections are defined in magnitude units by

$$BC = M_V - M_{bol}. \tag{1.3}$$

Stars like the Sun will have a relatively small bolometric correction since most of their flux is emitted in the visible band. O stars on the other hand emit mostly in the UV, and so it will require a larger correction from the visible magnitude. Since it follows a relation with spectral type, the BC can also be calibrated against the effective temperature of stars. Martins et al. (2005*a*) showed that for O stars

$$BC = 27.58 - 6.8 \log T_{eff}. \tag{1.4}$$

**Figure 1.3.** Helium lines change in relative strength with spectral type. Top to bottom: O6.5, O7, O7.5, O8.

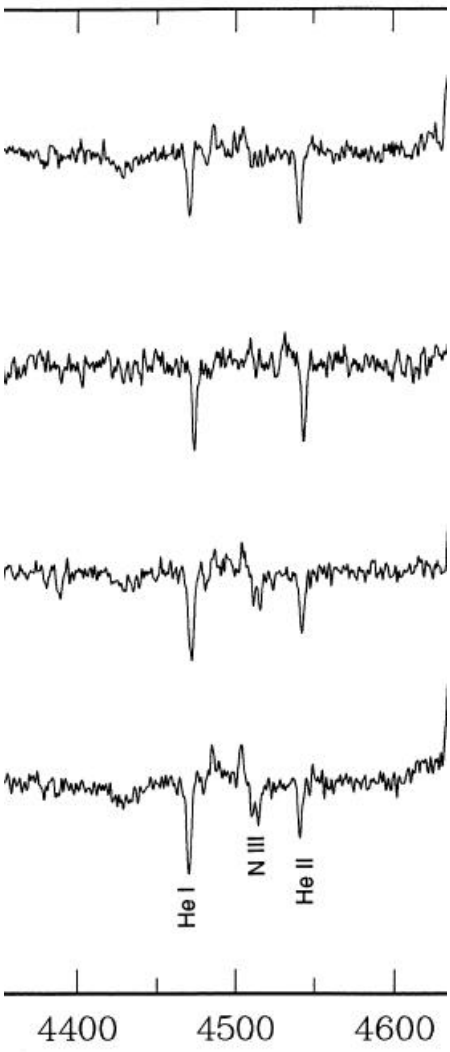


### 1.2.1 Modelling O stars

Local Thermodynamic Equilibrium (LTE) is valid if there is thermodynamic equilibrium at the local values of temperature and density. Under these conditions, the source function is given by a Planck function, $B_\nu(T)$, the excitation and ionization states of the gas are well-determined by the Boltzmann and Saha equations, and the particles follow a Maxwellian velocity distribution.

In the case of O stars, the LTE approximation breaks down and LTE models tend to under-predict the strength of spectral lines. To obtain adequate fits with LTE one needs unrealistically high values for the surface gravity ($\log g \sim 4.5$) compared to expected values

($\log g \sim$4.0), and helium abundances higher than the cosmic proportion. Non-LTE analysis is necessary to account for overpopulation of some atomic levels and underpopulation of others.

The first non-LTE analysis which dealt with hydrogen and helium lines in O stars was performed by Auer & Mihalas (1972), who showed that at high temperatures (>30000 K) LTE suffered complete breakdown. Using new NLTE techniques they fit profiles far better (see Fig. 1.4).

**Figure 1.4.** Fits to helium lines by Auer & Mihalas (1972), showing the improvement using NLTE

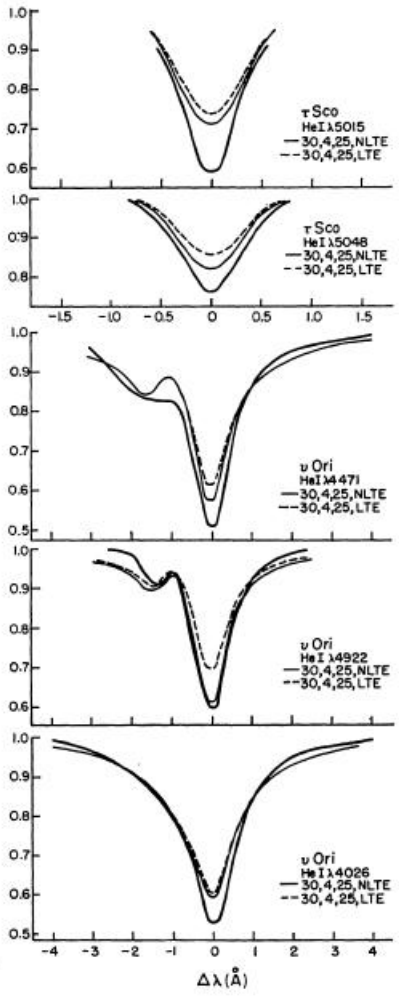


Huge advancement has taken place over the last few decades and there are several model atmosphere codes that deal with a variety of physical effects and processes (Hillier

& Miller 1998; Puls et al. 1996; Hubeny & Lanz 1995; Pauldrach et al. 1998; Hamann & Gräfener 2003). Through accurate modelling of O stars and comparing to observations, physical and wind parameters can be constrained and used to make predictions about the evolutionary behaviour of these stars.

## 1.3 Mass-loss and line-driven winds

Stellar winds due to mass-loss are the continuous outflow of material from the outer layers of stars into the interstellar medium. The closest example to earth of such a continuous outflow is our own Sun, which ejects mass via a relatively quiescent solar wind. It is a cool star ($\sim$ 5800K), but pressure expansion from an extremely hot (million Kelvin) corona drives material from the surface at a rate of about 2-3$\times 10^{-}14 M_{\odot} yr^{-1}$. The contrasting situation in hot stars, which don't have the surface convection zone required to produce mechanical energy to superheat a corona via magnetic re-connections, is that the stellar winds are at around the same temperature as the stellar surface. It is the intense radiative flux coming from the star's convective core that produces the necessary pressure to drive off matter.

The idea that atoms can become perturbed in a stellar atmosphere due to radiation pressure was discussed early in the twentieth century (e.g. Milne 1926). It became obvious that photons streaming from the stellar interior, carrying a momentum $h\nu/c$, could transfer that momentum to metal ions and force them out of the atmosphere via a radiative acceleration. It was appreciated that this would be efficient in spectral lines due to the Doppler effect. Work following the earliest UV observations of stars in the 1960s (e.g. Morton 1967) resulted in the realisation that if the acceleration gained by metal ions could be shared with the bulk plasma (hydrogen and helium) then a substantial amount of mass could be lost by the hottest stars. The first theories of line-driven winds were produced by Lucy & Solomon (1970) and Castor et al. (1975), and it became clear that such large rates of mass-loss would significantly affect the evolution of massive stars. Indeed the hottest stars are thought to lose a substantial fraction of their total mass during their relatively short lifetimes. Friend & Abbott (1986) improved on these early models by correcting for the finite size of the star (rather than considering it as a point) and accounting for the centrifugal force due to the star's rotation. The effect of these changes was to reduce expected mass-loss rates, increase the predicted terminal wind velocity and to cause

acceleration in the wind to be far more gradual. These new models were in far better agreement with observations. Work by Pauldrach et al. 1986; Pauldrach 1987; Pauldrach et al. 1994 also made great steps in making improvements to line-driven wind theory by adding in refined physics and allowing the calculations of synthetic ultraviolet spectra for comparison to observations taken by the likes of the *IUE* and *Copernicus* satellites. Subsequent codes, perhaps most notably CMFGEN (Hillier 1990; Hillier & Miller 1995, 1998) began to implement line-blanketing (the combined effect of multiple overlapping lines) into the treatment, resulting in changes to the predictions of fundamental physical parameters. The rest of this section focuses on how winds are thought to be driven by radiation pressure through spectral lines.

Let us first examine the effect of the stellar radiative force due only to the scattering of free electrons, which is a frequency-independent process. The flux of radiative energy at a radius $r$ is given by $L/4\pi r^2$, and corresponds to a radiative momentum flux of $L/4\pi r^2 c$, where $c$ is the velocity of light. The opacity of material intercepting this flux for electron scattering is $\kappa_e = \sigma_e/\mu_e$, where $\sigma_e$ is the Thomson scattering cross-section ($0.66 \times 10^{-24} cm^2$) and $\mu_e$ is the the mean atomic mass per free electron. The radiative acceleration from free electron scattering is merely the product of the radiative momentum flux and the opacity,

$$g_e(r) = \frac{\kappa_e L}{4\pi r^2 c} \tag{1.5}$$

The ratio of the radiative acceleration to the gravitational acceleration of the star is known as the Eddington parameter, and is a fixed constant for each star:

$$\Gamma_e = \frac{\kappa_e L}{4\pi G M c}. \tag{1.6}$$

For hot, massive stars this ratio approaches unity, meaning that in principal the scattering of free electrons needs only a modest extra effect in order to counteract gravity, allowing material to escape. It is not that the star as a whole exceeds the Eddington limit, but that material near the surface just needs some extra acceleration to exceed gravity and become unbound from the stellar surface. Acceleration through spectral lines accomplishes this feat. Interaction of incident photons of just the right frequency with

bound electrons in atoms will cause a scattering. This scattering has a resonance due to the precise frequencies at which the electrons can be excited. This resonance ensures that line scattering is far more efficient at imparting momentum to material than electron scattering, which is a grey process.

However, if the wind was not moving and subject to the Doppler effect, line absorption would mean that radiation would be completely absorbed by the lower layers of the stellar atmosphere, and the upper layers would not see radiation at the spectral line frequency. In the frame co-moving with the gas, the wind sees the photospheric radiation as red-shifted. The velocity gradient present in the atmosphere means that radiation not absorbed lower in the atmosphere can be absorbed higher up at a different frequency. In essence the Doppler effect allows atoms to absorb continuum radiation which has had its frequency changed such that it is now within the line profile. Radiation pressure in spectral lines is therefore a very efficient driving mechanism. The acceleration comes about as ultraviolet photons are absorbed and re-emitted in resonance lines of elements with relatively high abundances, particularly C, N, O and Fe (lower abundance elements such as P, S and Si also play a significant part). Momentum is transferred to the ions from different directions, but there is a net outward motion as other directions cancel each other out. The momentum gained by the metal ions is shared with other constituents of the wind that make up the bulk of the plasma, predominantly hydrogen and helium. This occurs via coulomb collisions. It can be shown that it takes around $10^9$ absorptions per absorbing ion (Lamers & Cassinelli 1999) to accelerate the wind to the terminal velocities ($v_\infty$) observed and that the terminal velocity is reached within a few stellar radii. Since the time taken to reach that terminal velocity is around $10^4$ seconds, the number of photons absorbed per second is about $10^5$. This means that only atomic transitions that have short lifetimes make a large contribution to the line-driving. This includes mostly strong resonance transitions producing lines like CIV (1550Å), NV (1240Å) and SiIV (1394, 1403Å).

An atom absorbs a photon when the photon frequency lies in the absorption line profile $\phi(\Delta\nu)$, where $\Delta\nu = \nu - \nu_0$. Since collisional broadening can generally be neglected in tenuous stellar winds, the line width is determined only by thermal motions of the gas and hence represented by a Gaussian function. Because the wind is moving, a photon will be absorbed if along its path it encounters an ion with the right velocity to Doppler shift it into the line profile. This position in the wind is known as the interaction region.

### 1.3.1 The Sobolev Approximation

Sobolev (1960) assumed that the interaction region in an expanding stellar atmosphere was infinitely narrow when deriving the equations of radiative transfer. This means that the line width $\phi(\Delta\nu)$ is very small compared to the velocity gradient in the wind. This is known as the Sobolev approximation, and the interaction region essentially reduces to a single point called the Sobolev point, at a radius $R_s$. The radiative transfer is hence reduced to a local problem and determined by the conditions at $R_s$. The line optical depth, normally an integration over distance, only needs to be evaluated across the local velocity gradient.

$\Delta\nu_G$ is defined as the width of a Gaussian and we assume that the spectral line profile extends to $1.5\Delta\nu_G$ either side of the line centre, $\nu_0$ (since the line absorption coefficient at $1.5\Delta\nu_G$ is less than 10% than that at the line centre). A photon of frequency $\nu_p$ emitted along a line $z$ can be absorbed by a line transition in its path if it encounters ions with a $z$-velocity such that its Doppler shift brings it within the line width of the transition, in the rest-frame of the ion. In other words,

$$\nu_0 - 1.5\Delta\nu_G \leq \nu_p \left(1 - \frac{v_z}{c}\right) \leq \nu_0 + 1.5\Delta\nu_G \tag{1.7}$$

Photons emitted with a frequency less than $\nu_0 - 1.5\Delta\nu_G$ will have too low a frequency to be absorbed by the transition anywhere in the wind. Photons with frequency greater than

$$\frac{\nu_0 + 1.5\Delta\nu_G)}{(1 - v_\infty/c)} \tag{1.8}$$

cannot be absorbed as they have too high a frequency.

The local optical depth in this scenario, known as the Sobolev optical depth, can be approximated as

$$\tau = \frac{\kappa\rho v_{th}}{dv/dr} \tag{1.9}$$

where $\kappa$ is the line opacity, $\rho$ is the local density, $v_{th}$ is the velocity due to the thermal

properties of the material and the denominator is the local velocity gradient. We can write the following general expression for the line acceleration

$$g_{line} \approx g_{thin} \frac{1 - e^{-\tau}}{\tau} \tag{1.10}$$

In a hot stellar wind many of the wind-driving lines are optically thick due to the relatively high density of the outflow, and in the case where $\tau \gg 1$,

$$g_{thick} \approx \frac{g_{thin}}{\tau} = \frac{L}{4\pi r^2 \rho c^2} \frac{dv}{dr} = \frac{L}{\dot{M} c^2} v \frac{dv}{dr} \tag{1.11}$$

where we have used the equation of mass continuity which defines the mass-loss rate as

$$\dot{M} \equiv 4\pi \rho v r^2 \tag{1.12}$$

This is a rather different expression than that which is seen in the optically thin ($\tau \ll 1$) limit, which is similar to the electron scattering case:

$$g_{thin} \equiv \frac{\kappa v_{th} \nu_0 L_\nu}{4\pi r^2 \rho c^2} \approx \frac{\kappa}{\kappa_e} \frac{v_{th}}{c} g_e \tag{1.13}$$

in which the assumption is that the line frequency $\nu_0$ is near the peak of the stellar luminosity spectrum and so $\nu_0 L_\nu = L$.

These expressions assume that the star acts as a point source (i.e. photons are radially streaming), that the Sobolev approximation holds and that each photon scatters just once.

Whilst the optically thin limit has a dependence upon the opacity, the optically thick limit instead is independent of it, and is proportional to the velocity gradient. This means that the rate at which stellar radiation is shifted into a resonance line transition depends on how steep the local velocity law is. This implies that an optically thick line force depends on the wind's rate of acceleration, rather than the Newtonian way of understanding force and acceleration, which is that the former causes the latter.

### 1.3.2 How to drive a wind

Hot stellar winds are in fact driven by a multitude of lines acting in concert. The number of optically thick lines driving a wind actually depends on the mass-loss rate itself. The first self-consistent formalism to solve radiative transfer including this effect was by Castor et al. (1975) (CAK), following Lucy & Solomon (1970). What follows is a simplified formulation showing how it is possible to drive a wind through spectral lines, but the full formal CAK derivation should be sought from the original work.

To begin with, the following simplifying assumptions are made

1. The star is considered as a point source, such that photons coming out of the photosphere are following the radial vector
2. The wind is driven only by *strong* lines, that is with an optical depth $\tau \gg 1$
3. The local velocity gradient at any point being considered is $\Delta v = \frac{dv}{dr}\Delta r$, and the range of frequencies absorbed by a line is dependent upon the Doppler formula

We use equation 1.11 to represent the acceleration due to one optically thick line, and then sum over all the lines we wish to include, leaving us with

$$g_{lines} = \frac{L}{\dot{M}c^2} N_{eff} v \frac{dv}{dr} \tag{1.14}$$

where $N_{eff}$ is a dimensionless quantity representing the effective number of lines driving the wind.

If we wish to determine the overall acceleration of the wind we must also include the effect of continuum opacity and of the counteracting inward gravity, although we may leave out gas pressure as a negligible effect. In essence

$$g_{tot} = g_{lines} + g_{cont} - g_{grav}. \tag{1.15}$$

If the continuum opacity is provided purely by electron scattering then we use equation

1.5 to represent the acceleration, and gravity by

$$g_{grav} = \frac{GM_*}{r^2} \tag{1.16}$$

changing equation 1.15 into

$$g_{tot} = g_{lines} + \frac{\kappa_e L}{4\pi r^2 c} - \frac{GM_*}{r^2}. \tag{1.17}$$

Using a substitution of Eddington's parameter $\Gamma_e = \frac{\kappa_e L}{4\pi c G M_*}$ we obtain

$$g_{tot} = g_{lines} - \frac{GM_*}{r^2}\left(1 - \Gamma_e\right). \tag{1.18}$$

We can then replace the term $M_*(1-\Gamma_e)$ by the effective mass, $M_{eff}$ giving us

$$g_{tot} = g_{lines} - \frac{GM_{eff}}{r^2}. \tag{1.19}$$

It is clear that if we wish the wind to be driven then we need the total radiative acceleration to be a positive value and therefore that $g_{lines} > \frac{GM_{eff}}{r^2}$ or

$$\frac{L}{\dot{M}c^2} N_{eff} v \frac{dv}{dr} > \frac{GM_{eff}}{r^2}. \tag{1.20}$$

In the limit that each photon in a stellar wind scatters only once, the mass-loss rate can be given as

$$\dot{M} \simeq N_{eff} L/c^2 \tag{1.21}$$

We can use some typical values for the luminosity and mass-loss rate to infer the number of optically thick lines that are required to drive a wind. Using $L \simeq 10^5 L_\odot$, $\dot{M} \simeq 10^{-6} M_\odot yr^{-1}$, then we find that we need of the order of hundreds of optically thick

lines in order to drive the acceleration of a typical O-star wind.

## 1.4 Measuring Mass-loss

Stellar winds are relatively dense (compared to the interstellar medium, for example) and therefore optically thick to many atomic transitions. In a stellar spectrum these scatterings within Doppler-shifted line-widths cause a characteristic wind profile to develop - a P-Cygni profile. It is named for the Luminous Blue Variable star P-Cygni, in which this spectral phenomenon was first appreciated as significant in the study of stellar winds.

Figure 1.5 demonstrated how these profiles are formed. As the stellar wind expands in all directions, we see different effects from different parts of the wind due to the perspective of the observer's vantage point. A column of expanding material in front of the stellar disk (F) scatters photons out of the line of sight, leading to an absorption trough in the spectrum. Since this part of the outflow is approaching the observer, the scattering absorption trough is blue-shifted in wavelength/frequency. This same scattering process is of course happening everywhere in the wind, but in the halo (H) of the wind seen around the stellar disk we see light scattered into the line of sight, leading to spectral emission. This emission occurs at a range of velocities from either the approaching or receding hemispheres and so produces a roughly symmetric profile (some asymmetry comes from the star occulting some of the wind (O)), which when superimposed upon the blue-shifted absorption gives us the characteristic shape seen in Figure 1.5. The precise shape and size of such P-Cygni profiles is dependent on a number of factors. The rate of mass-loss modifies the strength of the profile such that the greater the mass-loss, the higher the number of scattering ions at each velocity and so the deeper the absorption trough and more intense the emission peak. The precise shape of the whole profile is determined by the density spread of material in the line forming region, by the size of the wind region where scattering occurs compared to the star, and by the velocity law. Back-scattering of photons is a larger effect when the star is relatively large compared to the scattering region, and so the emission peak is reduced. If the line is formed close to the star and the wind is accelerating slowly, then matter will pile up in the line forming region and create more emission. The run of velocity with radius therefore has an effect on the shape of

**Figure 1.5.** How a P-Cygni profile is formed, from Lamers & Cassinelli (1999). See text for details.

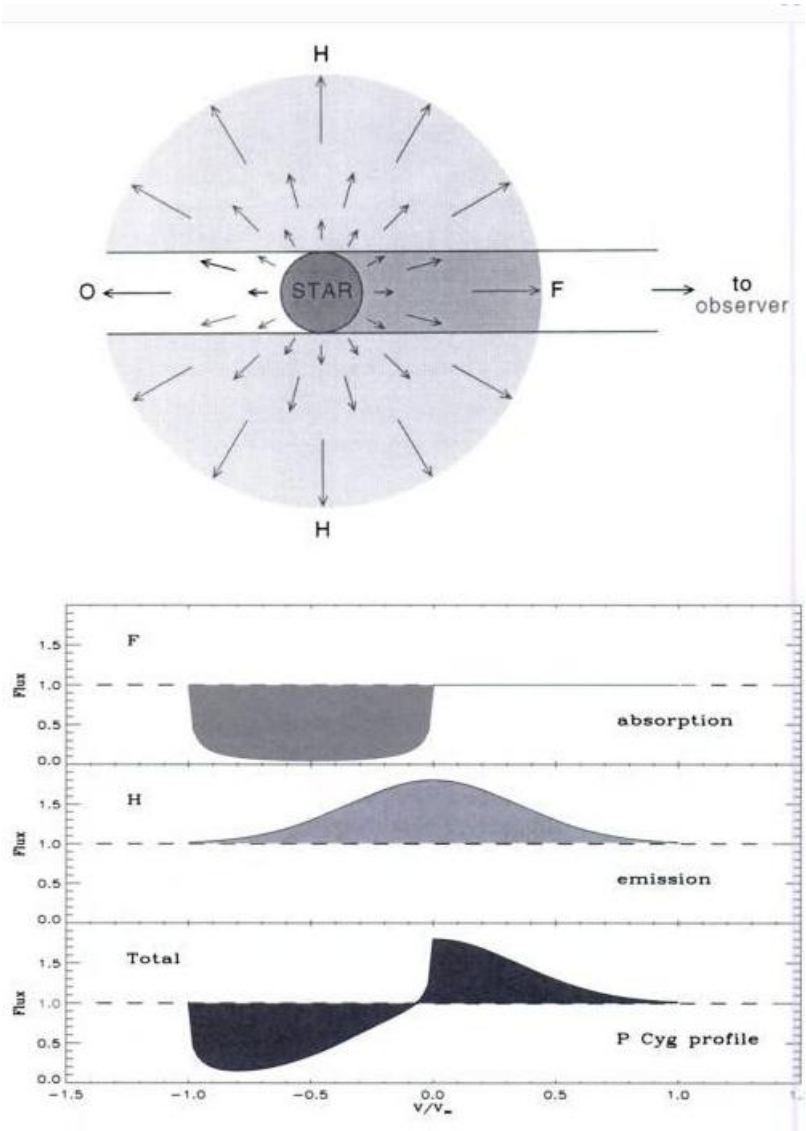

P-Cygni profiles. We assume a velocity law of the form

$$v(r) = v_0 + (v_\infty - v_0)\left(1 - \frac{R_*}{r}\right)^\beta \tag{1.22}$$

where $\beta$ dictates the 'steepness' of the velocity law, or how quickly the material accelerates. A low value of beta results in a quickly accelerating wind, whilst a high value corresponds to a slowly accelerating wind. In a quickly accelerating wind the emission peak of the P-Cygni profile will tend to be reduced compared to a slowly accelerating one. $\beta$ tends to have a value around 0.8 - 1.0 in O star winds, and is higher in cooler objects.

Terminal velocities of stellar winds are an important parameter and can be derived from measuring the position of the edge of saturated absorption troughs in P-Cygni profiles or the position of narrow absorption components in unsaturated lines (see Prinja et al. 1990). The terminal velocity is defined to be the most blueward point of zero intensity in a saturated P-Cygni profile, although due to macroturbulent motions in the wind there is some absorption at higher velocities.

Perhaps the most common method of measuring stellar wind parameters empirically through UV P-Cygni profiles is modelling using the 'Sobolev with Exact Integration' technique of Lamers et al. (1987), which will be described in detail in Chapter 5. It requires strong, unsaturated profiles to get an estimate of the product $\dot{M}\langle q_i\rangle A_E$, where $\dot{M}$ is the mass-loss rate, $\langle q_i\rangle$ is the ion fraction of the line being fitted, and $A_E$ is the elemental abundance. In general the abundance can be well constrained, and the ion fraction is often the main uncertainty, leading to issues such as the 'PV problem' (see §1.5). Problems with observing at UV wavelengths include the need to observe in space (the atmosphere absorbs most UV light), and the fact that interstellar extinction gets worse with decreasing wavelength (see Fig 1.4).

There are several other methods of determining mass-loss from hot stars, some of which are described briefly here. It was shown by Klein & Castor (1978) that the strength of the H$\alpha$ emission line, formed by recombination close to the photosphere, was sensitive to the mass-loss rate in the most luminous stars. By correctly fitting it the mass-loss parameter can be deduced. The technique was improved by Leitherer (1988) and Drew (1990), and adapted into a high-speed code (FASTWIND) by Puls et al. (1996). It is found that the line luminosity of H$\alpha$ is proportional to the quantity $(\dot{M}/v_\infty)^2$, so if the

**Figure 1.6.** Interstellar extinction gets greater in the ultraviolet.

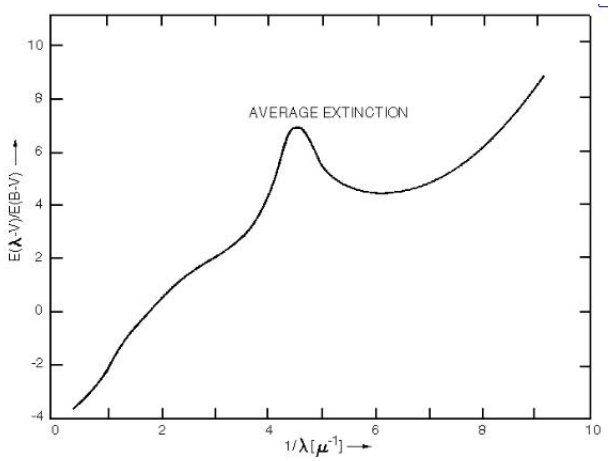


terminal velocity can be determined from another diagnostic (such as a saturated UV P-Cygni profile) then the mass-loss rate is straightforward to find out. A clear advantage of this technique is that the line in question lies in the optical part of the electromagnetic spectrum and is easily obtained from ground-based telescopes. On the other hand only the highest luminosity hot stars have high enough mass-loss rates for H$\alpha$ to display emission over their bright photospheric continua. The mass-loss rate of some less luminous stars can in theory be calculated by measuring how much the photospheric profile is 'topped up' by wind emission. For this method, one requires an accurate knowledge of the velocity law and a good model of the underlying photospheric profile. Since H$\alpha$ is formed through recombination it is a diagnostic which scales with the square of the density, and is therefore sensitive to wind-clumping (see §1.5).

Another key method for calculating mass-loss is by measuring the level of excess flux at radio and infrared wavelengths. Due to Brehmstrahlung free-free scattering, a star with an appreciable wind will have a higher radio flux than if there were no wind. The work of Wright & Barlow (1975) and Panagia & Felli (1975) showed that

$$\frac{\dot{M}}{v_\infty} = 0.095(F_\nu D^2)^{0.75} \left(\frac{\mu^2}{Z^2 \gamma_e}\right)^{0.5} (\nu g_{ff})^{-0.5} \tag{1.23}$$

where $\gamma_e$ is the number of free electrons per ion, $\mu$ is the mean atomic weight, $Z$ is the r.m.s. charge of atoms and ions, $D$ is the distance to the star and $F_\nu$ is the radio flux in

Janskys. The term $g_{ff}$ is the Gaunt factor for free-free emission given by

$$g_{ff} \simeq 1.37 T_w^{0.135} \lambda^{0.084} \tag{1.24}$$

where $T_w$ is the wind temperature and $\lambda$ is the wavelength in question.

**Figure 1.7.** Illustration of excess radio flux due to a wind, using the case of P-Cygni. From Lamers & Cassinelli (1999)

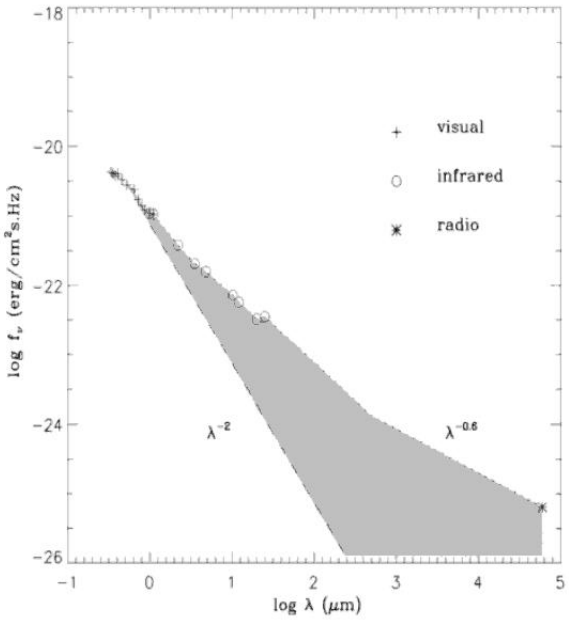


Abbott et al. (1980, 1981) followed this with investigations using the Very Large Array (VLA), whilst Lamers & Waters (1984*a*,*b*) refined the method and examined the possible effects of isothermal wind-clumping upon the flux levels. Perhaps the greatest advantage of this approach is that the excess radio flux emanates from the terminal wind velocity regime in the wind, and so the measurement is simple provided this quantity is known. On the downside, this kind of emission is weak so the method only really applies to nearby or very bright objects (although the improved sensitivity of the MERLIN and VLA arrays (e-MERLIN and EVLA) will allow more objects to be encompassed - see Chapter 7). One must also be able to gain information from other spectral regimes such as the ionization state of the gas. The distance should also be well determined. Another issue is that of

non-thermal radio emission. If a significant fraction of the observed radio flux is non-thermal then mass-loss rates derived in this way will be systematically overestimated. A number of O stars exhibit non-thermal radio emission, and binarity is likely to play a key role as non-thermal electrons are generated by wind-wind collisions.

Modelling of the X-ray emission spectrum can also yield an estimate of the mass-loss rate. O stars emit soft X-rays, likely due to shocked material accounting for 1% of the wind. The remainder of the wind is unshocked and absorbs X-rays. It can be shown (Cohen et al. 2010) for a model of the X-ray emission spectrum that

$$\tau_* \equiv \frac{\kappa \dot{M}}{4\pi R_* v_\infty} \tag{1.25}$$

where $\tau_*$ is a fiducial optical depth that fits the X-ray emission line profiles, $\kappa$ is the corresponding X-ray continuum opacity of the wind material, and the other symbols have their usual meanings. Since one can generally derive most or all of the other terms in this equation, the mass-loss rate can hence be determined as the only remaining free parameter. Importantly, the X-ray emitting matter in the wind is observed to have the same value of $\beta$ and $v_\infty$ as the bulk of the wind, so these can be derived from other diagnostics. This estimate of the mass-loss rate is dependent on the column density of material and so should not be affected by 'micro-clumping' (see §1.5 ).

**Table 1.1.** The advantages and disadvantages of different mass-loss diagnostics

| Diagnostic | Wind region sampled | Advantages | Disadvantages |
|---|---|---|---|
| UV P-Cygni | whole wind | - interactive fits possible<br>- many profiles available<br>in OB stars | - need ion fraction<br>- interstellar extinction<br>- need to observe above atmosphere |
| Radio | outer wind<br>($\sim 100R_*$) | - in $v_\infty$ region, no $v(r)$ needed<br>- no dependence on wind temperature<br>- lots of recent upgrades<br>to radio facilities, giving<br>enhanced sensitivity | - weak measure; only applies to<br>brightest and/or nearest objects<br>- need to know distance to star<br>- need $v_\infty$<br>- need chemical<br>composition/ionization state |
| H$\alpha$ | near star | - optical is easily accessible<br>- many existing observations | - only brightest objects<br>are in emission, insensitive<br>at later types<br>- clumping affects emission |
| X-rays | whole wind<br>(shocked region) | - resolution much improved<br>with recent observations<br>- no micro-clumping problem | - need $v_\infty$<br>- need good model of $\tau_*$ |

## 1.5 Important current issues in the study of O star winds

The standard model of radiatively driven stellar winds has been very successful in explaining observed spectra in various wavelength regimes. The CAK model with its updates and modifications is possibly one of the most successful theories in physics. However various observational and theoretical evidence points to the shortcomings of this theory in explaining the full picture. There are two chief lines of investigation that have shown the chasm that still exists in our understanding: that some stars appear to have winds with a lower mass-loss rate than predicted; and that winds appear to be structured on different scales. This section highlights the history and current nature of these challenges.

### Weak winds

An interesting theoretical prediction comes out of the equation of motion for a stellar wind. Using scaling relations one finds a modified wind-momentum rate, $D_{mom}$, which depends on luminosity:

$$D_{mom} = \dot{M} v_\infty (R_*/R_\odot)^{\frac{1}{2}} \propto \left( k \frac{L}{L_\odot} \right)^{\frac{1}{\alpha}} \tag{1.26}$$

where $\alpha \simeq 2/3$ for O stars. The logarithm is taken to give

$$\log D_{mom} \approx x \log (L/L_\odot) + D \tag{1.27}$$

with a slope $x$ and an offset $D$. This is known as the Wind-momentum Luminosity Relationship (WLR). It is shown to hold observationally for the hottest and most luminous stars and can be used to determine extra-Galactic distance scales (Kudritzki et al. 1995). As will be seen below however it does not hold for all hot stars.

The mass-loss rates derived for certain O stars have been unexpectedly low. The first evidence for winds thinner and weaker than theoretically predicted was provided by Chlebowski & Garmany (1991). In that study it was shown that mass-loss rates for late O-type dwarfs were up to a factor of 10 lower than expected from the scaling of $\dot{M}$ with $L$ seen for more luminous objects. Analysis of B stars by Kudritzki et al. (1991) and Drew et al. (1994) showed that lower than expected mass-loss rates were needed to fit

observations. The latter proposed that X-ray emission from an outer layer of shocked gas could be penetrating back towards the star and altering ionization conditions, and hence reducing mass-loss rate estimates by the increased ionization and reduced radiative acceleration.

Puls et al. (1996) showed by studying H$\alpha$ that the WLR curves downwards for later type stars with luminosities lower than $\sim 10^{5.3} L_{\odot}$, meaning a breakdown of this well-determined relation in O stars. Since however that study used H$\alpha$, which is not in emission for later type stars, only upper limits were derived, and there remains an uncertainty about mass-loss rates derived from almost purely photospheric H$\alpha$ profiles, as can be seen from Figure 1.9.

One way of explaining why some stars have weaker winds than expected is to consider the coulomb coupling of metals to bulk plasma. In the standard picture, it is predominantly the metal ions which drive the wind and they share their gained momentum via coulomb collisions with the hydrogen and helium, which form the main part of the wind. Springmann & Pauldrach (1992) demonstrated that there are limits to the single-fluid approach in which metals can share their acceleration. Indeed for thinner winds the metal ions can decouple from the rest of the plasma, and the terminal velocity drops. Babel (1995) showed how when using a multifluid method in which coulomb collisions are dependent upon the plasma parameters, there is a reduction in the expected mass-loss rates of A stars. A similar situation may be at work in late-type O dwarfs. Another effect that has the potential to partly explain weak winds involves 'shadowing' by photospheric lines. Babel (1996) found that if CAK theory is updated to include the effects upon the radiative force of the outward velocity, then corresponding mass-loss rates are lower for B stars. Puls et al. (1998) and Owocki & Puls (1999) showed the presence of a third possible effect. They demonstrated that deviations from a smooth wind and from the Sobolev approach, and the inclusion of extra terms in the velocity field near the transonic region of the wind can reduce the line acceleration leading to a lower mass-loss rate. Whilst none of these effects have been shown conclusively to be the case, it became clear from these studies that there were observational and theoretical grounds to be concerned about exactly what rate mass is being ejected from some stars.

Recent important studies have been performed by Martins et al. (2005*b*) and Bouret et al. (2005), in which NLTE fits are made to a number of O stars, with particular attention paid to later spectral types, likely to have the weakest winds. Generally in these studies it

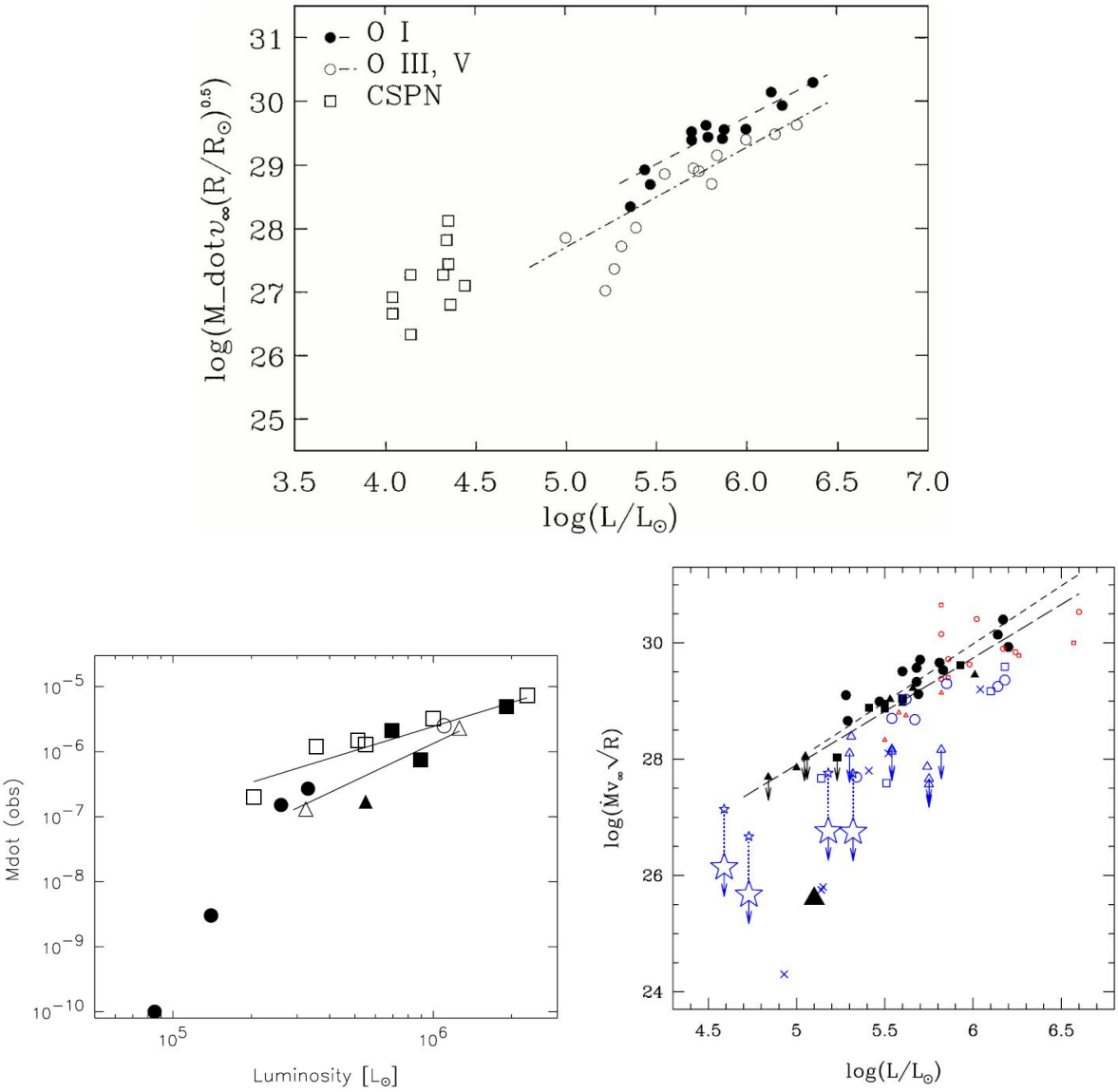


**Figure 1.8.** Wind-momentum Luminosity Relation from Kudritzki & Puls (2000), top panel, and Puls et al. (2008), bottom panels. Each show lower luminosity objects outside the tight relation seen for others. Bottom left: Mass-loss rates for O-dwarfs in NGC 346 (filled circles) compared to Galactic and other SMC stars (squares and triangles respectively). Bottom right: Filled and open symbols correspond to Galactic and LMC(small red)/SMC (blue) stars, respectively. Luminosity class V, III and I are represented by asterisks, squares and circles. The large triangle corresponds to 10 Lac.

is found that very low mass-loss rates, sometimes more than 2 orders of magnitude lower than theoretical models, are required in order to fit the UV resonance lines; any larger and the profiles simply do not match. This finding leaves only a few of possibilities: 1) the model atmosphere codes used to model the spectra of O stars have fundamental problems

**Figure 1.9.** At late O types the H$\alpha$ profile becomes insensitive to the mass-loss rate, so comparisons to this measure are somewhat questionable. From Puls et al. (2008).

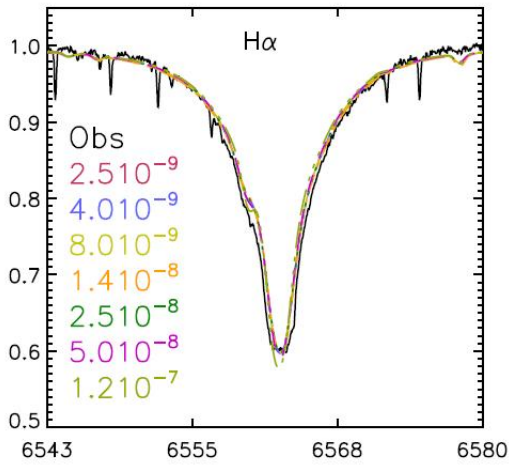


and their physics is not complete; 2) late O dwarfs really do have very low mass-loss rates, and it is the theoretical models at fault and there are knock-on problems to evolutionary tracks; or 3) there is some other physical phenomenon as yet unrecognised that is causing the current discordance.

The weak-wind phenomenon is a very important test of line-driven wind theory, and so it is essential to fully understand which of the above scenarios is most likely.

### Structure in O star winds

The assumption of a smooth and homogeneous outflow from hot massive stars works in a very general sense, but the details of the observations show how this cannot be the case, and indeed these winds have a structured nature, on both large and small scales.

In unsaturated P-Cygni profiles in the ultraviolet (but also in the optical in some cases) we see narrow absorption components (NACs) and discrete absorption components (DACs). These are regions of enhanced optical depth which are located at certain velocities out from the star (and hence appear at different points in the line profile). Since the Sobolev optical depth is a function of wind density, ion fraction and velocity gradient, one or more of these quantities must be changing non-monotonically with radius. This points to structure of some kind in the wind. It has been shown that NACs occur in just about all

O stars (Prinja & Howarth 1986) and that they are in fact the end-state of DACs (Prinja et al. 1987), and can be seen slowly accelerating outwards in wind profiles.

DACs appear to be persistent in a given object, in addition to being a phenomenon ubiquitous amongst O stars (Kaper et al. 1999). They appear to have some connection with the stellar rotation period, although the recurrence timescale of DACs is not necessarily the same as that of the rotation (Kaper et al. 1997). Massa et al. (1995) and Howarth et al. (1995) further explored these periodic absorption modulations (PAMs), showing that DACs do not necessarily occur concurrently with longitude on the star.

DACs are thought to be the spectroscopic manifestation of Co-rotating Interaction Regions (CIRs), which are regions of enhanced density that appear to have a spiral structure in the wind. It is based on the same idea in solar physics presented by Hundhausen (1972) (see Fig. 1.10) and explored in more detail for stellar winds by Mullan (1984) and Mullan (1986). They are not a spinning structure per se, but rather the density enhancements come from faster and slower flow of stellar wind interacting, possibly due to darker or brighter regions on the stellar surface. Hydrodynamic simulations by Lobel & Blomme (2008) (see Fig. 1.10) show CIRs to have a relatively low density contrast (between 0.99 and 1.21 of the mean density), and that tracer particles follow nearly straight lines radially out from the star, and so the spiral structures do not represent the directional flow of material, but the material flows through these regions.

Smaller scale structure or clumping has been noted from both observations and theoretical models. Lucy & Solomon (1970) pointed out in their analysis that there are expected to be strong instabilities in the driving of stellar winds, and so it has been monitored since, both observationally and theoretically. An attempt by Owocki et al. (1988) to treat these instabilities pointed to there being an extensive structure to a hot star wind that develops strong reverse shocks (reverse, that is in the co-moving frame - the shocks still propagate out from the star). This is an argument for a non-monotonic velocity field, something which is yet to be shown conclusively in observations. Feldmeier et al. (1997) presented a conclusion from their treatment that it was not the cooling of the reverse shocks that produced X-rays, rather it was the clump-clump collisions that took place.

Figure 1.11 shows results from Runacres & Owocki (2002) in which radiation hydrodynamical simulations of wind structure are performed out to distances of 100 stellar radii from the stellar surface. It clearly shows a structured velocity field, enhanced densities and void interclump spaces, and shocked heating and cooling through X-rays. Figure 1.12

**Figure 1.10.** Original conception of CIRs for the sun by Hundhausen (1972) (top), and a recent hydrodynamical model for a hot star by Lobel & Blomme (2008) (bottom).

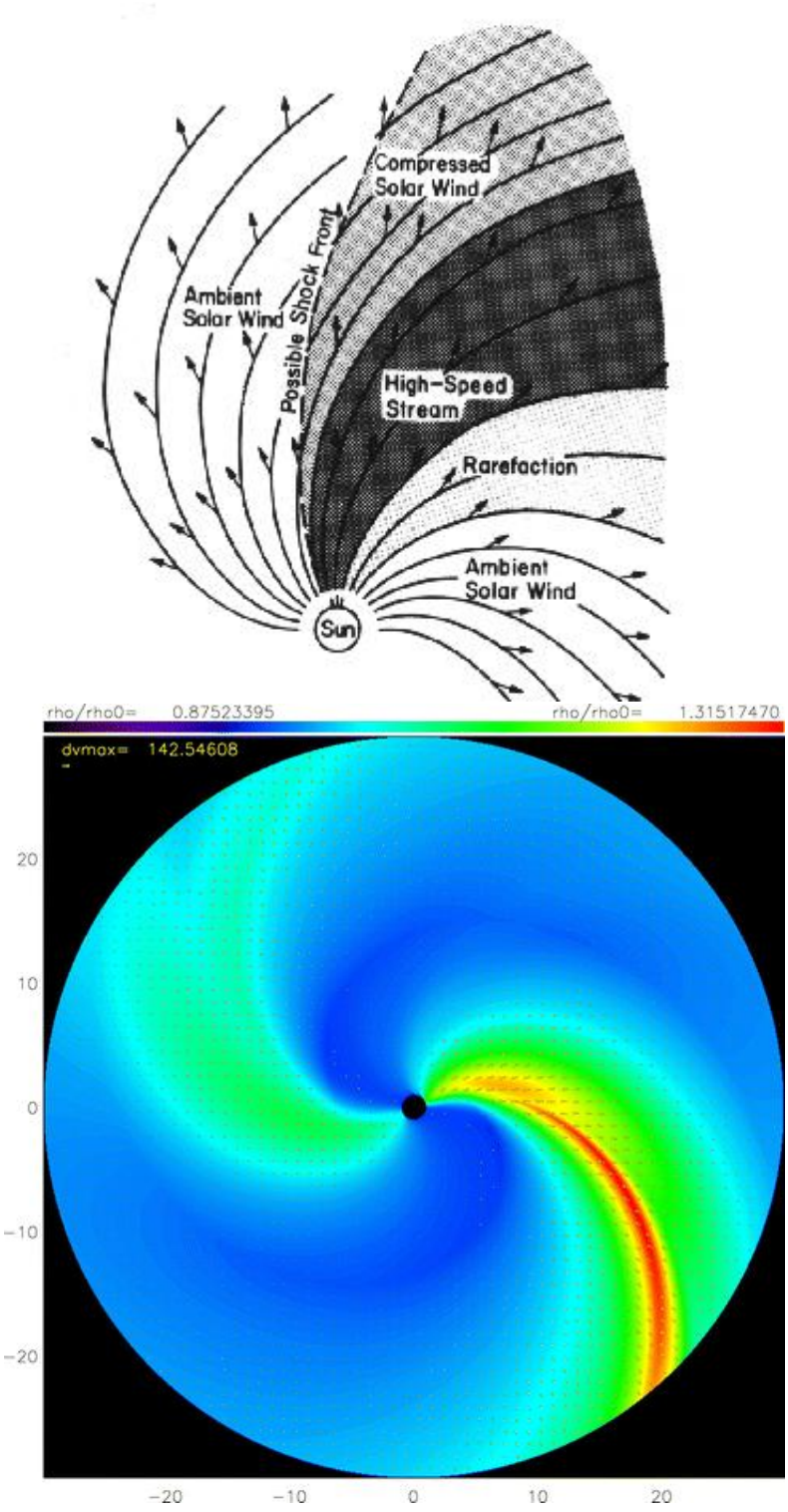

demonstrates the structure that forms in 2D simulations in which the line-force is unstable, from Dessart & Owocki (2005).

The velocity law seen in advanced models roughly follows the CAK one but with velocity enhancements corresponding to density reductions, and vice versa. This arises from the inherent instability in the line-driving.

Other lines of evidence for wind-clumping and small-scale structure in O stars, and also in other hot stars, include the following:

- As a phenomenon it was first invoked by Osterbrock & Flather (1959) as "extreme density fluctuations" around hot stars, and was used to explain why there were discrepancies between predicted and observed fluxes in the Orion nebula. It was later shown by Abbott et al. (1981) that the expected flux in the radio regime ought to be affected by the clumping in the stellar wind, and indeed the predicted mass-loss rate derived from radio free-free emission is lower by a factor of the root of the clumping factor compared to unclumped winds (see later for discussion about the clumping factor).

- Hillier (1991) showed that the electron scattering wings of recombination lines in Wolf-Rayet stars are weaker than predicted in smooth models, and perfect fits were been achieved using a simple routine inclusion of clumping parameters.

- An indirect line of evidence for clumping was found by Markova et al. (2004) and Repolust et al. (2004), where they showed that if the WLR for Galactic O stars was plotted as a function of H$\alpha$ profile type (whether it was in emission or not), then two distinct relations emerged. This is inconsistent with the basic prediction that wind-momentum rates of O stars should depend only on luminosity, and it was suggested that the difference was due to wind clumping, and that the phenomenon only really exhibited itself in the emission lines. Reconciliation between theoretical and observed trends could be brought about by introducing clumping of about a factor of 5.

- Davies et al. (2005) found that polarization measures of the wind of the LBV AG Car indicated a clumpy wind, specifically as opposed to a disk.

- The X-ray satellite observatory EINSTEIN discovered something which was perhaps surprising at the time - that O stars are soft X-ray emitters (e.g Harnden et al. 1979).

Follow-up observations confirmed this to be a widespread phenomenon in hot stars, and moreover that the luminosity of the X-rays appears to scale roughly with the bolometric luminosity of the star as $L_X \approx 10^{-7} L_{bol}$. This scatter was shown by XMM-NEWTON observations to be of order 40% (Sana et al. 2006) for the open cluster NGC 6231, with Nazé (2009) demonstrating a similar situation to be the case generally. The fact that intrinsic X-ray emission is fairly constant and is clearly correlated with the bolometric luminosity shows that it is related to the stellar and/or wind parameters. The X-ray emission has been attributed to shocks propagating in the wind due to the inherent instabilities in line-driving that give rise to a clumpy medium.

- Oskinova et al. (2004) showed that X-ray emission lines are much more symmetric than predicted by hydrodynamical models, and attributed this to the highly fragmented nature of the stellar wind allowing radiation to propagate from emission regions that would be obscured by a smooth wind.

- Emission lines show transient substructures (Eversberg et al. 1998; Lépine & Moffat 2008), implying temporary enhancements in optical depth. This constitutes a direct detection of clumping in a wind.

- UV resonance lines have black troughs and soft blue edges (Hamann 1981; Lucy 1982, 1983; Sundqvist et al. 2010), features that cannot be reproduced correctly by models unless a non-monotonic velocity field is introduced (e.g. Figure 1.11). A non-monotonic velocity field allows regions of enhanced optical depth to extend further out in the profile, and certain portions of rarefied gas can travel at velocities greater than terminal.

Fullerton et al. (2006) performed one of the most important studies in this area, fitting the PV resonance doublet in a sample of O stars, using empirical techniques (SEI - see Chapter 5). They derived accurate values for the product $\dot{M}\langle q_{P^{4+}}\rangle$, arguing that the $P^{4+}$ ion is dominant ($> 50\% P_{tot}$) in some objects, and so this quantity represents a direct estimate of the mass-loss rate to within a factor of 2. They find that the mass-loss rates gauged from this study are up to $\sim$ 120 times lower than those derived for the same stars by other means, and than theoretical predictions (Vink et al. 2000). The only way to reconcile this discordance is by invoking extreme clumping in the wind in order to

**Figure 1.11.** Plots from Runacres & Owocki (2002) showing how velocity, density and temperature vary with radius in a structured medium, from 1D hydrodynamical simulations.

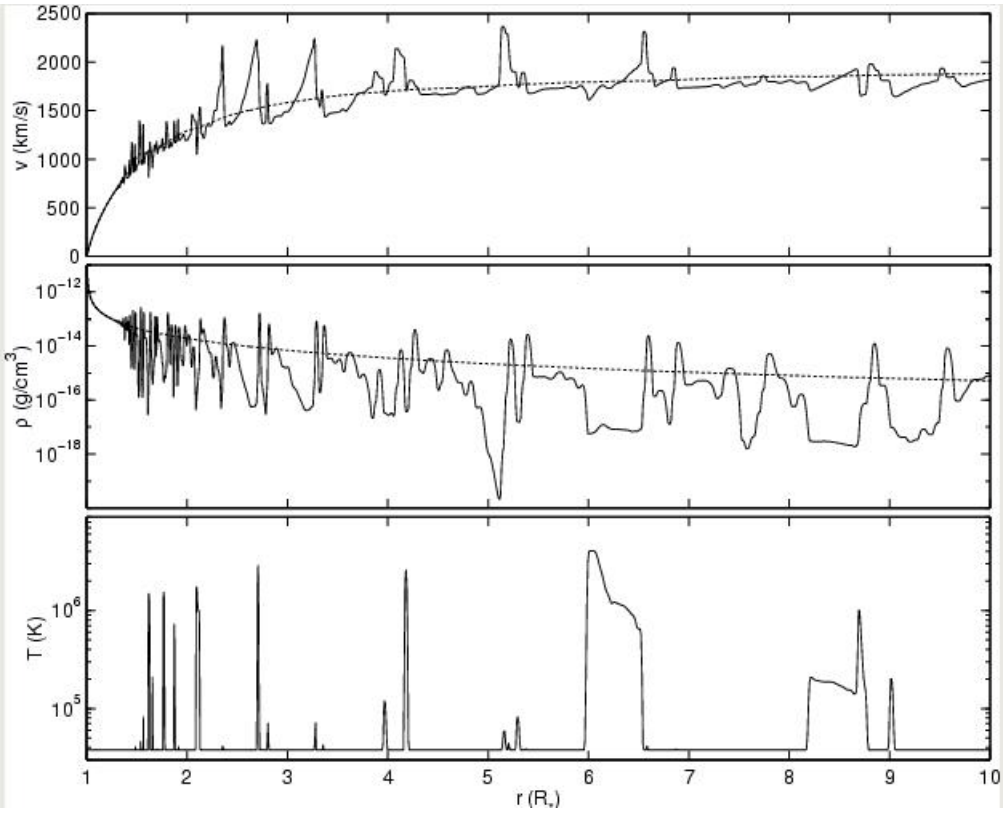


shift the ion balance via recombination, or by treating other forms of clumping (like that of Oskinova et al. (2007)) that affect UV resonance lines directly. Although Oskinova et al. (2007) are able to accommodate the effects of 'porosity' in the wind through their macro-clumping approach in modelling $\zeta$ Puppis, it may not be enough to counteract a discrepancy of this order. The key to the Fullerton et al. (2006) study is whether the $P^{4+}$ really is dominant or not, and there is a need to use other independent spectral diagnostics. Figure 1.13 shows the scale of the problem, where some estimates of mass-loss disagree by orders of magnitude.

#### Stratification of wind clumping

Knowledge of the radial stratification is important, since different mass-loss diagnostics are formed at different points in the wind, at different distances from the star (e.g. radio free-free is far out, H$\alpha$ mostly near the photosphere). It is therefore of use to know whether

**Figure 1.12.** Graphical representation of wind structure from Dessart & Owocki (2005).

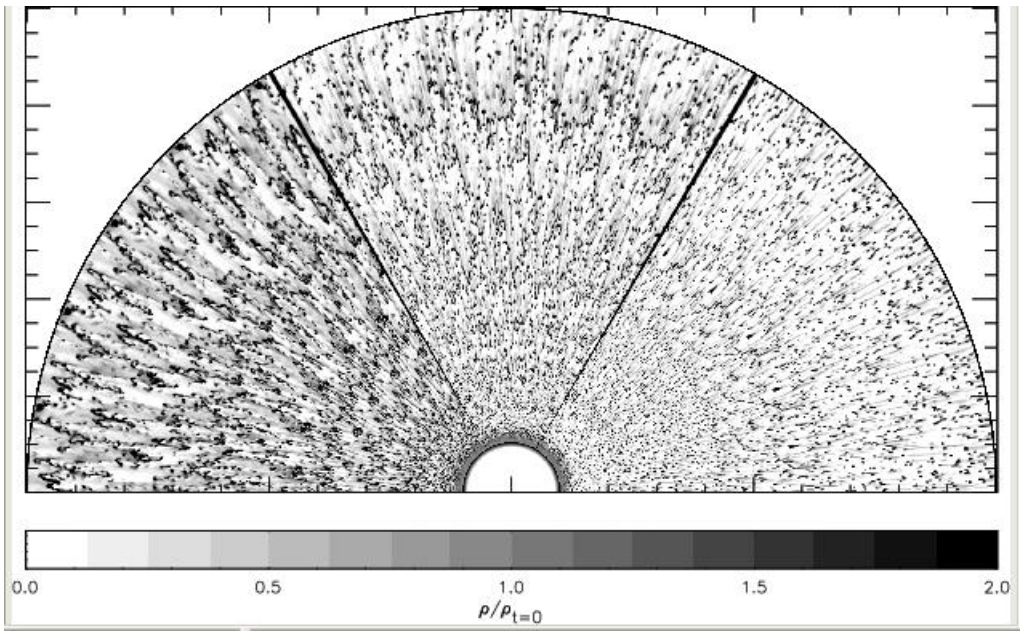


**Figure 1.13.** Comparison of mass-loss rates from Fullerton et al. (2006). The key is whether $P^{4+}$ is the dominant form of phosphorus.

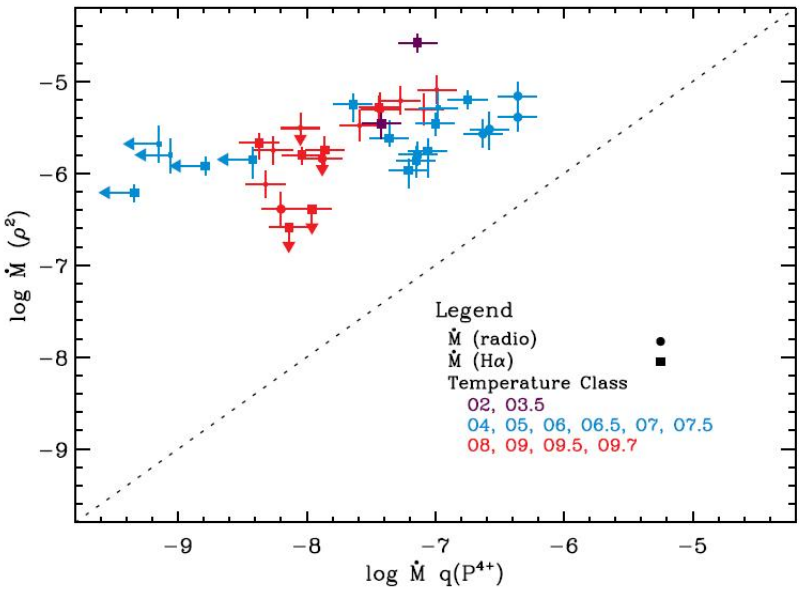

clumping is likely to affect the predictions of those diagnostics. Recent work by Runacres & Owocki (2005) and before that Runacres & Owocki (2002) showed that it is possible for structure to survive up to more than 1000 stellar radii, although this has not been proven conclusively with observations. The first observational study of the stratification of wind-clumping was by Nugis et al. (1998), who studied different diagnostics of mass-loss from the infrared to the radio in WR stars. They proposed that the clumping factor is unity (i.e. no clumping) near the wind-base, hits a maximum value somewhere in the region 5-10$R_*$, then returns to unity in the outer wind. Puls et al. (2006) found, however, that there is already significant clumping near the wind base. They modelled a sample of O stars with well-determined physical parameters, treating diagnostics from H$\alpha$ to the radio flux, and found *relative* clumping factors for different parts of the wind. They claim that clumping stays rather constant over much of the wind and drops off only at a larger distance from the star. For the weakest winds they find that the factors for the H$\alpha$ emitting region and the radio emitting region are the same. Najarro et al. (2008) confirmed that clumping seemed to be starting low down in the wind, as they studied various diagnostics at different wavelengths in the O3If$^+$ star CygOB2 #7, including some UV lines. They also discussed how ionization balance can be affected by clumping. Because clumping enhances recombination, where two adjacent stages have similar populations there is likely to be a net change in ionization state such that lines of the higher state can become weaker. This study was somewhat at odds with Puls et al. (2006) when it comes to clumping in the outer wind however, the former estimating much larger clumping factors at large radii than the latter. Although much has been accomplished in determining stratification of wind-clumping, much remains to be learned about the exact nature of clumping at different points in the wind. The Puls et al. (2006) study only yields *relative* clumping factors and not absolute ones, because all diagnostics used are $\rho^2$ dependent, and it is assumed that the outer wind is unclumped.

**Consequences of a structured wind**

Apart from the more obvious effects seen due to larger scale structure (DACs, CIRs etc.), there are a number of other consequences due in particular to different modes of clumping. There are two broad ways in which clumping can be formalised, namely micro-clumping, where clumps are optically thin and smaller than a photon mean free path, and there is a void interclump medium; and macro-clumping, in which the clumps are optically thick

and the size and geometry of clumps can become important. Clearly whether a clump is optically thin or thick depends upon the abundance, ion fraction and cross-section of the transition at hand.

In the micro-clumping approach, a volume filling factor approach is used. The fractional volume of the clumps is $f$, and $1/f$ is therefore the clumping factor. So for example if one-tenth of the volume in a stellar wind is occupied by the clumped material, the volume filling factor is 0.1 and the clumping factor is 10. The mass-loss rate derived from any diagnostic based on the square of the density (e.g. H$\alpha$, radio flux) must be scaled down by a factor $1/\sqrt{f}$ in the clumped models, to reproduce the spectra of the homogeneous models. Conversely, $\dot{M}$ derived from linear-density diagnostics (such as UV resonance lines) are not affected directly by micro-clumping, since the over-density is cancelled by there being a smaller absorbing or emitting volume of material. One important consequence of micro-clumping for this thesis is the fact that it can alter the ionization equilibrium because recombination is enhanced. Any form of clumping will increase the local density of the stellar wind medium and hence will affect the recombination rates of certain ions. This does not only increase the strength of lines that form due to recombination, but can also change the ionization balance in the wind and so change the appearance of other certain spectral lines that are not formed directly by recombination. The latter is thought more likely to display itself if the population of a certain ion is finely balanced, and perhaps needs only a small nudge in order to recombine to the lower stage.

In the macro-clumping approach, the size, separation and shape of clumps becomes important to know. There is a significant 'porosity' in the wind, and radiation is able to propagate through gaps between clumps. There is also the possibility of some parts of the wind becoming unimportant in the radiative transfer if they lie behind other clumps that are optically thick. With optically thick clumps the effective opacity becomes smaller since light can pass unattenuated through the wind gaps, and material is hidden in the clumps, and hence shielded from incident radiation. Since not all lines have same optical depth, this 'spatial porosity' affects some lines more than others. Oskinova et al. (2007) showed for $\zeta$ Puppis that UV resonance line profiles could be matched without having to invoke very low mass-loss rates, if the macro-clumping approach was used. The mass-loss rates derived there are lower than for a smooth wind, but higher than those for which micro-clumping was used. Macro-clumping has no effect on $\rho^2$ diagnostics and results in a reduction of mass-loss rates from the smooth case of a factor of 2-3, for single-density

diagnostics.

'Porosity' has also been invoked to explain some X-ray emission lines that are more symmetrical and less blue-shifted than predicted by theory. It is expected from a smooth wind that X-ray transitions occurring in the far (receding) portion of the wind ought to have their light attenuated by intervening material more than those on the near (approaching) side. This would cause an asymmetry and blue-shifted profile. If however there are gaps in the wind then flux can pass through even from the receding wind. The most recent results for $\zeta$ Puppis (Cohen et al. 2010) however require no porosity effects to fit the emission line spectrum, and find a mass-loss rate consistent with small-scale clumping.

In addition to the spatial porosity described above, Owocki (2008) suggested the possible role of a 'velocity-porosity'. In the line transfer, gaps in the velocity field allow light to travel through the wind independently of spatial porosity, and so physical scales are largely irrelevant in this context. The effect of this is to weaken the absorption trough of P-Cygni profiles in the UV/FUV by around 20-30%, which although significant is not enough to combat the supposed factor of 10 or more decrease in mass-loss rate proposed by Fullerton et al. (2006).

## 1.6 This thesis and how it is divided

There are several main questions that arise from the current literature and recent investigations. This thesis aims to provide some answers to the following:

- What are the effects of clumping and X-rays in O star winds?
- What are the main diagnostics of clumping and X-rays according to model UV, far-UV and optical spectra?
- How exactly are ion fractions of elements affected by X-rays and clumping?
- What is the current status of the mass-loss discrepancy in weak-winded stars?
- Can lines from successive ion stages of sulphur be used to shed light on the PV problem?
- What are the true mass-loss rates of the O stars?

This thesis is divided as follows; Chapter 2 is an account of how the model atmosphere code CMFGEN works, and how it was used to compute a grid of O star model atmospheres

in order to find out the effects of clumping and X-rays; Chapter 3 is a presentation of the grid in full, including an 'atlas' of some spectra; Chapter 4 is a presentation of ion fractions in O stars and how they behave under different circumstances; Chapter 5 presents an empirical analysis using fits to UV lines in O dwarfs; Chapter 6 details an investigation of the mass-loss of 5 O supergiants concentrating on three successive stages of sulphur; Chapter 7 is a concluding chapter which includes discussion and comments on the future observations and work that will help constrain the nature of mass-loss further.

This page is intentionally left almost blank

# Chapter 2

# Compilation of a grid of Galactic O star model atmospheres

*'The problem with troubleshooting is that trouble shoots back'*

Unknown Author

To study any astrophysical phenomenon in sufficient detail one must perform analysis of its emergent spectrum. Through spectral analysis we can learn fundamental physical properties about the object of study, such as temperatures, densities and chemical abundances, and hence constrain things such as the evolutionary properties of the system.

The modern approach to modelling the spectra of hot stars is a complicated one. One must use non-LTE methods due to the breakdown of local thermodynamic equilibrium at high temperatures and in extreme radiation fields. The flux of emergent radiation must be computed at all radiation frequencies of interest, and various equations governing the atomic properties of the gas must be satisfied. This can put strain upon computing resources, and in general high-performance machines are required to run the latest model atmosphere codes efficiently.

CMFGEN (Hillier & Miller 1998) is amongst the state of the art when it comes to modelling hot stars (for other codes currently in use, see Table 2.1). The preferred stellar models depend on the object being modelled. For hot stars with no discernible wind,

such as B dwarfs, TLUSTY is preferred as it treats line blanketing, and is simpler in it's assumptions than wind codes since it can assume plane-parallel geometry. For the case of a Wolf-Rayet star, which has a thick wind where the photosphere is not visible, CMFGEN and PoWR are preferred because they treat a spherical geometry. For stars with thin winds, where the photosphere is visible, CMFGEN is the preferred option because it utilises photosphere models from TLUSTY and deals with the wind too. FASTWIND is also an option for this type of object; it is simpler than CMFGEN and so will compute in far less time, but the models are hence not as sophisticated across the electromagnetic spectrum.

Line blanketing, which is the overlapping of line profiles due to many being tightly packed in wavelength space, needs to be treated because it has the effect of reducing the measured effective temperature through opacity effects. Also important is the treatment of wind blanketing, where due to the opacity of the wind, there is a thermal back-warming effect that causes a change in the perceived stellar temperature.

CMFGEN solves the radiative transfer equation in a spherical geometry under the constraints of radiative and statistical equilibrium, and a consistent solution is obtained through iteration. It is important to describe CMFGEN in some basic detail and so this will be done over the next few sections of this chapter. However, what is perhaps even more useful to this thesis is how the code is run, what challenges it presents, and how these are overcome to produce reliable results. Hence that is largely what this chapter will be concerned with, specifically in the context of a grid of O star models which was put together for this investigation. The compiling of this grid will be recounted in detail and the results presented in the following chapters.

## 2.1 CMFGEN

The transfer equation for material at velocity $v(r)$ in the co-moving frame, as solved by CMFGEN, can be given as

$$\mu\frac{\partial I(r,\mu,\nu)}{\partial r}+\frac{(1-\mu^2)}{r}\frac{\partial I(r,\mu,\nu)}{\partial \mu}-\left[\frac{\nu v(r)}{rc}\right]\left[(1-\mu^2)+\mu^2\left(\frac{d\ln v}{d\ln r}\right)\right]\frac{\partial I(r,\mu,\nu)}{\partial \nu} = \eta(r,\nu)-\chi(r,\nu)I(r,\mu,\nu) \tag{2.1}$$

**Table 2.1.** Table 1 from Puls (2008), comparing the current state of the art regarding NLTE stellar atmosphere codes.

| | Detail/Surf. (Butler) | TLUSTY (Hubeny) | CMFGEN (Hillier) | WM-basic (Pauldrach) | FASTWIND (Puls) | PoWR (Hamann) | PHOENIX (Hauschildt) |
|---|---|---|---|---|---|---|---|
| geometry | plane-parallel | plane-parallel | spherical | spherical | spherical | spherical | spherical/ pl.-parallel |
| blanketing | LTE | yes | yes | yes | approx. | yes | yes |
| line transfer | observer's frame | observer's frame | comoving frame (CMF) | Sobolev | CMF | CMF | CMF/ obs.frame |
| temperature structure | radiative equilibrium | radiative equilibrium | radiative equilibrium | $e^-$ thermal balance | $e^-$ thermal balance | radiative equilibrium | radiative equilibrium |
| photosphere | yes | yes | from TLUSTY | approx. | yes | yes | yes |
| diagnostic range | no limitations | no limitations | no limitations | UV | optical/IR | no limitations | no limitations |
| **major** application | hot stars with negl. winds | hot stars with negl. winds | OB(A)-stars, WRs, SNe | hot stars w. dense winds, ion. fluxes, SNe | OB-stars, early A-sgs | WRs | stars below 10 kK, SNe |
| comments | no wind | no wind | start model required | no clumping | explicit/ backgr. elements | | molecules included, no clump. |
| execution time | few minutes | hours | hours | 1 to 2 h | few min. to 0.5 h | hours | hours |

for frequency of incident radiation $\nu$ which propagates in the direction $\mu \cos\theta$ to the radius vector $r$. $\eta$ and $\chi$ are the emissivity and opacity terms respectively, and the effects of aberration and advection are neglected as per Mihalas et al. (1976).

When considering statistical equilibrium we assume that for each level of an atom the rate of electron departure from that level to all other levels by all collisional *and* radiative processes is equal to the rate of arrival from all those other levels to that level. In algebraic form,

$$\sum_{j \neq i} N_i(R_{ij} + C_{ij}) = \sum_{j \neq i} N_j(R_{ij} + C_{ij}) \tag{2.2}$$

where $i$ and $j$ are two levels in a model atom, $N_x$ is the number of electrons populating level $x$, and $R$ and $C$ are the rates of arrival from other levels due to radiative and collisional processes respectively. This is a steady-state scenario in which level populations are locally constant.

In order to compute the temperature structure in the wind, CMFGEN assumes that

radiative equilibrium holds in the co-moving frame. This can be summarised in the form

$$\int_0^\infty \chi[J(\nu) - S(\nu)]d\nu = 0 \tag{2.3}$$

where $\chi$ is the absorption coefficient, $J(\nu)$ is the frequency dependent mean intensity of radiation, $S(\nu)$ is the source function equal to $\eta_\nu/\chi_\nu$, the ratio of emission to absorption coefficients, which are statistical terms describing the addition and removal of radiation and the subsequent effect on the emergent radiation from the star.

On each iteration, corrections to the temperature and atomic level populations are obtained by linearising all the equations. When the code has converged to within a specified level, an observer's frame calculation is begun and a corresponding spectrum computed.

### 2.1.1 Solving radiative transfer

Various methods of solving the equations of radiative transfer have been employed with various attributes such as computation time, speed of convergence, etc. The radiative transfer equation can be expressed in simple terms as

$$\mu \frac{dI_{\mu\nu}}{d\tau_{\mu\nu}} = I_{\mu\nu} - S_\nu \tag{2.4}$$

where as before $I$ is the specific intensity and $\mu = \cos\theta$. If one assumes complete frequency redistribution and no overlapping in the continuum then the formal solution to this equation is given by

$$I_{\mu\nu} = \Lambda_{\mu\nu}[S] \tag{2.5}$$

This solution can be given in terms of the frequency-averaged mean intensity $J$:

$$\bar{J} = \Lambda[S] \tag{2.6}$$

where

$$\bar{J} = \int J_\nu \phi_\nu d\nu \tag{2.7}$$

and

$$\bar{\Lambda} = \int \Lambda_\nu \phi_\nu d\nu \tag{2.8}$$

where $\phi_\nu$ represents the normalised absorption profile.

Equation 2.7 is then rewritten as a finite matrix that operates on a vector of source function values at different depth points $d$:

$$J_d = \sum_{d'}^{D} \Lambda_{dd'} S_{d'} \tag{2.9}$$

Here it is assumed that the lambda operator is represented by a finite matrix, whereas theoretically it should be infinite since it operates on a continuous function of position. In this case though the source function is treated as discrete. The equation of statistical equilibrium for a two level atom is then written as

$$S = (1 - \epsilon)\bar{J} + \epsilon B \tag{2.10}$$

where $\epsilon$ is the collisional destruction probability and $B$ is the Planck function.

**Ordinary and Accelerated Lambda Iteration**

The method of Complete Linearisation (CL), developed first by Auer & Mihalas (1969), had a set of equations that dealt with how material responds to radiation at every depth and frequency, but also how the radiation field reacts to changes in the material properties. The difficulty in solving the radiative transfer equation lies in dealing with the coupling of physical parameters such as depth, angle and frequency. To tackle this, the lambda iteration method was developed. In the simplest case equations 2.6 and 2.10 can be

combined and the source function written as

$$S = (1 - \epsilon)\Lambda[S] + \epsilon B \tag{2.11}$$

If $\Lambda$ is defined as a linear operator then this can be solved in one simple step:

$$S = [1 - (1 - \epsilon)\Lambda]^{-1}\epsilon B \tag{2.12}$$

In practice though, due to the coupling between parameters mentioned above, $\Lambda$ is likely to be a large matrix, so an iterative approach is used. The most simple method is to use 'ordinary' lambda iteration, where an initial guess $S^0$ is supplied and a solution is found through a series of improved source functions $S^n$, determined by the iteration formula

$$S^{n+1} = (1 - \epsilon)\Lambda[S^n] + \epsilon B \tag{2.13}$$

and then a formal solution can be found for each individual frequency point. The downside when applying this technique to stellar atmospheres is that a large number of iterations are required to obtain convergence. Indeed, Lambda iterations generally stabilise the model rather than converging to a solution.

Because of this the idea of an 'accelerated' lambda iteration scheme was developed by Scharmer (1981) and subsequently by Olson et al. (1986). The difference is that the operator is chosen to be approximate and local. The difference between formal and approximate solutions to the radiative transfer equation is what 'drives' the iterations. Formally, $\Lambda$ is split by specifying the approximate lambda operator $\Lambda^*$:

$$\Lambda = \Lambda^* + (\Lambda - \Lambda^*) \tag{2.14}$$

changing the iteration scheme to

$$S^{n+1} = (1-\epsilon)\Lambda^*[S^{n+1}] + (1-\epsilon)(\Lambda - \Lambda^*)[S^n] + \epsilon B \tag{2.15}$$

requiring a matrix inversion of $\Lambda^*$ to solve:

$$S^{n+1} = [1-(1-\epsilon)\Lambda^*]^{-1}[S^{n+1}] + (1-\epsilon)(\Lambda - \Lambda^*)[S^n] + \epsilon B \tag{2.16}$$

In this equation $[1-(1-\epsilon)\Lambda^*]^{-1}$ acts as an acceleration operator, speeding up the iteration compared to ordinary lambda iteration. If $\Lambda^* = 0$ is inserted then the formula reverts to ordinary lambda iteration, and $\Lambda^* = \Lambda$ reduces back to the 'exact' method as in CL. The authors who developed this technique achieved a balance between an operator which is easy to invert, but that retains the properties of the exact operator.

### 2.1.2 Line-blanketing and Super-levels

Although certain strong lines (e.g. CIV, NV, OVI) are the main drivers of hot stellar winds, a significant contribution to the opacity comes from the combined effect of many other weaker metal lines. This is known as line-blanketing, and is important to consider in order to achieve an accurate spectrum. In NLTE this effect needs to be accounted for such that radiative and statistical equilibrium can be satisfied consistently. The problem faced in trying to simulate the effect of weaker lines is that there may be of order $10^6$ to $10^7$ transitions to consider in order to get level populations right, which is beyond the reach of most computing facilities, both in terms of CPU and memory requirements. To combat this, CMFGEN uses the super-level approximation first described by Anderson (1989). The approach assumes that certain levels at similar energies within an ion behave similarly, and this group of levels is called a super-level. Within this group the departures from LTE are deemed to be the same. It means that the number of 'levels' for which departure coefficients must be determined is reduced, often by around a factor of ten. The numbers of levels and super-levels chosen in this thesis is given in Table 2.4. CMFGEN evaluates all the radiative and collisional processes using a full model atom, and so all the different transitions occur at the correct wavelengths. Levels which are grouped together

should belong to the same spectroscopic multiplet and have the same parity. The choice of the number levels and super-levels is about striking a balance between the speed of the calculation and the accuracy of the results, a choice which was made for this study and which will be discussed later in this chapter. Obviously one must not use too many super-levels as to do so would defeat the object of the exercise.

The assumptions employed regarding super-levels in CMFGEN are thus:

$$\sum_{i}^{F} n_{ij} =^{S} n_j \tag{2.17}$$

and

$$\sum_{i}^{F} n^*_{ij} =^{S} n^*_j \tag{2.18}$$

with departure coefficient $b$ defined by

$$b =^{F} n_{ij}/^{F}n^*_{ij} =^{S} n_j/^{S}n^*_j \tag{2.19}$$

where the asterisk denotes the LTE population, $^{S}n_j$ is the population density of super-level $j$ and $^{F}n_{ij}$ refers to the population density of the full level $i$, which is a member of super-level $j$. These expressions completely specify the relationship between any atomic level and its super-level. Hillier & Miller (1998) emphasise that super-level formalism is a natural extension of LTE, in which a single super-level is essentially being used to describe all levels at all ionization stages.

The inclusion of line-blanketing in codes has led to a downward revision of the effective temperature scales of O stars by 1-2kK (see for example Martins et al. (2002) compared to Vacca et al. (1996)).

There are both advantages and disadvantages to using the super-level formalism. On one hand, very many transitions can be treated whilst running a code over a manageable time, and LTE is fully recovered at depth in the atmosphere. However, there is no quick and simple way to assign levels and super-levels, at least not one that can be prescribed for all possible models. It is mostly by trialling initial models that one finds the best

numbers to use. There is also the possibility that small inconsistencies will arise between the radiative and statistical equilibrium equations, and this is likely to cause problems with convergence of the model. On the whole, however, it is a system which works and which produces realistic output when one takes time and care to specify constraints carefully.

### 2.1.3 Density Structure

CMFGEN, as a non-hydrodynamic code, does not compute the wind density structure from first principles. Rather, it must be specified in one of the following ways: 1) a beta-type velocity law is attached to a hydrostatic structure with a fixed density scale height; 2) a parametrised velocity law is specified; or 3) a velocity law is attached to a density structure as specified by the NLTE plane-parallel code TLUSTY (Hubeny & Lanz 1995). Option 1 is only really used in the absence of one of the other two options. Option 2 is ideal for Wolf-Rayet stars and luminous blue variables (LBV) since their winds are dense and optically thick, meaning the underlying hydrostatic structure is not probed by spectroscopy, and so the lines *and* continuum are formed in the wind. O stars, however, do display their photospheric spectra and one must use option 3 in order to correctly simulate the photosphere-wind connection smoothly. All these methods require $R_*$ (stellar radius), $L$ (stellar luminosity), $\dot{M}$ (mass-loss rate), the velocity law and all stellar abundances to be assigned.

Specified forms of the velocity law include

$$v(r) = \frac{\left(v_0 + (v_\infty - v_0)\left(1 - \frac{R_*}{r}\right)^\beta\right)}{\left(1 + \frac{v_0}{v_{core}} \exp\left(\frac{R_* - r}{h_{eff}}\right)\right)} \tag{2.20}$$

where $v_{core}$ is the velocity in km s$^{-1}$ at the stellar radius when $v_0 \gg v_{core}$, $v_0$ is referred to as the photospheric velocity, $v_\infty$ is the terminal velocity of the flow, $h_{eff}$ is the scale height of the photosphere in units of stellar radius (the distance over which the density is diminished by a factor $e$) and $\beta$ is the speed of the velocity law (which tends to range from 0.5 to 4.0 for massive stars).

When hydrostatic structure is to be specified by TLUSTY, a file is read by CMFGEN which contains tabulated $R_*$, $v(r)$ and $\sigma = dlnv/dlnr - 1$. This file is produced by a subroutine of the CMFGEN package which utilises a TLUSTY output file, and requires

the stellar radius, the maximum desired radius to compute to, the mass-loss rate, the terminal velocity, $\beta$, the scale height of $\beta$ (usually set to $0.2R_*$) and the number of depth points. The subroutine allows points with optical depth greater than 100 to be omitted, but ensures that a sufficient optical depth is achieved to probe the whole wind.

The number of depth points in the model must be carefully selected. For Wolf-Rayet stars 40 is usually sufficient but for O stars 60 or more gives the best convergence of the code (see later discussion about convergence - §2.2.3).

### 2.1.4 Implementing clumping and X-rays

CMFGEN treats clumping in the micro-clumping approach described in the introduction chapter (§1.5). That is, it assumes density enhancements to be optically thin. This means that it has a direct effect on the processes which rely on the square of the density, and so we expect emission lines like H$\alpha$ that are formed due to recombination to be increased in strength when the clumping factor is increased. As stated in Najarro et al. (2008), if two adjacent ionization stages have similar populations, then clumping will increase recombinations and reduce the number of scatterers in the lower level, making the corresponding line weaker.

To implement clumping in practice in CMFGEN, a filling factor approach as introduced by Hillier & Miller (1999) is used, where the volume filling factor $f$ is given by

$$f = f_\infty + (1 - f_\infty)e^{-\frac{v(r)}{v_{cl}}} \tag{2.21}$$

where $f_\infty$ is the density contrast in the gas (i.e. the proportion of volume actually taken up by matter) and $v_{cl}$ is the velocity at which clumping becomes important. One selects these two parameters according to the likely scenario, and the code manual suggests values of $f_\infty = 0.1$ and $v_{cl} \sim 200kms^{-1}$, although a lower onset velocity is often used for O stars. The choice for this investigation will be discussed later. In practice when a clumping factor is introduced, for the case of diagnostic lines that depend on the square of the density, to obtain the same profiles as for a smooth wind, the mass-loss rate must

be multiplied by a factor $\sqrt{f}$ (where $f$ is less than unity), so

$$\dot{M}_{clumped} = \dot{M}_{smooth}\sqrt{f} \tag{2.22}$$

A parametrised approach is also taken for the effects of X-rays (Hillier et al. 1993). In reality the X-rays emanating from a stellar wind are thought to be connected phenomenologically to the shocks and clumping. However, as a parametrisation CMFGEN does not link these processes directly in terms of radiative transfer. Rather there is an ambiguity in how to interpret X-ray filling factors if the clumping is switched on, and one can choose whether the clumped densities are used to evaluate the X-ray emissivity or whether the emissivity is multiplied by the clumping factor. In the second case the X-ray emissivity is preserved if $\dot{M}/f$ is held fixed.

Because it is merely a parametrisation and not full X-ray radiative transfer (but see Zsargo et al. (2009)), the effect of the X-rays can be best diagnosed by inspecting output and ensuring the X-ray luminosity is consistent with observations. One chooses values for each of the following parameters:

- **Filling factor 1/Filling factor 2:** the X-ray emission is proportional to the square of the local density multiplied by the filling factor. For lower mass-loss rates it is sometimes necessary for a filling factor to exceed unity to match observed X-ray luminosities (as stated in the CMFGEN manual, and very important in this study).

- **Shock temperature:** usually chosen to be a few hundred times the program unit of $10^4$ K.

- **Shock velocity:** the scale height in km s$^{-1}$ where shocks become important in the wind, usually taking a value of around 400km s$^{-1}$. Cohen et al. (2010) find the onset of shocks to be at a radius of approximately $1.5R_*$, by which time the wind has been accelerated to or past 400km s$^{-1}$.

- **Slow X-rays:** a boolean option determining whether X-rays are included *gradually* in the model, which may improve convergence of the code.

- **Initial value for filling factors:** the initial value for each of the filling factors that is used to start convergence, gradually working up to the specified final value. Very

much a model-dependent number that must sometimes be determined by trial and error to get good convergence.

- **Maximum continuum frequency:** this is set to a higher value when X-rays are present (something greater than $1000 \times 10^{15} Hz$), to ensure that high enough frequencies are included to cover the Auger ionization edges.

The last point about Auger ionization is an important one (also see Macfarlane et al. (1993)). Some ions (e.g. $O^{5+}$) have ionization potentials much higher than that of $He^{+}$ (54.4 eV) which means they cannot be abundantly produced by photoionization from the ground state due to stellar flux shortward of $228\mathring{A}$ being drastically attenuated by bound-free absorption of $He^{+}$. Instead there must therefore be another process causing the formation of these 'super-ions'. Auger ionization is the process by which a high energy X-ray photon removes two electrons from an ion like $O^{3+}$ and produces $O^{5+}$, explaining why larger than expected OVI profiles are seen in hot stars. CMFGEN takes this process into account when introducing X-rays, and it is indeed borne out in the spectra and ionization of certain species, as the next chapter will discuss in more detail.

So bringing X-rays into the analysis is a case of changing the above parameters and inspecting the code output, then changing them as necessary in the next model to converge on the desired X-ray luminosity.

## 2.2 Running the code

The actual business of running the CMFGEN code is conducted through a series of input scripts and data files which are set up by the user. The key files needed are listed below with a small amount of information on each. Each new model to be run has its own directory and contains each of the following files and directories:

- **batch.sh** - This script simply sets up and links all the necessary directories so that the main program cmfgen_dev.exe knows where to find everything. It includes setting a temporary directory to store important files between iterations of the code. One of the most important things it sets is the location of the atomic data directory. The atomic data itself will be discussed below.

- **VADAT** - This is essentially a large look-up table for the code containing all the input parameters, both physical and computational. Stellar radius, wind velocity law,

mass-loss rate, effective temperature, clumping factors, X-ray implementation are all set, in addition to how to treat convergence with different acceleration methods (when to switch to Lambda iterations, whether to use Ng acceleration[1] etc.).

- **MODEL_SPEC** - Sets the number of depth points to be used in the model, the level structure to be used for different atomic species, and a handful of other options. For the level structure one selects the number of 'important levels', the number of super-levels and the total number of levels in the model atom for each species. The number of important levels and the number of super-levels are generally set to be identical.

- **IN_ITS** - This file simply determines the number of iterations to perform, and will do all of these unless the code converges to the point specified in VADAT first. One can select 'normal' iterations or Lambda iterations, and whether to switch off Lambda iterations and to return to normal after the first one. In general, around 40 iterations suffice, unless there are convergence difficulties, in which case some models may need 100 or more iterations.

- **RVSIG_COL** - This file is user-generated and is made using an output file from the plane parallel code TLUSTY, using one of the programs bundled with CMFGEN, tlusty_vel.exe. This is used in constructing the velocity law for the wind such that hydrostatic conditions at the photosphere are preserved. It essentially yields a beta-type velocity law matched to the hydrostatic structure such that the velocity law and its first derivative are continuous, and is matched just below the sonic point. The file contains tabulated radius (R), velocity (v) and sigma = $dlnv/dlnr - 1$.

- **obs** - This directory contains the program cmf_flux.exe which is used to perform the observers frame calculation.

During the running of the code it is possible to check the status of the model by interacting with a couple of files which are updated on every iteration. By inspecting the file OUTGEN one can observe how many iterations have been performed and how close the code is to convergence. Typing the command

```
grep Max OUTGEN
```

[1]Ng acceleration is a mathematical technique used to help iterative codes converge faster, the details of which are beyond the scope of this thesis.

will retrieve an output ending something like

```
Maximum % increase at depth   1 is  5.63E-02
Maximum % decrease at depth   1 is  5.64E-02
Maximum % increase at depth  30 is  1.99E-02
Maximum % decrease at depth   1 is  1.77E-02
Maximum % increase at depth  30 is  9.41E-03
Maximum % decrease at depth  37 is  5.12E-03
```

which indicates that the last three iterations have had largest corrections to populations of order $10^{-2}$ or $10^{-3}$%, and which depth points in the atmosphere correspond to those corrections. The command

```
grep Lumin OUTGEN | wc -l
```

will return the number of iterations that have occurred, since the luminosity of the star is output on each iteration. In addition one can inspect the contents of the file CORRECTION_SUM, which summarises the number of corrections being performed at each depth point in the atmosphere and hence indicating if there is a particular problem at a particular depth.

### 2.2.1 Atomic data

An obvious need, when synthesising the spectra of stellar atmospheres containing many atomic species, is to have reliable and comprehensive atomic data. CMFGEN uses the latest data available from a number of sources, namely The Opacity Project (Seaton 1995), the Iron Project (Pradhan et al. 1996), the Atomic Spectra Database at NIST Physical Laboratory and Kurucz & Bell (1995). Many different model atoms can be included, but in this investigation H, He, C, N, O, Si, P, S and Fe were used.

There are some uncertainties with regard to the atomic data that arise from such cases where observed energy levels and wavelengths are simply not known, although these are rare and have little impact upon the working of the code. Caution is advised by the code's author (Hillier & Miller 1998) when it comes to determining abundances using CMFGEN because some levels are combined into a single level and the strength and location of the line is affected. This is not a major issue in this study as no abundance determinations of stars is attempted.

The data files used are as follows, where XXX is a dummy for a particular ion.

- **XXX_F_OSCDAT** - this file contains energy levels and oscillator strengths in tabulated format.
- **XXX_F_TO_S** - information on which levels are to be grouped together as super-levels.
- **XXX_COL_DATA** - a table of collisional data (excitation strengths, etc.).
- **PHOTXXX_A** - photoionization cross sections for each level. The '_A' indicates that the final state is the ground state of the next ionization state. A '_B' would indicate that it is an excited state.
- **DIEXXX** - A list of low temperature dielectronic recombination lines from Nussbaumer & Storey (1983). Not always used.

One of the keys to working successfully with the atomic data is to find a balance between speed of code running time and accuracy in the model. In theory, including many more levels and super-levels increases the running time and memory usage but improves the accuracy of the model, whereas including fewer levels will result in a quicker run but the spectrum will not be as detailed or accurate. In general it was possible in this work to find a good balance between these two approaches such that the spectrum was detailed enough and the code ran in a reasonable time (less than the maximum permitted wall-clock limit of 36 hours set by the cluster computer being used).

### 2.2.2 Understanding and processing output

CMFGEN comes bundled with a number of subroutines for processing the output into usable plots and information. These are detailed below.

- **cmf_flux** - this program is used to compute the spectrum in the observer's frame, since CMFGEN computes it in the Co-Moving Frame (CMF). The spectrum in the observer's frame is more accurate, particularly for O stars, especially for lines formed in the photosphere. Spectra are calculated for a variety of turbulent velocities (5, 7.5, 10 and 15 km $s^{-1}$).

- **DISPGEN** - a display package for a host of parameters. Using it, one can plot T, $v$, departure coefficients, populations and ionization fractions as a function of radius, column density, depth and other parameters.

- **PLT_SPEC** - another plotting package which allows the manipulation and plotting of the output spectra (either co-moving or observer's). In addition, one can normalise the spectrum by the continuum, apply rotational or instrumental broadening, or apply a velocity shift

The overall method used in this study is shown in a flowchart in Figure 2.1.

### 2.2.3 Dealing with convergence

Models do not necessarily converge to the desired level (chosen usually to be 0.1%) using normal iterations. This can be due to a number of factors, but principally the chosen stellar parameters. The atmosphere can be intrinsically unstable, and small changes in stellar parameters may lead to large changes in populations at some depths. In some cases one or several levels at one or several depths in the atmosphere may have very poor estimates for the level populations, with successive iterations seeming not to have any effect. These populations often turn out to be anomalous compared to neighbouring ones and can be changed by hand to be closer to neighbouring depths. This does not always work however, and one is sometimes left with an unconverged model and must establish whether the anomalous levels and depths are causing a problem to the spectrum and physical attributes of the model. This can be accomplished by performing a sequence of iterations, both normal and Lambda, and comparing the spectrum and other key output files to those from before the sequence. If no discernable change has occurred then the levels were not causing a problem and the model can be accepted (albeit with a caveat related to the above).

## 2.3 Motivation for the new grid

There are a couple of dominant motivations for producing a grid of models covering the entire O star range over a span of luminosity classes. Firstly, accurate and well thought out models that include as many realistic physical processes as possible (such as X-ray flux and clumping) ought to lead to reasonable estimates of the ion fractions for different elements.

**Figure 2.1.** A flowchart demonstrating the running of models for the grid

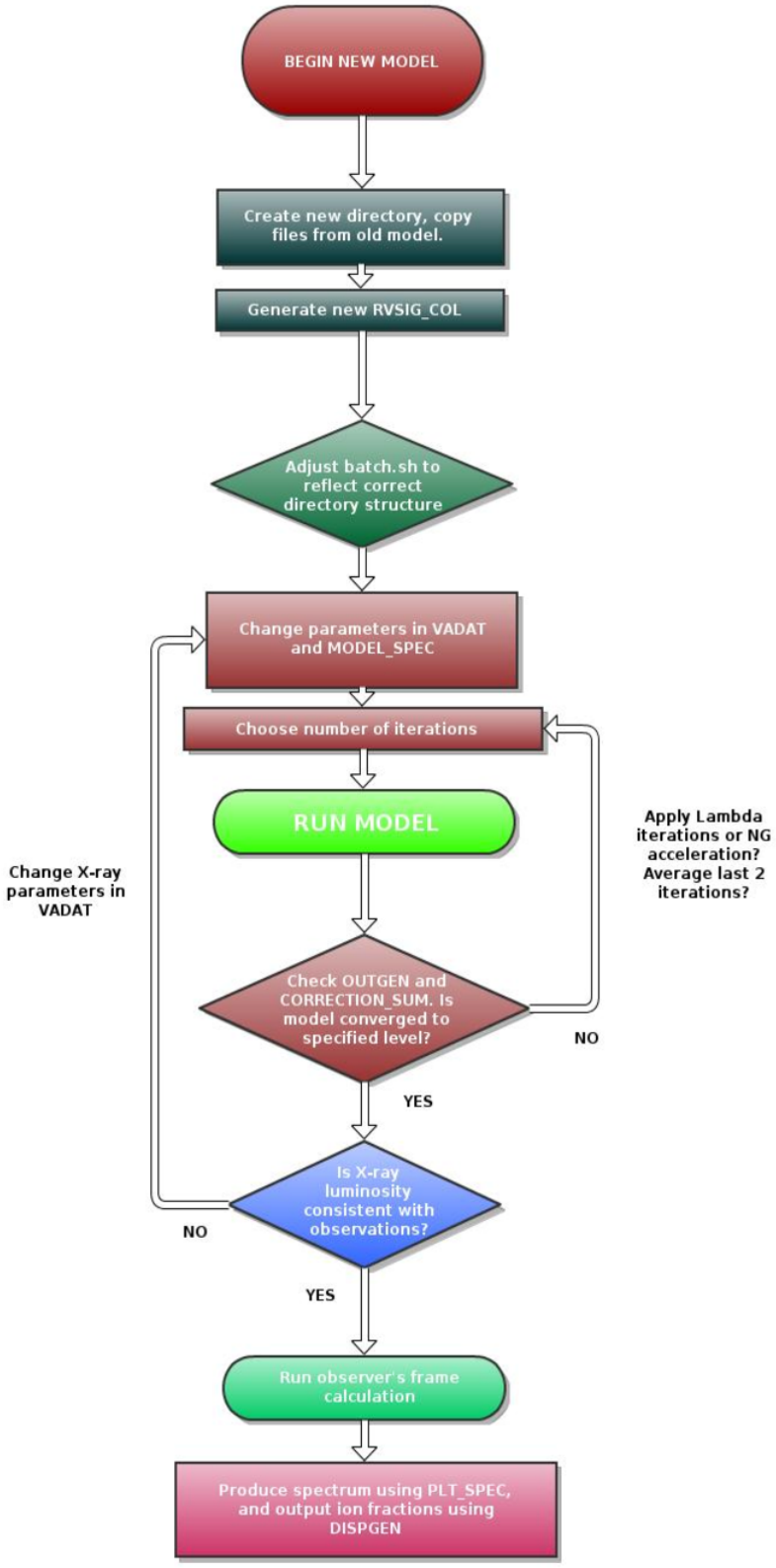

This is useful for disentangling ion fractions from mass-loss rate in empirical analysis, as will be seen in Chapter 4. Secondly, one can use a model from the grid as a starting point for fitting an observed spectrum (such as in Chapter 6). The main motivation for compiling such a grid as this is the need to assemble representative spectra for a set of wind and physical parameters that cover the whole O star range, such that the broad effects of clumping and X-rays can be assessed. Individual profiles are not matched, but the emphasis is on a broad analysis of how well CMFGEN predicts spectra with different wind parameters.

An initial grid was quickly composed to test the code's specific setup on the local system. As a quickly composed grid intended only for tests it did not include all of CMFGEN's capabilities and exhibited spectra which were unrealistic at later types and lower luminosity classes. Because only a simple velocity law was used that did not connect properly to the photosphere, the model did not penetrate to deep enough optical depths and resulted in spectra like that seen in Figure 2.2. In this spectrum, photospheric lines actually appear to be in emission, and most of the resonance lines in the ultraviolet are very large and wind-dominated. We know from observations that late O-type dwarfs do not tend to have strong UV wind profiles like those seen in this spectrum.

The full final grid needed to have representative spectra, and account for all the physical effects in the stellar wind. This included a treatment of clumping (which in the case of CMFGEN is the micro-clumping formalism) and the propagation of X-rays due to shocked wind material. It was deemed that the parameter space covered by the grid should reflect actual observed objects rather than purely theoretical calibrations such as that of Martins et al. (2005*a*). With this in mind, parameters were gathered from recent studies which employed NLTE analysis to *fit* the spectra of actual objects. These would then be extrapolated/interpolated to fill the full parameter space of the O star range. This way of compiling the grid was chosen rather than having a grid based on effective temperature and log gravity at round number values. Rather, the grid became regularly spaced in these quantities *after* a calibration from actual objects.

Computation of the grid took place using UCL's Legion cluster, a high-performance machine composed of over 2500 cores. CMFGEN is not compatible with MPI (Message Passing Interface) which would allow the code to run over dozens of processors and in a fraction of the time. To do this would involve re-writing vast portions of the driving code. However, it can run across four cores locally on one processing unit, so the code

**Figure 2.2.** Spectrum of a late O dwarf (O8 V) from the test grid. The profiles are far too large and the photospheric lines go into emission, due to the lack of proper connection between wind and photosphere.

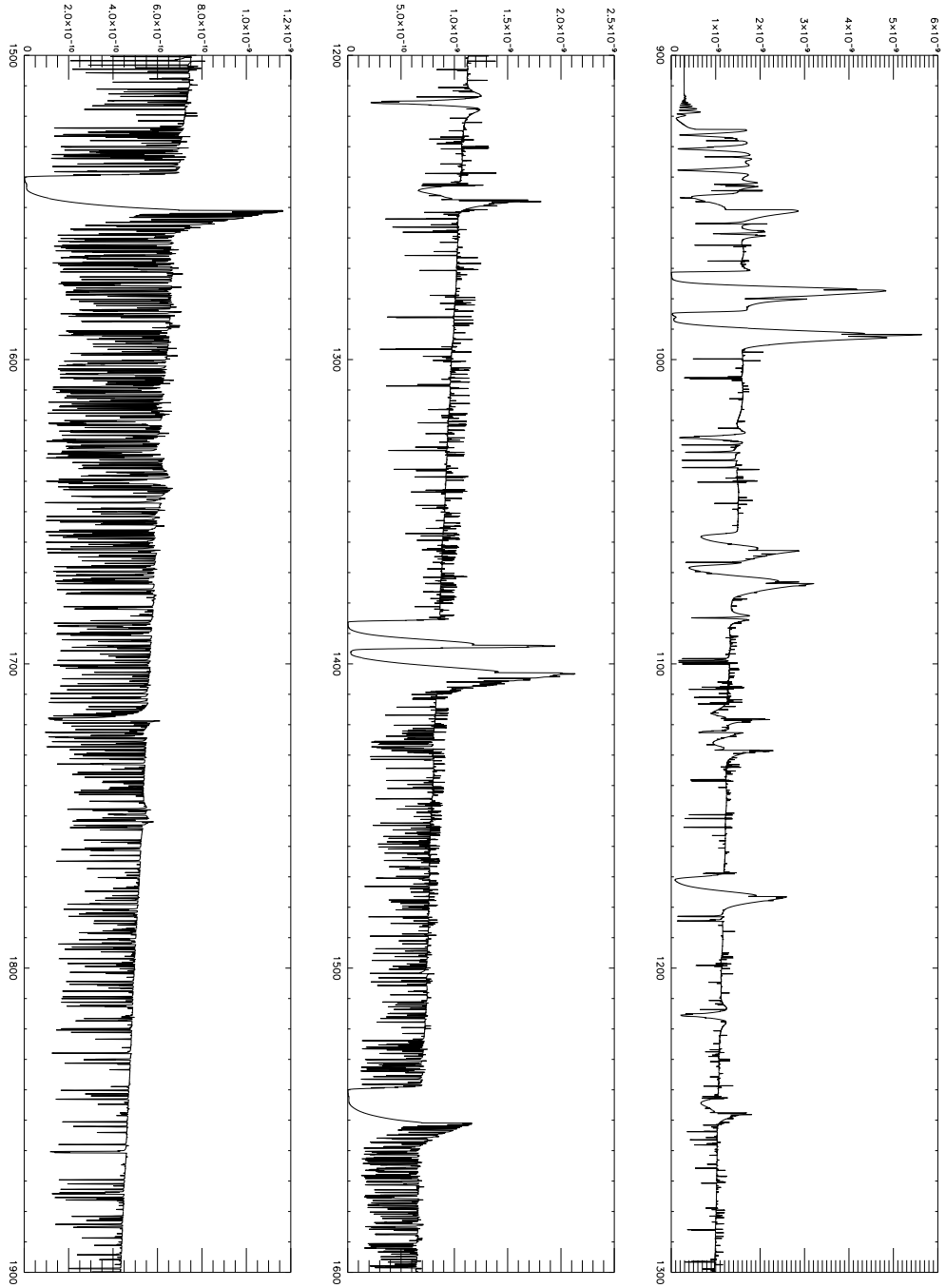

was compiled using vectorisation loops, optimising it to run somewhat faster. The general gain in runtime was seen to be only a matter of about ten minutes spread over four cores, compared to a total running time of up to 24 hours. This took up four cores for one model, and greater use could be made of computing resources by running multiple instances of single-core models, so this is generally what was done. Due to the nature of Legion,being a cluster machine that runs jobs from a queue, it was not possible to interact with the code during the run (in order to observe the speed of convergence, how many iterations had been performed etc.). There was, however, a testing ground available which acted more like a normal desktop machine, and did not require queued jobs. This was used to assess how well some models were converging, and to introduce X-rays into models, a process that requires some amount of interaction to change from normal iterations to Lambda iterations and back again as and when X-rays cause convergence problems. Although Legion is a fast machine which ran through models quite quickly, the overheads brought about by the inability to interact with all models, and certain instances of convergence difficulties that could not be easily resolved, led to the model-running process taking much more time than expected. However, parameter space was quite well populated, so interpolation could be performed if required. In addition, certain models that did not converge to the fully specified level, but had only a few depths at a few levels causing problems, were included in the final grid and are flagged as such. The models successfully converged for further use are given in summary at the end of this chapter.

## 2.4 Parameters for the grid

An initial literature search was performed to find all the recent studies that fitted spectra for stellar parameters. Preference was given to those which used CMFGEN, although recent results using FASTWIND (Santolaya-Rey et al. 1997; Puls et al. 2005) were also utilised. CMFGEN analyses have no wavelength limitation and treat line-blanketing fully, whilst most other codes do not share these attributes. FASTWIND, however, does provide a rigorous enough treatment for stellar parameters. Other more speedy analyses such as the pure H$\alpha$ work of Markova et al. (2004) were used as a check on the parameters after calibration, and comparisons were made with the results of Vink et al. (2000, 2001) and the calibrations of Martins et al. (2005$a$).

The sources used to derive parameters are fairly heterogeneous, coming from more

than one modelling technique and more than one wavelength region. It must be stressed again however that the primary goal of this study is to assemble a *representative* grid of models, and the final adopted parameters do agree well with those from the most recent analyses. This approach is in fact necessary, since no single study in literature can provide a complete set of parameters to cover the whole O star range satisfactorily. Further, the grid is derived from only a few sources, and not a large number of them. Given the broad agreement with literature values of fundamental parameters, this approach is satisfactory.

The literature sources found to contain fits and derived parameters which were eventually used in this investigation were those from Martins et al. (2005*b*), Bouret et al. (2005) and Repolust et al. (2004). Table 2.2 shows the values from each of these literature sources for each spectral type that was available, and Table 2.3 is the final set of parameters used in the grid, after a calibration described in the next section. Type O2 supergiants have been omitted since they are so rare.

As suggested by the CMFGEN manual, for O stars the number of depth points in the model was chosen to be 60 or more. This is because the wind is more tenuous than in WR stars and so needs to be more regularly sampled to get the correct temperature and density structure. In some cases where it seemed as though a model would not converge due to a problem in a specific part of the wind, it was re-run with a larger number of depth points, effectively sampling more finely; the intention being to remove any discontinuities. This was largely successful and means that some models in the final grid have 65, 70 or even 75 depth points in the wind. The only complication that this led to was times such as when a model with 75 depth points was needed as an input model for one that was initially specified to have 60. There are small subroutines to deal with this, which re-grid the output from a model onto a new number of depth points for use in the new model.

As stated before, the key to choosing the number of levels and superlevels in the atomic data is balancing between having a high enough number of levels for the model to be accurate, but low enough such that computation time is reasonable. Figure 2.3 shows the comparison between spectra from models that differ only in the specification of the atomic data. The details of the spectrum are almost identical in the wind lines, with small inaccuracies in the photospheric lines in the model with fewer lines specified. The difference in computation time was around a factor of 5. Taking this into account, the final atomic data used is listed in Table 2.4.

The greatest uncertainties in the final set of parameters are for the giants. Because

**Table 2.2.** Literature values for stellar parameters. References are Repolust et al. (2004) (R), Bouret et al. (2005) (B) and Martins et al. (2005*b*) (M). The set of parameters for one O5 III star was not fully derived in the source work.

| Spectral Type | $T_{eff}$ kK | $\log g$ | $R/R_\odot$ | $v_\infty$ (km s$^{-1}$) | $\log L/L_\odot$ | $M/M_\odot$ | $\dot{M}$ $10^{-6} \times (M_\odot \mathrm{yr}^{-1})$ | ref. |
|---|---|---|---|---|---|---|---|---|
| I | | | | | | | | |
| 4 | 39.0 | 3.60 | 19.7 | 2300 | 5.90 | - | 1.80 | B |
| 4 | 39.0 | 3.55 | 19.4 | 2250 | 5.90 | 53.9 | 8.80 | R |
| 5 | 37.5 | 3.45 | 16.8 | 2350 | 5.70 | 30.7 | 8.52 | R |
| 6 | 36.0 | 3.55 | 21.1 | 2250 | 5.83 | 62.2 | 6.85 | R |
| 7 | 35.0 | 3.45 | 18.7 | 2150 | 5.68 | 37.5 | 6.32 | R |
| 7 | 34.5 | 3.30 | 19.3 | 2200 | 5.68 | 28.2 | 3.48 | R |
| 9 | 31.5 | 3.10 | 21.2 | 2100 | 5.60 | 21.7 | 5.30 | R |
| 9 | 33.0 | 3.45 | 16.6 | 2150 | 5.47 | 29.0 | 1.79 | R |
| 9.5 | 32.0 | 3.20 | 22.9 | 2050 | 5.69 | 31.4 | 2.15 | R |
| 9.5 | 29.0 | 2.97 | 32.5 | 1550 | 5.83 | 37.6 | 6.04 | R |
| III | | | | | | | | |
| 5 | 41.0 | 3.80 | 18.2 | 2800 | 5.93 | 78.7 | 5.58 | R |
| 5 | 40.0 | 3.60 | - | - | 5.60 | - | 1.73 | R |
| 6.5 | 37.0 | 3.55 | 12.3 | 2500 | 5.41 | 20.3 | 1.39 | R |
| 7.5 | 34.5 | 3.50 | 15.7 | 2550 | 5.50 | 35.9 | 1.41 | R |
| 7.5 | 35.0 | 3.50 | 14.0 | 2450 | 5.42 | 26.1 | 1.08 | R |
| 9 | 32.5 | 3.35 | 12.9 | 1150 | 5.23 | 24.6 | 0.41 | R |
| V | | | | | | | | |
| 3.5 | 46.5 | 4.00 | 10.4 | 3100 | 5.66 | 39.8 | 2.64 | R |
| 3.5 | 46.0 | 3.95 | 15.9 | 3250 | 6.01 | 83.3 | 3.45 | R |
| 3.5 | 44.0 | 4.00 | 19.9 | 3000 | 6.12 | 144.0 | 0.56 | M |
| 4 | 41.5 | 4.00 | 11.9 | 2800 | 5.57 | 51.0 | 0.32 | M |
| 4 | 41.0 | 3.90 | 11.5 | 3100 | 5.53 | 39.0 | 1.63 | R |
| 4 | 43.5 | 4.00 | 12.0 | 3000 | 5.66 | - | 0.25 | B |
| 5 | 40.5 | 3.70 | 12.8 | 3200 | 5.60 | 30.4 | 1.28 | R |
| 5 | 41.0 | 3.75 | 12.0 | 2800 | 5.56 | 30.0 | 0.32 | M |
| 5 | 40.0 | 4.00 | 11.9 | 2900 | 5.51 | 52.0 | 0.18 | M |
| 6.5 | 38.0 | 4.00 | 9.6 | 1900 | 5.23 | 33.0 | 0.01 | M |
| 6.5 | 37.0 | 4.00 | 10.0 | 2800 | 5.22 | 36.0 | 0.056 | M |
| 7.5 | 36.0 | 4.10 | 6.4 | 1750 | 4.79 | 19.0 | 0.017 | M |
| 9 | 33.0 | 4.00 | 8.4 | 1200 | 4.87 | 26.0 | 0.0013 | M |
| 9 | 34.0 | 4.00 | 9.7 | 1300 | 5.05 | 34.0 | 0.001 | M |
| 9.5 | 32.0 | 3.65 | 8.9 | 1550 | 4.87 | 20.2 | 0.18 | R |
| 9.5 | 33.0 | 4.05 | 7.5 | 800 | 4.77 | 23.0 | 0.00032 | M |
| 9.5 | 33.0 | 4.00 | 6.6 | 1200 | 4.66 | 16.0 | 0.00032 | M |

**Table 2.3.** Final set of calibrated parameters for the grid of O star models

| Spectral Type | $T_{eff}$ (kK) | $\log g$ | $\log L/L_\odot$ | $\log \dot{M}$ ($M_\odot$ yr$^{-1}$) | $R/R_\odot$ | $M/M_\odot$ | $v_\infty$ (km s$^{-1}$) |
|---|---|---|---|---|---|---|---|
| I | | | | | | | |
| 3 | 40.5 | 3.68 | 5.89 | -5.10 | 18.05 | 56.94 | 3150 |
| 4 | 39.0 | 3.60 | 5.83 | -5.15 | 18.17 | 47.97 | 2323 |
| 5 | 37.6 | 3.52 | 5.78 | -5.20 | 18.45 | 41.16 | 1885 |
| 5.5 | 36.8 | 3.48 | 5.75 | -5.22 | 18.61 | 38.18 | 2280 |
| 6 | 36.1 | 3.44 | 5.72 | -5.25 | 18.68 | 35.09 | 2300 |
| 6.5 | 35.3 | 3.41 | 5.69 | -5.27 | 18.87 | 33.43 | 2180 |
| 7 | 34.6 | 3.37 | 5.67 | -5.29 | 19.20 | 31.54 | 2054 |
| 7.5 | 33.9 | 3.33 | 5.64 | -5.32 | 19.32 | 29.14 | 1980 |
| 8 | 33.1 | 3.29 | 5.62 | -5.34 | 19.80 | 27.92 | 1528 |
| 8.5 | 32.4 | 3.25 | 5.59 | -5.37 | 19.97 | 25.88 | 1941 |
| 9 | 31.6 | 3.22 | 5.56 | -5.39 | 20.28 | 24.91 | 2007 |
| 9.5 | 30.9 | 3.17 | 5.53 | -5.41 | 20.49 | 22.67 | 1797 |
| III | | | | | | | |
| 3 | 45.3 | 3.98 | 6.15 | -4.78 | 19.46 | 132.09 | 3340 |
| 4 | 43.0 | 3.87 | 5.99 | -5.03 | 17.97 | 87.38 | 3100 |
| 5 | 40.8 | 3.77 | 5.83 | -5.30 | 16.60 | 59.24 | 2810 |
| 5.5 | 39.7 | 3.71 | 5.75 | -5.43 | 15.99 | 47.87 | 2770 |
| 6 | 38.6 | 3.66 | 5.67 | -5.57 | 15.42 | 39.71 | 2560 |
| 6.5 | 37.5 | 3.60 | 5.59 | -5.70 | 14.90 | 32.29 | 2618 |
| 7 | 36.4 | 3.55 | 5.51 | -5.84 | 14.43 | 26.97 | 2598 |
| 7.5 | 35.3 | 3.50 | 5.43 | -5.98 | 13.99 | 22.60 | 2176 |
| 8 | 34.2 | 3.44 | 5.35 | -6.12 | 13.59 | 18.58 | 2125 |
| 8.5 | 33.1 | 3.39 | 5.27 | -6.24 | 13.23 | 15.70 | 2255 |
| 9 | 32.0 | 3.33 | 5.18 | -6.38 | 12.77 | 12.72 | 1883 |
| 9.5 | 30.8 | 3.28 | 5.11 | -6.52 | 12.71 | 11.24 | 1721 |
| V | | | | | | | |
| 3 | 44.9 | 3.95 | 5.87 | -5.50 | 14.35 | 67.03 | 3188 |
| 4 | 43.0 | 3.95 | 5.69 | -6.00 | 12.72 | 52.65 | 2950 |
| 5 | 41.0 | 3.95 | 5.52 | -6.50 | 11.50 | 43.06 | 2874 |
| 5.5 | 40.1 | 3.95 | 5.42 | -6.72 | 10.72 | 37.38 | 1960 |
| 6 | 39.1 | 3.95 | 5.33 | -6.98 | 10.16 | 33.61 | 2557 |
| 6.5 | 38.1 | 3.95 | 5.24 | -7.23 | 9.65 | 30.31 | 2457 |
| 7 | 37.1 | 3.95 | 5.15 | -7.47 | 9.17 | 27.40 | 2278 |
| 7.5 | 36.2 | 3.95 | 5.07 | -7.73 | 8.79 | 25.14 | 1977 |
| 8 | 35.2 | 3.95 | 4.98 | -7.97 | 8.38 | 22.86 | 1750 |
| 8.5 | 34.2 | 3.95 | 4.89 | -8.23 | 8.00 | 20.85 | 1970 |
| 9 | 33.3 | 3.95 | 4.80 | -8.47 | 7.61 | 18.85 | 1443 |
| 9.5 | 32.3 | 3.95 | 4.71 | -8.71 | 7.29 | 17.31 | 1490 |

**Figure 2.3.** Comparison of two models for which the only difference is the specification of atomic data. A region from both the ultraviolet and the optical is displayed. Black shows a model with more detailed atomic data, which took $\sim$ 40 hours to compute and a further 8 hours to compute the observer's frame calculation. Red shows a less detailed model that took $\sim$ 16 hours to compute plus an observer's frame calculation, and is nearly as accurate.

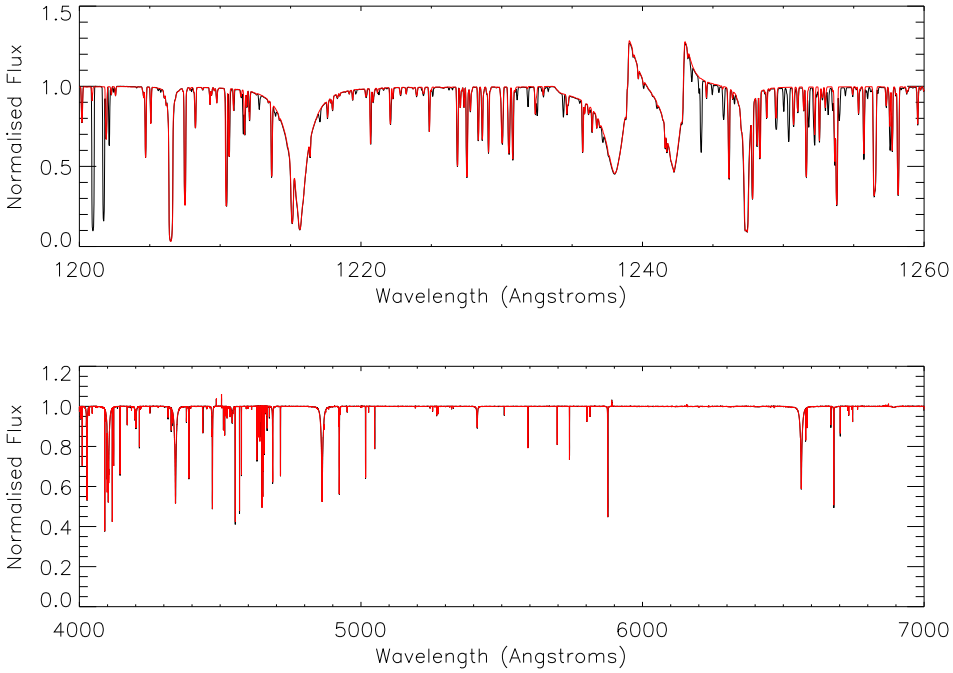


the sample of giants observed and whose spectra have been fitted is rather limited, it is difficult to apply any great certainty to the calibration. The luminosities derived from the calibration for early type giants is higher that that of the corresponding supergiants, which seems infeasible. In addition, the giants' surface gravities in the grid do not match well to other estimates. Given the lack of calibration objects available to use for giants, the poor quality of the final calibration, and the fact that subsequent uses of the grid in this thesis are only for supergiants (Chapter 6) and dwarfs (Chapter 5), giants are left out of further analysis. A good approximation to a giant's spectrum and parameters can be achieved by interpolating between supergiant and dwarf models.

For the final grid to be computed, a standard set of abundances and rotational velocities were adopted. The chosen rotational velocity was 100 km $s^{-1}$. This is largely representative of O stars (Howarth et al. 1997; Penny 1996), although in reality there is rather a lot of scatter. The value chosen is perhaps more consistent with O dwarfs, as O supergiants are expected to have spun down by their evolutionary stage. This value is

**Table 2.4.** Atomic data used in grid. The final column indicates the dataset from which the values were derived.

| Ion | Important Levels, Super-levels, Levels | Dataset |
|---|---|---|
| HI | 20, 20, 30 | 5dec96 |
| HeI | 45, 45, 69 | 5dec96 |
| HeII | 22, 22, 30 | 5dec96 |
| CIII | 52, 52, 84 | 23dec04 |
| CIV | 59, 59, 64 | 5dec96 |
| NIII | 41, 41, 82 | 24mar07 |
| NIV | 50, 50, 76 | 5dec96 |
| NV | 41, 41, 49 | 5dec96 |
| OIII | 88, 88, 170 | 15mar08 |
| OIV | 53, 53, 72 | 5dec96 |
| OV | 32, 32, 56 | 5dec96 |
| OVI | 25, 25, 31 | 5dec96 |
| SiIII | 20, 20, 33 | 5dec96 |
| SiIV | 22, 22, 33 | 5dec96 |
| PIV | 30, 30, 90 | 15feb01 |
| PV | 16, 16, 62 | 15feb01 |
| SIII | 24, 24, 44 | 3oct00 |
| SIV | 51, 51, 142 | 3oct00 |
| SV | 30, 30, 83 | 3oct00 |
| SVI | 28, 28, 58 | 3oct00 |
| FeIII | 103, 103, 1425 | 7feb05 |
| FeIV | 74, 74, 540 | 18oct00 |
| FeV | 50, 50, 220 | 18oct00 |
| FeVI | 44, 44, 433 | 18oct00 |
| FeVII | 29, 29, 153 | 18oct00 |

still acceptable for all stars, and any models derived from the current set could easily have this changed to match a specific object. The abundances of Asplund et al. (2005) were adopted for all models in the grid. These are solar values, which will be acceptable for all typical O stars represented in the grid. There are potential issues when stars modelled fall into ON or OC categories and have enhanced abundances, and in addition the supergiants are more likely to have slightly different values from solar as they are more evolved. The H-relative abundances used in the grid are given in Table 2.5.

### 2.4.1 Spline or calibration?

The full possible range of Galactic O star parameters is not evenly or completely sampled by observations. The result of this was that some interpolation or extrapolation was required to completely cover the intended parameter space of the grid. The issue here was

**Table 2.5.** Abundances used in the grid

| Element | Relative Solar Abundance by number |
|---|---|
| He | 0.0851 |
| C | $2.45\times10^{-4}$ |
| N | $6.03\times10^{-5}$ |
| O | $4.57\times10^{-4}$ |
| Si | $1.38\times10^{-5}$ |
| P | $2.29\times10^{-7}$ |
| S | $1.38\times10^{-5}$ |
| Fe | $2.82\times10^{-5}$ |

how exactly this interpolation and extrapolation should be performed. Initially a spline curve was fitted to each of the existing sets of parameter values such that the line passed through each. What this did however was lead to some unrealistic numbers at the extremes of parameter space, such as an early spectral type that was far too hot, or a dwarf with an unrealistically high surface gravity. Because of this, and in an effort to make the grid more generally representative, a line of best fit was drawn though the existing parameters as a function of spectral type, and values were read off for each spectral type. This was justified in that almost all the necessary parameters do follow some trend with spectral type. The only parameter which was treated differently was the terminal velocity, which although following a trend from early to late type, has a rather larger scatter than other parameters, as can be seen in Figure 8 of Prinja et al. (1990), for example (reproduced here as Figure 2.4). For spectral types with objects in the literature, a simple average of available values was used for the terminal velocity. For the gaps in the grid a straightforward interpolation was used.

Figures 2.5 to 2.16 show the mean parameters for $T_{eff}$, $\log g$, $L_*$ and $\dot{M}$ compared to both the source literature values and to values from other investigations, where appropriate. These were calibrated as described above to give the final set of parameters. This set of plots was produced to give a check on how closely the grid parameters matched those from different literature, both observational and theoretical.

### 2.4.2 X-rays and clumping for the grid

Since part of the motivation for putting together this grid was to explore the effects of different clumping factors in the wind and the difference between a wind that had no explicit X-ray input and one that does, it was important to specify carefully how these

**Figure 2.4.** Scatter in terminal velocity from Prinja et al. (1990). O and B stars are represented by circles and triangles respectively; filled in symbols represent measures from the saturated edge at $v_{black}$, whilst open symbols represent measures from the velocity of the Narrow Absorption Component (NAC).

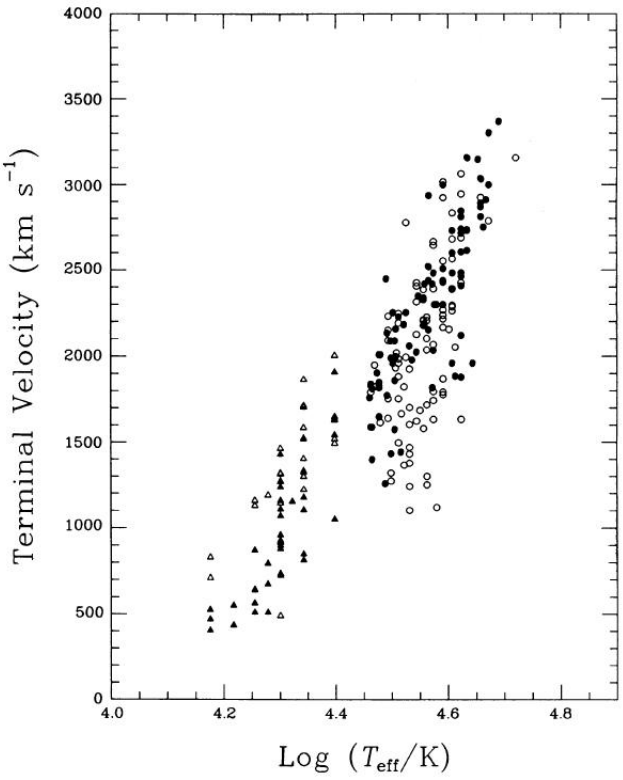


were to be included.

X-rays were included as prescribed in §2.1.4, such that the ratio $L_X/L_{bol}$ was in the range 0.8 - 3×10$^{-7}$. This was a lengthy process since one must inspect the X-ray luminosity in the model output and then readjust the X-ray parameters in a new model to obtain the desired X-ray output luminosity. As such some models were produced with X-ray luminosities outside the desired range. They were re-run until the X-ray luminosity was in the correct range, but the original models were kept in order to investigate the effects of X-rays further. Some of these models were utilised, as can be seen in Chapter 3.

Different studies recently have preferred different clumping factors. Bouret et al. (2005) argue that filling factors of order 0.05 and smaller are required to reproduce observations, whereas Fullerton et al. (2006), amongst others, believe that a more modest 0.1 is more appropriate. To assess the effects of clumping fully, and taking into account both these arguments, the grid was run for an unclumped wind ($f = 1$), a moderately clumped wind ($f = 0.1$) and a strongly clumped wind ($f = 0.05$).

**Figure 2.5.** Effective temperature scale for supergiants. References are Martins et al. (2005*a*), Markova et al. (2004) and Repolust et al. (2004). The values for this study agree with all others to within 2000 K, and much more closely for much of the O star range, although the profiles were not matched explicitly in the present work.

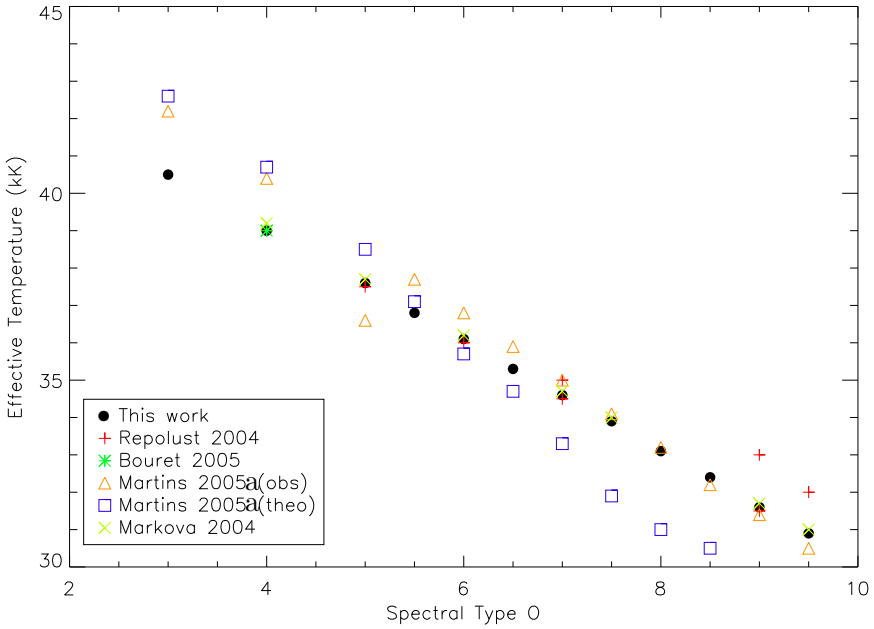


**Figure 2.6.** Effective temperature scale for giants. References as for supergiants. Agreement is to within 2000 K for most of the scale, diverging at type O3.

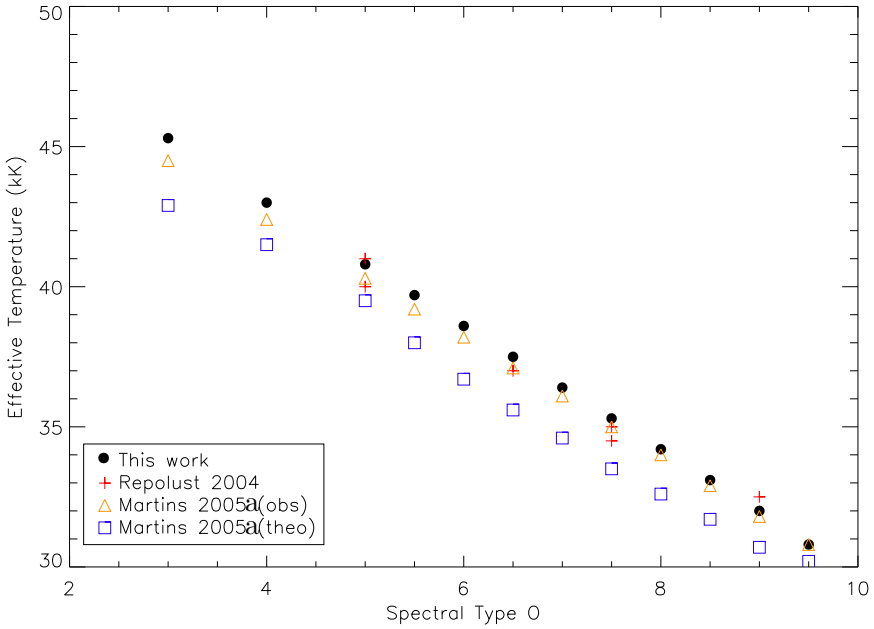

**Figure 2.7.** Effective temperature scale for dwarfs. References are as before, plus Martins et al. (2005*b*). The agreement is very close to other scales.

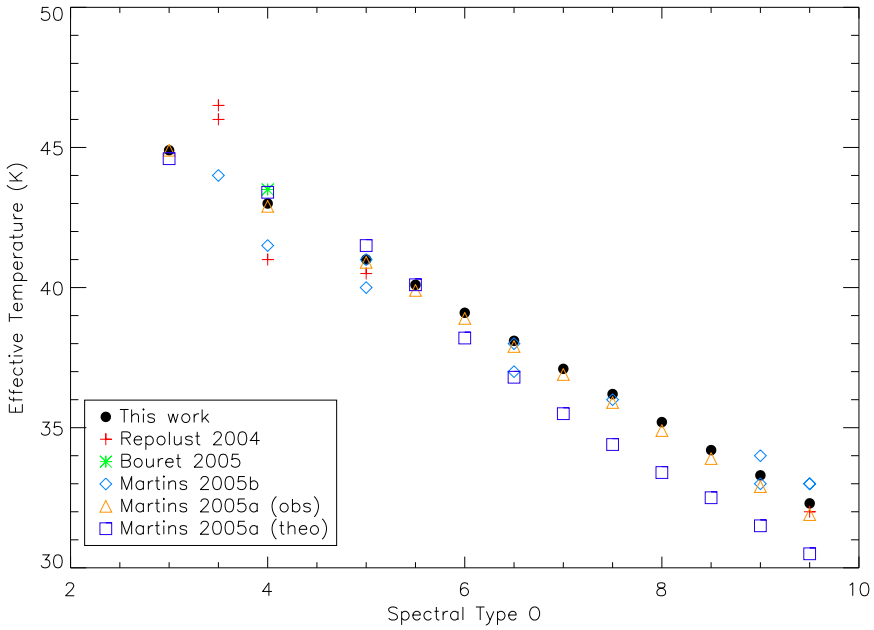


**Figure 2.8.** Surface gravity scale for supergiants. The values for this study are in good agreement with other scales, although there seems to be a larger scatter at later types.

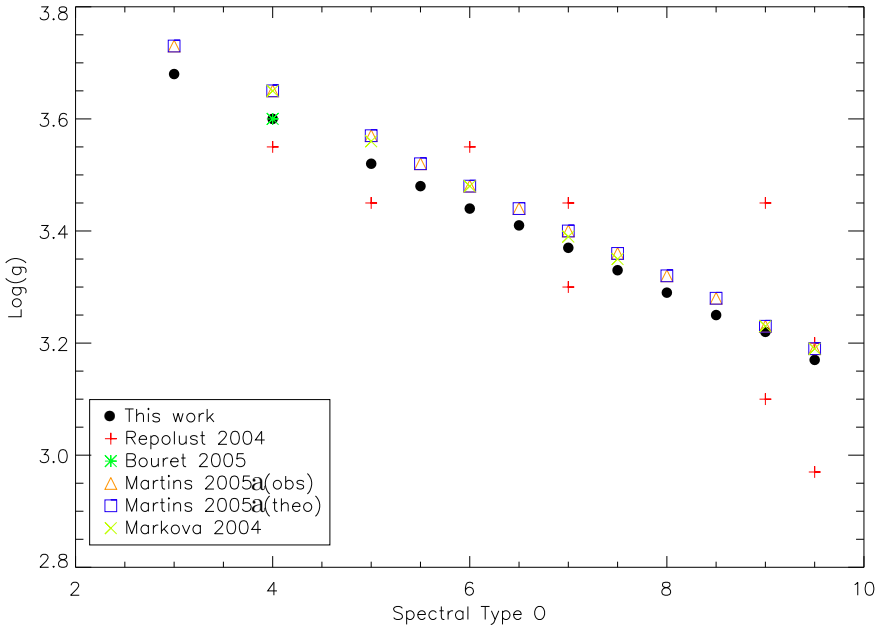

**Figure 2.9.** Surface gravity scale for giants. This study has values which are based on a very limited number of actual objects, and as such seem at odds with the scale of Martins et al. (2005*a*).

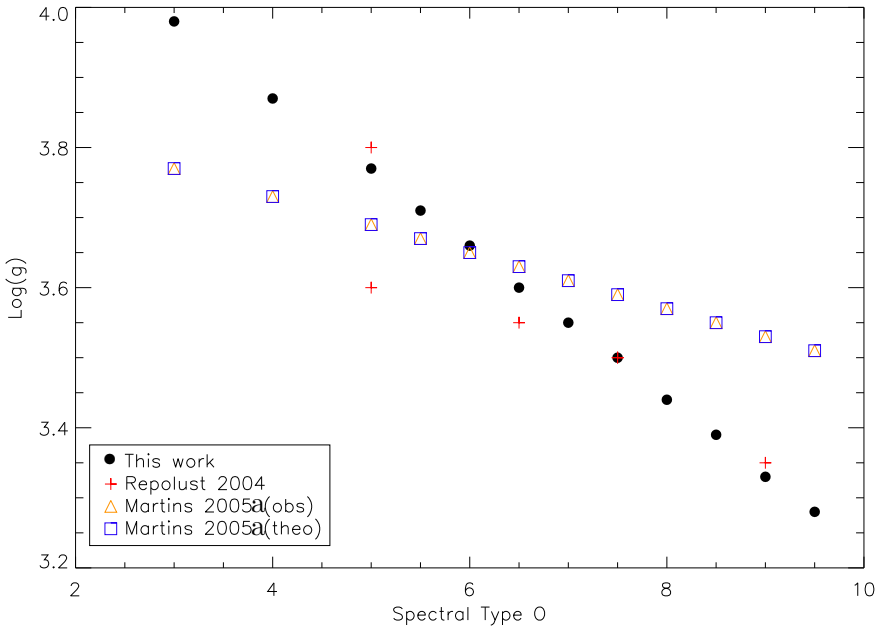


**Figure 2.10.** Surface gravity scale for dwarfs. There is considerable scatter from the observational points, but the clear trend is for log $g$ to be roughly constant across the range of spectral types. A constant value of 3.95 was chosen to best reflect literature parameters.

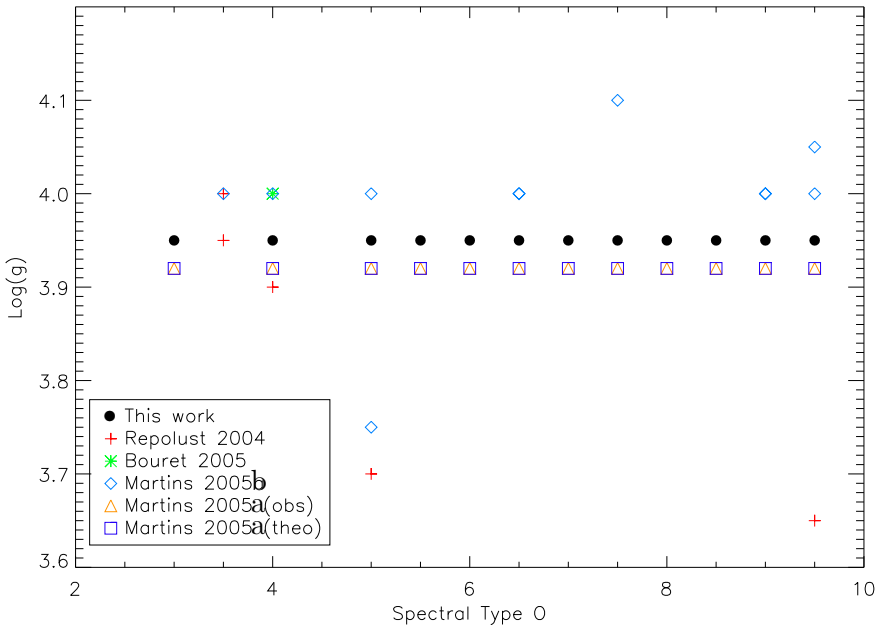

**Figure 2.11.** Luminosity scale for supergiants. The scale derived here is in relatively good agreement with theoretical and observational comparisons, albeit with some scatter.

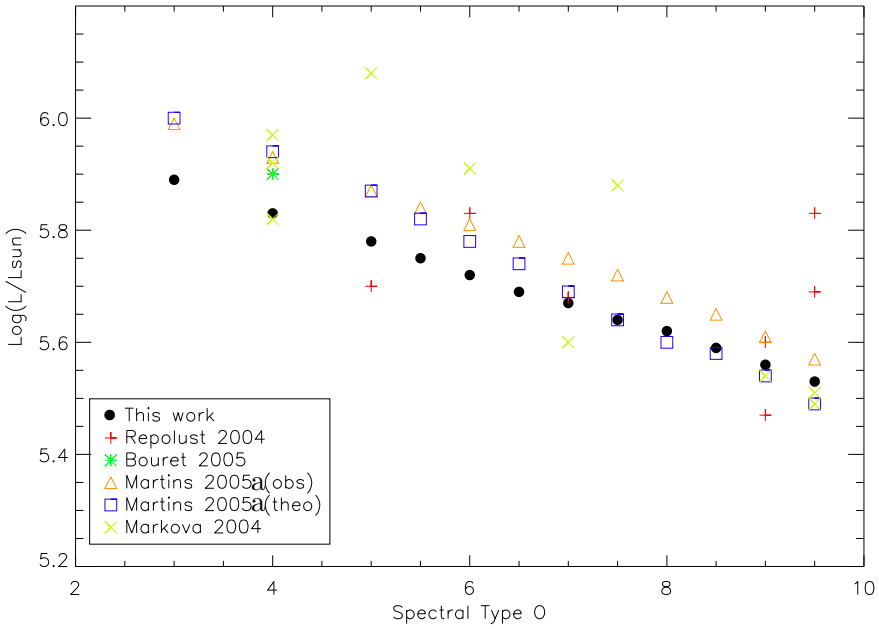


**Figure 2.12.** Luminosity scale for giants. The agreement with other sources is very close.

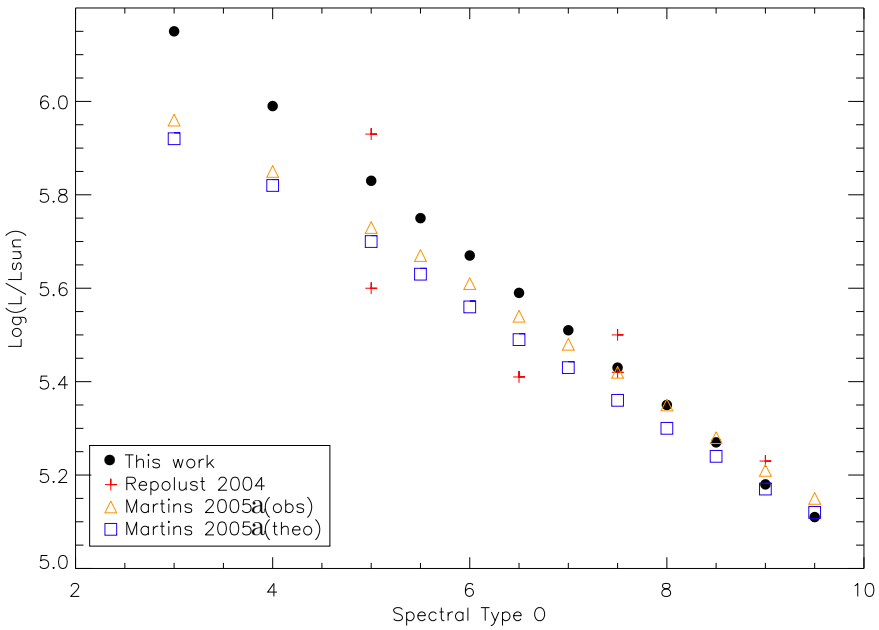

**Figure 2.13.** Luminosity scale for dwarfs. The values from this study match other estimates and theoretically derived values quite closely.

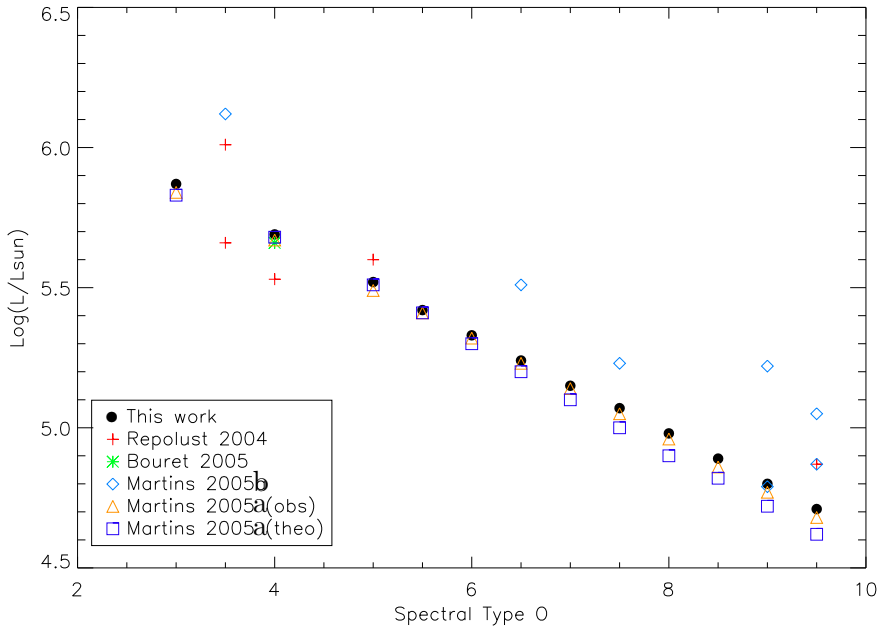


**Figure 2.14.** Mass-loss rates for supergiants. When all sources of literature are considered there is quite a large scatter in points. The Vink et al. (2000) mass-loss recipe predicts generally lower rates than are calibrated in this investigation, whereas the pure H$\alpha$ study of Markova et al. (2004) prefers generally higher values. This is no doubt tied into the current uncertainties involved in estimating mass-loss in O stars.

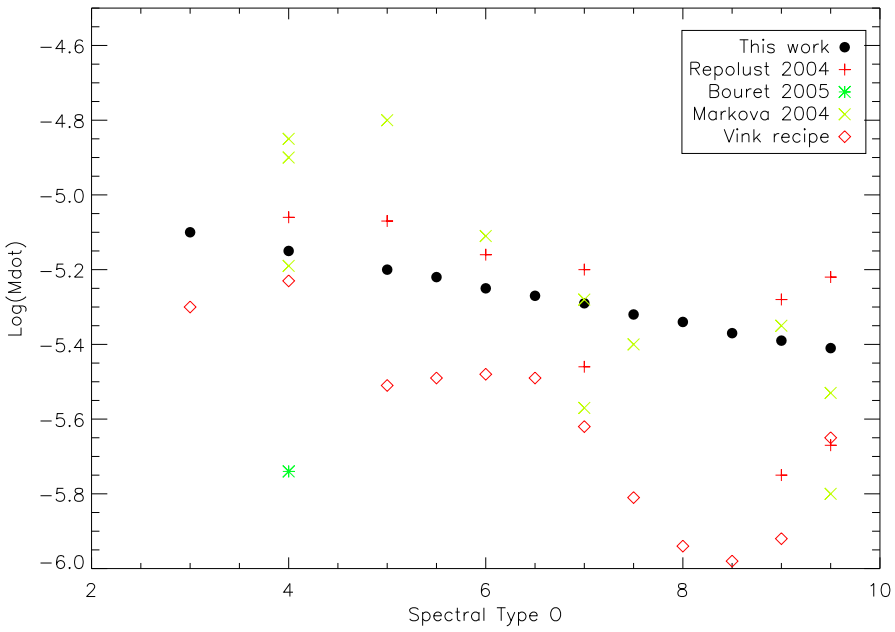

**Figure 2.15.** Mass-loss rates for giants. There is a relatively close agreement here, but there is a very small number of actual objects to compare to.

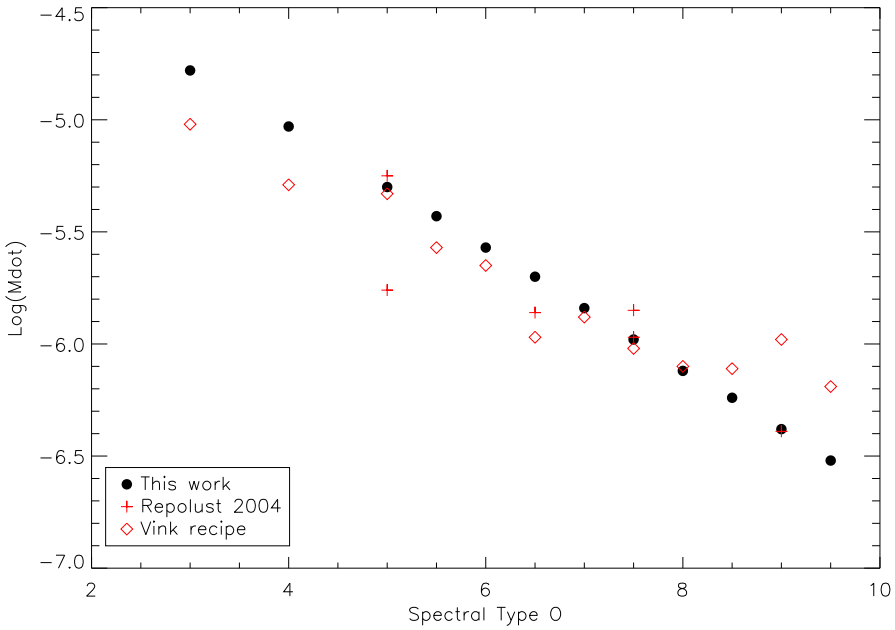


**Figure 2.16.** Mass-loss rates for dwarfs. The values chosen for this study tend to follow the observed values (which is no surprise as they contributed to their calibration). They are consistently lower than those from the Vink et al. (2000) recipe, and those of Repolust et al. (2004), which are upper limits.

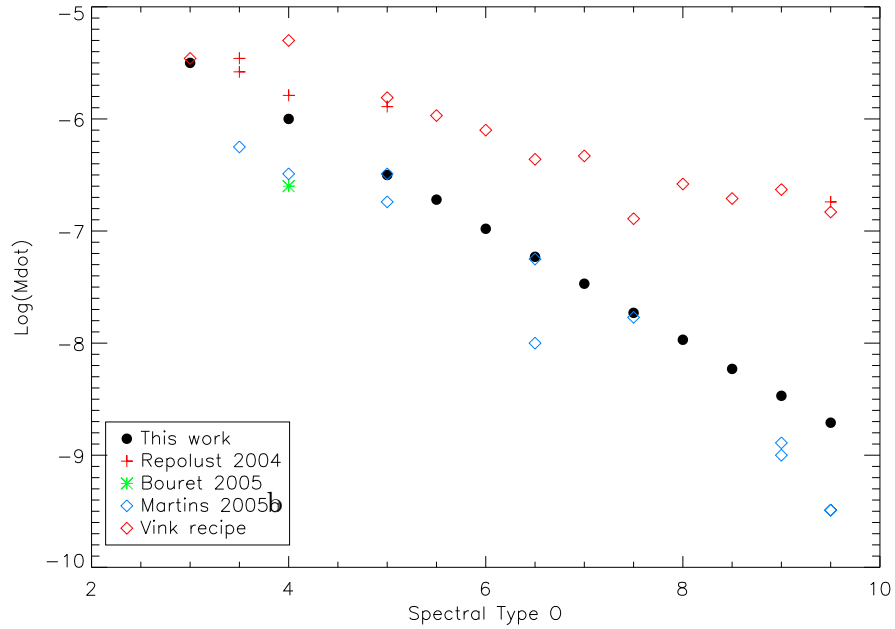

### 2.4.3 Literature Sources

The sources from which parameters were gathered are now discussed in a little more detail, in addition to the works to which further comparisons were made. Repolust et al. (2004), Bouret et al. (2005) and Martins et al. (2005*b*) were used to derive parameters; Martins et al. (2005*a*) and Markova et al. (2004) were used afterwards as a comparison to further confirm the suitability of parameters.

- Repolust et al. (2004) - This paper analysed a sample of Galactic O stars that was originally treated by Puls et al. (1996), but the newer analysis included a treatment of line-blanketing, and found a reduction of 1-2kK in the temperature scale compared to previous work. The analysis was performed on H and He lines in the optical, fitting to spectra taken using the Issac Newton Telescope (INT) and at the European Southern Observatory (ESO). They claim that a typical clumping factor of 5 (i.e. a filling factor of 0.2) is required for optical mass-loss measures to match theoretical ones.

- Bouret et al. (2005) - This work undertook the analysis of the far-UV spectra of a Galactic O4 dwarf and O4 supergiant. TLUSTY and CMFGEN were used to derive stellar parameters and surface composition for the two stars. The authors match profiles for the UV and also in the optical if low mass-loss rates (a factor 3 or more lower than previous values) and high clumping factors (0.002 and 0.004) are used.

- Martins et al. (2005*a*) - New calibrations were of O star parameters. It includes an 'observational' scale based on recent spectroscopic studies, somewhat similar to the calibration performed in this thesis, and a 'theoretical' scale using interpolations on a CMFGEN grid. This provides perhaps the most important comparison to the parameters derived here.

- Martins et al. (2005*b*) - Here, a sample of Galactic dwarfs was studied using CMFGEN, with a concurrent analysis of UV wind lines and optical lines. Rather low mass-loss rates (as low as $\log \dot{M} = -9.5$) were derived in this study. The focus was very much to 'track the conditions under which weak winds appear'.

- Markova et al. (2004) - Although mainly a pure $H\alpha$ analysis, this study involves drawing together parameters from other recent investigations, and so offers another check on the parameters for the current grid.

## 2.5 The grid

The set of models for giants was not completed due to the reasons set forth in § 2.4. A fuller grid could be produced in the future, which includes a full set of giants. For now it is assumed that phenomenologically their spectra lie somewhere between those of dwarfs and supergiants, and they are not included in further work on the grid. Tables 2.8 and 2.9 show the models that were completed. A few receive flags due to incomplete convergence (having a few levels at a few depths that do not converge to better than 0.1%), but are deemed well converged enough to use since the majority of levels and depths had minimal corrections. The strongly clumped dwarf models are rather sparsely sampled by the grid in terms of converged models, and there is little crossover between X-ray and non-X-ray models for these. For this reason they will not be used to draw conclusions about the trend of any parameter with spectral type. In future further effort can be put into yielding convergence for the full spectral type range in these models.

To confirm that the produced models conform to standard optical spectral types, they were measured using the Conti & Alschuler (1971) classification scheme, updated in Conti & Frost (1977). Those works define spectral type according to the respective equivalent widths of HeI and HeII lines:

$$W' = \log W(HeI_{4471}) - \log W(HeII_{4541}). \tag{2.23}$$

where spectral type is assigned according to the scheme set out in Table 2.6. The measurements and resulting spectral types are set out in Table 2.7. Most agree with Conti spectral types, and any that do not are half a spectral sub-type different. Since the measurements of log equivalent width ratio can be up to 0.1 in uncertainty, this means that the spectral type assignments in this investigation can be considered consistent with existing classification schemes.

In total out of an intended 216 models covering a range of spectral types, luminosity classes, clumping scenarios and X-ray scenarios, a total of 116 models are included in the final grid after dropping the giants and unconverged models. Not included in this number are the large number of test models and models accumulated during the process of computing a representative X-ray luminosity. The total computing time for all of these was well in excess of 10000 hours. The next two chapters present main results from the

**Table 2.6.** Conti spectral type assignments.

| Spectral Type | W′ range |
|---|---|
| O4 | < -0.6 |
| O5 | -0.45 to -0.6 |
| O5.5 | -0.3 to -0.45 |
| O6 | -0.2 to -0.3 |
| O6.5 | -0.1 to -0.2 |
| O7 | 0 to -0.1 |
| O7.5 | 0 to +0.1 |
| O8 | +0.1 to +0.2 |
| O8.5 | +0.2 to +0.3 |
| O9 | +0.3 to +0.45 |
| O9.5 | > +0.45 |

**Table 2.7.** Spectral types assigned in this study.

| | Supergiants | | Dwarfs | |
|---|---|---|---|---|
| Spectral Type | W′ | SpTy | W′ | SpTy |
| O4 | -0.64 | O4 | -0.61 | O4 |
| O5 | -0.42 | O5 | -0.37 | O5.5 |
| O5.5 | -0.30 | O5.5 | -0.3 | O5.5/O6 |
| O6 | -0.21 | O6 | -0.23 | O6 |
| O6.5 | -0.14 | O6.5 | -0.15 | O6.5 |
| O7 | -0.09 | O7 | -0.07 | O7 |
| O7.5 | -0.02 | O7 | -0.01 | O7.5 |
| O8 | +0.01 | O7.5 | +0.07 | O7.5 |
| O8.5 | +0.17 | O8 | +0.20 | O8.5 |
| O9 | +0.23 | O8.5 | +0.28 | O8.5 |
| O9.5 | +0.41 | O9 | +0.35 | O8.5 |

grid for spectra and ion fractions as a function of X-rays and wind-clumping.

**Table 2.8.** Grid completion for supergiants. An 'X' signifies a converged model, and those with incomplete but satisfactory convergence are asterisked (see text).

| | No X-rays | | | X-rays | | |
|---|---|---|---|---|---|---|
| | $f = 1$ | $f = 0.1$ | $f = 0.05$ | $f = 1$ | $f = 0.1$ | $f = 0.05$ |
| 3 | | X | X | X | X | X |
| 4 | X | X | X | X | X | X |
| 5 | X | X | X | X | X | X |
| 5.5 | X | X | | | X | X |
| 6 | X | X | X | X∗ | X∗ | X |
| 6.5 | X | X | X | X | X | X |
| 7 | X | X | X | X | X | X |
| 7.5 | X | X | X | X | X | X |
| 8 | X | X | X | X | X | X |
| 8.5 | X | X | X | | | |
| 9 | X | X | X | X | X | X |
| 9.5 | X | X | X | X | X | X |

**Table 2.9.** Grid completion for dwarfs. An 'X' signifies a converged model, and those with incomplete but satisfactory convergence are asterisked (see text).

| | No X-rays | | | X-rays | | |
|---|---|---|---|---|---|---|
| | $f = 1$ | $f = 0.1$ | $f = 0.05$ | $f = 1$ | $f = 0.1$ | $f = 0.05$ |
| 3 | X | X | X | X | X | X |
| 4 | X | X | X | X | | |
| 5 | X | X | | X | X | X |
| 5.5 | X | X | X | | X | |
| 6 | X | | X | X | | |
| 6.5 | X | X∗ | | X | X | X |
| 7 | X | | | X | X | |
| 7.5 | X | X | X | X | | |
| 8 | X | | | X | | |
| 8.5 | X | | | X | X | |
| 9 | X | X | X∗ | X | X | |
| 9.5 | X | X∗ | X∗ | X | X | X |

This page is intentionally left almost blank

# Chapter 3

# The effects of clumping and X-rays on Galactic O star spectra

*'Insanity: doing the same thing over and over again and expecting different results.'*

Albert Einstein

The emergent spectrum of a star will look different depending upon the physical parameters of the star. The optical spectrum of O stars has long been known to vary as a function of effective stellar temperature, surface gravity, luminosity, chemical composition. Before detailed studies of ultraviolet spectra from *IUE* were undertaken, it was not clear whether the shorter wavelength spectra would have similar line profile trends with spectral type and luminosity class. However the atlas and papers of Walborn and Panek (Walborn & Panek 1985; Walborn et al. 1985; Walborn & Panek 1984*a*,*b*) concluded that the ultraviolet spectra of the majority of O stars, including their wind features, show strong trends that correlate with those seen in the optical. Particular effects discussed include the dependence of the strength of the SiIV resonance doublet with stellar luminosity, the trend of spectral phenomena seen in main sequence O stars, and the O stars with enhanced N and C abundances. Perhaps most important was simply that most O stars can be calibrated by spectral type using wind features, implying that O-type stellar winds are governed by fundamental physical parameters of the star. As a result it can be said that the study of

stellar wind features in O stars can 'strongly constrain physical theories for the origin of the winds' (Walborn et al. 1985).

This chapter is a presentation of the spectra calculated in the CMFGEN grid described in the previous chapter. It is ordered so as to discuss how well the spectra match available observations, how spectra are predicted to be affected by clumping and X-rays in the wind, and whether we can constrain the most likely set of clumping and X-ray parameters to describe an O star wind. As such, what follows is a series of plots from different wavelength regions. So as to be concise only six spectral types of star are displayed in this chapter; an early-, mid- and late-type O star for each of the supergiant and dwarf luminosity classes. Giants are omitted since the set of models was not completed for them (see Chapter 2). Firstly models are compared in the *IUE* short wavelength range ($\sim$ 1200-1800 Å), and in the optical region, focusing particularly on the comparison of the H$\alpha$ profile with observations. Secondly the *FUSE* range ($\sim$ 900-1200 Å) is examined, again to see the effects of clumping and X-rays in particular. The aim throughout is not to 'fit' profiles, but rather to observe trends across spectra in the grid for models which are representative of typical objects.

## 3.1 Archival observational datasets

Observations which were used to compare to the models in this chapter were gathered through the Multimission Archive at STScI (MAST). This archive stores data for many NASA missions including Hubble, *FUSE* and *IUE*. In order to obtain spectra with well known spectral types to compare to models, initially the Galactic O star catalogue (Maíz-Apellániz et al. 2004; Sota et al. 2008) was consulted to find all the objects in the spectral type category at hand. Each object was sought on MAST and a preview was examined to gauge which was the optimum spectrum available in terms of signal-to-noise. The appropriate spectrum was downloaded and normalised by fitting a spline curve using continuum regions of the spectrum.

Spectra in the *IUE* range were the most straightforward to work with, being relatively free of interstellar lines and hence easy to normalise, and also coming ready from the archive in a choice of two wavelength regions (rather than several shorter wavelength traces as for *FUSE*). One chooses the wavelength region, either short (1150-1975Å) or long (1850-3350Å), and the dispersion (high or low). The short wavelength range (SWP)

was chosen because it includes all the UV wind lines of interest in O stars, whereas the longer range (LWR/P) is mostly devoid of such features. High dispersion spectra were used in order to be able to pick out all the lines in the best detail possible, since the shape of lines is important as well as their strength.

The *FUSE* range is covered by several spectra for each observation. There are four detection channels and two gratings, of LiF and SiC. This means there are 8 segments covering the approximate range 905Å to 1187Å (see Table 3.1). Almost any given wavelength will have two spectra covering it, and so all eight were examined and those with the best signal-to-noise selected to form a complete spectrum for the whole range by putting them together to form a single spectrum. These tended to be all those spectra through channel 1. The 2BSiC or 2ALiF traces were used to bridge the gap between 1ASiC and 1BLiF. The task of normalising these spectra is particularly difficult at shorter wavelengths due to both the large number of interstellar lines obscuring the continuum, and the relative weakness of this part of the spectrum due to extinction. These effects are briefly discussed later in the chapter.

**Table 3.1.** *FUSE* spectrum segments

| Segment | Approximate wavelength range in Å |
|---|---|
| 1ASiC | 1004-1090 |
| 1BSiC | 905-992 |
| 1ALiF | 988-1082 |
| 1BLiF | 1095-1187 |
| 2ASiC | 917-1005 |
| 2BSiC | 1017-1104 |
| 2ALiF | 1087-1179 |
| 2BLiF | 979-1074 |

Comparisons are made to observed H$\alpha$ profiles, taken directly from the mass-loss studies which are referenced in the figures.

## 3.2 UV and optical spectra

One function of the comparison of model spectra with observations is as a reality check, that they match what is seen in nature closely enough that any conclusions drawn from them are reasonable. The level which is deemed to be reasonable is that the general

strength and shape of profiles are similar by eye, not that there is an exact fit, because each model is only representative of the spectral class and lines do vary somewhat within a type due to slight changes in physical parameters. Let us begin with the *IUE* and optical regions.

### 3.2.1 Early-type Supergiant

#### Comparison to UV observations

Figure 3.1 shows four different versions of the model for an O4 supergiant alongside the *IUE* spectrum of a typical object, in this case the famous $\zeta$ Puppis. These models show clumping and X-rays either turned on or off, and these are signified in the figure by 'X' for X-rays and 'Cl' for clumping. The models all seem reasonable, with similarly sized and shaped profiles to observations across the spectrum. There is some variation between models to be discussed, but the general morphological properties are consistent with an early supergiant. This is encouraging and implies that the models are quite accurate at this wavelength range. The line shortward of NV is that of Lyman $\alpha$, and does not enter the discussion much further because it is dominated by the effects of interstellar absorption in most observed spectra, not by the wind.

#### Effects of clumping and X-rays on the UV

Figure 3.2 displays the main wind profiles in closer detail, showing the effect of X-rays, the effect of clumping when X-rays are not present, and the effect of clumping when X-rays are present. The NV profile seems to respond to the effect of X-rays quite strongly at this spectral type, presumably as the extra energy input allows ionization out to higher wind velocities. The SV excited line also shows a small change when X-rays are added, but all other profiles show little or no response to the addition of X-rays in the model. In the scenario with no X-rays, the NV profile is changed by the effects of moderate clumping, but not much more by strong clumping. The same can be said of the SiIV and HeII wind profiles. The only other line to show any change with clumping in the absence of X-rays is CIV. The emission peak increases in strength as the wind becomes more strongly clumped, but we can perhaps assume that generally only a small change is seen because the profile is saturated and the addition of more absorbers (by enhancing the local density) is having only a limited effect. When X-rays are included, clumping has the same effects

**Figure 3.1.** Models for an O4 supergiant compared with an IUE spectrum of a typical object ($\zeta$ Puppis). X denotes X-rays and Cl denotes clumping.

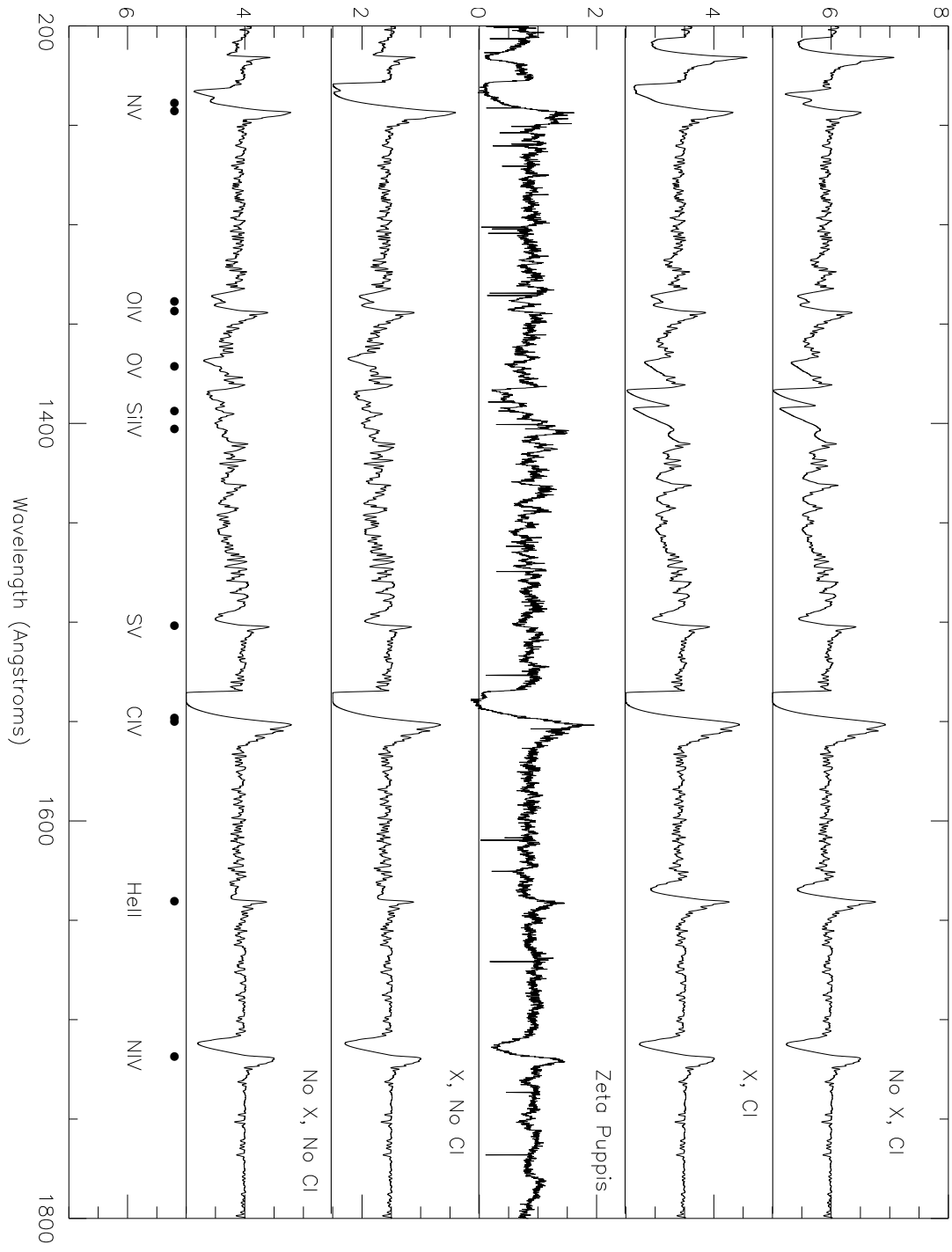

**Figure 3.2.** Profiles in the IUE range for an O4 supergiant. From top to bottom: NV, OIV, OV/SiIV, SV, CIV, HeII and NIV. Left panels: smooth with no X-rays (black) and smooth with X-rays (red). Middle panels: smooth with no X-rays (black), moderate clumping with no X-rays (red) and strong clumping with no X-rays (green). Right panels: as for middle panel but with X-rays included.

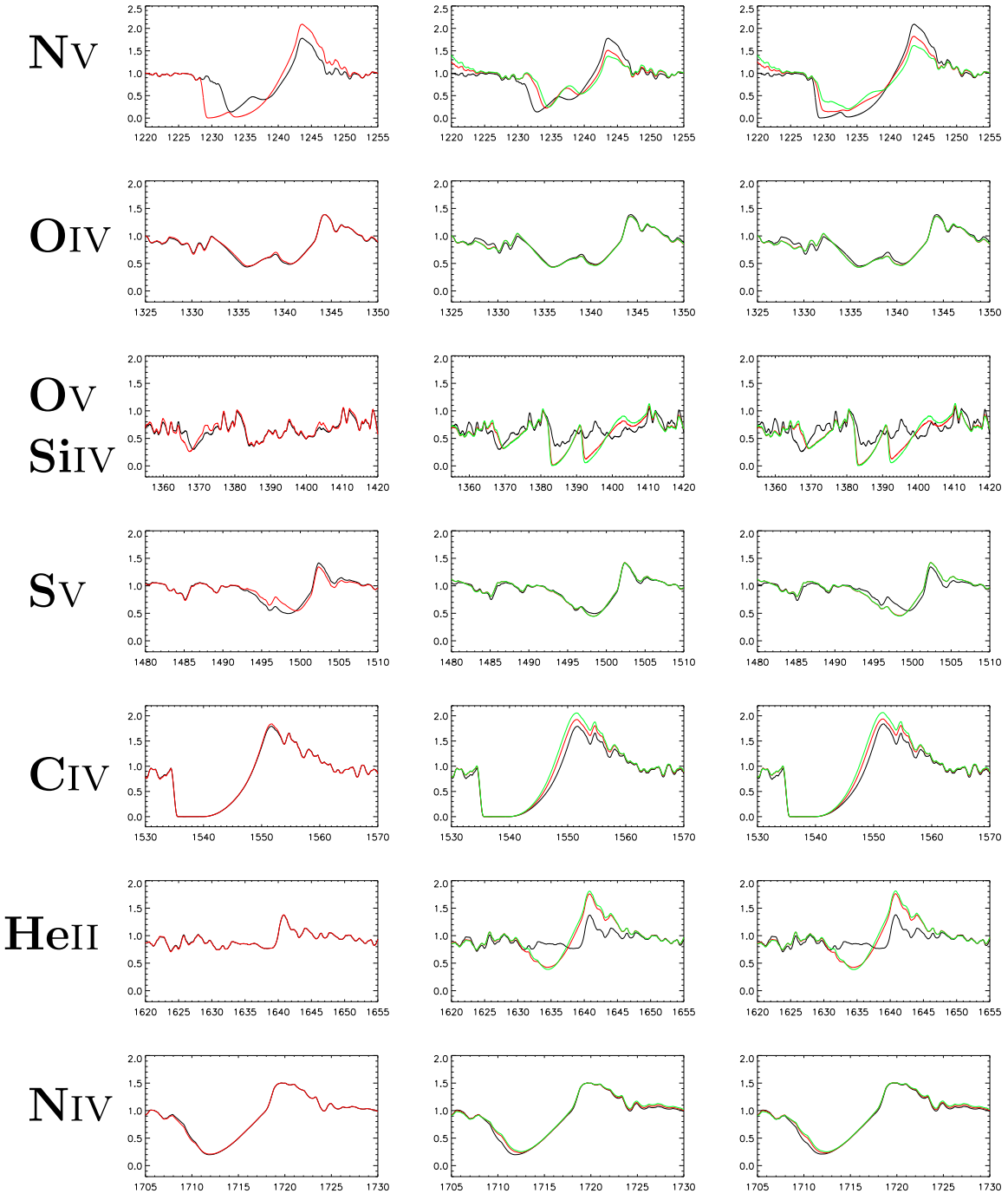

**Figure 3.3.** The effects of X-rays and clumping on the FeIV lines in the UV for an O4 supergiant. The range of lines in question is shown by bars, although there are also Fe lines lying over the He II profile. Top panel: smooth with no X-rays (black) and smooth with X-rays (red). Middle panel: smooth with no X-rays (black), moderate clumping with no X-rays (red) and strong clumping with no X-rays (green). Bottom panel: as for middle panel but with X-rays included.

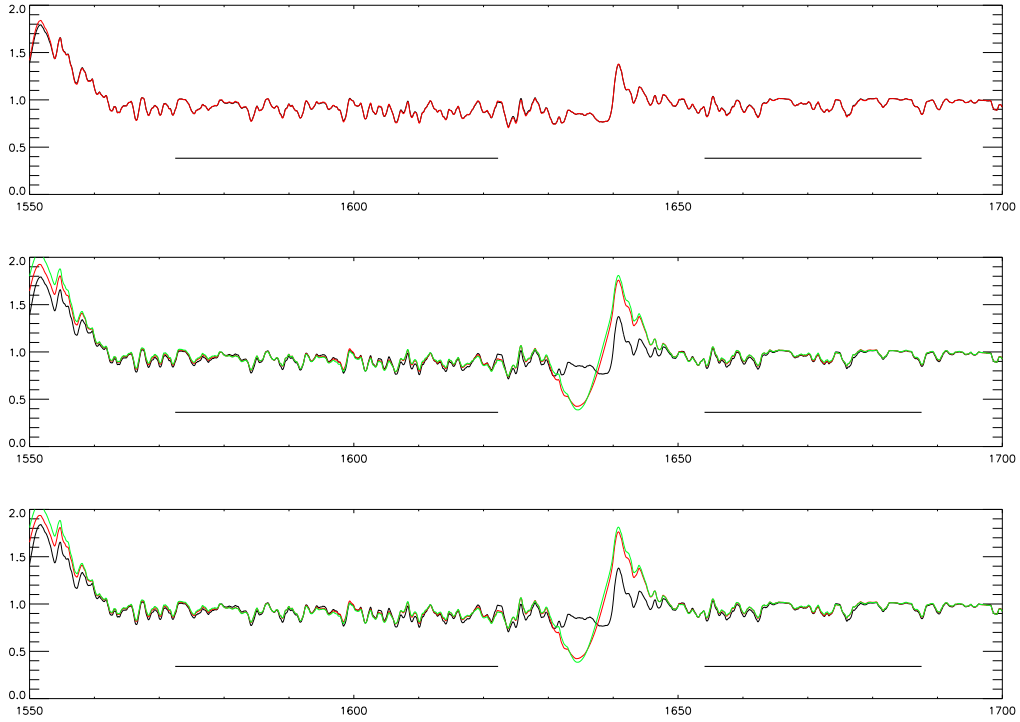


on most profiles, the exceptions being those that were shown already to be affected by X-rays anyway. It is interesting that clumping seems to affect the strength of the SiIV doublet quite strongly (through altering the ionization balance) since this line is known to be sensitive also to luminosity. At early types then the models predict there to be a degeneracy of some kind between clumping and luminosity for this specific line, since both can affect the strength of SiIV.

The main diagnostics we should use to distinguish between likely X-ray and clumping scenarios in early O supergiants are NV and HeII, but there seems to be some difficulty involved in interpreting the SiIV line. We must discover whether we could use any other diagnostics to better constrain the scenario to be used.

Figures 3.3 and 3.4 show the UV regions where there are many FeIV and FeV lines respectively. At hotter types like O4 we expect there to be more in the way of FeV than FeIV as the hotter temperatures cause more atoms to be photoionized, and that is indeed

**Figure 3.4.** The effects of X-rays and clumping on the FeV lines in the UV for an O4 supergiant. The range in question is shown by a bar, although there are also FeV lines that lie over the OV and SiIV profiles. Top panel: smooth with no X-rays (black) and smooth with X-rays (red). Middle panel: smooth with no X-rays (black), moderate clumping with no X-rays (red) and strong clumping with no X-rays (green). Bottom panel: as for middle panel but with X-rays included.

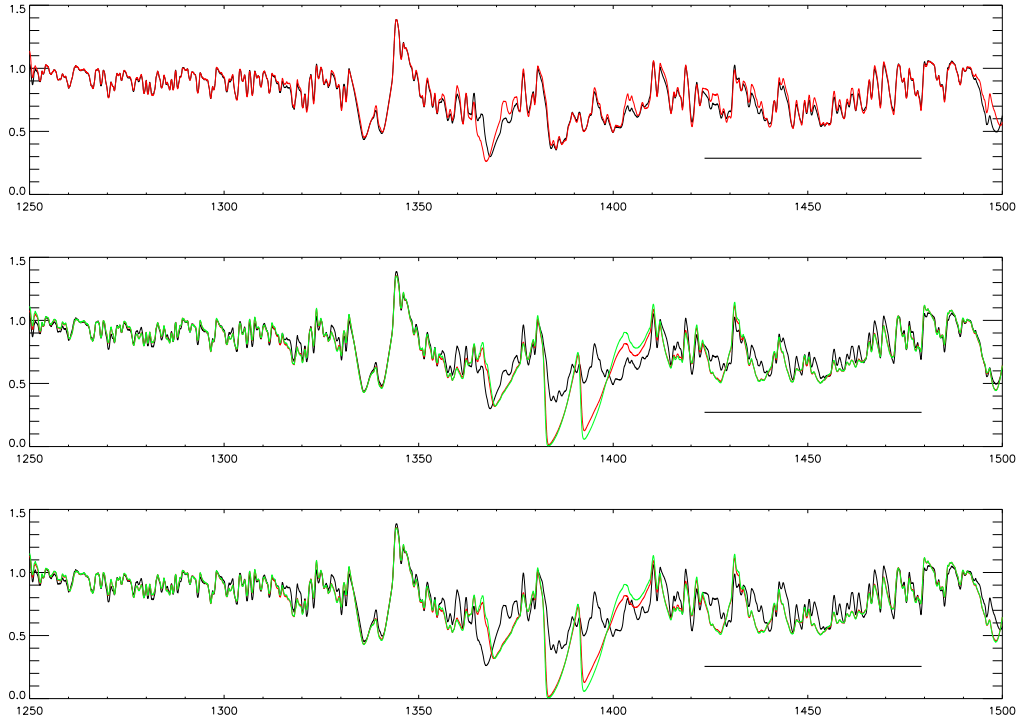


what is seen. Although it is not a very large effect, clumping the wind seems to strengthen some of the FeV profiles around the region of SiIV. Note that Figure 3.1 seems to indicate that the unclumped models are closer to predicting the correct spectrum of Fe at this spectral type, meaning a higher luminosity is required in this model to exactly reproduce the SiIV spectrum of $\zeta$ Puppis directly, or that the effective temperature is too high. The model effective temperature at this spectral type is 39kK and the model luminosity is $6.7 \times 10^5 L_\odot$. Accepted values from studies such as Martins et al. (2005*a*), Oskinova et al. (2007) and Repolust et al. (2004) are slightly hotter (40kK), ruling out the possibility that the model wind is too hot to form SiIV, and slightly more luminous ($8 \times 10^5 L_\odot$). This small gap between the model and a specific object may be the reason for the problem in computing an accurate SiIV profile. Only the models incorporating X-rays predict a sufficiently deep NV profile, and only the unclumped models produced an apparently accurate iron spectrum. It could be that rather than being completely unclumped (which

**Figure 3.5.** The effects of X-rays and clumping on the optical region of the spectrum for an O4 supergiant. Top panel: smooth with no X-rays (black) and smooth with X-rays (red). Middle panel: smooth with no X-rays (black), moderate clumping with no X-rays (red) and strong clumping with no X-rays (green). Bottom panel: as for middle panel but with X-rays included. Below are typical H$\alpha$ profiles, from Puls et al. (1996), together with fits from that work. These show the variation that could be expected at similar spectral type.

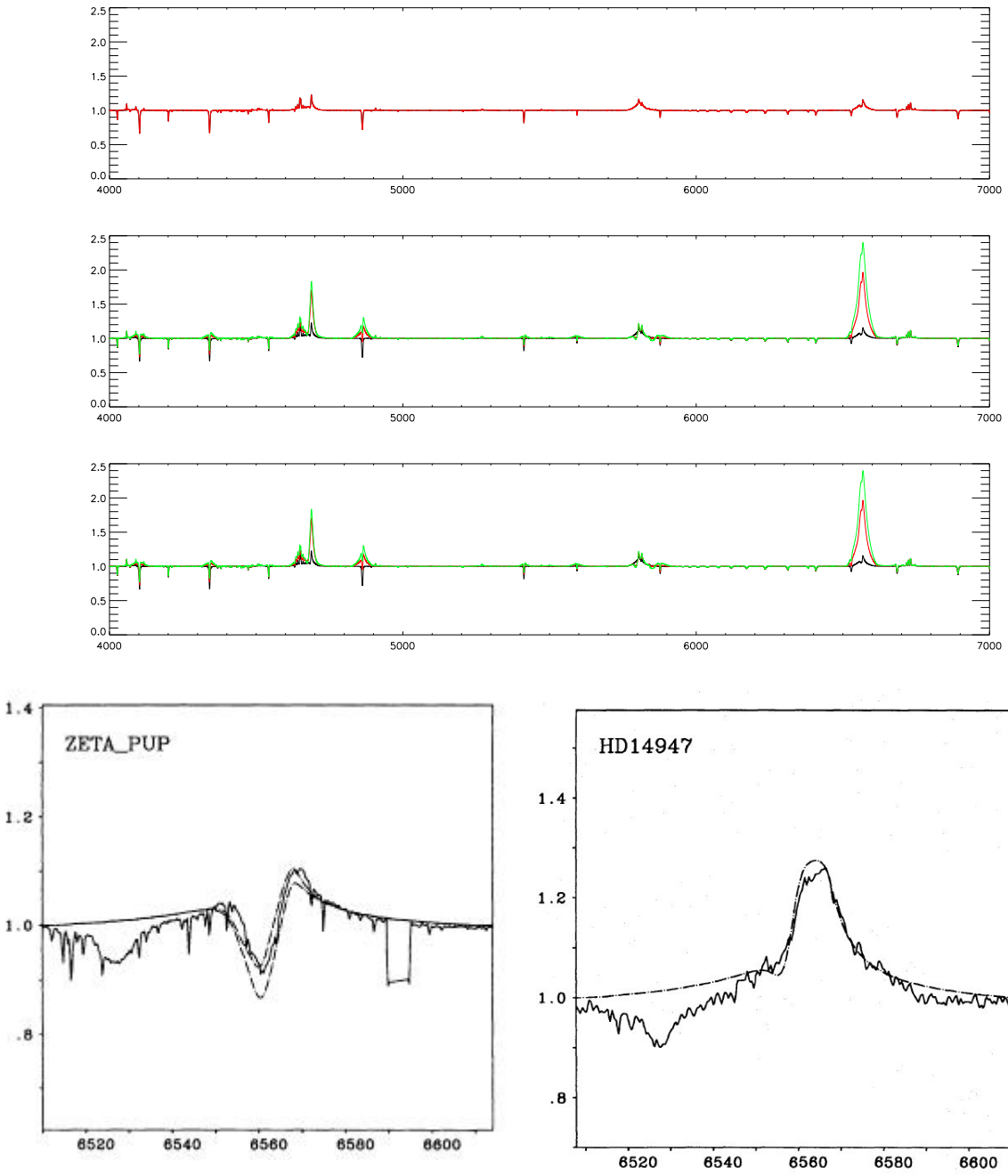

seems an unrealistic approximation given the literature discussed in the introduction), the volume filling factor is simply closer to unity than that used to represent moderate clumping in these models.

**Effects of clumping and X-rays on the optical**

Figure 3.5 shows the models in the optical range from 4000 to 7000 Å, and observed H$\alpha$ profiles from $\zeta$ Puppis from Puls et al. (1996). The X-ray input has no effect on the optical spectrum. This is presumably because H$\alpha$ is formed close in to the star by recombination but X-rays do not become important until the wind has reached higher velocities. H$\alpha$ is formed mostly in the first few stellar radii, whilst the CMFGEN parametrisation of X-rays has them beginning at a wind velocity of 400km s$^{-1}$, which corresponds to only around 0.5 stellar radii out from the photosphere. Since this means the H$\alpha$ forming and X-ray emitting regions are somewhat concurrent, we must assume that at lower velocities the X-rays are not able to significantly influence the recombination of hydrogen. Also the photoionization potential of hydrogen (13.6eV) is rather far away from the X-ray regime and H is almost completely ionized in any case. The chosen onset of X-rays in the models is consistent with recent estimates from simulations by e.g. Cohen et al. (2010).

Clumping has the same effect whether there are X-rays included or not. All this means that inspecting the optical range tells us nothing about which X-ray scenario to use in these models, but much about the clumping scenario. The Balmer series lines and several He lines react to changes in the clumping scenario, more so for the addition of moderate clumping than for the change from moderate to strong clumping. The closest H$\alpha$ profile to that observed for $\zeta$ Puppis is the one with no clumping, however since there is a degeneracy between mass-loss rate and clumping it could be that the mass-loss rate for $\zeta$ Puppis is in fact around a factor 2-3 lower and the wind is clumped. The model shows very little absorption component, but as can be seen in comparing $\zeta$ Puppis to HD 14947 it is possible to see some variation in the absorption among similar spectral types. In Puls et al. (1996), $\zeta$ Puppis is assigned a mass-loss rate of $6\times10^{-6}M_{\odot}yr^{-1}$ and HD 14947 $7.5\times10^{-6}M_{\odot}yr^{-1}$. The mass-loss rate adopted for this model is $7\times10^{-6}M_{\odot}yr^{-1}$, which explains why it better reproduces the H$\alpha$ profile of HD 14947.

More discussion will be presented on this later in the chapter when the FUV spectra are described. For now we are left with the following scenario: for early O supergiants the UV spectrum is best matched (although not 'fitted' - see chapter introduction) by a

weakly-clumped wind with a need for the inclusion of X-rays. The optical spectrum also implies only low clumping is needed to produce a realistic spectrum, although the exact mass-loss rate is and important factor.

### 3.2.2 Mid-type Supergiant

#### Comparison to UV observations

Figure 3.6 shows the four different models for an O6.5 type supergiant alongside HD 163758 (O6.5 Iaf). Unlike the early-type star, the models are more consistent in predicting the shape and size of the SiIV doublet, albeit possibly with a reduced emission peak[1]. Elsewhere along the spectrum the models do a good job computing the wind features accurately, with the notable exception of NV for some clumping and X-ray scenarios.

#### Effects of clumping and X-rays on the UV

Figure 3.7 shows the profiles in the *IUE* range in more detail. It is immediately obvious that most of the profiles are neither affected by clumping or X-rays in any significant way. This is more likely to do with how saturated lines like SiIV and CIV are, or for others that they are excited lines and so the ion population is not high enough for changes to be seen. The stark exception to this is NV, which responds to both clumping and X-rays quite strongly. It is clear from Figure 3.6 that X-rays are essential to produce a large enough NV profile to match the observations, again through increased ionization. The fact that NV changes so much with X-rays and clumping implies that nitrogen may be in quite a fine balance of ionization for this spectral type, and that it only takes a relatively small enhancement in recombination or photoionization to drastically alter the profile. This effect could well apply to CIV and SiIV if they were not already so saturated. The NIV line at 1719Å shows some small variation with clumping. SiIV gains a slightly stronger emission peak through enhanced clumping but not enough to be easily noticed through the noise inherent to *IUE* observations. In addition the shape of HeII is changed a small amount by adding clumping, but again not by enough that this change would be seen in currently available observations. What is seen quite clearly in both SiIV and HeII is that moderate clumping causes a change in the profile from the smooth case, and that a more strongly clumped wind does not alter the profile much further.

[1]It is possible the peak in the observations is a data artefact, but there is only one spectrum on the archive. Other observations of stars at the same spectral type show some variation in SiIV emission peak.

**Figure 3.6.** Models for an O6.5 supergiant compared with an IUE spectrum of a typical object (HD 163758).

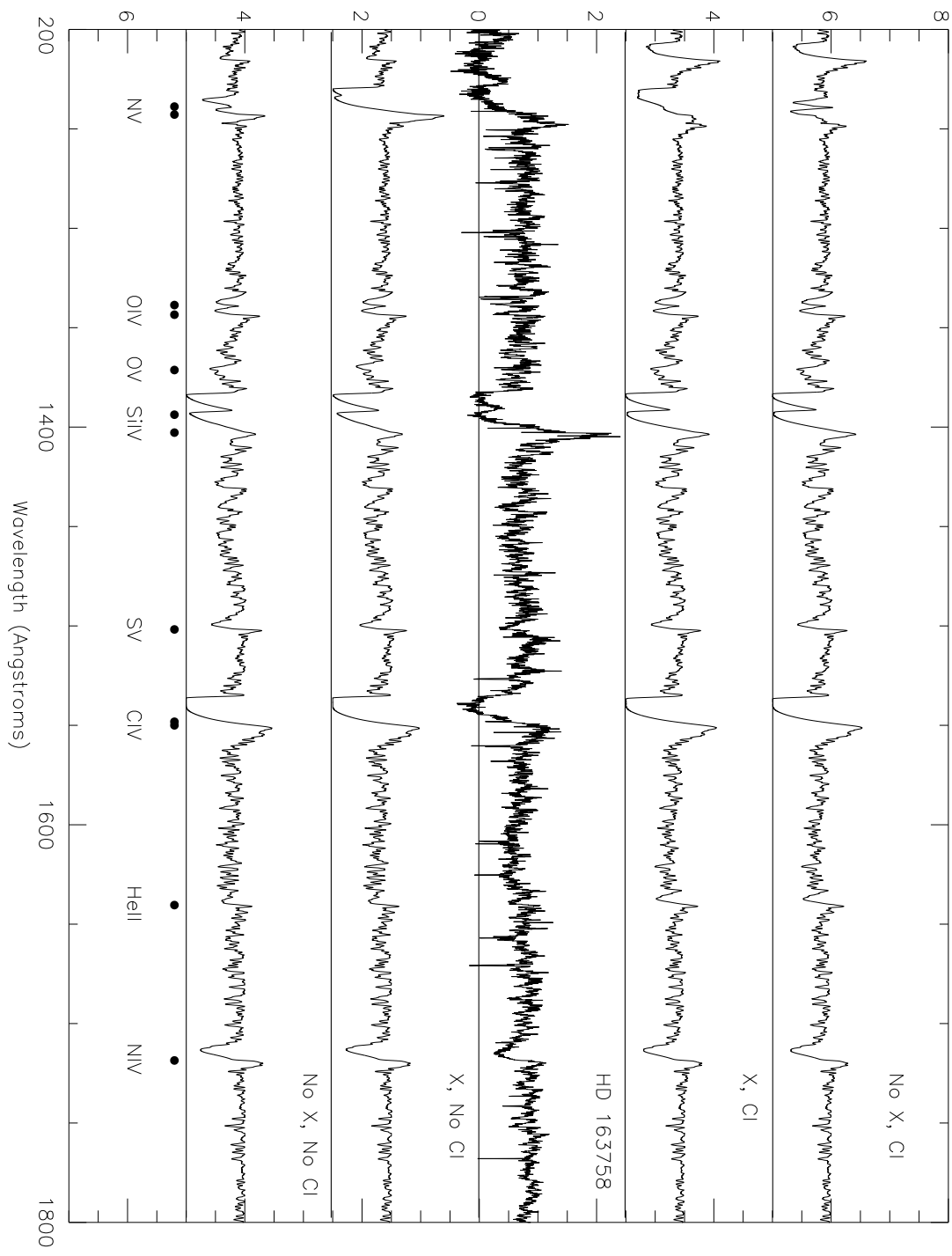

**Figure 3.7.** Profiles in the IUE range for an O6.5 supergiant. From top to bottom: NV, OIV, OV/SiIV, SV, CIV, HeII and NIV. Left panels: smooth with no X-rays (black) and smooth with X-rays (red). Middle panels: smooth with no X-rays (black), moderate clumping with no X-rays (red) and strong clumping with no X-rays (green). Right panels: as for middle panel but with X-rays included.

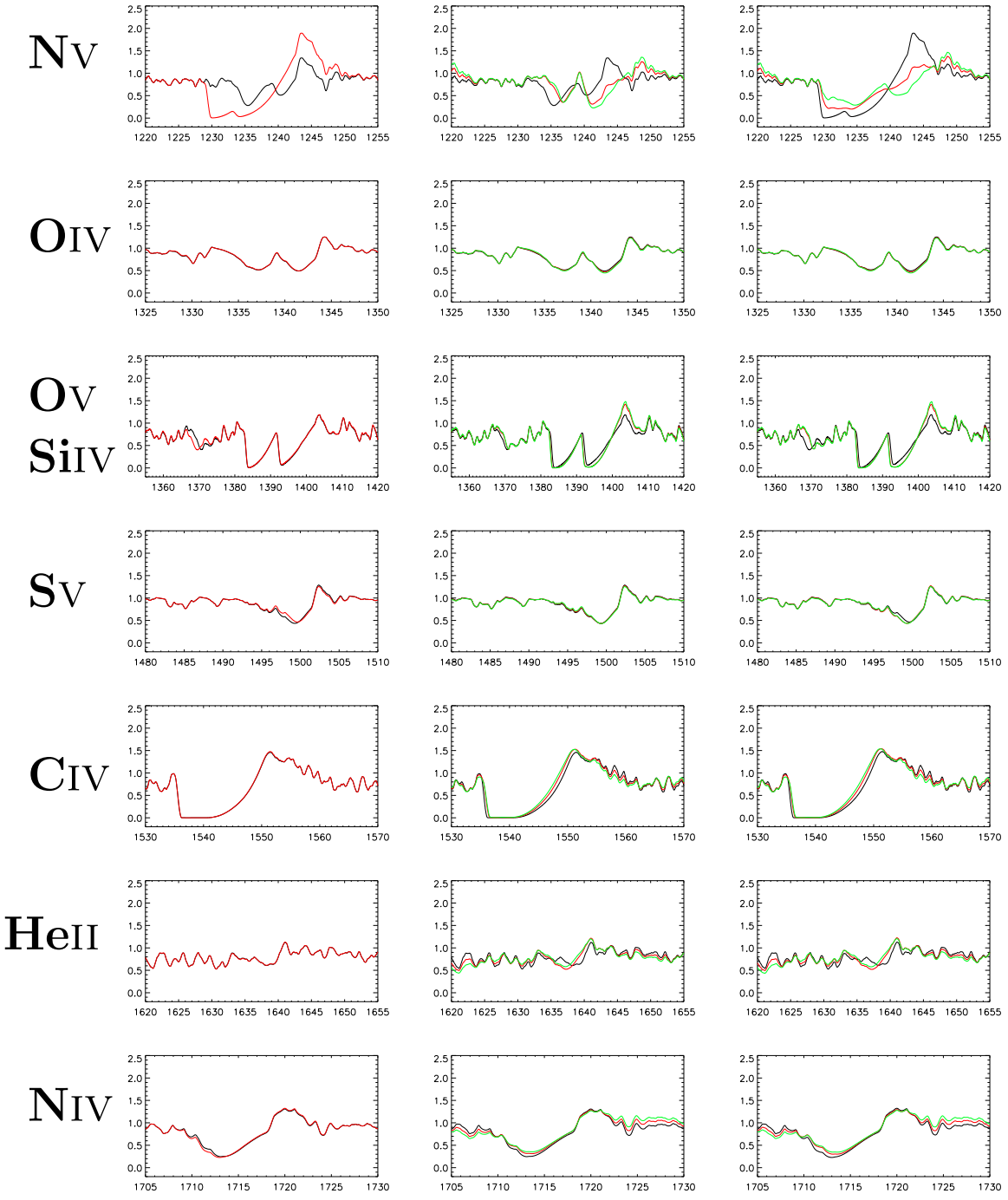

**Figure 3.8.** The effects of X-rays and clumping on the FeIV lines in the UV for an O6.5 supergiant. The range of lines in question is shown by bars, although there are also Fe lines lying over the HeII profile. Top panel: smooth with no X-rays (black) and smooth with X-rays (red). Middle panel: smooth with no X-rays (black), moderate clumping with no X-rays (red) and strong clumping with no X-rays (green). Bottom panel: as for middle panel but with X-rays included.

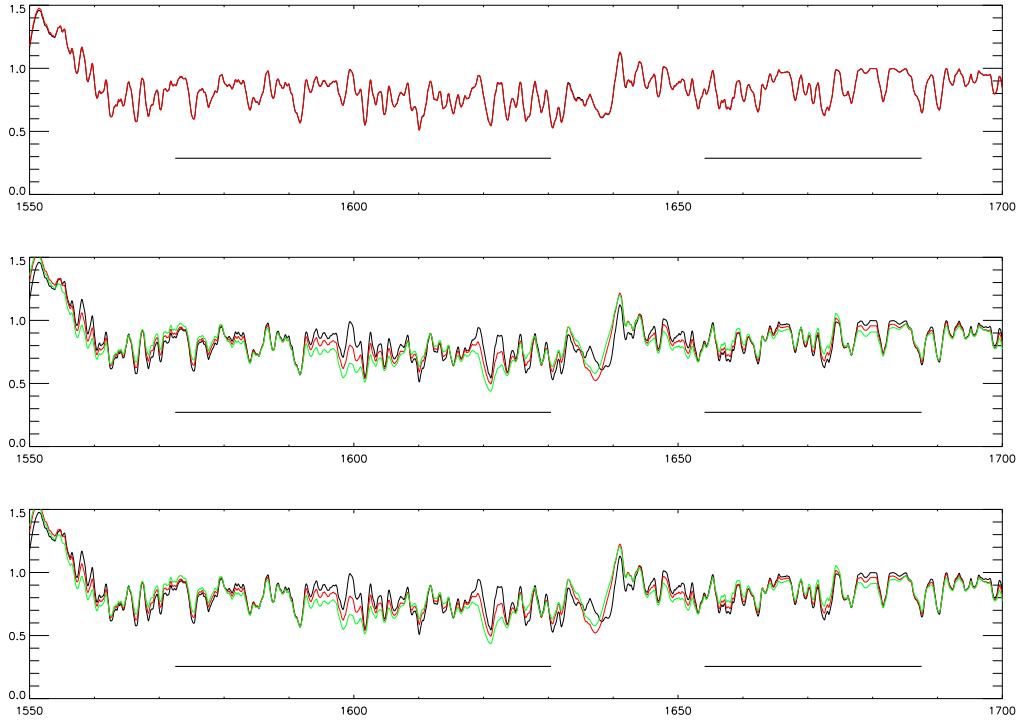


Figures 3.8 and 3.9 show the regions with many FeIV and FeV lines. In both cases we see that X-rays don't play a role in changing the line profiles beyond the 'numerical noise' of the code. Unlike the O4 supergiant, FeV is no longer affected much by clumping; this has been taken on by the FeIV lines near HeII. We expect FeIV to be strengthening and FeV to be weakening as stellar effective temperature decreases, and so perhaps it is not surprising that the effects of clumping are more visible at later types. It is not clear whether this could be used as a diagnostic of clumping in O stars - the difference seen in Fig. 3.8 would likely be lost in the noise of observations.

From looking purely at the UV spectra, one can see that X-rays are required. In order to work out the best clumping scenario it is necessary to look elsewhere.

**Figure 3.9.** The effects of X-rays and clumping on the FeV lines in the UV for an O6.5 supergiant. The range in question is shown by a bar, although there are also FeV lines that lie over the OV and SiIV profiles. Top panel: smooth with no X-rays (black) and smooth with X-rays (red). Middle panel: smooth with no X-rays (black), moderate clumping with no X-rays (red) and strong clumping with no X-rays (green). Bottom panel: as for middle panel but with X-rays included.

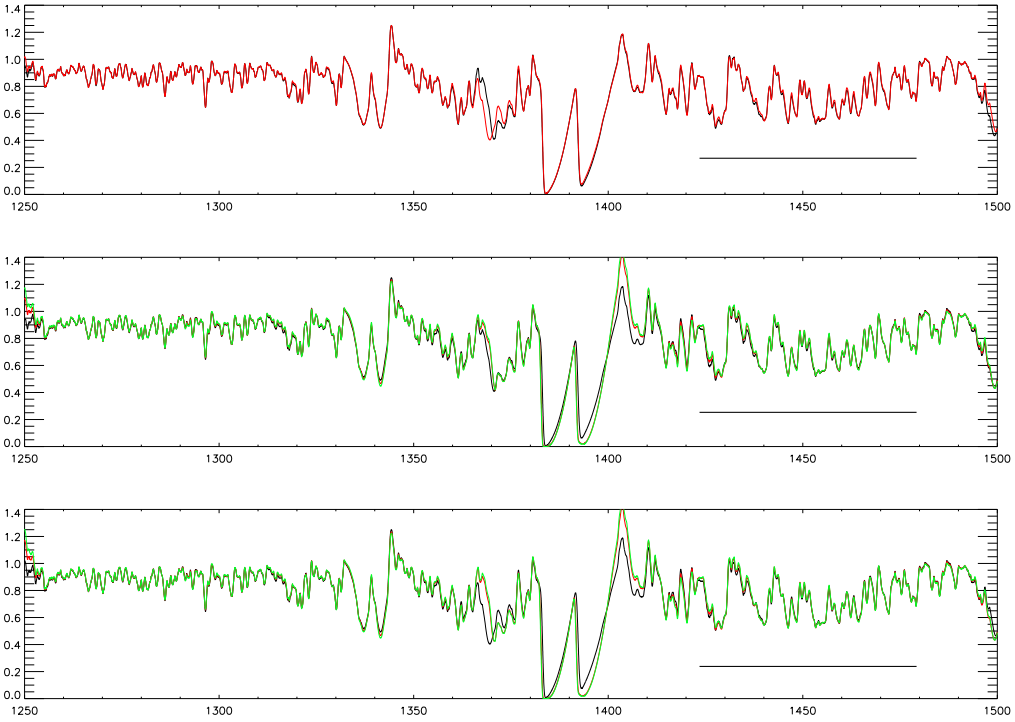


#### Effects of clumping and X-rays on the optical

Figure 3.10 shows the optical spectrum from 4000 to 7000Å and a typical observed H$\alpha$ profile, this time of HD 210839 ($\lambda$ Cep - O6 I). The scenario that matches best is that with minimal clumping, assuming that the mass-loss rate of the grid model is representative of the spectral class. This 'most representative' case still does not have the absorption seen in the observed profile, indicating that the particular mass-loss rate of HD 210839 is a little lower than the model. As expected, clumping has a strong effect on Balmer series lines and He lines.

### 3.2.3 Late-type Supergiant

#### Comparison to UV observations

Figure 3.11 shows the comparison between models and an observed spectrum (HD 149404 - O9 Ia). At first glance it seems once again that NV is the only profile that varies

**Figure 3.10.** The effects of X-rays and clumping on the optical region of the spectrum for an O6.5 supergiant. Top panel: smooth with no X-rays (black) and smooth with X-rays (red). Middle panel: smooth with no X-rays (black), moderate clumping with no X-rays (red) and strong clumping with no X-rays (green). Bottom panel: as for middle panel but with X-rays included. Below is a typical H$\alpha$ profile, from Markova et al. (2004).

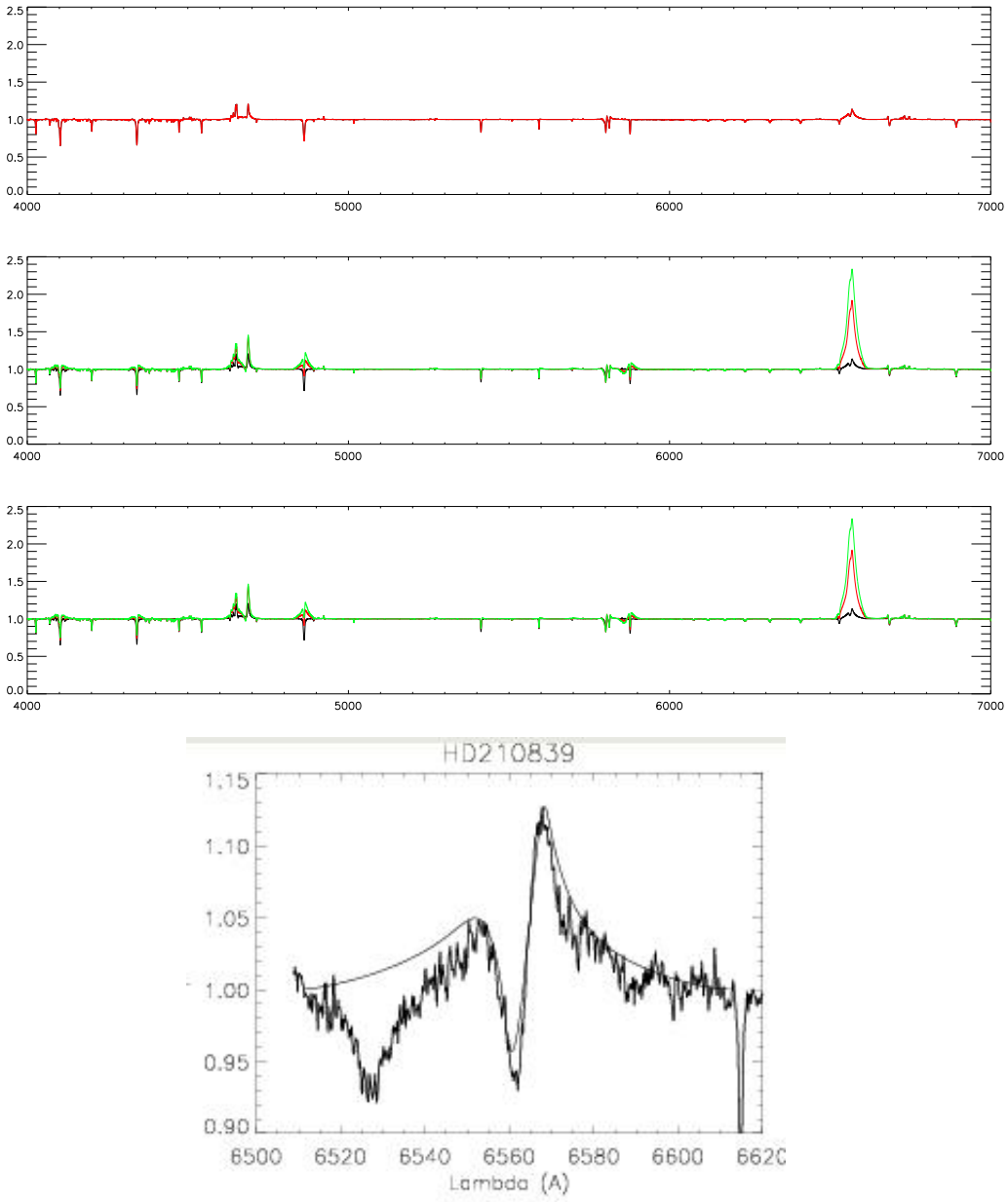

**Figure 3.11.** Models for an O9 supergiant compared with an IUE spectrum of a typical object (HD 149404).

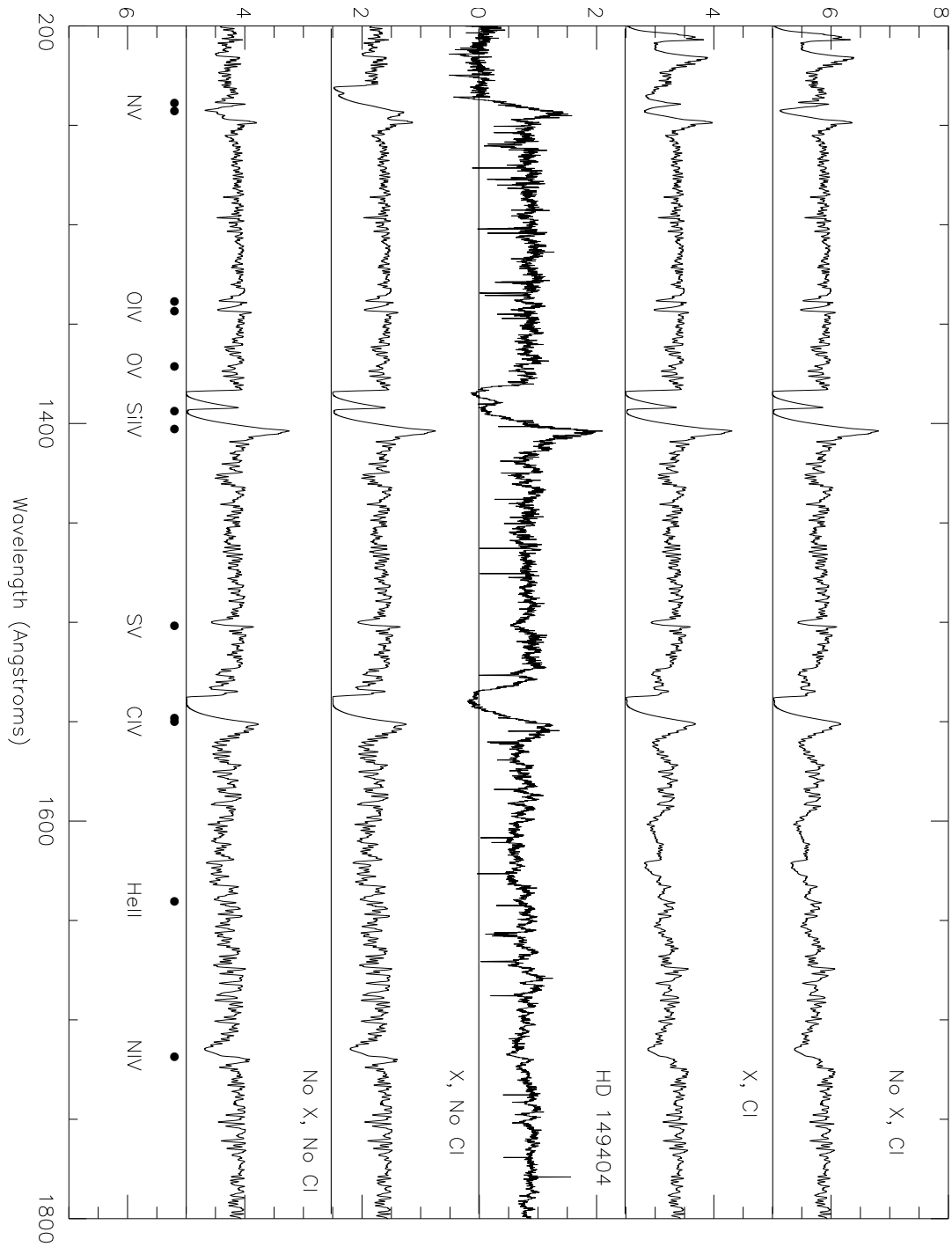

**Figure 3.12.** Profiles in the IUE range for an O9 supergiant. From top to bottom: NV, OIV, OV/SiIV, SV, CIV, HeII and NIV. Left panels: smooth with no X-rays (black) and smooth with X-rays (red). Middle panels: smooth with no X-rays (black), moderate clumping with no X-rays (red) and strong clumping with no X-rays (green). Right panels: as for middle panel but with X-rays included.

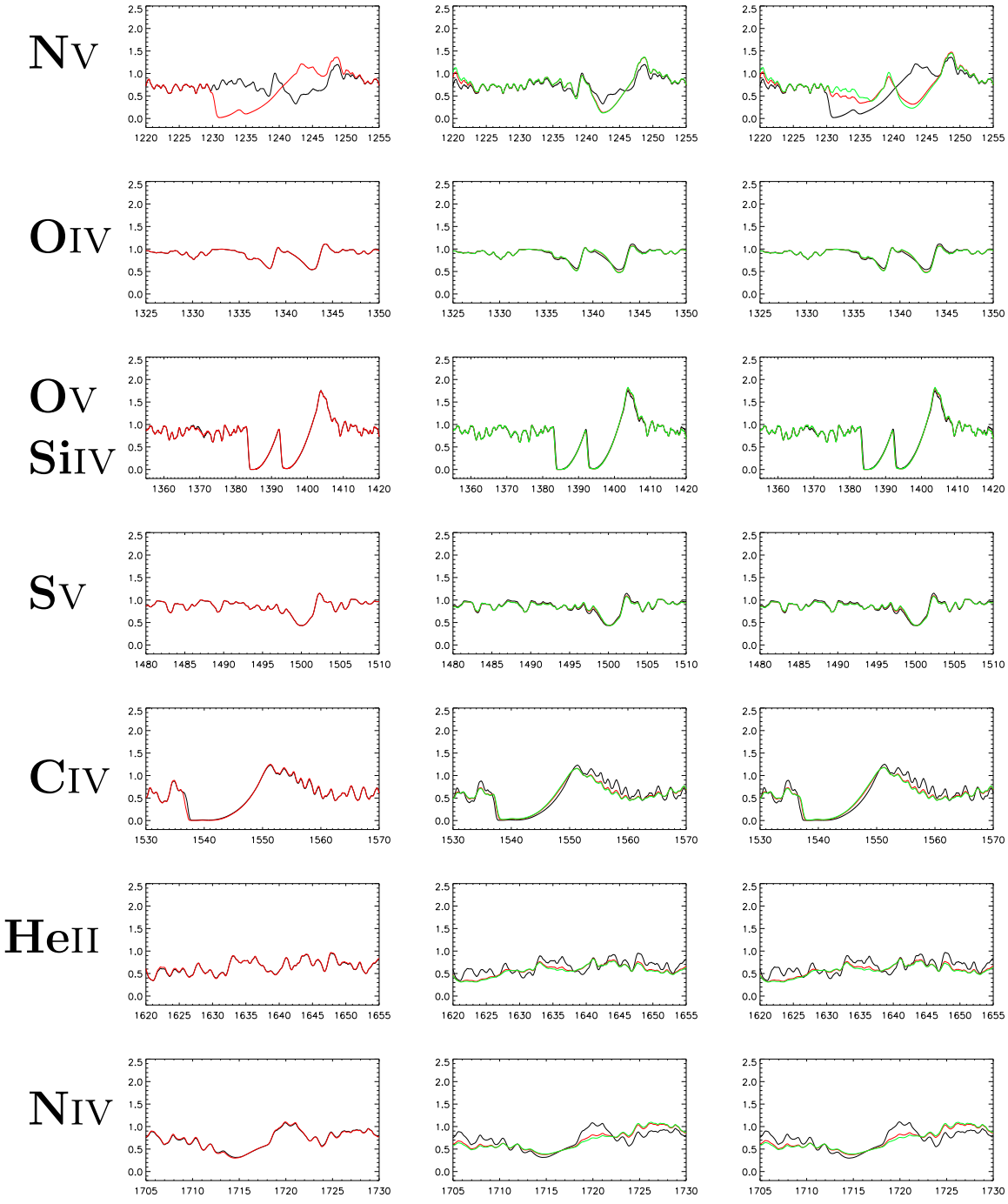

**Figure 3.13.** The effects of X-rays and clumping on the FeIV lines in the UV for an O9 supergiant. A HeII wind profile is now absent. Top panel: smooth with no X-rays (black) and smooth with X-rays (red). Middle panel: smooth with no X-rays (black), moderate clumping with no X-rays (red) and strong clumping with no X-rays (green). Bottom panel: as for middle panel but with X-rays included.

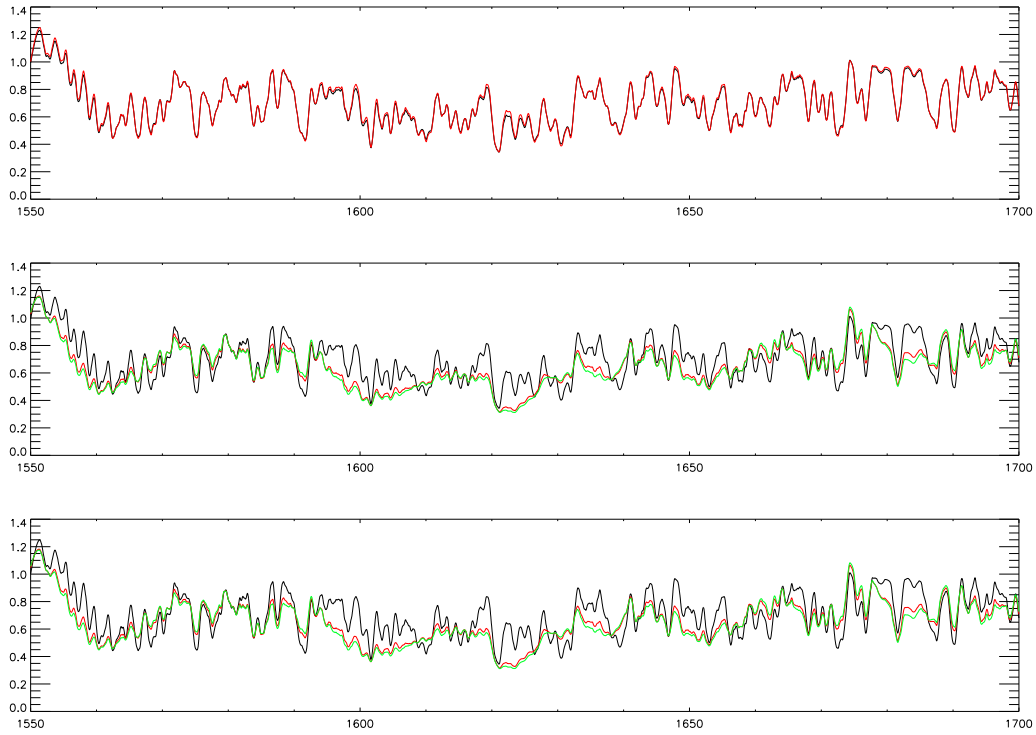


significantly from model to model, but all the model spectra appear realistic over the rest of the range in question. As for the earlier type models, we might expect CIV and SiIV to demonstrate a similar effect if they weren't already very deep lines.

#### Effects of clumping and X-rays on the UV

From Fig. 3.12 it can be seen indeed that NV is the only profile to show significant changes from one clumping or X-ray scenario to another. The changes seen with clumping factor around HeII and NIV appear to be at least partly due to the underlying FeIV spectrum, as seen in Fig. 3.13, which is stronger than at earlier spectral types, as expected. The changes seen in the FeIV spectrum now seem to be of the order that could be detected more easily above the noise in observations. Looking back at Fig. 3.11 it is difficult to use this to decide which clumping scenario to prefer. NV seems to demand the use of X-rays as before, and in this case may even go so far as to exclude clumping at the level implemented in the model. A look at other O9 supergiants (e.g. HD 148546 and HD

**Figure 3.14.** The effects of X-rays and clumping on the FeV lines in the UV for an O9 supergiant. The range in question is shown by a bar, although there are also FeV lines that lie over the OV and SiIV profiles. Top panel: smooth with no X-rays (black) and smooth with X-rays (red). Middle panel: smooth with no X-rays (black), moderate clumping with no X-rays (red) and strong clumping with no X-rays (green). Bottom panel: as for middle panel but with X-rays included.

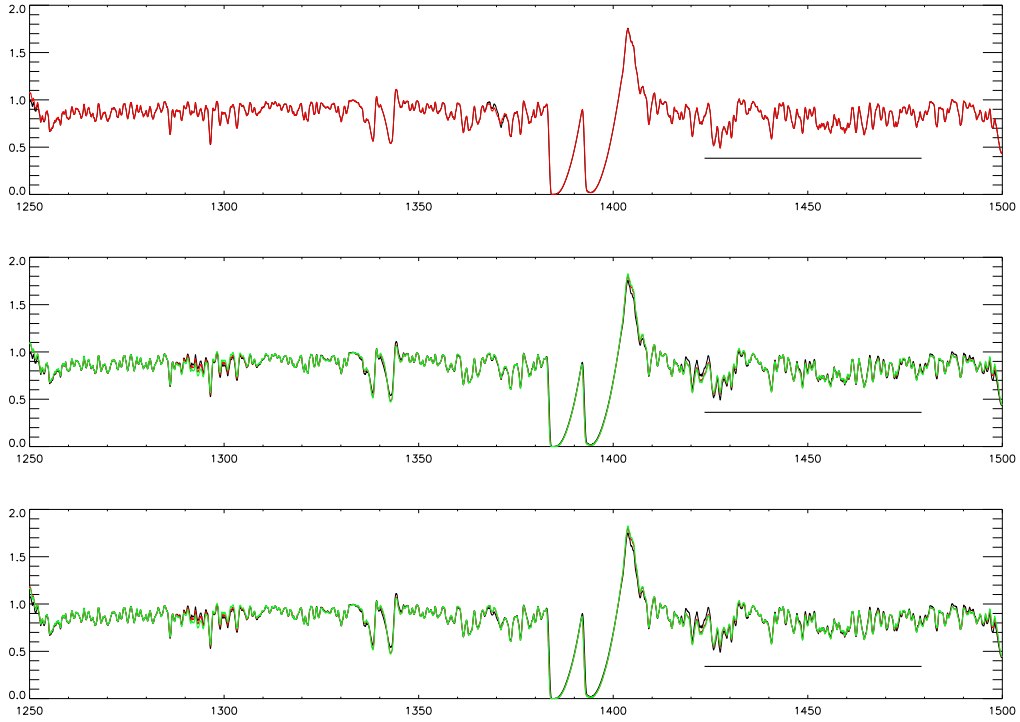


210809) seems to confirm this. It is clear that NV can be used as a firm indicator of the presence or strength of X-rays, if no measurement of X-ray flux is available.

#### Effects of clumping and X-rays on the optical

Figure 3.15 is the plot of the optical region of the model spectrum for O9 I. Again, as expected, the optical region is unaffected by a change in X-ray input to the models, and the clumping scenario has the same effect regardless of X-ray input. Most of the effect of strengthening H$\alpha$ is achieved by moderate clumping. The H$\alpha$ profile from a typical object, HD 30614 ($\alpha$ Cam - O9.5 Ia) is best represented by the unclumped model, although the model emission peak only reaches 1.1 of the continuum level compared to the observed 1.2. A mild modification of the mass-loss rate or clumping factor would bring it into agreement; since the CMFGEN model has an almost identical mass-loss rate to the study of Markova et al. (2004), a suggested volume filling factor closer to unity might be appropriate.

**Figure 3.15.** The effects of X-rays and clumping on the optical region of the spectrum for an O9 supergiant. Top panel: smooth with no X-rays (black) and smooth with X-rays (red). Middle panel: smooth with no X-rays (black), moderate clumping with no X-rays (red) and strong clumping with no X-rays (green). Bottom panel: as for middle panel but with X-rays included. Below is a typical H$\alpha$ profile, from Markova et al. (2004).

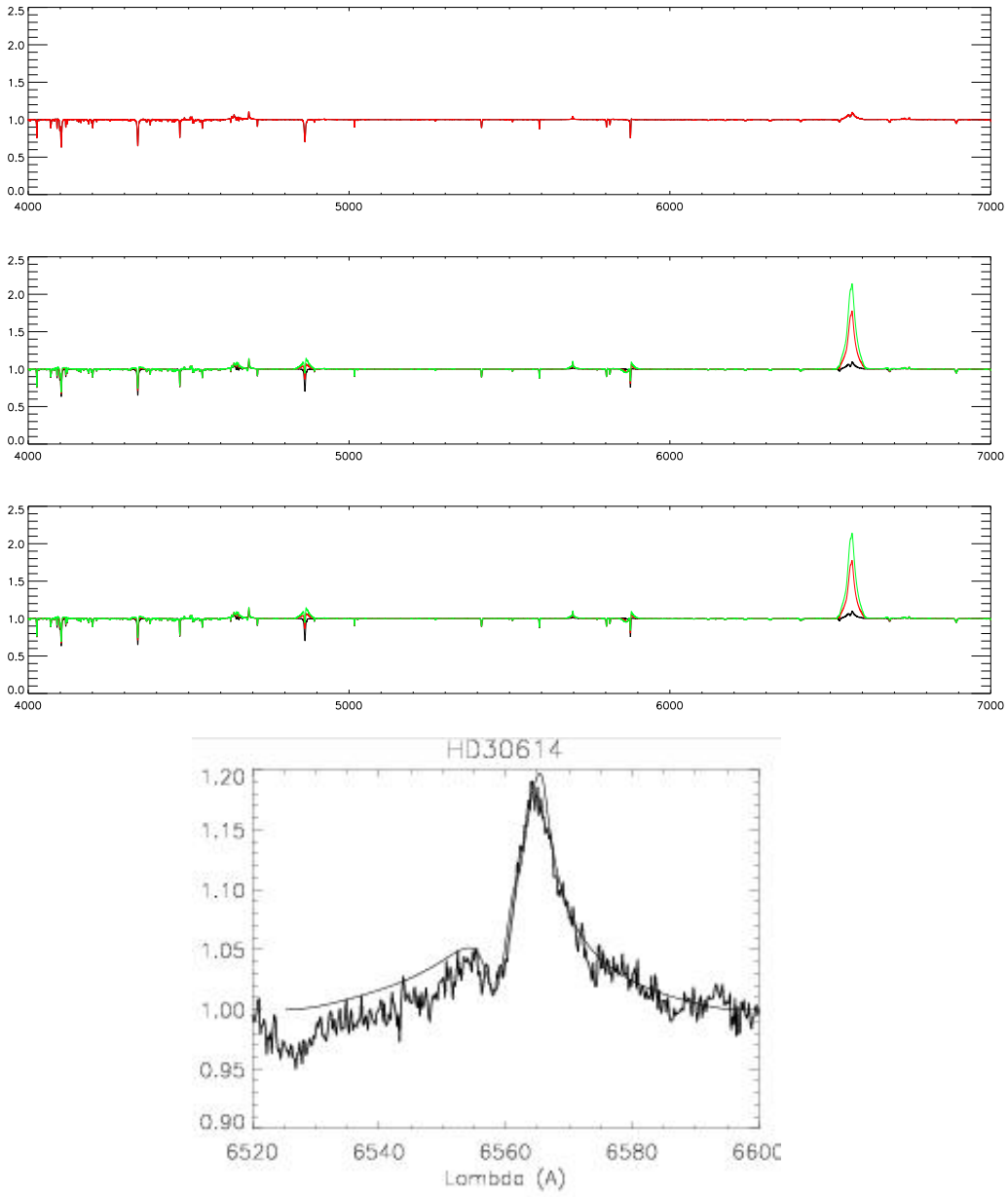

### 3.2.4 Early-type Dwarf

#### Comparison to UV observations

Figure 3.16 shows the comparison between the models and an observed O3 dwarf spectrum (HD 93205). Broadly the overall morphology of the models is in keeping with observation, with NIV and OV being over-predicted in strength in all cases.

#### Effects of clumping and X-rays on the UV

In Figure 3.17 it can be seen that unlike the supergiant models, in early dwarfs it is difficult to see effects of X-rays on NV, as the profiles are of very similar strength in all four scenarios. This is probably the saturation effect discussed earlier for CIV and SiIV in supergiants. There are no other profiles in the IUE range that allow a proper discernment of X-ray scenario. Clumping on the other hand appears to have various lines that give it away. The clumped models show stronger OIV, SV, HeII and NIV lines than the unclumped ones, with SV, HeII and NIV showing the clearest changes from a smooth to a clumped outflow.

#### Effects of clumping and X-rays on the optical

As in the supergiant cases, and as expected, the O3 dwarf model spectra demonstrate no dependence of the optical profiles on X-rays, but a definite relation to the clumping factor (Figure 3.20). When compared to the H$\alpha$ profile of HD 93205, the unclumped model clearly shows the best agreement. The minor 'top-up' in emission seen in HD 93250 could be reproduced by increasing the mass-loss rate or introducing a small amount of clumping. It is clear that, as expected, the H$\alpha$ profile is highly sensitive to clumping.

The best scenario for clumping from both the optical and the UV is a very low level of clumping. This gives the closest match to profiles in both wavelength regimes.

### 3.2.5 Mid-type Dwarf

#### Comparison to UV observations

The model spectra in Figure 3.21 all look broadly the same as the observed spectrum of HD 206267, and the NV profile is the only thing that changes significantly from one scenario to another.

**Figure 3.16.** Models for an O3 dwarf compared with an IUE spectrum of a typical object (HD 93205).

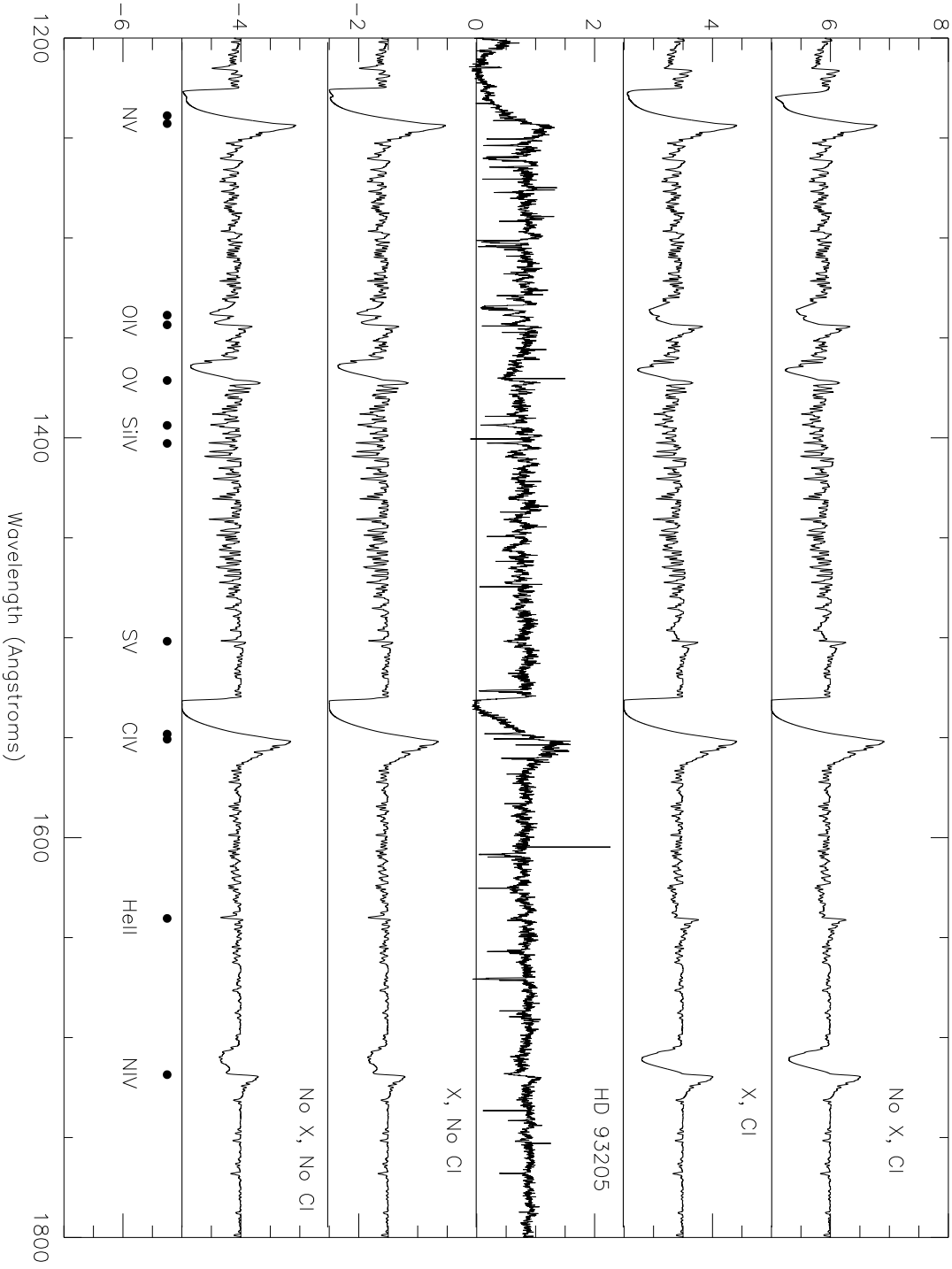

**Figure 3.17.** Profiles in the IUE range for an O3 dwarf. From top to bottom: NV, OIV/OV/SiIV, SV, CIV, HeII and NIV. Left panels: smooth with no X-rays (black) and smooth with X-rays (red). Middle panels: smooth with no X-rays (black), moderate clumping with no X-rays (red). Right panels: as for middle panel but with X-rays included.

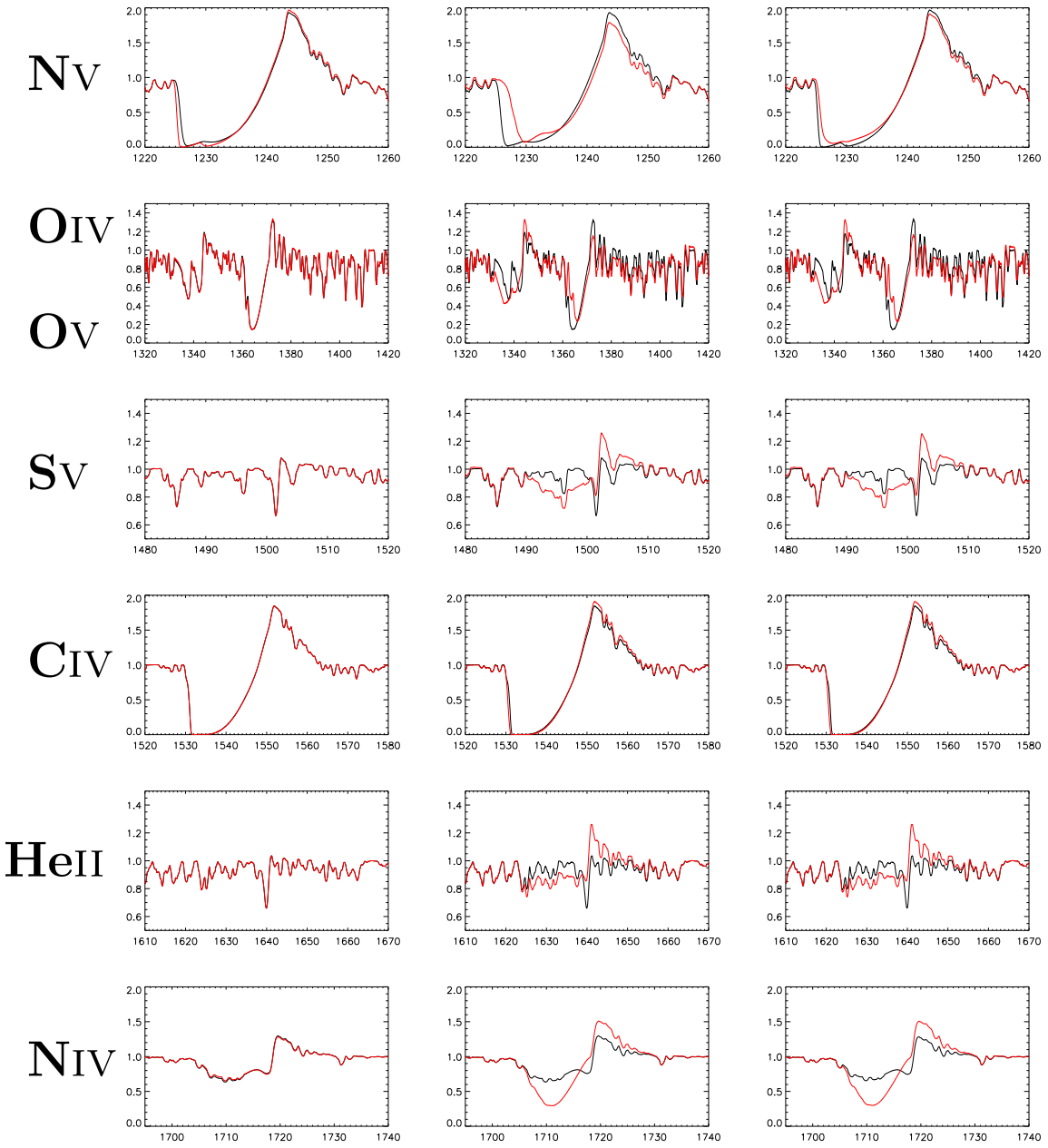

**Figure 3.18.** The effects of X-rays and clumping on the FeIV lines in the UV for an O3 dwarf. Only the HeII line appears to change.

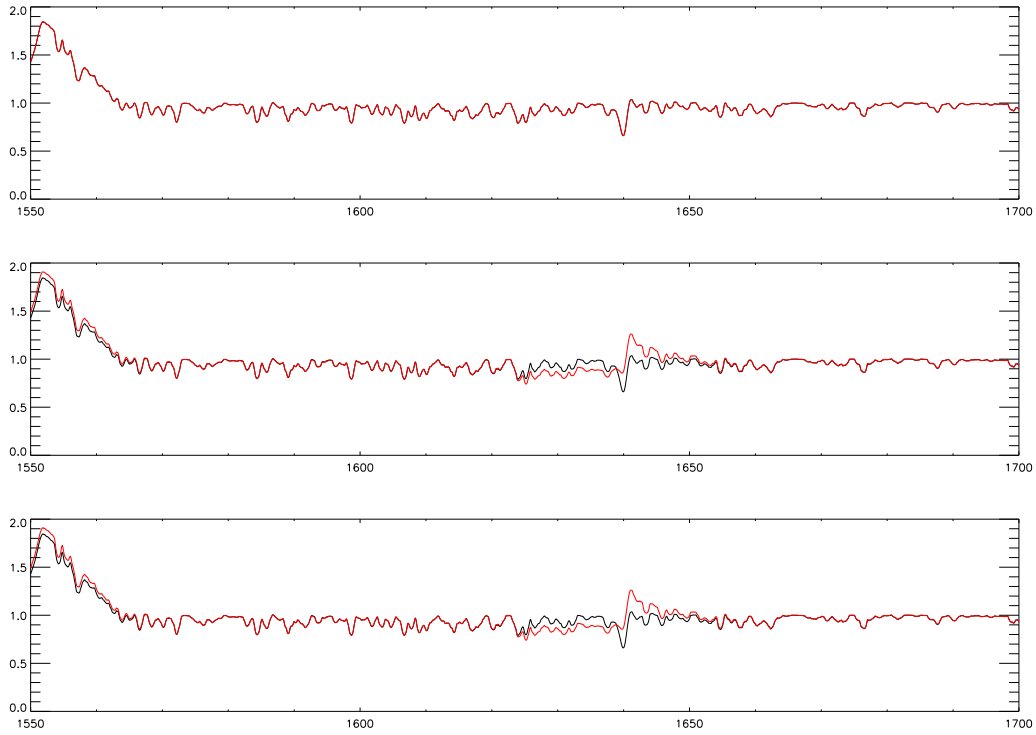


#### Effects of clumping and X-rays on the UV and optical

In Figure 3.22 NV seems somewhat degenerate in sensitivity to clumping and X-rays, which makes it difficult to decide the best scenario for either from only this profile. A model with X-rays and clumping produces a similar strength profile to one that has neither.

In addition the optical range (Figure 3.23) is unaffected by either changing the clumping scenario or the input of X-rays. The lack of change with clumping must now be because the profiles are purely photospheric - the wind is not strong enough to produce a wind component to lines like H$\alpha$. Further constraints are needed from the FUV, described later in this chapter.

### 3.2.6 Late-type Dwarf

#### Comparison to UV observations

The model spectra (see Figure 3.24) are all similar to the observed spectrum of HD 209481 with differences occurring in the NV profile, as for the early-type dwarf. In addition to this the models do not quite produce the correct shape of CIV profile; all but that with

**Figure 3.19.** The effects of X-rays and clumping on the FeV lines in the UV for an O3 dwarf. The range in question is shown by a bar, although there are also FeV lines that lie over the OV and OIV profiles. Top panel: smooth with no X-rays (black) and smooth with X-rays (red). Middle panel: smooth with no X-rays (black), moderate clumping with no X-rays (red) and strong clumping with no X-rays (green). Bottom panel: as for middle panel but with X-rays included.

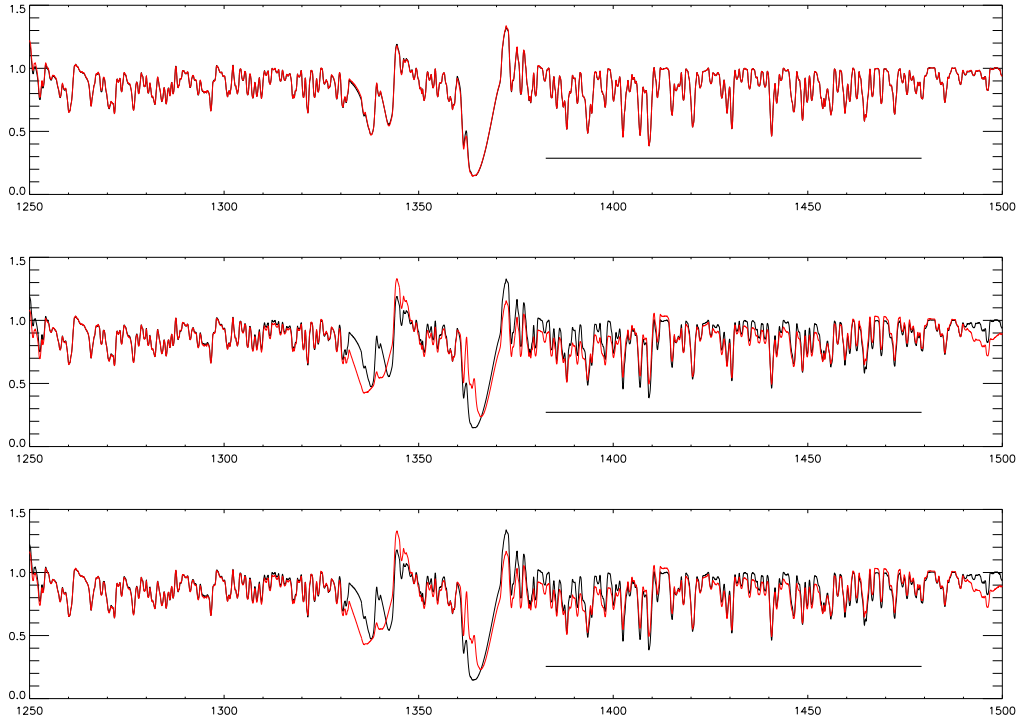


X-rays and no clumping reach zero intensity, unlike the observed profile. This implies that X-rays are important to consider when interpreting the CIV line, in agreement with Martins et al. (2005*a*).

#### Effects of clumping and X-rays on the UV and optical

X-rays are definitely needed to produce a realistic NV profile, and in fact the X-rays also reduce the strength of CIV in this later type object. The latter effect must be due to the X-rays ionizing CIV to CV and/or CVI. This may also be happening in earlier type models and be masked by the strength of the profile. At this later spectral type, because the CIV doublet is not saturated, this effect can demonstrate itself. Figure 3.27 shows the effects of X-rays as a function of spectral type amongst the later type dwarfs, whilst Figure 3.28 shows that at the latest types it plays a far more dominant role than does the mass-loss rate. This demonstrates how important it is to get the X-ray level right in the model when

**Figure 3.20.** The effects of X-rays and clumping on the optical region of the spectrum for an O3 dwarf. Below is a typical H$\alpha$ profile from Puls et al. (1996).

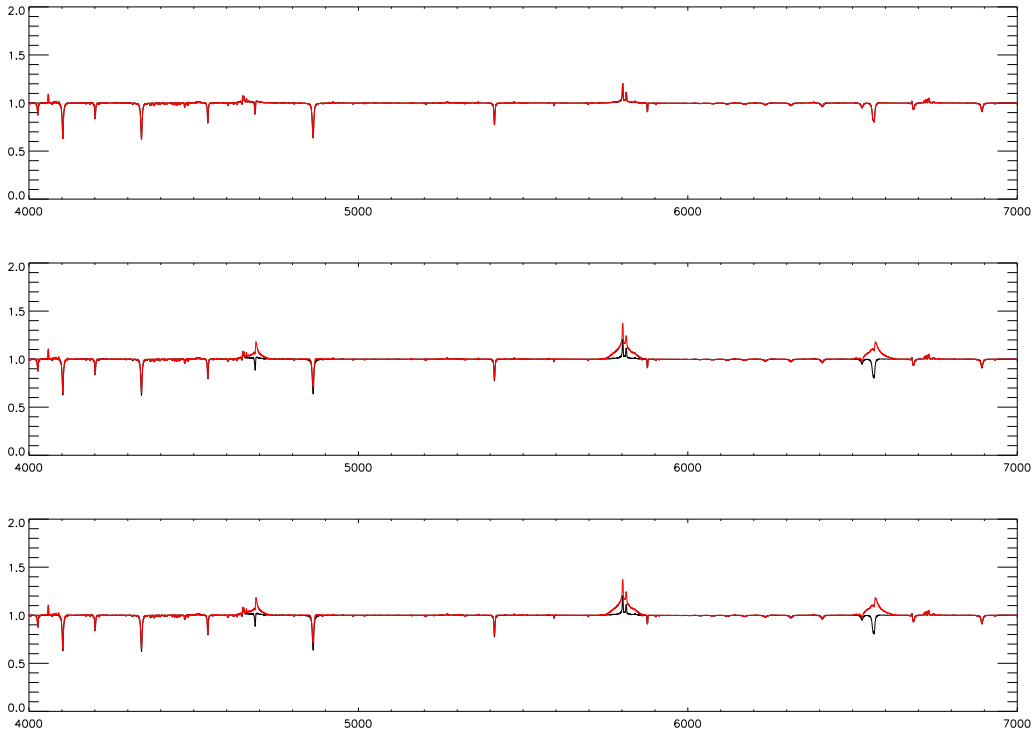


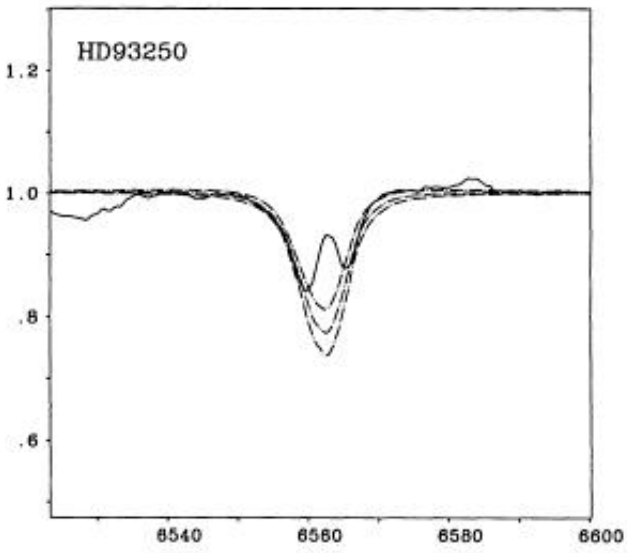

**Figure 3.21.** Models for an O6.5 dwarf compared with an IUE spectrum of a typical object (HD 206267).

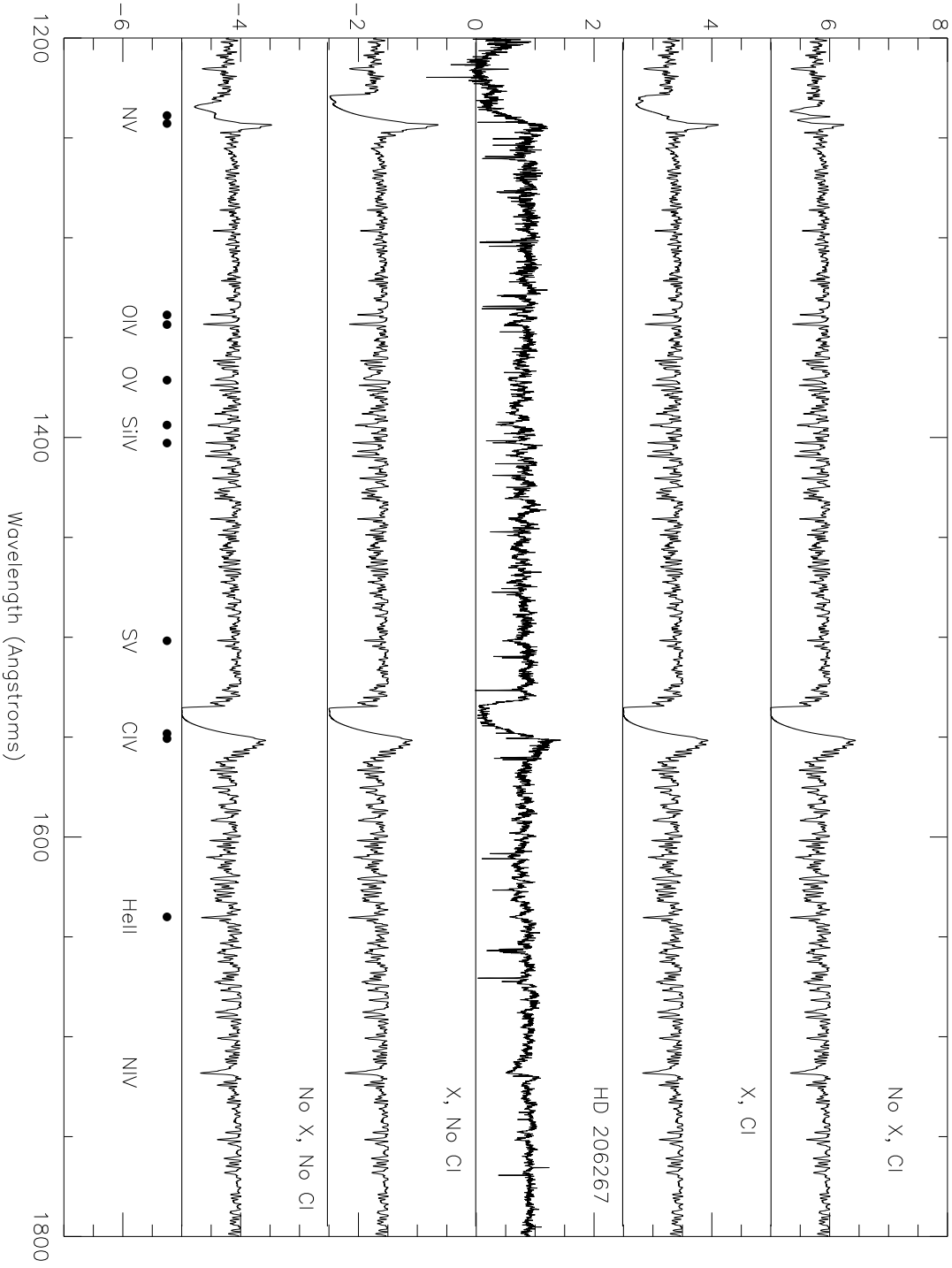

**Figure 3.22.** Profiles in the IUE range for an O6.5 dwarf. From top to bottom: Nv, Ov, Civ and Niv. Left, middle and right panels as for O3 V.

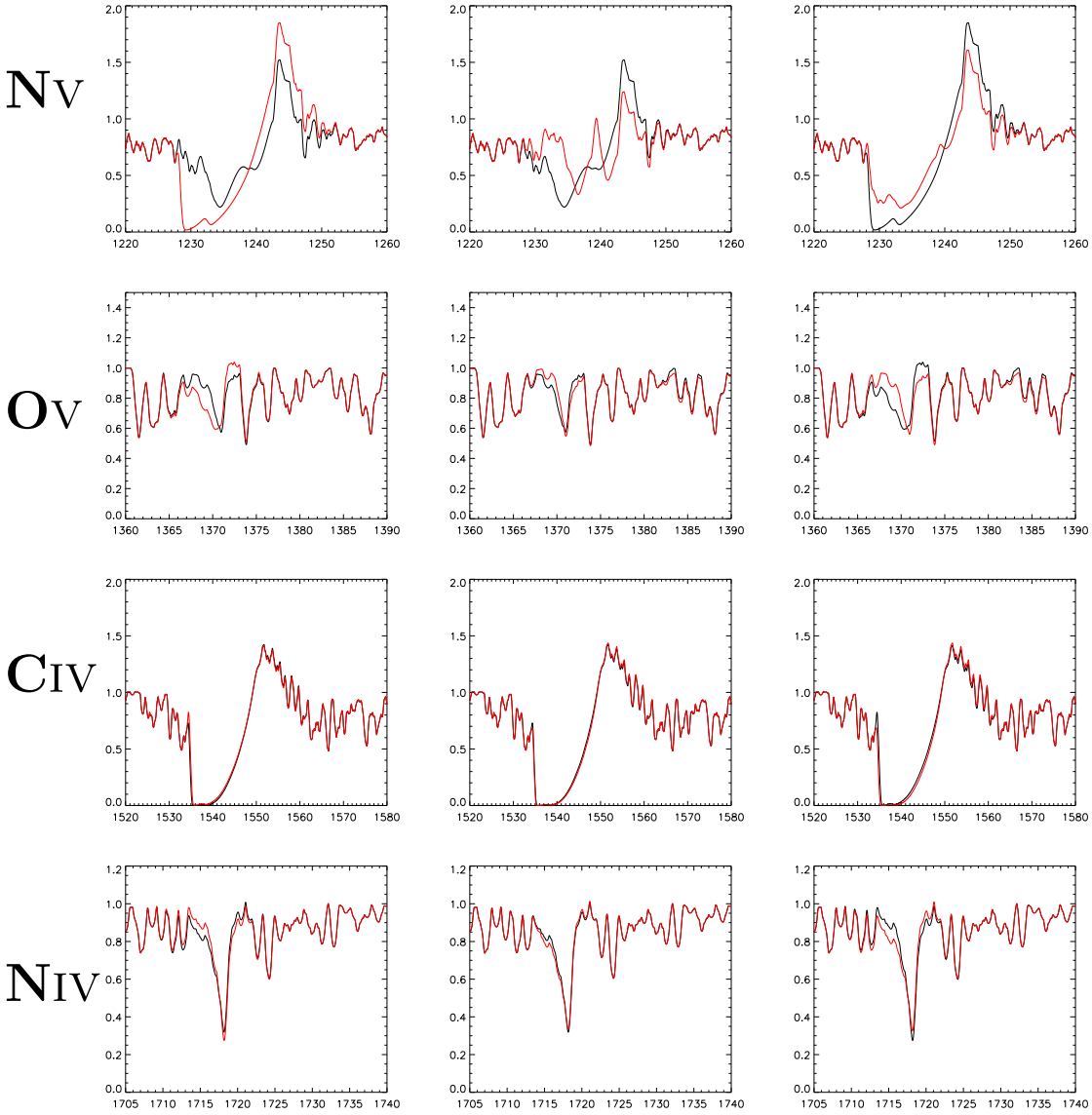

**Figure 3.23.** Optical spectrum for an O6.5 dwarf. Neither clumping nor X-rays show discernable differences at this spectral type, for those models that had converged satisfactorily. Below is a typical H$\alpha$ profile from Markova et al. (2004).

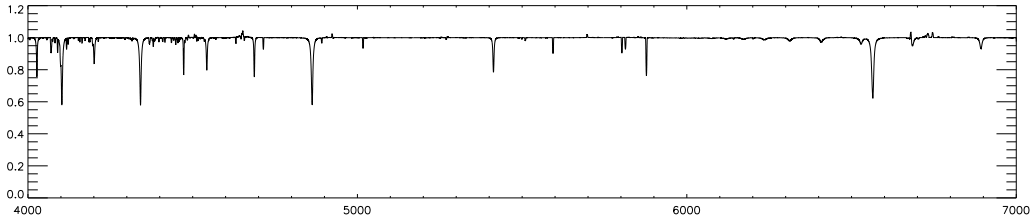


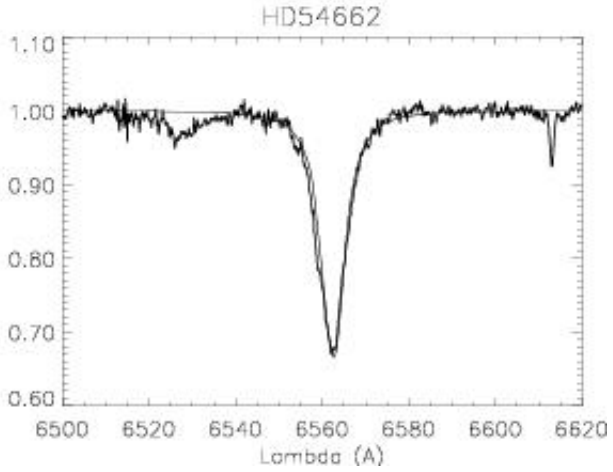

**Figure 3.24.** Models for an O9 dwarf compared with an IUE spectrum of a typical object (HD 209481).

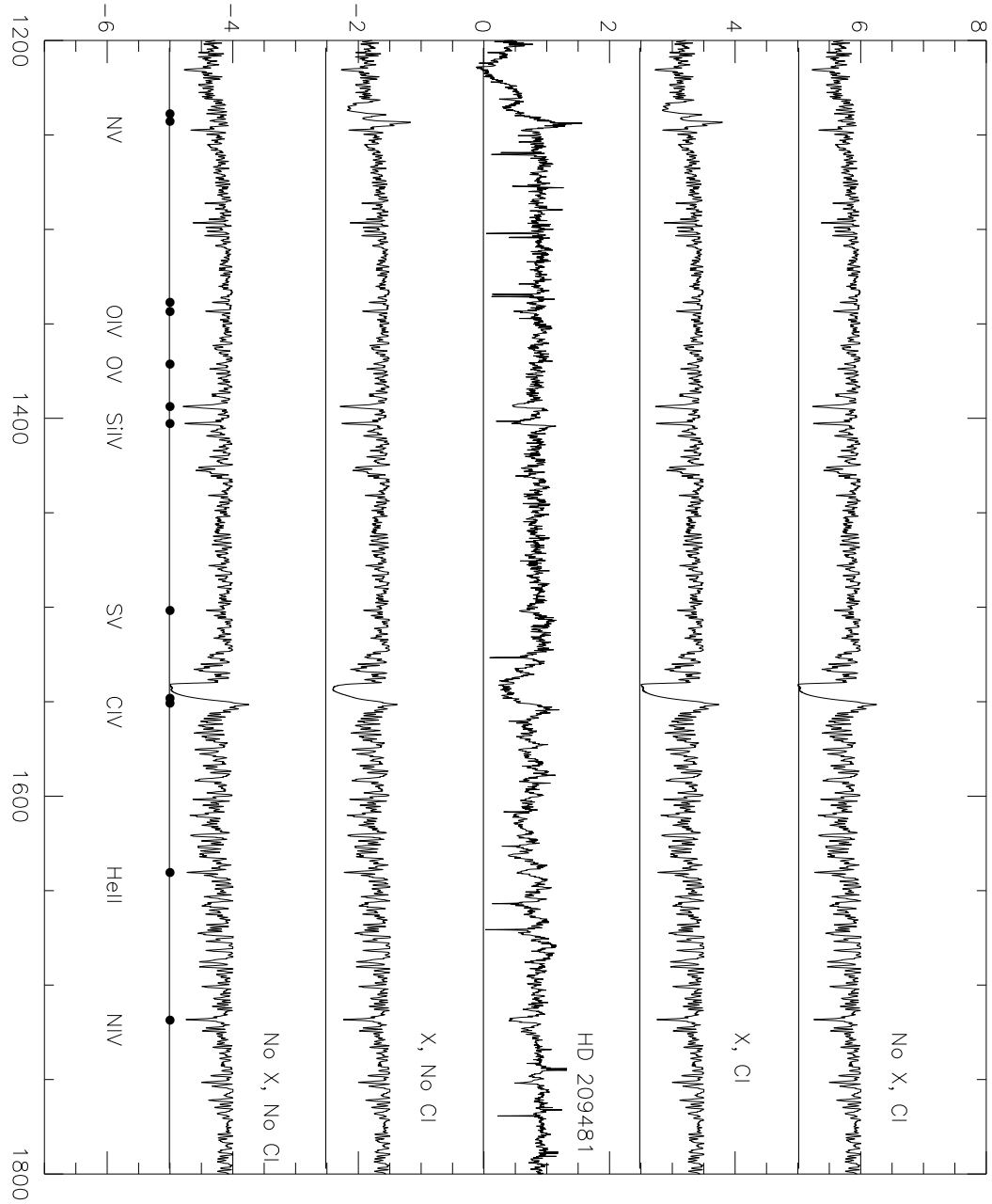

trying to predict quantities such as mass-loss rate from UV resonance lines. In the coolest late-type dwarfs, X-rays have the dominant effect.

The optical range offers no further insight into the X-ray or clumping scenario, as with the O6.5 models. Again, further clarification will be sought from the FUV part of the spectrum.

**Figure 3.25.** Profiles in the IUE range for an O9 dwarf. Top: NV, bottom: CIV. Left, middle and right panels as for O3 V.

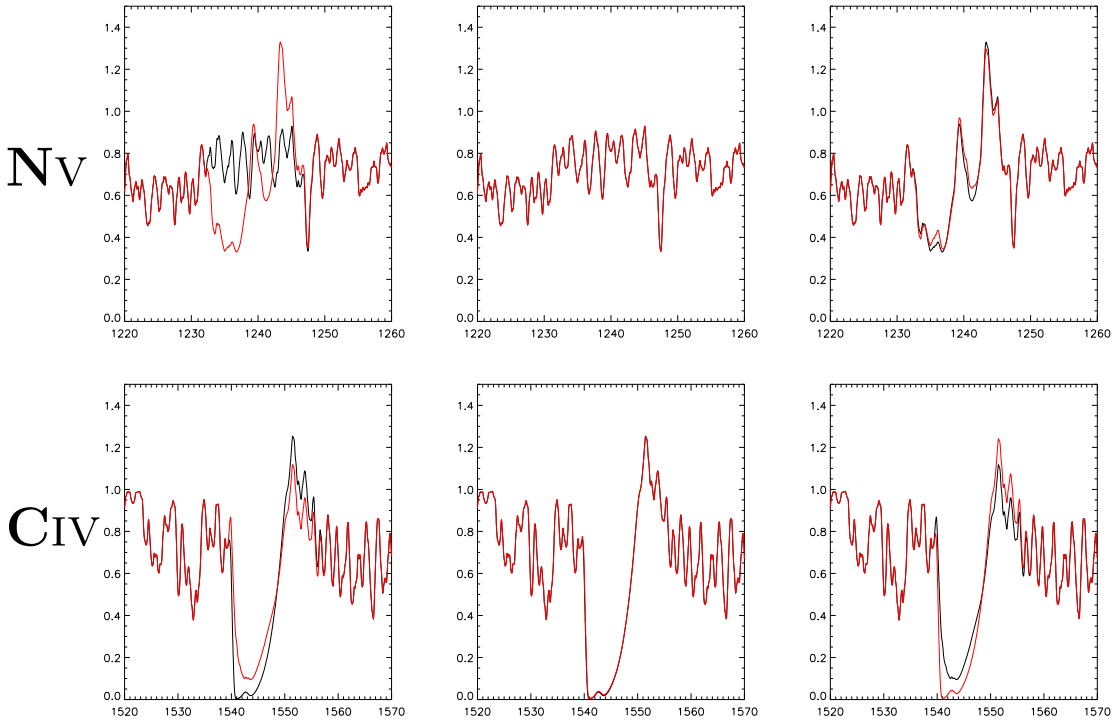

**Figure 3.26.** Optical spectrum for an O9 dwarf. Neither clumping nor X-rays show discernable differences at this spectral type. Below is a typical H$\alpha$ profile from Martins et al. (2005*a*) (HD 46202), including a fit from that work.

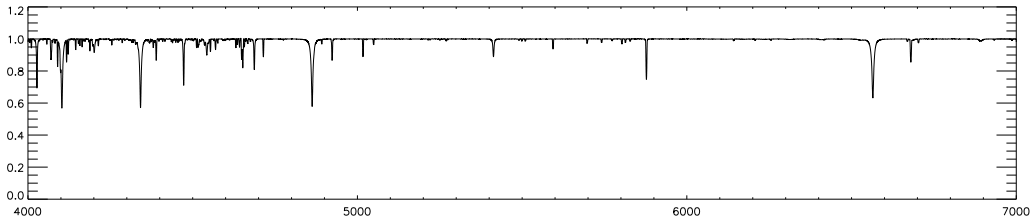


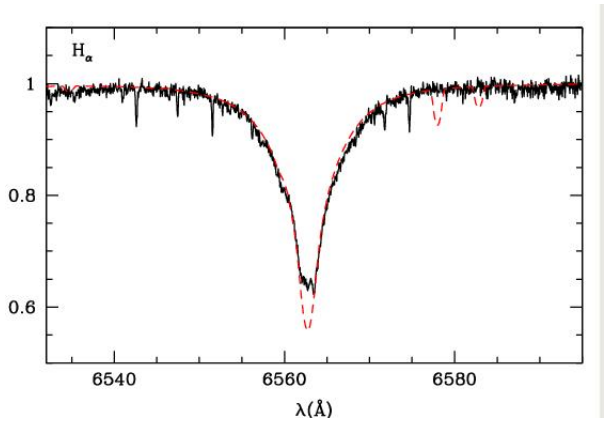

**Figure 3.27.** Effects of X-rays as a function of spectral type. Black: negligible X-rays; red: standard X-rays; green: high X-rays

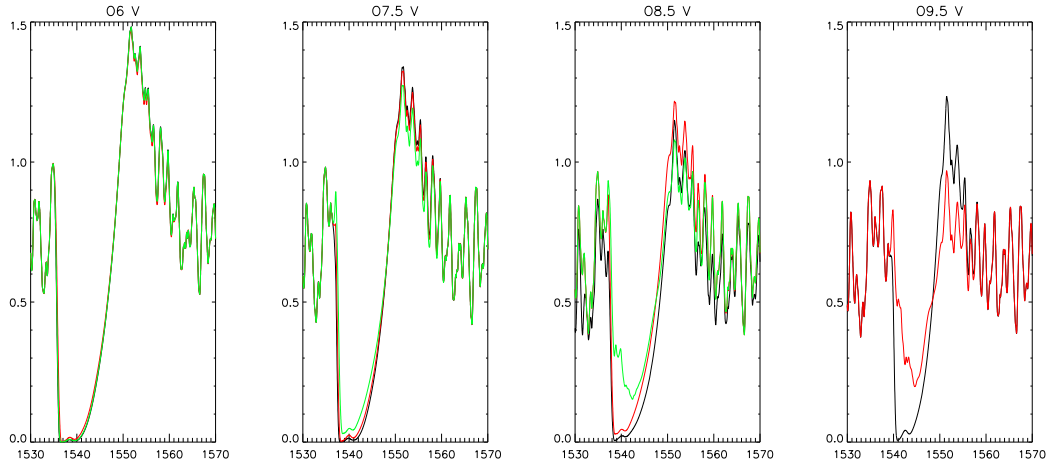


**Figure 3.28.** Effects of X-rays on CIV compared to mass-loss rate for a late spectral type (O9.5) dwarf. Black: No X-rays, $\dot{M} = 2 \times 10^{-9}$; red: X-rays, $\dot{M} = 2 \times 10^{-9}$; green: No X-rays, $\dot{M} = 9 \times 10^{-10}$

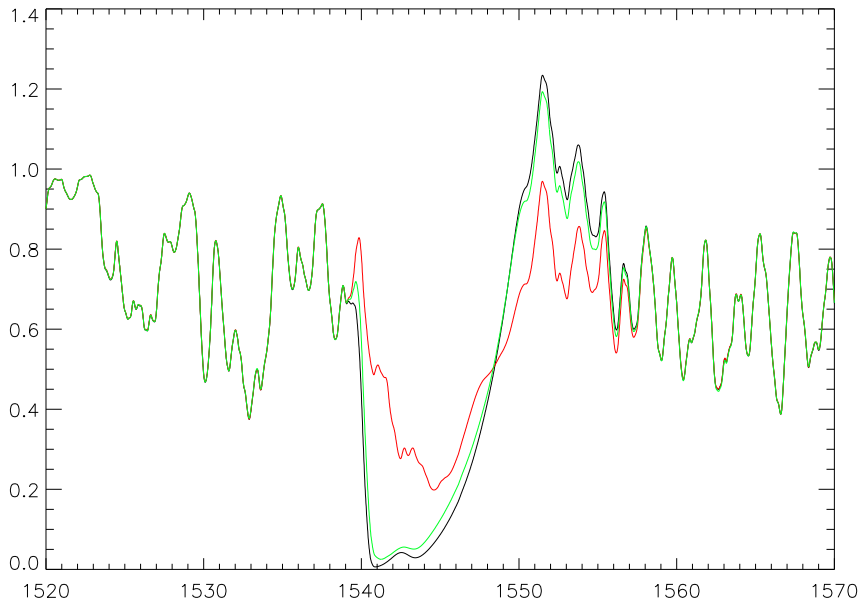

## 3.3 FUV model Spectra

In this section, the far-ultraviolet (∼900-1200Å) portions of the model spectra are shown. For Galactic stars, interstellar extinction affects spectra more than in, say, the Magellanic Clouds. This is because most stars in the Milky Way lie in the plane of the disc and so we observe them through a comparatively dense column of the interstellar medium, which is also mostly in the disc. The Magellanic Clouds are above the plane of the Galaxy, and hence seen through a lower column density of interstellar particles. They also have lower extinction internally. In addition to being dependent on Galactic latitude and column density, interstellar extinction also has a wavelength dependence. This causes more violet lines and continuum to be attenuated than redder ones. For this reason, it is more difficult to obtain a good, clean spectrum in the far-UV of a Galactic object, unless you are fortunate enough to find one in an interstellar 'hole'. Another side to this effect that 'pollutes' the spectrum of a star in the far-UV is the large number of interstellar lines that occupy this part of wavelength space. This makes analysis of the line profiles rather difficult, unless one is interested in the interstellar lines themselves.

The first real attempt to compile a far-UV atlas of Galactic O stars was by Pellerin et al. (2002), who also included models of interstellar lines as shown in Figures 3.29 to 3.31. These figures demonstrate how greatly interstellar lines dominate the spectrum for different column densities of material. The work of Pellerin et al. (2002) offers both a useful comparison and reality check for the models used in this investigation, and also highlights how useful it is to have far-UV model spectra when most observations of Galactic O stars are so polluted by interstellar effects.

CMFGEN offers the option to correct for the effects of interstellar HI and $H_2$, and it is possible to match individual spectra this way. However in this study the emphasis is on analysing a grid that is representative of O star spectra, not to match individual objects. For this reason the correction for interstellar lines was not done; rather the effects of what is going on beneath that interstellar pollution is observed in the models.

Figures 3.32 to 3.37 show an early, mid and late type object for the supergiants and dwarfs, for each clumping and X-ray scenario.

It is important to establish the most realistic scenario for clumping and for X-rays according to this part of the spectrum, and to find out if it helps clarify the situation further to what has been seen in the other wavelength ranges earlier in the chapter. What

**Figure 3.29.** Contribution from interstellar $H_2$ and HI lines in the far-UV, from Pellerin et al. (2002), continued in Figures 3.30 and 3.31

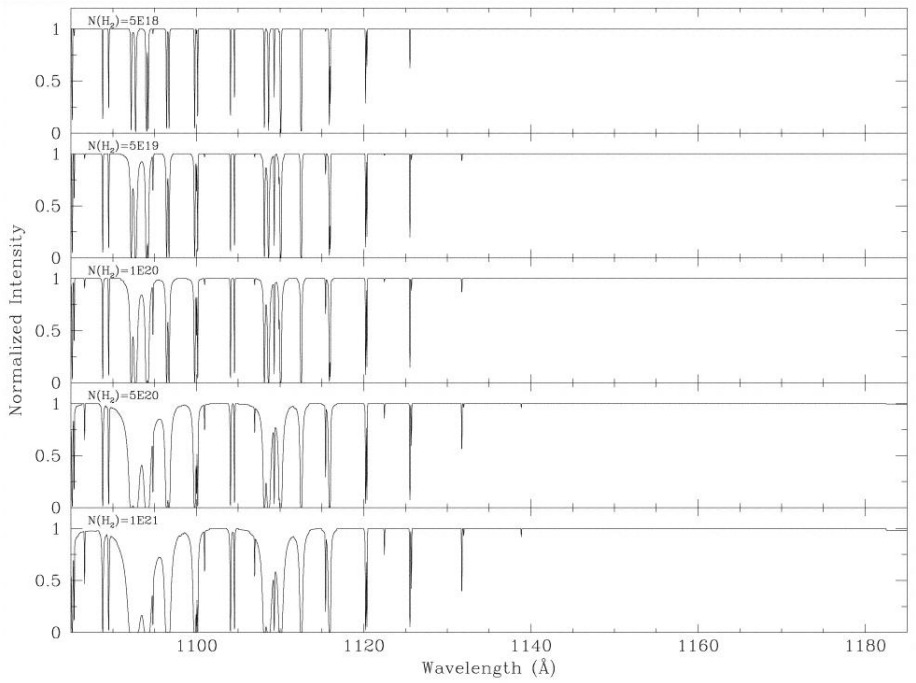


follow are comments on the far-UV model spectra of early, mid and late type supergiants and dwarfs with these aims in mind.

**Early-type Supergiant**

Figure 3.32 shows the comparison of all model X-ray and clumping scenarios and observations for an O4 supergiant. The main lines affected by clumping are PIV (951Å), NIV (955Å), NIII (990Å), SIV (1063, 1073Å) and CIII (1176Å). It appears that NIII is strengthened quite considerably by the addition of clumping, and NIV is slightly weakened. This is what we might expect if recombination is enhanced by clumping. We expect unsaturated lines to display changes more clearly than saturated ones, and also resonance lines to be more affected than excited ones since the populations lie mostly in the ground state in a stellar wind. It may be for this reason that NIII (a resonance line) is more affected than NIV (an excited one). CIII is similarly strengthened when clumping is introduced, as is SIV. All this implies that the far-UV spectrum is rather sensitive to clumping effects due to population changes. It is difficult to make a direct comparison to observations at the bluer end of the spectrum because of interstellar effects described before. What is implied

**Figure 3.30.** Contribution from interstellar $H_2$ and HI lines in the far-UV, from Pellerin et al. (2002), continued

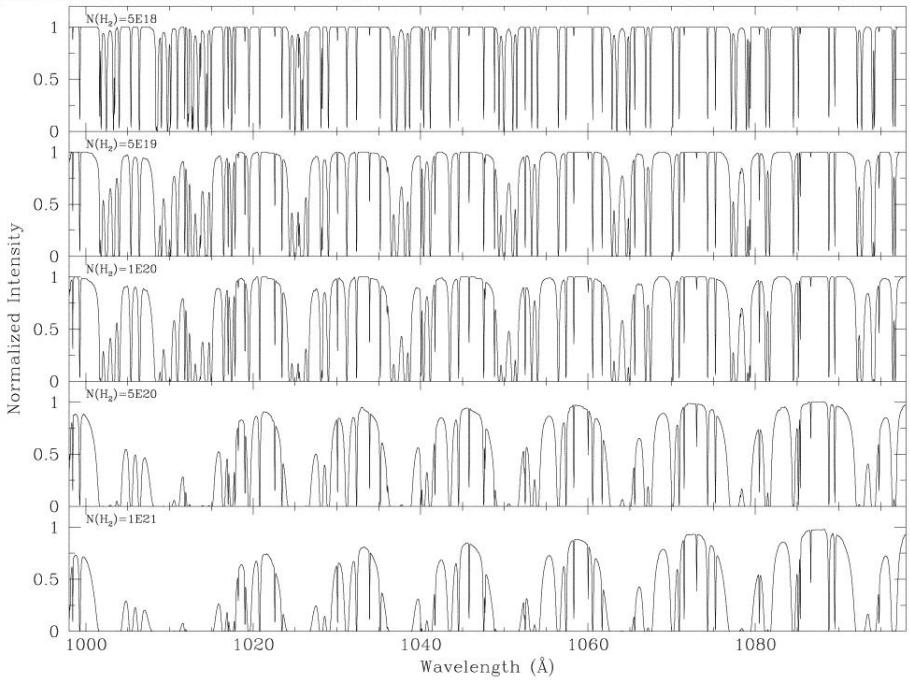


**Figure 3.31.** Contribution from interstellar $H_2$ and HI lines in the far-UV, from Pellerin et al. (2002), final part

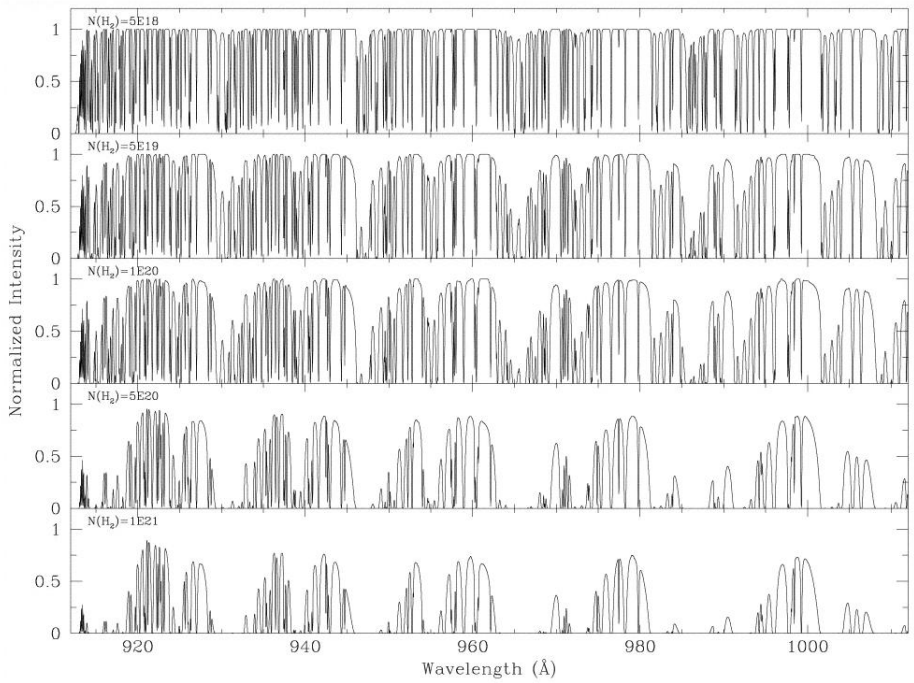

**Figure 3.32.** FUV spectra for an O4 supergiant. See Table 3.2 for the list of lines corresponding to marked dots

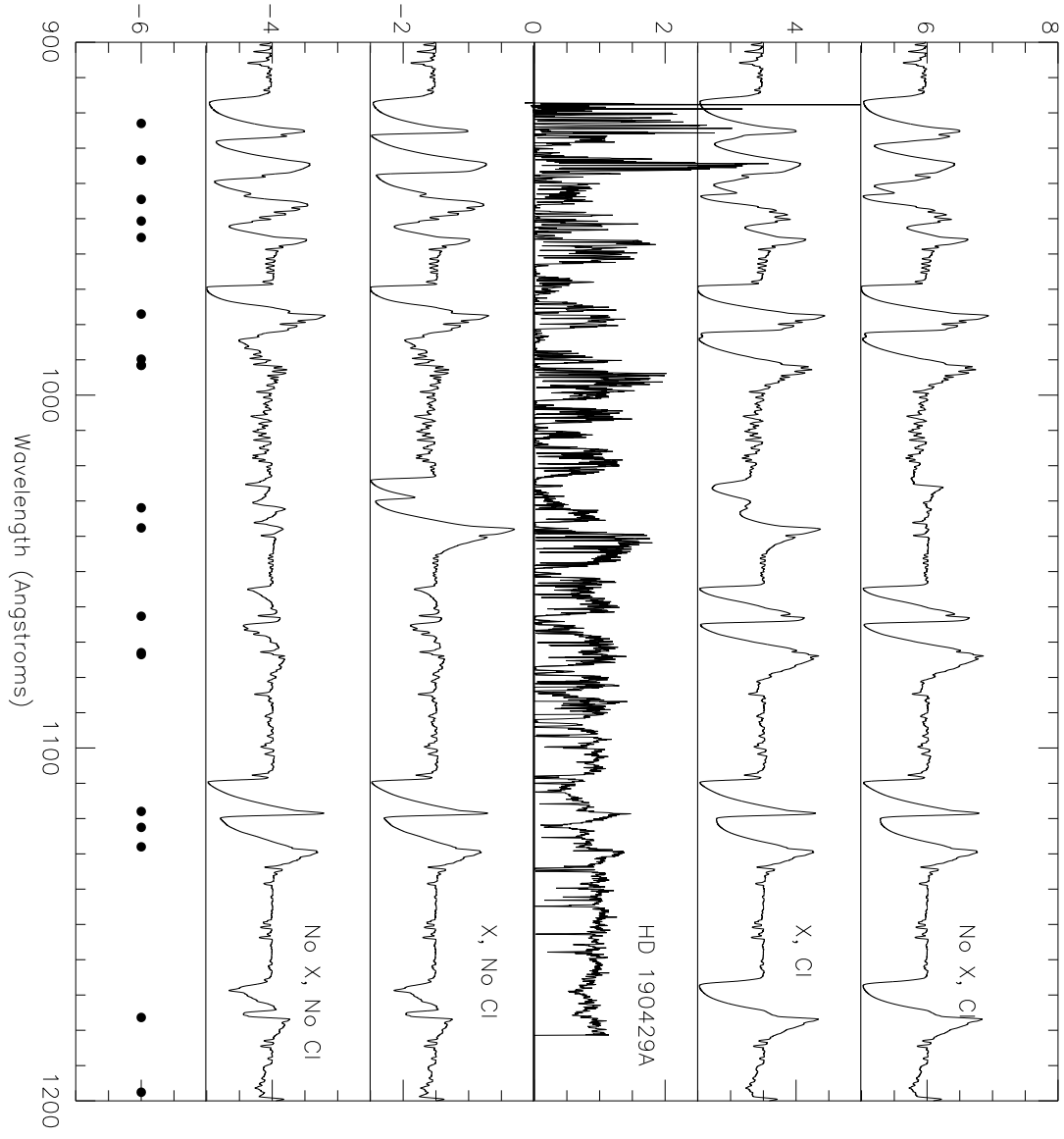

**Table 3.2.** Important lines in FUV spectra

| Line | Wavelength(s) in Å |
|---|---|
| NIV | 923 |
| SVI | 933.38, 944.52 |
| PIV | 950.66 |
| NIV | 955.34 |
| CIII | 977.02 |
| NIII | 989.80, 991.51, 991.58 |
| OVI | 1031,93, 1037.62 |
| SIV | 1062.66, 1072.97, 1073.52 |
| PV | 1117.98, 1128.01 |
| SiIV | 1122.49, 1128.34 |
| CIII | 1176.37 |
| SIII | 1197.56 |

though is that the strength of the NIII lines is best reproduced by models with clumping, although perhaps not as strong a clumping factor as used in these models. With NIII and also SIV though there is bound to be some degeneracy present between clumping factor and mass-loss rate. What seems quite certain is that X-rays are essential to reproduce something like a realistic OVI profile at 1032, 1038Å. Clumping has an additional effect on OVI, acting conversely to the input of X-rays. Taken together with the UV and optical parts of the spectrum, the most likely scenario seems to be one with X-rays and using a clumping factor weaker than the 'moderate' one, assuming the other physical parameters are representative of the class.

PV is predicted too strong in all four models. Oskinova et al. (2007) show how porosity treatments can reduce the strength of PV whilst leaving density-squared diagnostics relatively unaffected. But in these models it can be seen that SIV, a single-density diagnostic, grows with clumping factor and so presumably the effects of porosity would leave us with a SIV line which is too large, through enhancing the density. This is a problem and may mean that there is something beyond the current treatments of porosity going on.

#### Mid-type Supergiant

Figure 3.33 shows the four scenarios for models and an observed spectrum of an O6.5 supergiant. They all broadly match the observational spectrum at longer wavelengths, but it is difficult to say the same of the shorter wavelength portion due to interstellar effects in the spectrum of HD 210839. Realistically this limits the comparison to wavelengths

**Figure 3.33.** FUV spectra for an O6.5 supergiant. See Table 3.2 for the list of lines corresponding to marked dots

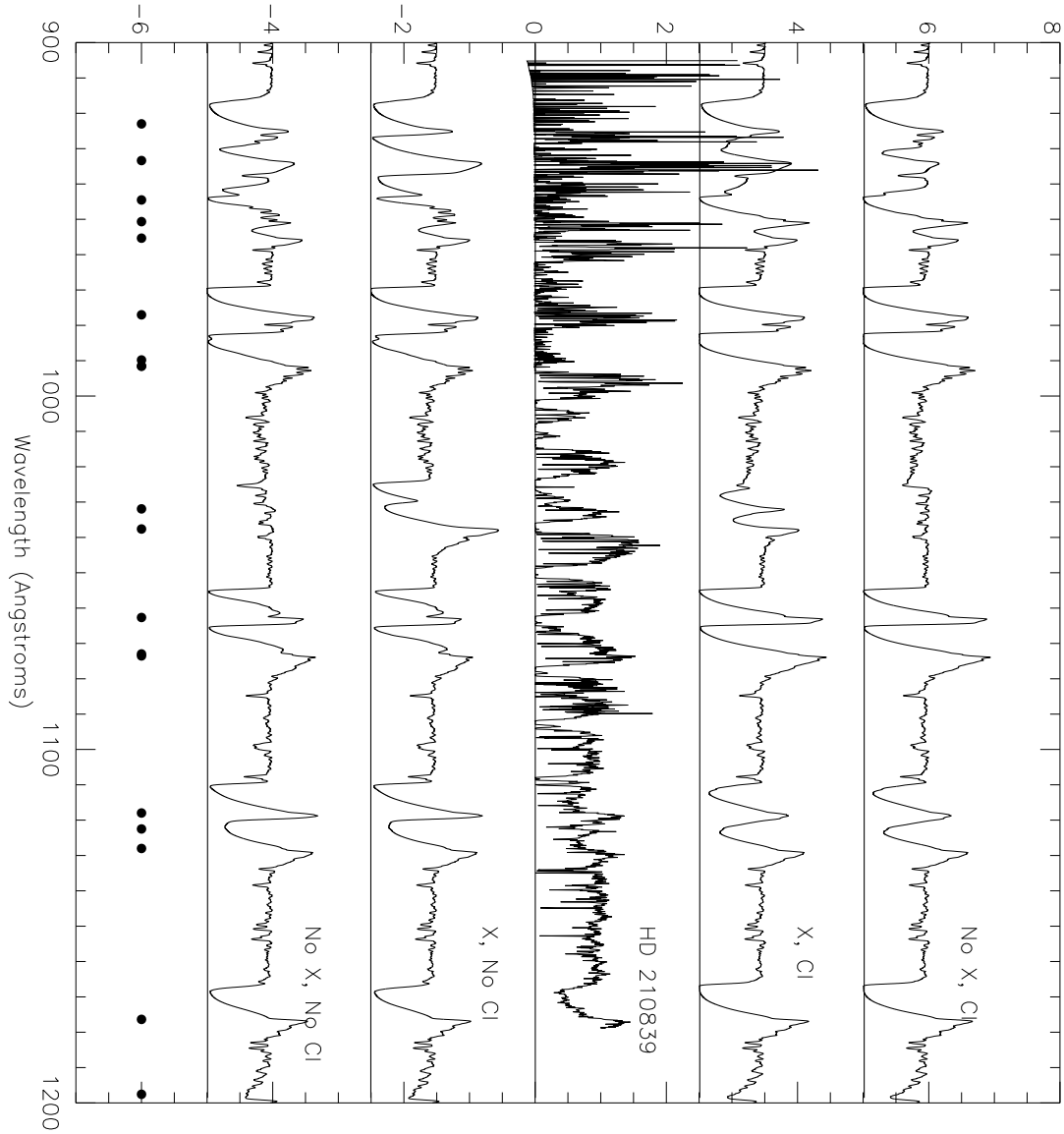

longer than about 1000Å, and even then it is only CIII, and possibly PV that are free of interstellar pollution. There are not currently any archival spectra of Galactic O stars at this wavelength available which are better. In the models, the lines most sensitive to clumping alone are the SiIV doublet at 1063, 1073Å and possibly PIV, although the latter is blended and more difficult to assess. SiIV is unfortunately blended with interstellar lines in the observations, but tracing an implied path of the profile over the top of the interstellar lines seems to suggest that the unclumped models are more accurate. The X-ray situation is not entirely clear but again OVI may only be reproduced by a model with the presence of X-rays, leading to the same conclusion from the *IUE* range NV doublet. It is probably fair to say that the OVI line would be similar in size to that in the observations of other supergiants if it were not dominated by interstellar lines, since X-rays have been shown quite consistently to cause a large wind line. In the models OVI is once again affected by clumping when X-rays are implemented. As with the O4 model PV is predicted to be too strong by the models in all four scenarios, although the clumped models have slightly weaker profiles than the unclumped ones. This effect has led others to predict very high clumping factors or low mass-loss rates for these objects (Bouret et al. 2005; Fullerton et al. 2006).

**Late-type supergiant**

The only lines that appear to change with scenario in the models (3.34) are OVI, due to clumping and X-rays, and PV, due to clumping. Again it can be seen that X-rays are necessary to give a realistic OVI line strength. PV and SiIV are too large though to be considered realistic. Now porosity effects, or something else, are called on to reduce PV *and* SiIV.

**Early-type Dwarf**

Where the IUE range yielded no help with discerning the X-ray scenario, the FUV range (3.35) makes it clear that X-rays are needed to produce a realistic OVI profile. The strength of PV is best reproduced by unclumped models, although in reality a small level of clumping might be appropriate, if porosity effects are ignored. CIII seems stronger when clumping is switched on in the models. It requires a spectrum with not too much pollution from interstellar lines to deduce the clumping scenario from this line.

**Figure 3.34.** FUV spectra for an O9 supergiant. See Table 3.2 for the list of lines corresponding to marked dots

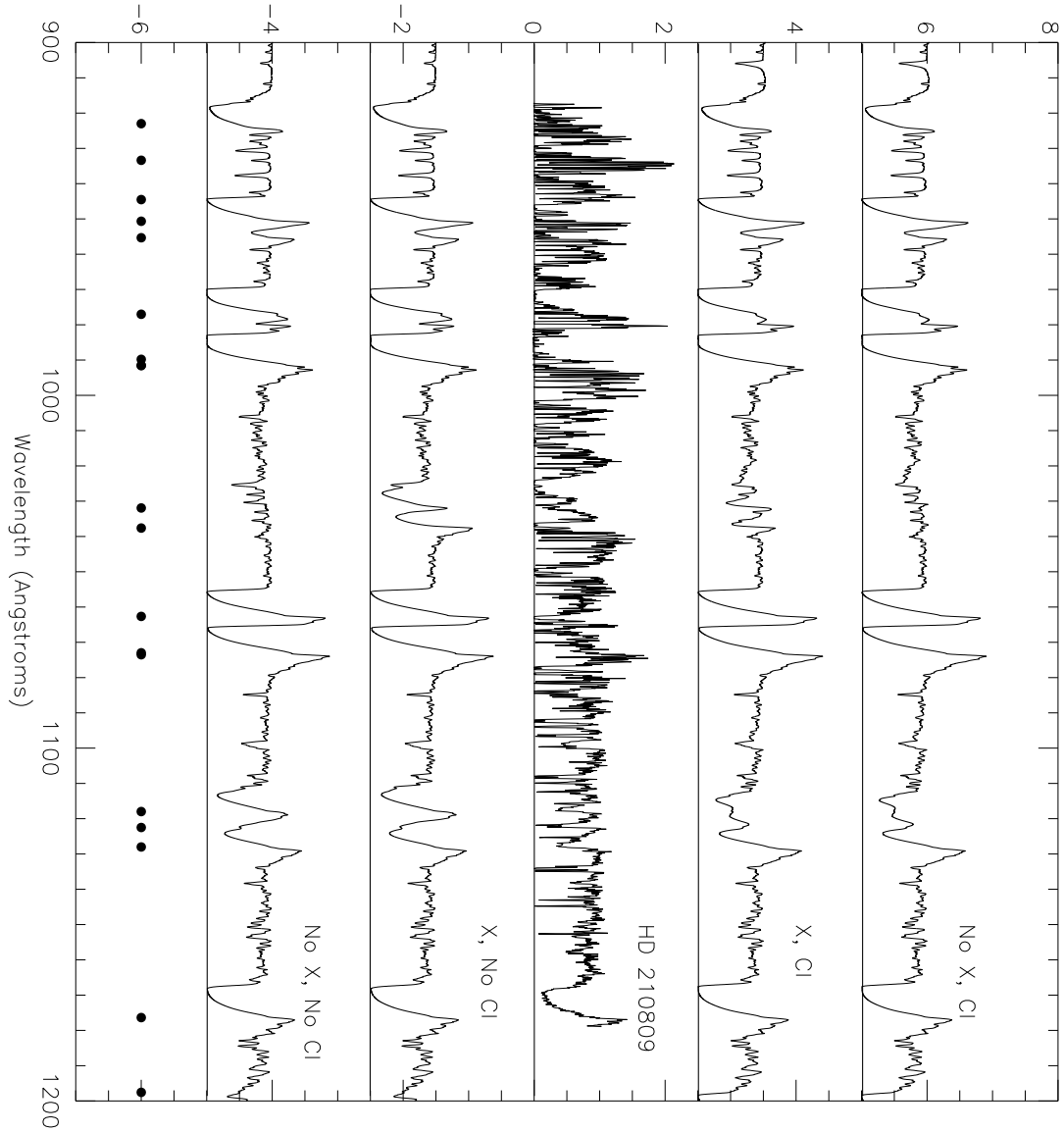

**Figure 3.35.** FUV spectra for an O3 dwarf. See Table 3.2 for the list of lines corresponding to marked dots

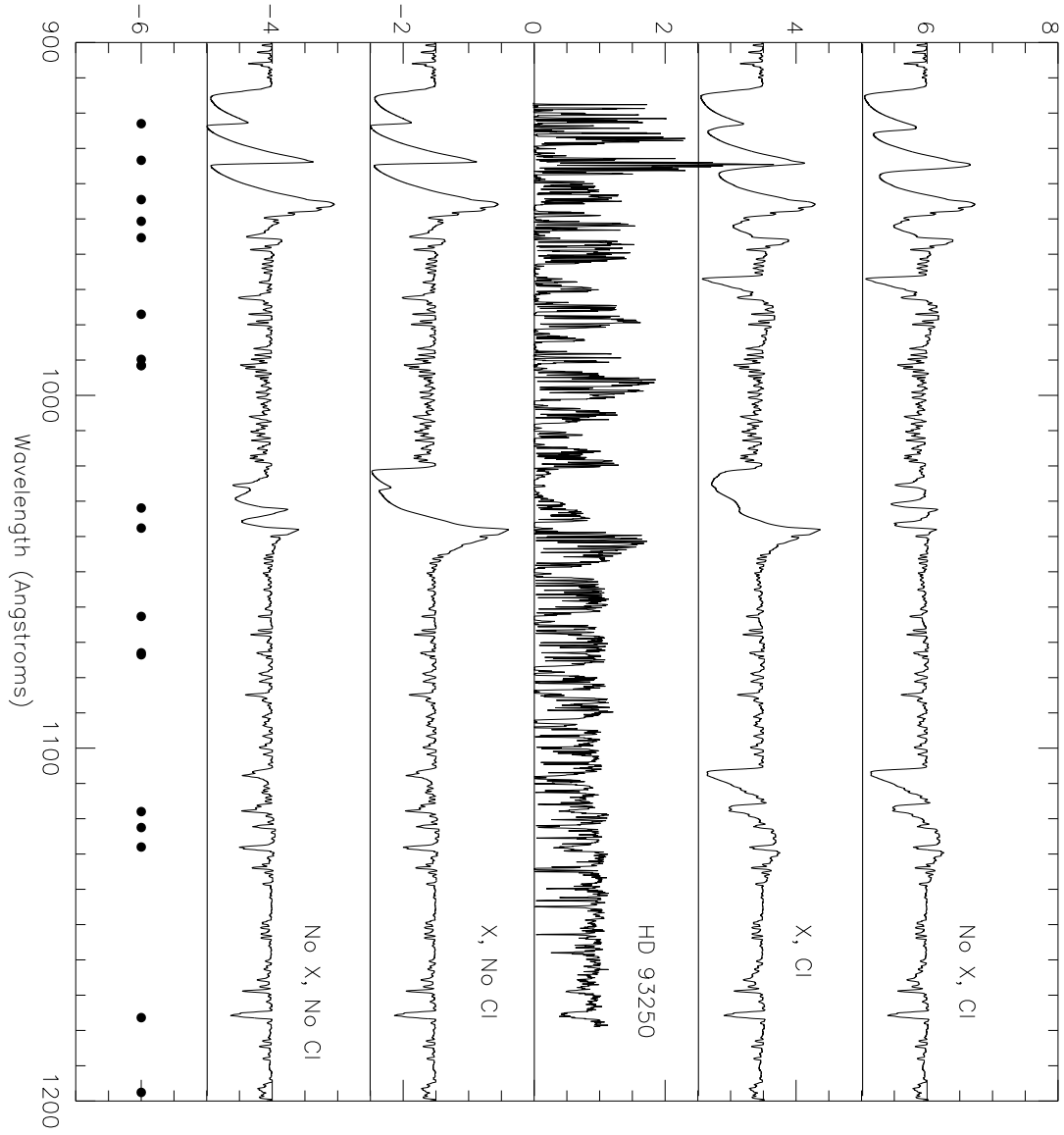

**Figure 3.36.** FUV spectra for an O6.5 dwarf. See Table 3.2 for the list of lines corresponding to marked dots

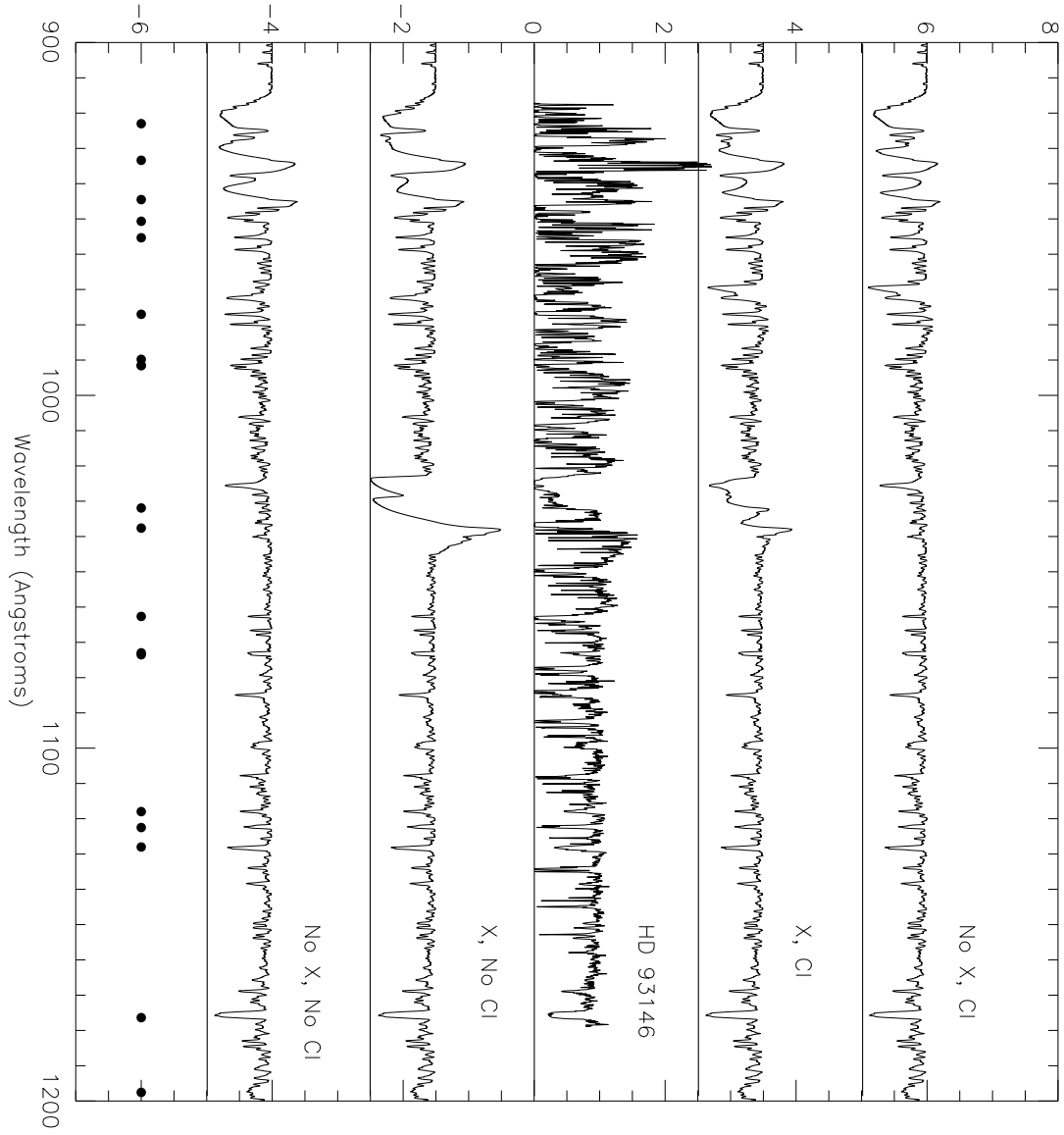

**Mid-type Dwarf**

The X-ray scenario was unclear from the IUE range and optical range. It is clear from the comparison of models with FUV observations of HD 93146 (O6.5 V ((f))) that X-rays are indeed required, although perhaps at a slightly lower level than in the model to match the spectrum of HD 93146 explicitly (3.36). There are no obvious anomalies in the model spectra when comparing them to the observed spectrum. Clumping could not be discerned earlier in the chapter, but here the model that best matches the observation is that *with* clumping. The problem here is that OVI is affected by both clumping *and* X-rays, as with supergiants . So whilst we can be quite sure of the need for X-rays, the clumping scenario is elusive. CIII does not react to clumping as strongly as for the early type object, and lies in the 'difficult' portion of the spectrum anyway.

**Late-type Dwarf**

By this late type, we already know from the *IUE* spectra that X-rays are required both to make NV strong enough and CIV weak enough. From the FUV (3.37) it seems that clumping and X-rays both affect OVI as in the mid-type dwarf. This means that one can effectively choose a balance between these to match the profile and gain no further information on the clumping scenario. CIII shows a minor change with clumping as before, but perhaps not enough to be visible in observations containing many interstellar lines.

## 3.4 Test Calculations - Clumping vs. Wind-density

It can be argued that since the product of mass-loss rate and clumping factor is not being kept constant in probing the clumping phenomenon, it is actually wind density that is being tested. It is hence worthwhile being explicit about what the likely differences would be between varying only the clumping factor, and keeping the product of mass-loss and clumping factor constant (i.e. reducing the mass-loss rate accordingly).

Since the actual mass-loss rate in CMFGEN is assumed to be spatially constant when model winds are clumped, this mass-loss rate is still related to the mean density via the mass-continuity equation. Because a void interclump medium is assumed,

$$\rho_{clumps} = \frac{\bar{\rho}}{f}, \tag{3.1}$$

**Figure 3.37.** FUV spectra for an O9 dwarf. See Table 3.2 for the list of lines corresponding to marked dots

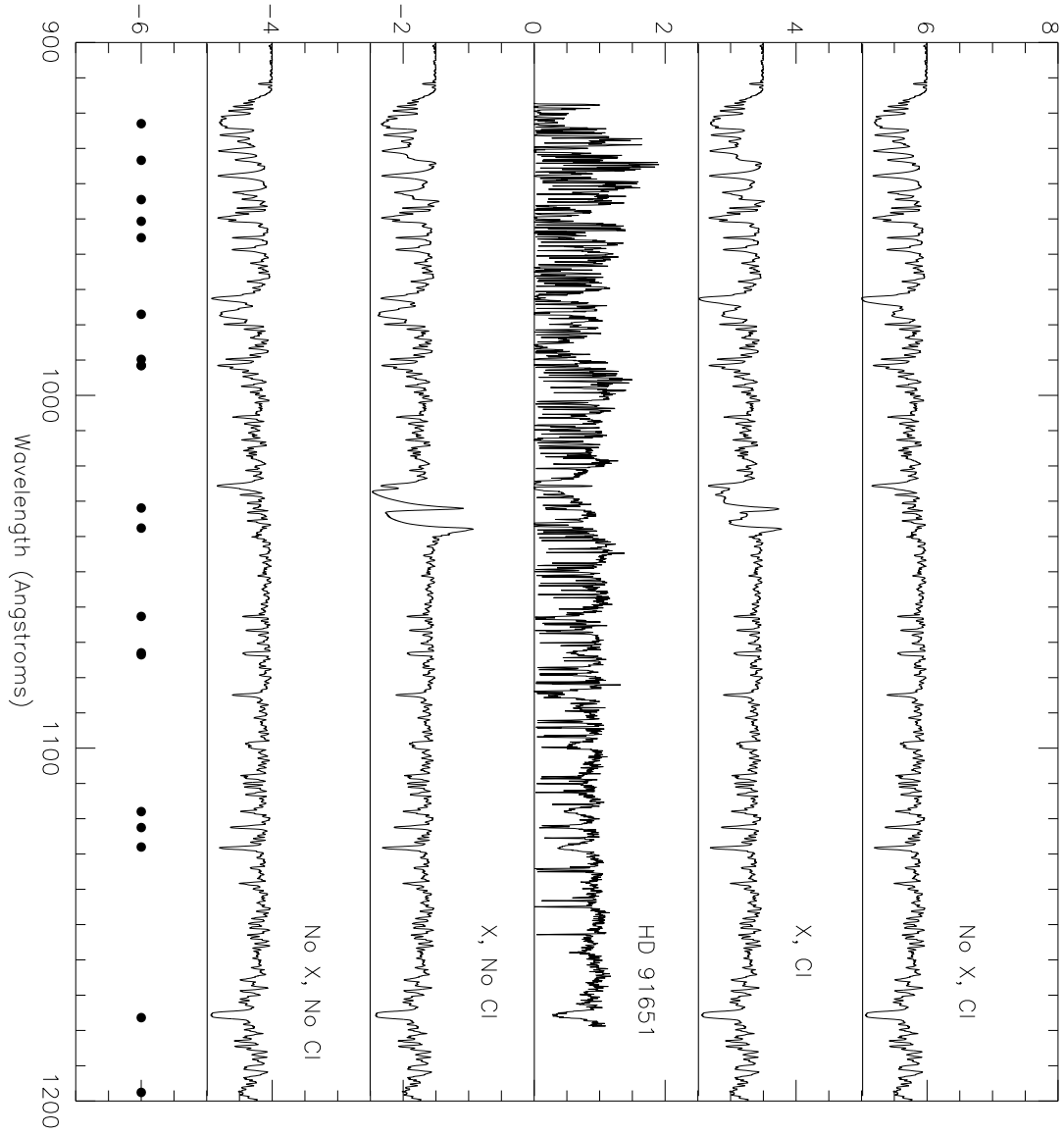

where $f$ is the volume filling factor. If only $f$ is varied and not the mass-loss rate, then the density in the clumps is being directly changed. With a higher clump density, ion and electron densities will be increased and so

- lines sensitive to density will be strengthened in emission
- the number of recombinations will be increased and so the ionization will be reduced

The combination of the two above effects could cause either an increase *or* a decrease in the overall emission.

So for density-squared diagnostic lines (such as H$\alpha$),

$$\dot{M}_{clumped} = \frac{\dot{M}_{smooth}}{\sqrt{f}}, \tag{3.2}$$

but for diagnostics that are linearly dependent on density (such as UV resonance lines), the details of the ionization structure in the wind will determine exactly what the effect on a given line is. Overall, we expect UV resonance lines to change in some way whether only the clumping factor is altered or if the product of mass-loss rate and clumping is kept constant.

Because of this subtlety, a small set of test CMFGEN calculations were been performed. For early-, mid- and late-type stars of both dwarf and supergiant luminosity class, models were run where the product of mass-loss rate and clumping factor is kept constant. The UV and FUV spectra are compared to the equivalent models with smooth winds, and those where only clumping factor has changed. These appear in Figures 3.38 and 3.39. In this exercise the late-type dwarf model could not be made to reach a sufficient level of convergence using any of the possible techniques. It is possible that the part of parameter space these late-dwarfs occupy is not possible with the current version of CMFGEN. The remaining five models' spectra are discussed below.

Each of the spectra in Figures 3.38 and 3.39 show the unclumped model spectrum in black, the model with an altered clumping factor in red, and the model with constant $\dot{M}\sqrt{f}$ in green. They will be referred to mostly by the colours in the plot as a shorthand in the text that follows.

For the early-type supergiant, the model that stands out as most different is in red, where only the clumping factor has been altered. This scenario has a greater affect on the

**Figure 3.38.** Spectra from test calculations where the product of mass-loss rate and clumping factor has been kept constant. Black: unclumped, red: enhanced clumping factor only, green: enhanced clumping factor, with mass-loss reduced accordingly

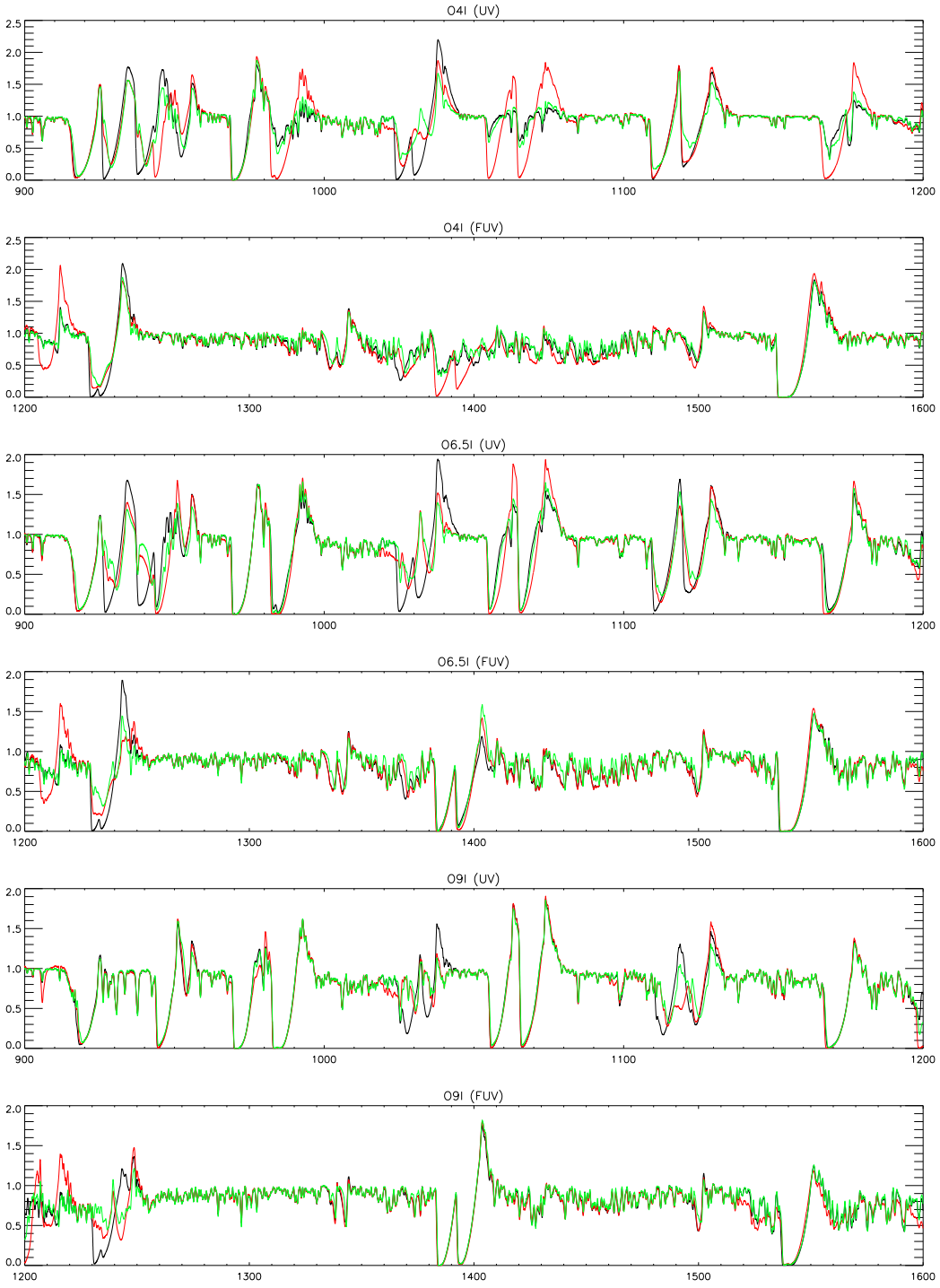

**Figure 3.39.** Spectra from test calculations where the product of mass-loss rate and clumping factor has been kept constant. Black: unclumped, red: enhanced clumping factor only, green: enhanced clumping factor, with mass-loss reduced accordingly

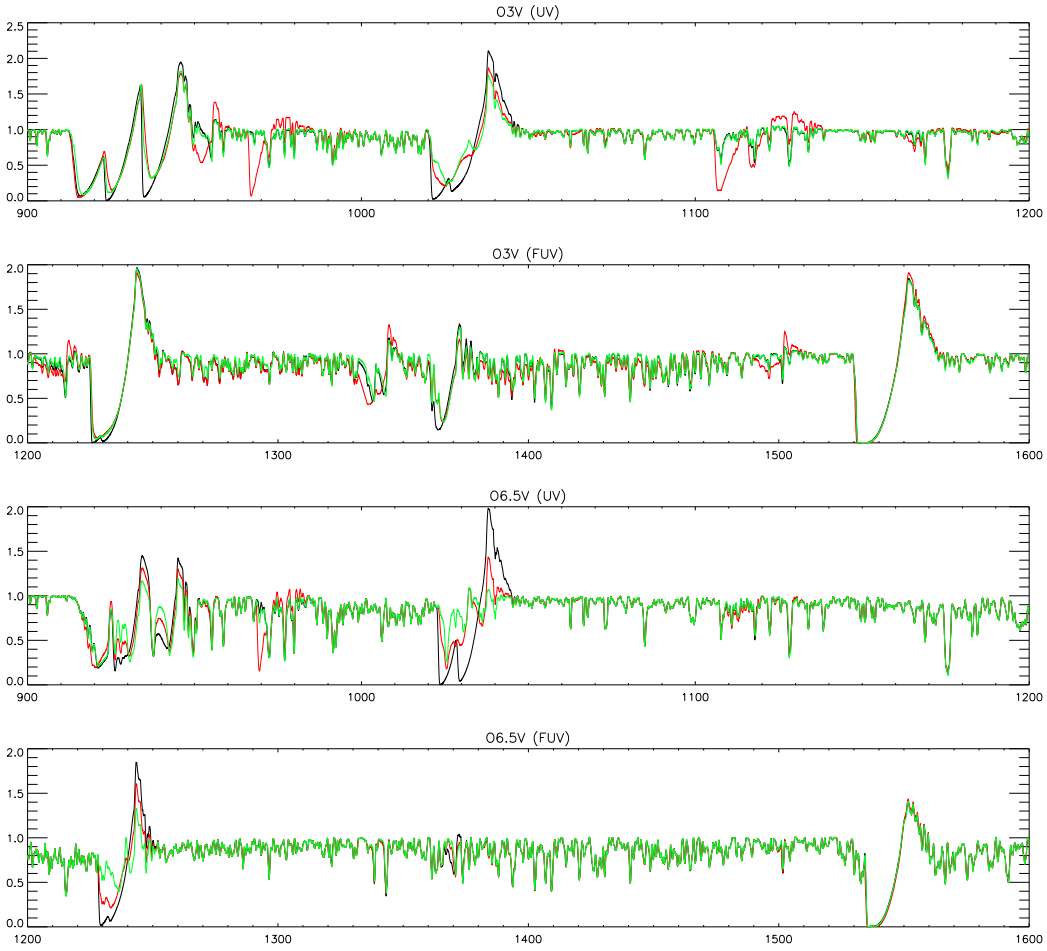

spectrum than if the mass-loss rate is reduced accordingly (in green). The line profiles where this has a very noticeable effect are PIV(951Å), NIV(955Å), the NIII triplet around 990Å, the SIV triplet around 1060-1070Å, CIII(1176Å) and SiIV(1400Å). The other major wind lines appear less affected by this change. Generally speaking the spectrum without a reduced mass-loss rate (red) has stronger lines than the one *with* a reduced mass-loss rate. This is not the case, however, in the lines known to be strongly affected by X-rays (NV and OVI). In most of the rest of the lines, the effect of reducing the mass-loss rate is to reduce the impact of the change in clumping, but not eliminate it entirely. PV seems uniquely affected - whilst increasing only the clumping factor has little effect, the corresponding reduction of mass-loss rate reduces the profile size to less than the unclumped model.

For the mid-type supergiant, the differences between the three spectra are much smaller than in the early-type one. This is likely because the unclumped models have lines that are more saturated, and hence the changes brought about by mass-loss rate and clumping alterations do not appear as strongly.

By the late-type supergiant the only lines to have noticeable changes are OVI, PV and NVI. In OVI both clumped models are very similar, implying that a changed mass-loss rate has little effect compared to clumping for this line. A similar situation exists for PV, although it is less clear due to the presence of a SiIV line between the PV components. NV shows how delicate the situation is for some UV lines. Adding clumping reduces the profile size, and then reducing the mass-loss rate reduces the profile size even further. The interplay between the different effects described before lead to rather a complex situation to decipher.

The early-type dwarf spectrum shows again how the effect can be different for different lines. Whilst for SVI (933, 945Å), both clumped models match each other but are different to the unclumped model, for PV (1118, 1128Å), it is the red model (clumped but without a reduced mass-loss rate) that stands out on its own.

For the mid-type dwarf, the differences have boiled down to just a few lines. OVI and NV show a similar pattern. Adding clumping to the model reduces the profile size, and then reducing the mass-loss rate reduces it still further. By contrast CIII (977Å) shows a larger profile than the others for the red model, that with increased clumping only.

Generally it can be seen that the way mass-loss rate and clumping operate together is far from straightforward and is in fact worthy of further, more involved investigation. This finding acts as a caveat to this chapter's conclusions.

## 3.5 Chapter Conclusions

A set of model stellar atmospheres has been computed and compiled from CMFGEN, covering spectral types O3 to O9.5 and luminosity classes I and V. Side-by-side comparisons to observations have been made as a consistency check (actual fits are not attempted). The spectra show morphological agreement with *IUE* and *FUSE* observations, and are hence reliable with regard to drawing conclusions about the physical parameters of the stars. By observing the behaviour of profiles in the UV, FUV and optical regions of the spectra, comments have been made about the effects of micro-clumping and the input of X-rays. Figure 3.3 shows a summary of the models that are most representative of the available observed spectrum. For the FUV, this is mostly deduced from the longer wavelength part of the spectrum.

**Table 3.3.** Most representative models. This table gives a summary of the most appropriate model in each case, based on visual inspection. Two ticks are given in any case for which two models cannot be distinguished in suitability.

| | No X, No Cl | No X, Cl | X, No Cl | X, Cl |
|---|---|---|---|---|
| Supergiants (UV) | | | | |
| Early-type | | | √ | |
| Mid-type | | | √ | √ |
| Late-type | | | | √ |
| Dwarfs (UV) | | | | |
| Early-type | √ | | √ | |
| Mid-type | | | √ | |
| Late-type | | | √ | |
| Supergiants (FUV) | | | | |
| Early-type | √ | | √ | |
| Mid-type | | | √ | |
| Late-type | | | √ | |
| Dwarfs (FUV) | | | | |
| Early-type | | | √ | |
| Mid-type | | | √ | √ |
| Late-type | | | | √ |

It is clear that the only way to produce realistic NV and OVI profiles is to incorporate X-rays correctly in the computation of the model atmospheres, since the ionizing effect of X-rays is crucial to the balance between successive ion stages. Whilst the *presence* of X-rays is obvious, it is more difficult to discern the *exact level* of X-ray input from NV

and OVI profiles alone, since they also appear to react to changes in the clumping factor. An increased level of clumping has an effect counter to the X-rays, causing enhanced recombination. The populations relating to NV and OVI are hence likely to be in quite a fine balance with adjacent stages. An important caveat at this point is from the study of Zsargo et al. (2009), who tentatively make the case for OVI being formed entirely by a tenuous interclump medium, and claim that the OVI line profile in $\zeta$ Puppis can only be formed this way. This means that an X-ray parametrisation in the current implementation of CMFGEN, combined with pure micro-clumping, cannot truly predict OVI lines. This reinforces the conclusion here that all one can say from the models is that X-rays are an important parameter to consider in producing realistic OVI and NV wind lines, but more in-depth study needs to be performed to make further comment. The latest simulations in the X-ray domain are those by Cohen et al. (2010), who concentrate on X-ray emission lines. Their 1D models are the state of the art regarding X-ray effects in O stars, and in addition provide a new method for determination of mass-loss rates.

In the current grid of CMFGEN models, the inclusion of X-rays is particularly important for reproducing the CIV resonance doublet in later type dwarf models because they make it weaker, populating $C^{4+}$ and/or $C^{5+}$ instead. The effect of this is greater, the later the spectral type, and is greater than the effect of changing the mass-loss rate by a significant factor at the latest types (see Fig. 3.28), or changing the clumping factor. The reason this effect is not seen at earlier spectral types is probably that CIV is saturated anyway, and changes to the population by X-rays does not exhibit itself in the profile.

In most models there are lines that diagnose the change in clumping factor. In some this can be seen as the strength of an NIII profile increases, as an NIV one decreases, for example. In most models, the number of wind lines that reveal the effects of clumping is greater in the FUV than in the UV, partly because saturation affects more lines in the UV. The level of clumping that is most consistent with observations of both UV and optical regions is low, assuming the physical parameters in the models to be truly representative. Some profiles cannot be matched with any clumping scenario, most notably PV, which has been shown in the literature to be reduced by the effects of a porous wind, or one where optically thick clumps are present. However, it is perhaps not 'porosity' per se that is needed in the treatment, but a treatment of optically thick clumps in general. Sundqvist et al. (2010) have shown that only moderate clumping factors are required to adequately reduce the strength of PV in supergiants, if the clumps are optically thick,

by utilising a velocity-porosity. By contrast where line formation is concerned, a spatial porosity treatment requires rather significantly higher clumping to reduce the profiles, and its main effect is at the bluer edge of lines.

Other factors that can affect unsaturated UV profiles that are not addressed directly in this work include $\beta$-law and density scale height (Hillier et al. 2003) and abundances (Crowther et al. 2002). Additionally, some apparently photospheric profiles have been shown to be affected by clumping (Hillier et al. 2003).

In the absence of a full multi-wavelength model atmosphere approach that employs all possible effects of small-scale structure (micro-clumping, spatial porosity, velocity porosity, optically thick clumps), the spectra shown here represent an extensive exploration of parameter space in terms of the treatments of X-rays and clumping.

# Chapter 4

# Ion fractions in O star winds

*'Observations always involve theory.'*

Edwin Hubble

Stellar winds from hot stars are made up of electrons and ions, and the number density of these at different points in the expanding atmosphere is dependent, amongst other factors, upon the relative abundance of elements and the energy conditions in the wind. The exact balance of the number of different ions of an element is determined by the competing processes of photoionization (ejection of electrons from atoms by photons with sufficient energy) and recombination (the capture of an electron by an ion). One of the benefits of performing radiative transfer is the ability to predict both the total ionization equilibrium of a stellar wind, and the radial stratification of ion balance. Knowledge of the ion fractions of elements has applications such as those presented in later chapters.

This chapter is a presentation of the ionization conditions in O star expanding atmospheres as predicted by CMFGEN, according to the grid detailed in Chapter 2. The run of different ion fractions with effective stellar temperature is the main focus, along with an analysis of the effect of both wind-clumping and X-rays on the ion balance of carbon, nitrogen, oxygen, phosphorus, sulphur and silicon. Dominant ions are identified, and comparisons are made with some other claims of dominance in the literature.

## 4.1 Procedure for deriving ion fractions

CMFGEN includes amongst its many output files the information necessary to compute the fractional abundance of an ion relative to the total elemental abundance, as a function of radius. This was calculated for each of the O star models using the subroutine DISPGEN, and each was then summed in velocity space over the entire wind and normalised to include only the contribution from between 0.2 and 0.9 of the terminal velocity. This step was taken to be able to make direct comparisons with values of $\dot{M}\langle q_i \rangle$ in the study contained in Chapter 5. In that chapter, empirical fits are undertaken and normalised to the range 0.2-0.9$v_\infty$ so as to avoid variable phenomena at high velocity, and the recognised difficulty in fitting the emission portions of wind profiles. Further details are to be found in Chapter 5.

## 4.2 Ion Fractions

Figures 4.1 to 4.23 show the sets of ion fractions for both supergiants and dwarfs for each of the elements C, N, O, P, S and Si. In the following parts of this section comments on these figures are given, with particular attention afforded to the pertinent issues of dominant ions and the effects of clumping and X-rays upon the ion balance.

### 4.2.1 Supergiants

The models for type O7I that include both clumping and X-rays could not be made to converge satisfactorily with the normal level of X-rays (as defined by observations - $L_X/L_{bol} \sim 10^{-7}$). They could however be made to converge for an X-ray input an order of magnitude greater. For this reason the models with extra X-rays are included in the plots for illustrative purposes, to show that for some supergiants at least there is a non-negligible effect of adding extra X-ray flux.

- **Carbon** - Looking first at the linear scale plot in Figure 4.1, we see that the unclumped scenario including no (or at least negligible) X-rays shows $C^{3+}$ to be the dominant ion of carbon for most of the O star range (greater than 50% from 31-40 kK). As expected from energy considerations, $C^{3+}$ recombines to $C^{2+}$ with progression to later types (lower effective temperatures), and is photoionized to $C^{4+}$ moving to earlier types (higher effective temperatures). This expectation comes from that

**Figure 4.1.** Supergiant ion fractions for carbon. Black = $C^{2+}$, red = $C^{3+}$, green = $C^{4+}$. 'X' stands for X-rays and 'Cl' for clumping factor.

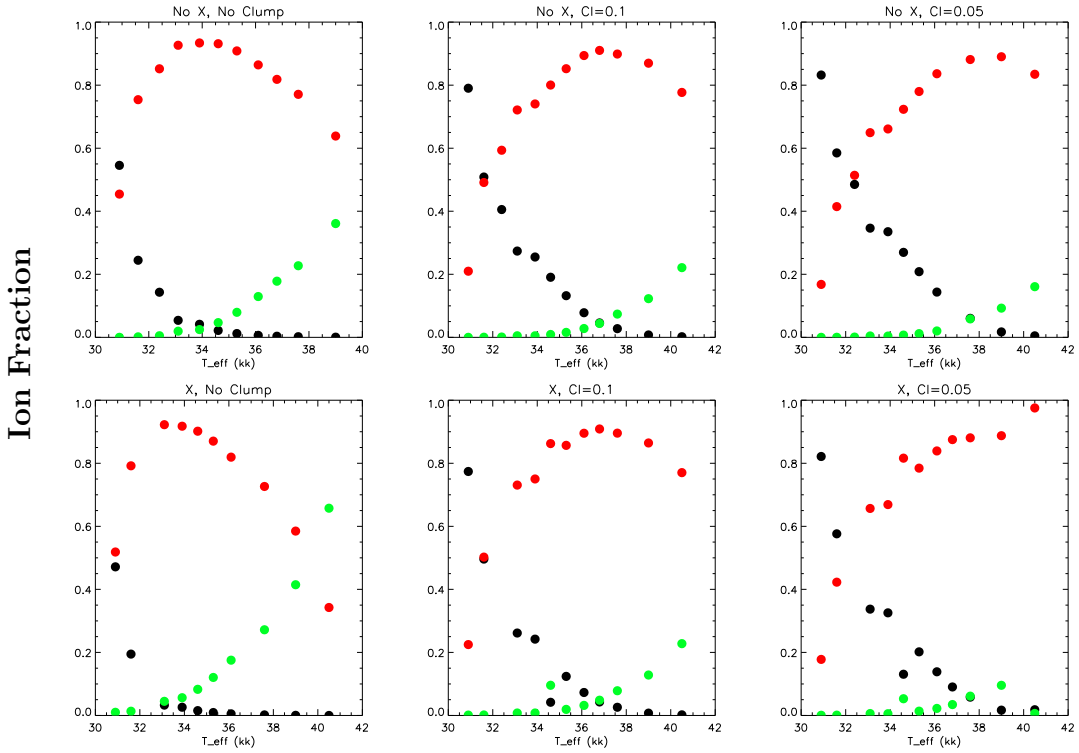


fact that earlier types have more intense radiation fields and hence a greater abundance of ionizing photons. The fraction of $C^{2+}$ climbs towards lower temperatures and so is expected to be dominant in the B star range. As we change from an unclumped wind to a moderately clumped one, but retain only a negligible contribution from X-rays, we see a very similar situation, albeit one in which the change in dominance from $C^{2+}$ to $C^{3+}$ seems to be at slightly hotter temperatures. The crossover now seems to happen at about 32kK rather than at 31kK. This effect is due to the enhanced density brought about by clumping, leading to a higher rate of recombination. The same effect appears to reduce the fraction of $C^{4+}$ and increase that of $C^{3+}$ at the hotter end of the temperature scale. This overall effect is exaggerated slightly as we move to the more strongly clumped scenario. We see roughly the opposite happen on the introduction of X-rays into the wind; for no clumping $C^{2+}$ never quite becomes dominant, whilst $C^{4+}$ is the dominant form of carbon at the hotter end of the scale. The presence of the high energy X-rays is driving a move to higher ionization stages. The clumped winds with X-rays exhibit largely the same behaviour as for the non X-ray winds, with a slightly anomalous point at 40.5kK

**Figure 4.2.** Supergiant ion fractions in log scale for carbon. Black = $C^{2+}$, red = $C^{3+}$, green = $C^{4+}$. 'X' stands for X-rays and 'Cl' for clumping factor.

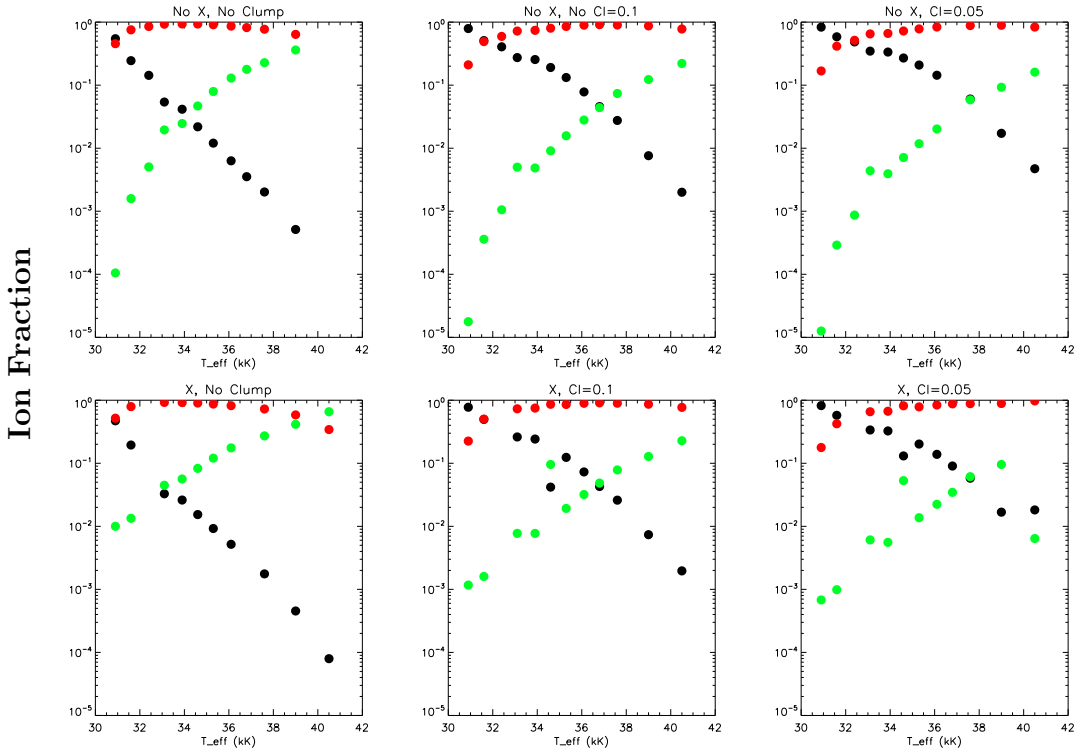


(O3I) in the strongly clumped scenario. This point corresponds to the O3I model, which shows nothing peculiar in its spectroscopic output, and the model's observed X-ray luminosity falls well within the literature range. It is however amongst the lowest levels of X-ray input (within allowed limits) for all strongly clumped X-ray models. This could be demonstrating a sensitivity of the model to the exact X-ray strength. Increasing the X-rays to an order of magnitude higher than usual at type O7I (34.6kK) has little effect on $C^{3+}$, with a proportionally larger effect on the other ion stages. The effect is greater for a more strongly clumped situation, but generally it seems to show that it takes quite a large change in the observed X-ray luminosity before there is a great effect on the carbon ion fractions. Looking now at the log scale plot in Figure 4.2 we see the effects we expect but more clearly for $C^{2+}$ and $C^{4+}$. In each case clumping has the effect of reducing the population of $C^{4+}$ by up to an order of magnitude at the cooler end and increasing $C^{2+}$ by up to an order of magnitude at the hotter end. The presence of X-rays works opposite to clumping, and again by up to an order of magnitude in fraction. The presence of the extra X-rays in the O7I models increases the population of $C^{4+}$ by about a

**Figure 4.3.** Supergiant ion fractions for nitrogen. Black = $N^{2+}$, red = $N^{3+}$, green = $N^{4+}$, blue = $N^{5+}$. 'X' stands for X-rays and 'Cl' for clumping factor.

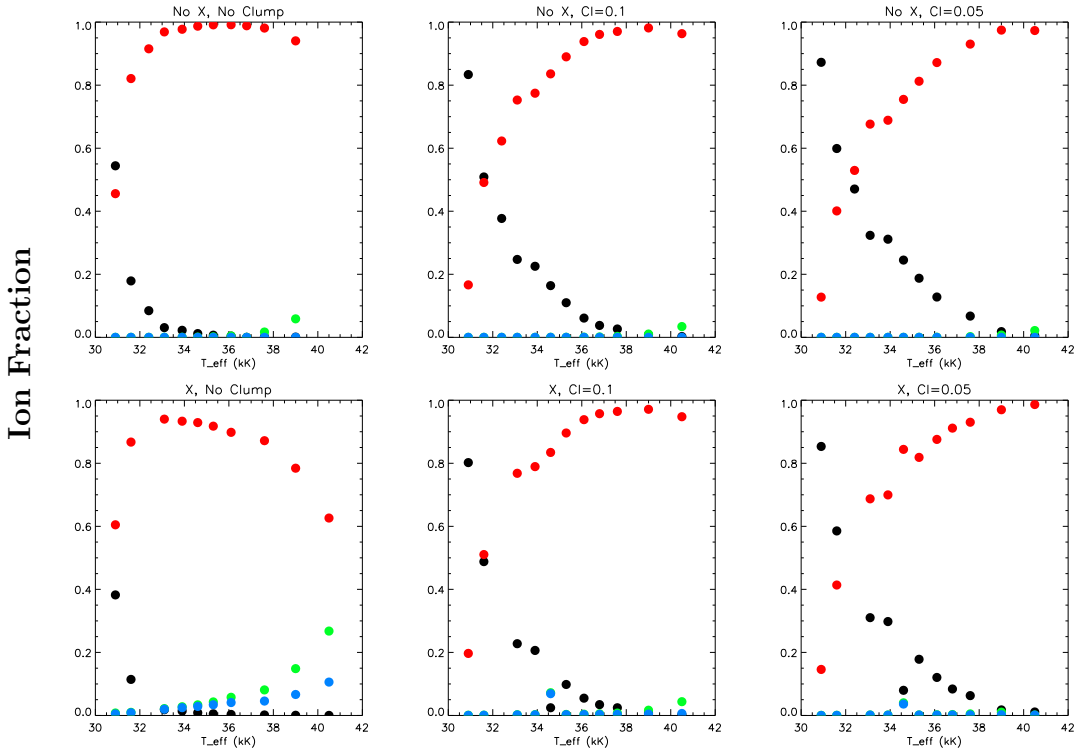


factor of ten, highlighting the importance of getting the X-ray input right in models. The sensitivity of models to X-rays is further highlighted by the strongly clumped X-ray model for O3I (40.5kK), where only a slightly weaker X-ray input causes the ion fractions of $C^{2+}$ and $C^{4+}$ to fall well out of the trend. Generally we see again that the addition of moderate clumping to a model is enough to achieve any effect, and further enhancement of the clumping has very little further effect.

- **Nitrogen** - From the linear plots in Figure 4.3 we see that in the unclumped models, $N^{3+}$ appears to be the dominant form of nitrogen throughout almost the whole O star range, with $N^{2+}$ increasing for later types. $N^{4+}$ begins to rise at the hotter end but remains at less than 10% of the total. Recombination causes a drop in $N^{3+}$ and a rise in $N^{2+}$ at the cooler end, with an implied gain in $N^{3+}$ and drop in $N^{4+}$ at the hotter end. $N^{5+}$ remains negligible for the whole temperature range. X-rays have the largest influence on the unclumped winds, as they appear to cause $N^{3+}$ to be fully dominant over the full temperature regime of O stars, although the actual amount at most temperatures is lessened through photoionization. The X-rays seem to make

**Figure 4.4.** Supergiant ion fractions in log space for nitrogen. Black = $N^{2+}$, red = $N^{3+}$, green = $N^{4+}$, blue = $N^{5+}$. 'X' stands for X-rays and 'Cl' for clumping factor.

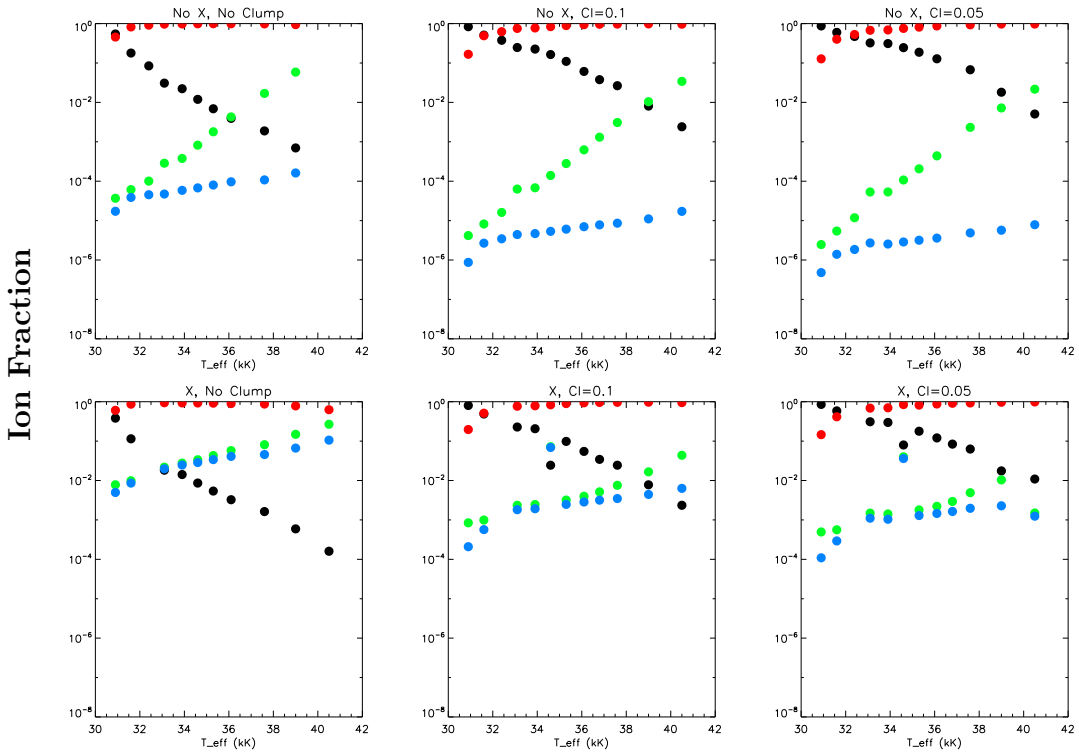


much less difference in the clumped models, which is to be expected since X-ray photoionization and recombination brought about by clumping are counteracting processes. The plots for clumped models are very similar for both X-ray and non-X-ray models. As with carbon, the extra X-ray energy for the O7 supergiants has more of an effect on the lower ion stages in the more strongly clumped scenario. We see again from the log scale plots in Figure 4.4 that moderate clumping achieves most of the effect of changing the population, and that extra clumping does little more. Apart from this it is important to highlight that the $N^{4+}$ ion is never dominant in the O star range, despite the Nv resonance doublet appearing very strong in the synthetic spectra produced in the last chapter.

- **Oxygen** - In all clumping and X-ray scenarios the dominant ion goes from being $O^{2+}$ to $O^{3+}$ as the effective temperature increases (Figure 4.5). As with both carbon and nitrogen the crossing point between $O^{2+}$ and $O^{3+}$ moves to higher temperatures as clumping is introduced, due to the changing balance between recombination and photoionization. Again, the X-rays affect the ionization balance of the unclumped

**Figure 4.5.** Supergiant ion fractions for oxygen. Black = $O^{2+}$, red = $O^{3+}$, green = $O^{4+}$, blue = $O^{5+}$, yellow = $O^{6+}$. 'X' stands for X-rays and 'Cl' for clumping factor.

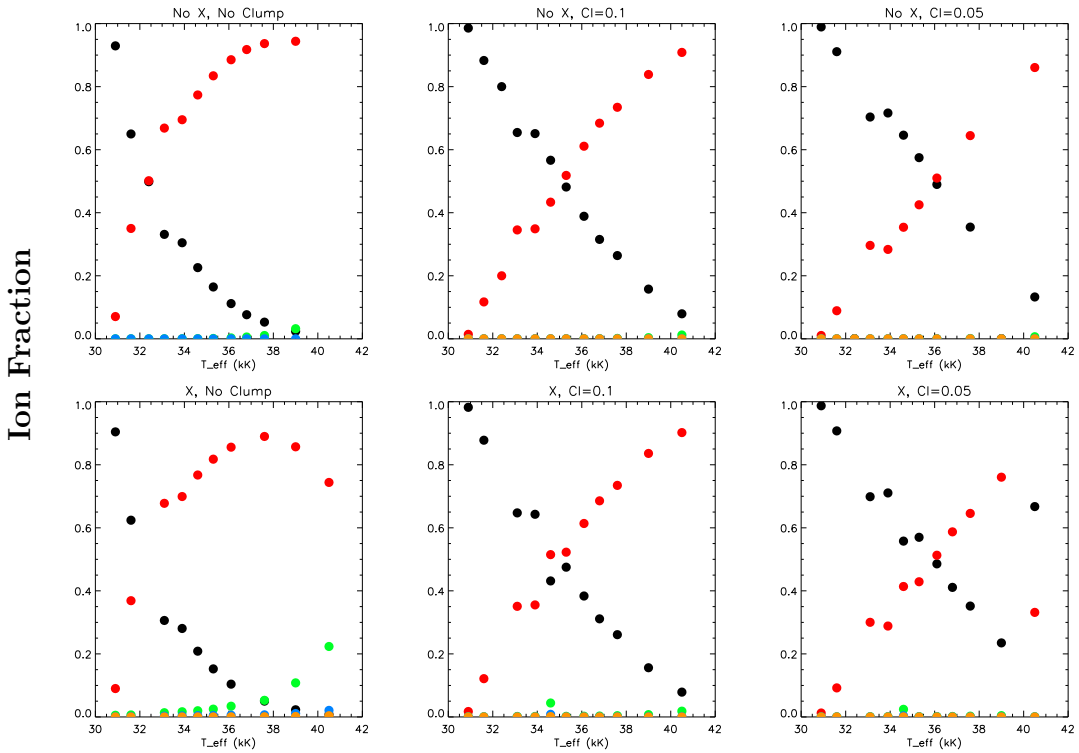


scenario the most, as we see a definite increase in the fraction of $O^{4+}$ and a decrease of $O^{3+}$. This is not coupled with any discernable change in the strengths of the OIV and OV profiles in the corresponding models; these are excited transitions. In the unclumped scenario the X-rays cause the fraction of $O^{5+}$ to increase by a factor of 600[1] at the hotter end of the temperature scale, although this cannot be seen on the scale of the plot. This is accompanied by an obvious change in the strength of the OVI line in the FUV. At the same temperatures, the $O^{6+}$ fraction is increased a factor of 2000, but there is no observable line that this corresponds to in the UV or FUV. Again there is an anomalous point in the X-ray and strongly clumped models corresponding to the O3I model, presumably due to the slightly lower X-ray input in this model, again showing how sensitive some ions are to this physical attribute. Generally the effect of X-rays on the dominant oxygen ions does not seem great, but is proportionally much greater on the higher stages. The O7I clumped and X-ray models do not show very much deviation from the trend compared to other

[1]Exact numbers can be sought directly from CMFGEN's output files

**Figure 4.6.** Supergiant ion fractions in log space for oxygen. Black = $O^{2+}$, red = $O^{3+}$, green = $O^{4+}$, blue = $O^{5+}$, yellow = $O^{6+}$. 'X' stands for X-rays and 'Cl' for clumping factor.

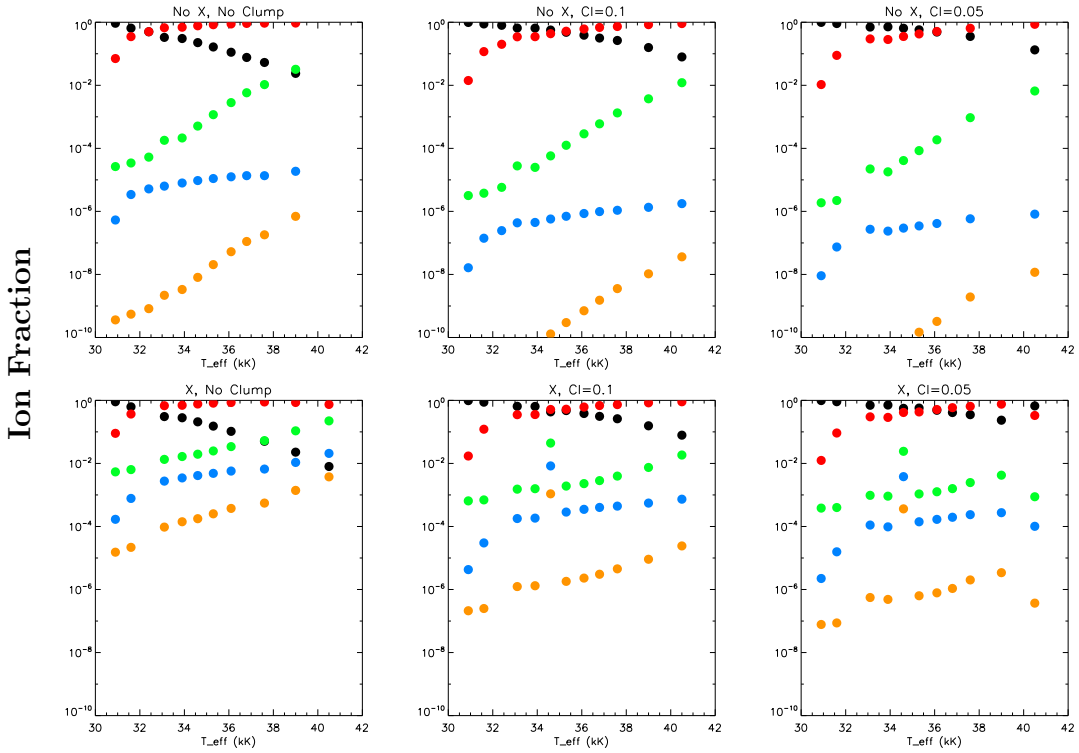


elements, according to the linear plot. In the log scale plot in Figure 4.6 however the extra X-rays cause an obvious difference in the proportion of the higher ion stages. Interestingly, from the strongly clumped X-ray plot we see that the deviation of $O^{2+}$ and $O^{3+}$ in the O7I (34600K) model from the trend is far less than the O3I (40500K) model. The O7I model has an X-ray luminosity of a factor of ten greater than surrounding models, whereas the O3I model' X-ray luminosity is rather closer to that of the surrounding points. This implies that, at least for strongly clumped models, X-rays have a far greater effect on lower ion stages at higher temperatures.

- **Phosphorus** - Knowledge of these ion fractions is particularly pertinent given the Pv problem (Fullerton et al. 2006), which is discussed in Chapter 1 and §1.5. In that study, derivation of mass-loss rates is highly dependent on the supposed dominance of $P^{4+}$ for some subset of O stars. This will be discussed in some more detail later in the chapter. In Figure 4.7 $P^{4+}$ appears dominant in non-X-ray models from 31 to 39kK for the unclumped scenario, from 33 to beyond 41kK in the moderately clumped scenario and from 34.5 to beyond 41kK in the strongly clumped scenario.

**Figure 4.7.** Supergiant ion fractions for phosphorus. Black = $P^{3+}$, red = $P^{4+}$, green = $P^{5+}$. 'X' stands for X-rays and 'Cl' for clumping factor.

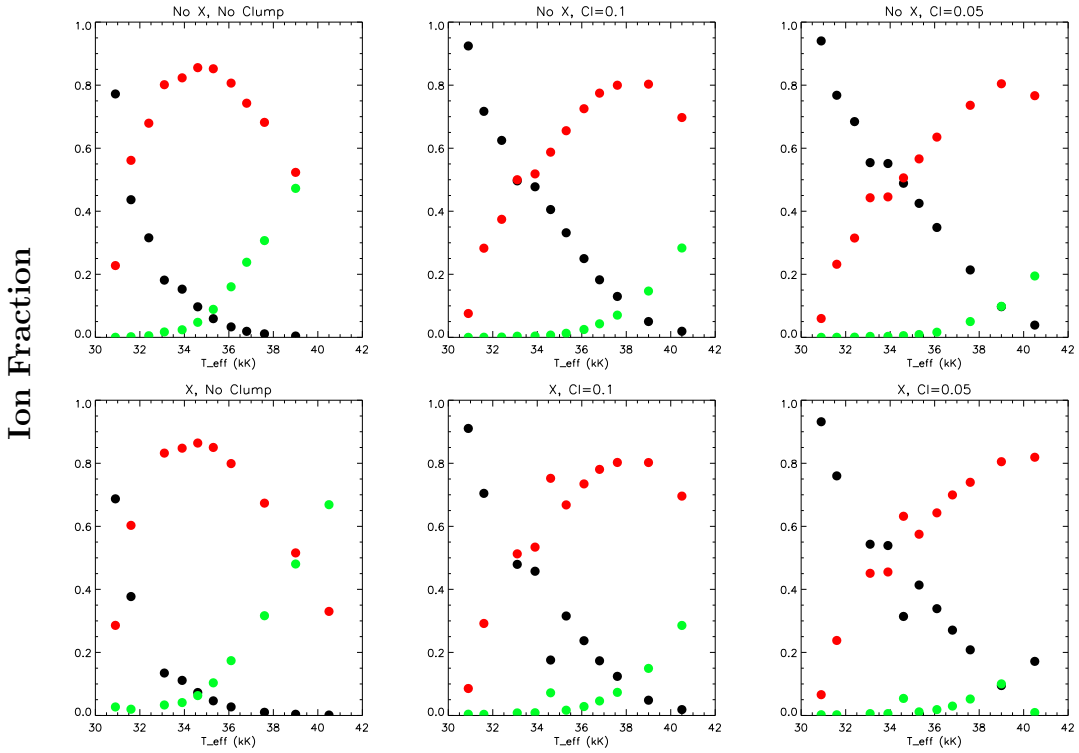


The pattern of the crossing point at lower temperatures (between $P^{3+}$ and $P^{4+}$) moving to higher temperatures is followed, and the higher stage ($P^{5+}$) becomes weaker at higher temperatures as recombination increases over photoionization. The pattern does not really change in the X-ray models apart from the anomalous models discussed already. The trends seen for phosphorus are very similar to those in carbon, since their ions have very similar ranges of ionization potentials (see Fig 1 in Massa et al. (2003)).

- **Sulphur** - For the coolest O stars the $S^{3+}$ ion is dominant in all scenarios, and transitions to $S^{4+}$ at hotter temperatures as clumping gets stronger (see Figure 4.9). $S^{5+}$ plays a role at hotter temperatures but declines with clumping as recombination increases and photoionization decreases. The main role of X-rays is to strongly increase the fraction of $S^{6+}$ in the unclumped scenario, whilst decreasing $S^{4+}$. This is likely an Auger ionization effect as the latter is stripped of two electrons. Sulphur is important in that for O stars there are three successive ion stages with corresponding lines visible in the UV and FUV - SiV (1063, 1073 Å), SV (1502 Å) and SiVI (933, 945

**Figure 4.8.** Supergiant ion fractions in log space for phosphorus. Black = $P^{3+}$, red = $P^{4+}$, green = $P^{5+}$. 'X' stands for X-rays and 'Cl' for clumping factor.

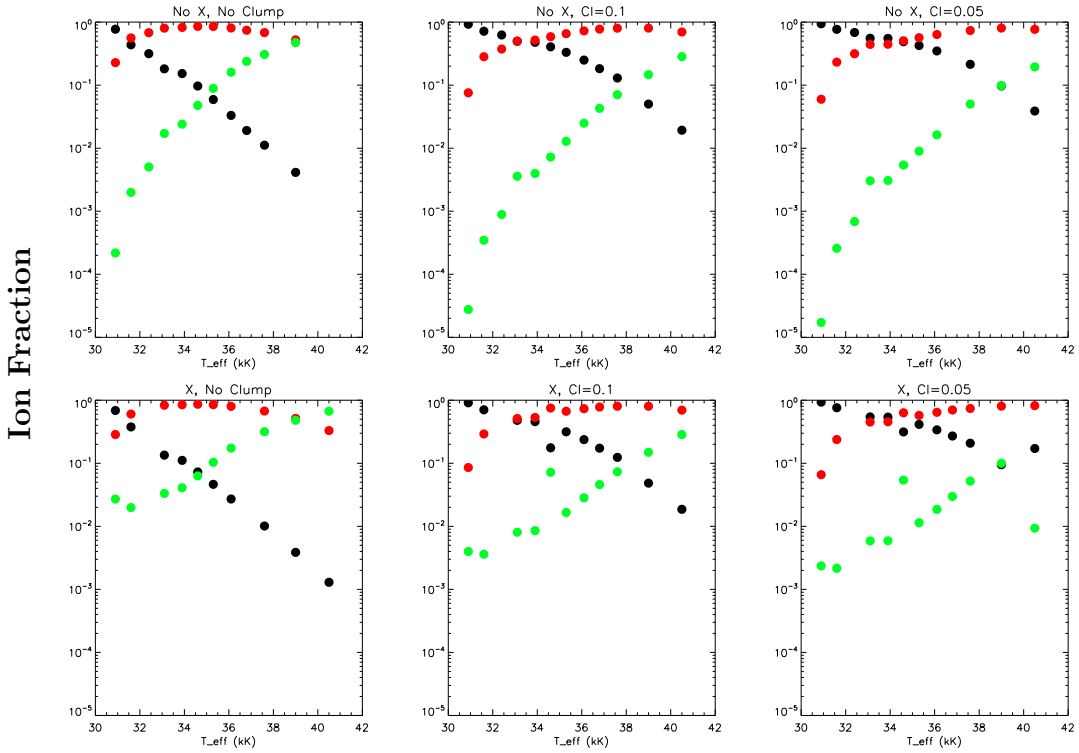


Å). This provides an opportunity to study mass-loss quite extensively in the wind of O stars, since these three stages account for almost all the sulphur in some models. The only model where another stage has a significant contribution is the unclumped X-ray model, and since it is believed by many authors that supergiant winds are at least moderately clumped we might wish to rule this out. It certainly makes the question of how strongly supergiant winds are clumped an important one. Chapter 6 will deal with sulphur spectral line diagnostics in depth.

- **Silicon** - As seen in Figure 4.11, the dominant ion stage of silicon for much of the O star range is $Si^{4+}$, with $Si^{3+}$ taking over at lower temperatures for all the clumped models. Qualitatively this has a concurrent trend with the increase in strength of the SiIV profile with decreasing effective stellar temperature. There is little difference between X-ray and non-X-ray models where the clumped scenarios are concerned, and in the unclumped models, X-rays cause a decline in the proportion of $Si^{4+}$ over the O star range. In some of the plots it is clear that the ion fractions in the models do not sum to unity, meaning that a significant ion has not been included, most likely

**Figure 4.9.** Supergiant ion fractions for sulphur. Black = $S^{3+}$, red = $S^{4+}$, green = $S^{5+}$, blue = $S^{6+}$. 'X' stands for X-rays and 'Cl' for clumping factor.

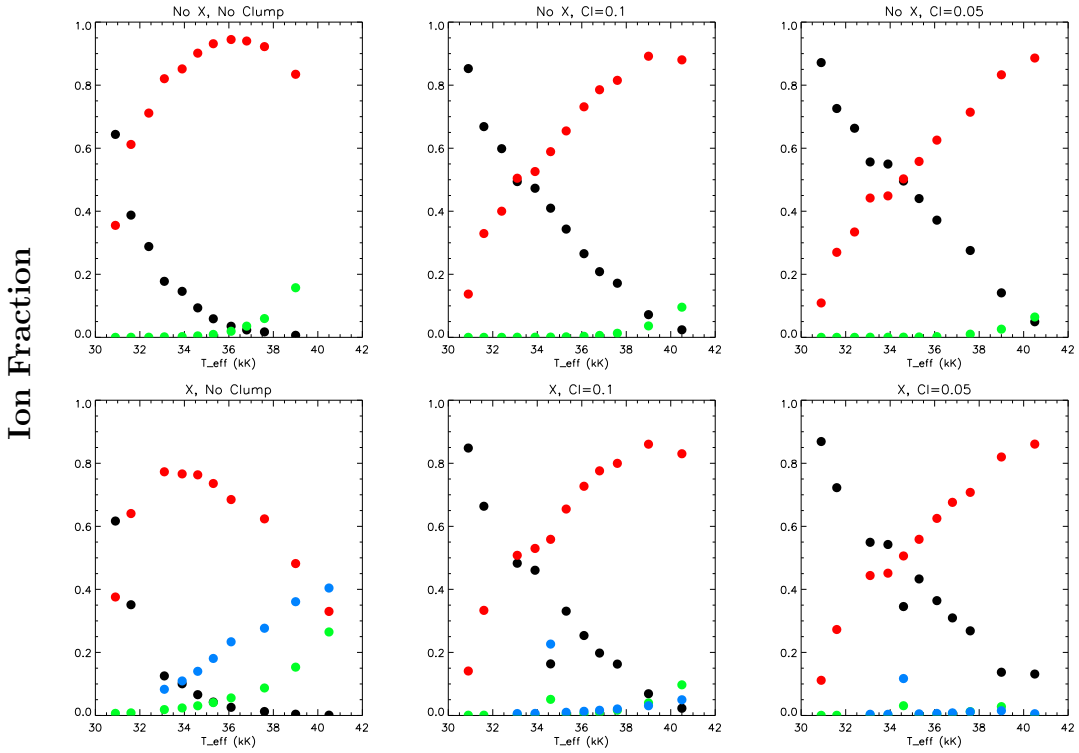


$Si^{5+}$. This is deduced since the unclumped X-ray models ought to show the transfer in population from one stage to another as extra ionization occurs, and so it must be a higher stage that is missing. The NIST Atomic Spectra Database (Ralchenko 2005) shows there to be a large number of transitions in the UV and FUV that correspond to $Si^{5+}$, although it is unlikely to be seen in the wind, the relatively good agreement in the spectra of current models suggests that the effect on spectra will not be great. The effect of adding extra X-rays seems to have a more limited effect than for other elements, and this is borne out in the changes in profiles from model to model as discussed in the previous chapter.

### 4.2.2 Dwarfs

Since the grid's parameter space could not be adequately filled for the strongly clumped scenario, only the unclumped and moderately clumped ion fractions are shown and discussed in the case of O dwarf stars. Since we see in supergiants that the difference between ion fractions for the moderately and strongly clumped cases is small, it is likely that we

**Figure 4.10.** Supergiant ion fractions in log space for sulphur. Black = $S^{3+}$, red = $S^{4+}$, green = $S^{5+}$, blue = $S^{6+}$. 'X' stands for X-rays and 'Cl' for clumping factor.

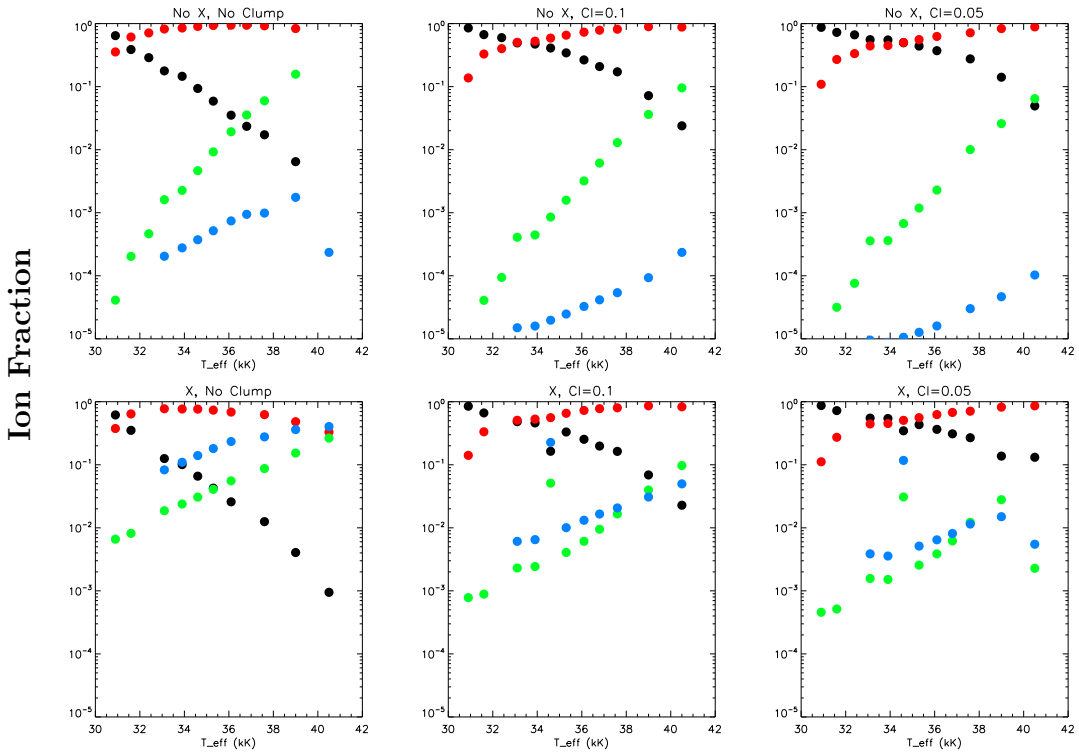


don't lose out on much information in doing this.

- **Carbon** - In Figure 4.13, a familiar pattern is seen for the non-X-ray model ion fractions; for the unclumped case $C^{3+}$ is dominant up to 35kK at which point the balance shifts in favour of $C^{4+}$. For the clumped case this shift occurs at a higher temperature; about 39-40 kK. In addition it appears that through the interplay of recombination and photoionization the fraction of $C^{2+}$ is increased by clumping at the cooler end. When X-rays are present the picture in the cooler half of the plot changes completely. $C^{4+}$ is dominant for the entire O star range, whilst $C^{3+}$ never achieves a fraction greater than about 0.3. There is a suggestion of a peak in $C^{3+}$ at around 34-35 kK, which could mislead efforts to derive $\dot{M}$ in empirical investigations (see Chapter 5), since a peak in $\dot{M}\langle q_i \rangle$ is often assumed to be due to a very dominant ion fraction (e.g. Fullerton et al. 2006). If clumping is introduced then it becomes unclear whether any ion is dominant for a portion of the temperature range. The jagged appearance of the trend could be down to the slightly different 'observed' X-ray luminosities in the models. Although they are all within the range allowed

**Figure 4.11.** Supergiant ion fractions for silicon. Black = $Si^{2+}$, red = $Si^{3+}$, green = $Si^{4+}$. 'X' stands for X-rays and 'Cl' for clumping factor.

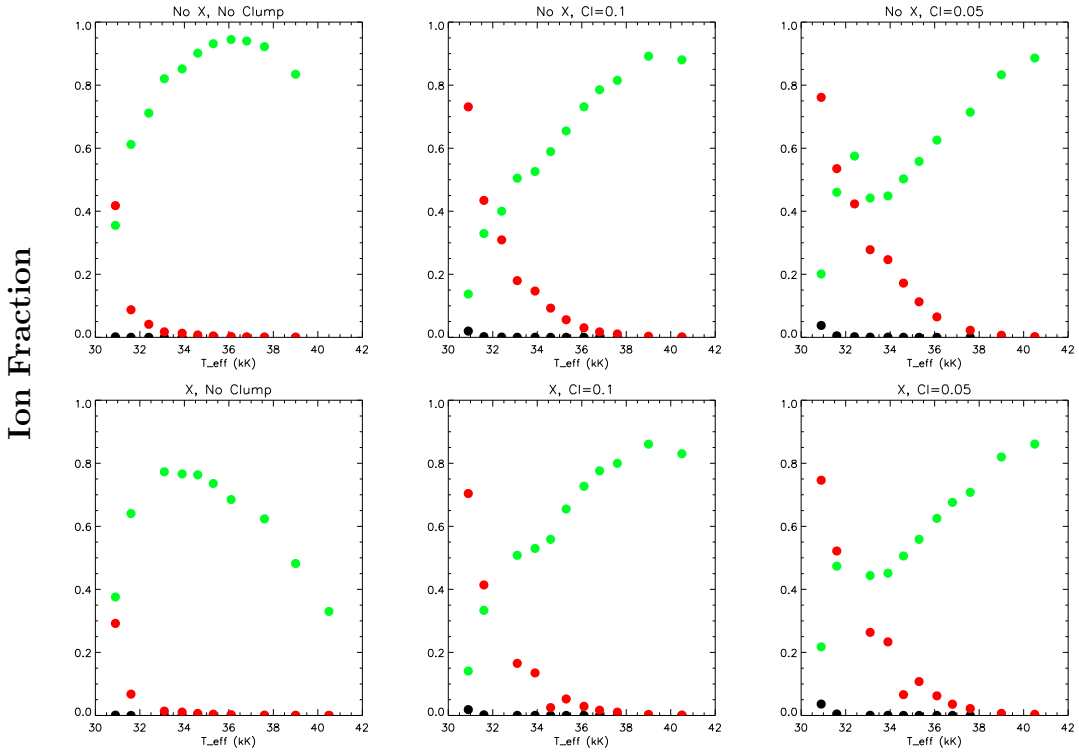


by observations, they differ somewhat due to the ad hoc way in which X-rays are introduced in CMFGEN. The general differences seen between the models with and without X-rays seem to suggest that they are a much more important factor for later type O dwarf stars than for other O stars. Figure 4.14 highlights the effects on $C^{2+}$. X-rays have a stronger effect at lower temperatures, which is consistent with what is observed for the other ions. In the previous chapter CIV profiles were compared for different X-ray strengths at the same spectral type (see Fig. 3.37). In the third panel of that figure we see the difference between 'normal' strength X-rays ($L_X/L_{bol} = 1\times10^{-7}$) and 'strong' X-rays ($L_X/L_{bol} = 4\times10^{-7}$). The latter is actually just within the range which is observed in O stars and yet it reduces $q_{C^{3+}}$ from 0.27 to 0.085, increasing $q_{C^{4+}}$ from 0.73 to 0.92. This is quite a difference considering both are feasible levels of X-rays to be observed. Since the latter produces the more realistic line profile we perhaps must favour a lower ion fraction corresponding to CIV.

**Figure 4.12.** Supergiant ion fractions in log space for silicon. Black = $Si^{2+}$, red = $Si^{3+}$, green = $Si^{4+}$. 'X' stands for X-rays and 'Cl' for clumping factor.

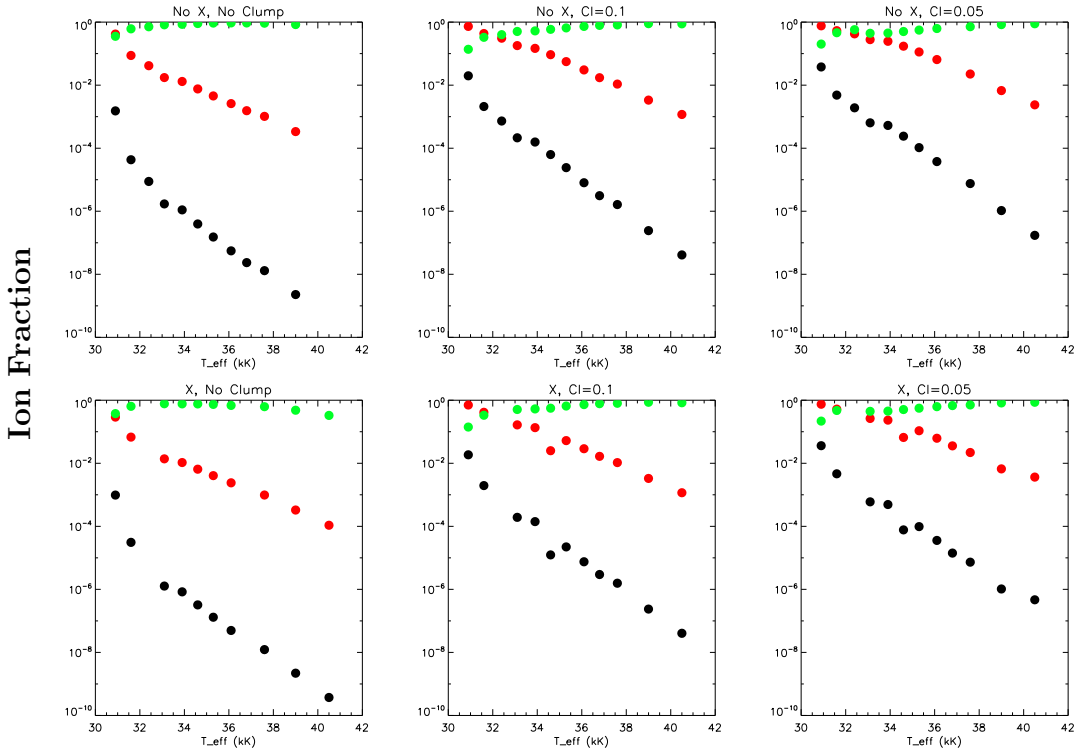


- **Nitrogen** - Shown in Figure 4.15, $N^{3+}$ is the dominant form of nitrogen for most of the O star range in the unclumped, non-X-ray models, and for the whole range in the clumped version without X-rays. Again this is expected due to recombination effects. The situation when X-rays are implemented is more complex than other elements thus far. A general trend in the unclumped model can be seen, with $N^{5+}$ gradually declining with temperature, and $N^{3+}$ and $N^{4+}$ roughly increasing. However the trend lines are not smooth; the ion fractions seem to be very sensitive to the input of X-rays. This can be seen approximately in the values of $L_X$ seen for the individual models; when a point in the ion fraction plot seems out of place the corresponding X-ray luminosity is also slightly further from $10^{-7}$, although still within allowed values observationally. This fits with the NV profiles seen in the previous chapter which show a strong dependency on the X-rays. If both model NV profiles and model N ion fractions are strongly dependent on X-rays then it is fair to assume that at a single spectral type (i.e. effective temperature range) one can expect to see a range of strengths of NV profiles in observed spectra which is due to both mass-loss rate *and* X-ray ionization. The clumped X-ray models seem to return to the level of the

**Figure 4.13.** Dwarf ion fractions for carbon. Black = $C^{2+}$, red = $C^{3+}$, green = $C^{4+}$. 'X' stands for X-rays and 'Cl' for clumping factor.

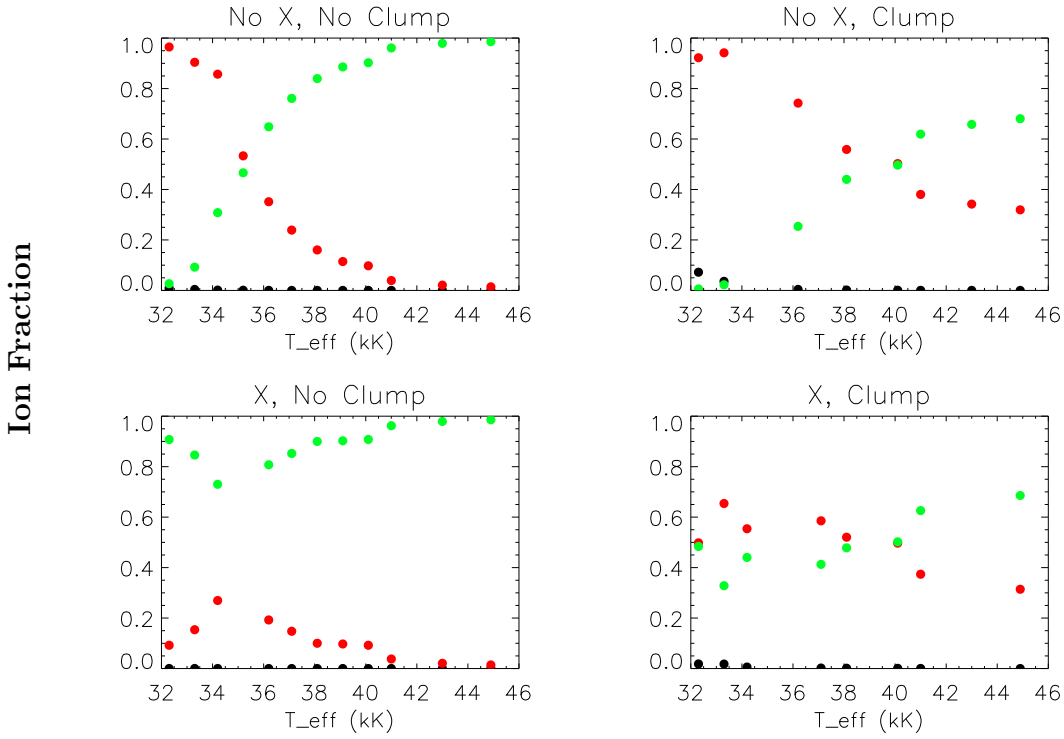


non-X-ray case at higher temperatures, but again there is a definite effect seen at lower temperatures, adding evidence to the idea that the winds of later type O stars react more strongly to X-rays than do those of earlier type. The plots with log scale (Fig. 4.16) show the great effect of X-rays across the temperature range though, with a gain of up to six orders of magnitude for $N^{5+}$ at some temperatures, and of four orders of magnitude for $N^{4+}$. Overall the biggest boosts in ion fraction occur at the lower temperature end.

- **Oxygen** - in many ways the ion fraction plots for oxygen (Fig. 4.17) echo those of nitrogen for O dwarfs. In the unclumped non-X-ray case $O^{3+}$ is dominant from lower temperatures until around 43kK, where $O^{4+}$ takes over. Clumping has the usual effect, reducing $O^{3+}$ at lower temperatures and increasing it at higher ones. X-rays have a very obvious effect in the unclumped case, with clear superionization causing an increase in $O^{4+}$ and even leading to a significant presence of both $O^{5+}$ and $O^{6+}$. The rather jagged nature of the traces with temperature again indicates the sensitivity of oxygen ions to X-rays. In the clumping scenario we see the main

**Figure 4.14.** Dwarf ion fractions in log space for carbon. Black = $C^{2+}$, red = $C^{3+}$, green = $C^{4+}$. 'X' stands for X-rays and 'Cl' for clumping factor.

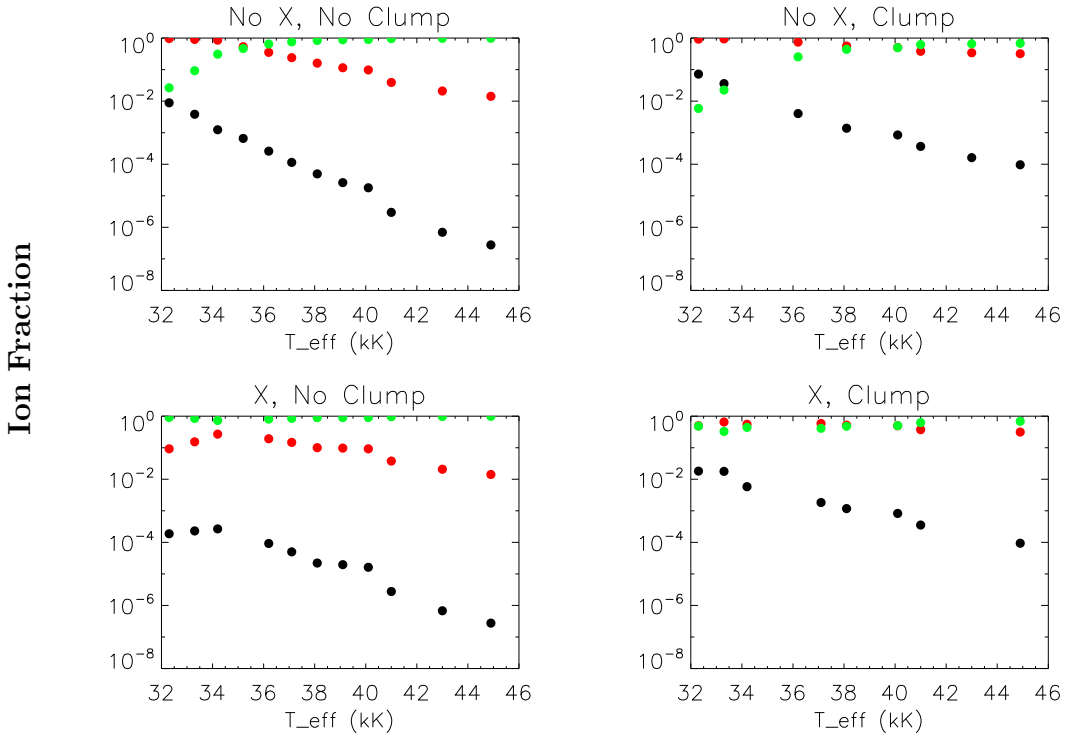


changes from non-X-ray models at lower temperatures again. The implication is that the size of OVI profiles and the fractions of O ions are rather sensitive to X-rays, the former not being simply a function of mass-loss and luminosity. The log-scale plot (Fig. 4.18) shows how easily the fraction of $O^{2+}$ is raised by just moderate clumping. When X-rays are switched on, clumping raises this quantity by 2 or 3 orders of magnitude at the expense of the higher stages.

- **Phosphorus** - The clump and X-ray free models show $P^{4+}$ to be dominant at lower temperatures, switching to $P^{5+}$ at around 36kK (Fig. 4.19). Clumping has the same effects in the crossing points between ions as with other elements, where the balance of recombination and photoionization changes as the local density changes. In this case it is the change in dominance from $P^{4+}$ to $P^{5+}$ that moves to higher effective temperatures. When comparing the non-X-ray models to those with X-rays, we see a situation where $P^{5+}$ remains dominant for the whole O star range if there is a smooth wind, but $P^{4+}$ is dominant for most of the temperature range if there is moderate clumping. This makes it very important to correctly determine

**Figure 4.15.** Dwarf ion fractions for nitrogen. Black = $N^{3+}$, red = $N^{4+}$, green = $N^{5+}$. 'X' stands for X-rays and 'Cl' for clumping factor.

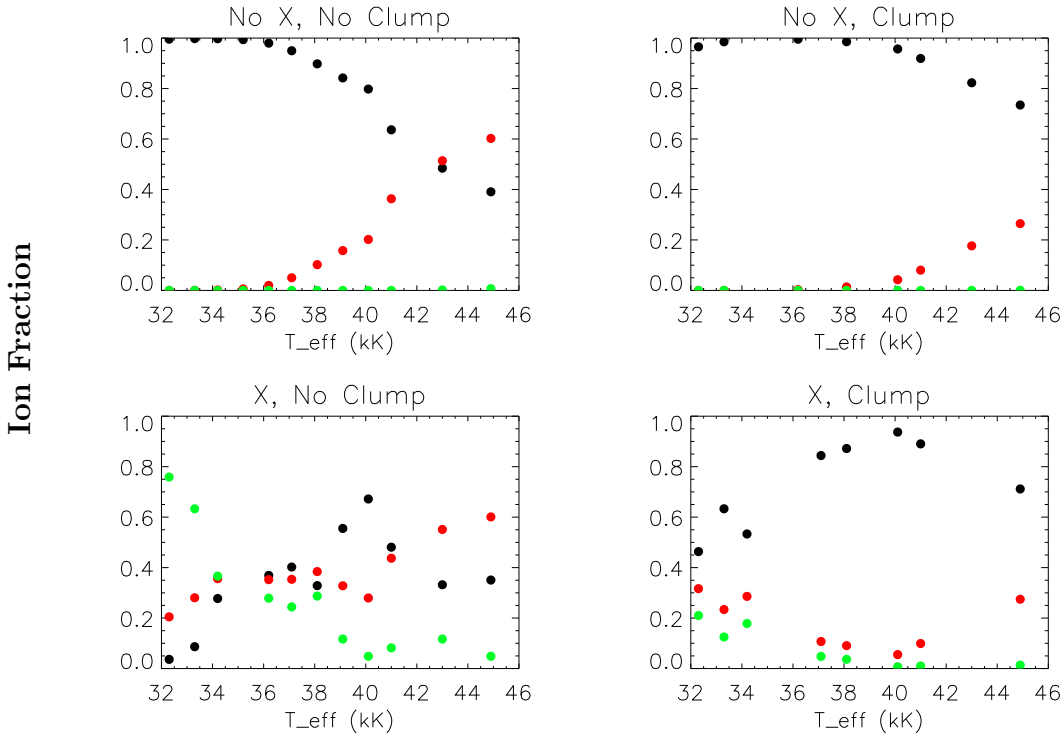


the clumping scenario if phosphorus lines are to be used for empirical mass-loss determination, which is feasible for early type dwarfs. The log plots (Fig. 4.20) show the effects of X-rays and clumping on $P^{3+}$ in particular. Again, X-rays have the greatest effect of reducing this ion at lower temperatures, and clumping increases by a couple of orders of magnitude at some temperatures.

- **Sulphur** - The situation is simple for the non-X-ray models (Fig. 4.21). Unclumped winds are expected to have $S^{4+}$ as the dominant ion up until about 41kK whereupon $S^{5+}$ takes over. Moderate clumping causes $S^{4+}$ to be dominant for the full temperature span. X-rays cause a significant fraction of $S^{6+}$ to be formed, both in smooth and clumped winds. This ion is predicted to be dominant for the later type O stars if there are X-rays, with $S^{5+}$ taking over if the wind is smooth or $S^{4+}$ if it is not. Again we see the ionization balance completely altered by the presence of X-rays, in a way that is much stronger than in supergiants. The log plots show this especially (Fig. 4.22), where $S^{6+}$ is promoted to the ion with the highest population at some

**Figure 4.16.** Dwarf ion fractions in log space for nitrogen. Black = $N^{3+}$, red = $N^{4+}$, green = $N^{5+}$. 'X' stands for X-rays and 'Cl' for clumping factor.

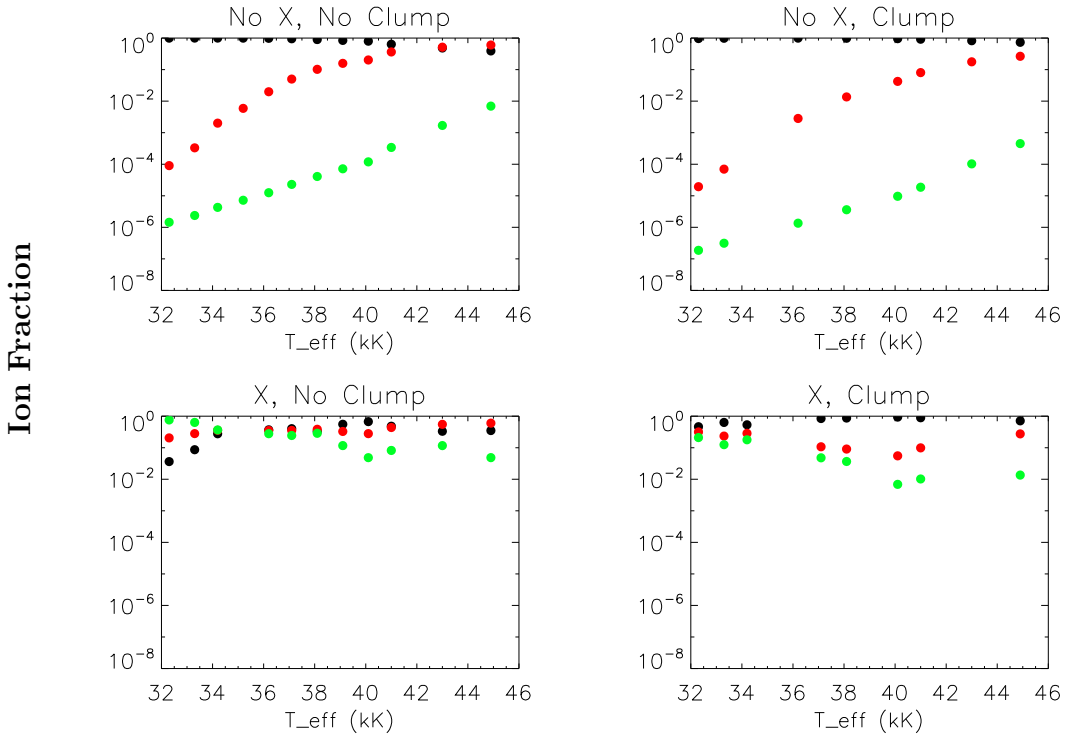


temperatures. The strongest effects are seen at lower temperatures for all ions.[1]

- **Silicon** - this provides us with the simplest situation of all, as can be seen in Figure 4.23, in which $Si^{4+}$ is predicted to account for almost 100% of the element at all temperatures and in all X-ray and clumping scenarios. In this case a log plot would be superfluous and so is omitted.

## 4.3 Chapter conclusions: the effects of clumping and X-rays

Tables 4.1, 4.2, 4.4 and 4.5 summarise the ranges of dominance for each ion that is dominant at some temperature range, in some scenario. Dominance is given in two categories; greater than 50%, and greater than 75% of the elemental total. The second category is a more stringent test of dominance, and from this we can determine with confidence which ion we expect to be dominant, regardless of the clumping and X-ray scenario employed.

[1] Unfortunately, the $S^{6+}$ ion fractions could not be retrieved from the non-X-ray models because the relevant files were lost in an upgrade of the UCL Legion cluster, and could not be derived again without a complete and time-consuming re-compilation of CMFGEN. We can certainly say it is not dominant in these models since the other ions total to very nearly unity.

**Figure 4.17.** Dwarf ion fractions for oxygen. Black = $O^{2+}$, red = $O^{3+}$, green = $O^{4+}$, blue = $O^{5+}$, yellow = $O^{6+}$. 'X' stands for X-rays and 'Cl' for clumping factor.

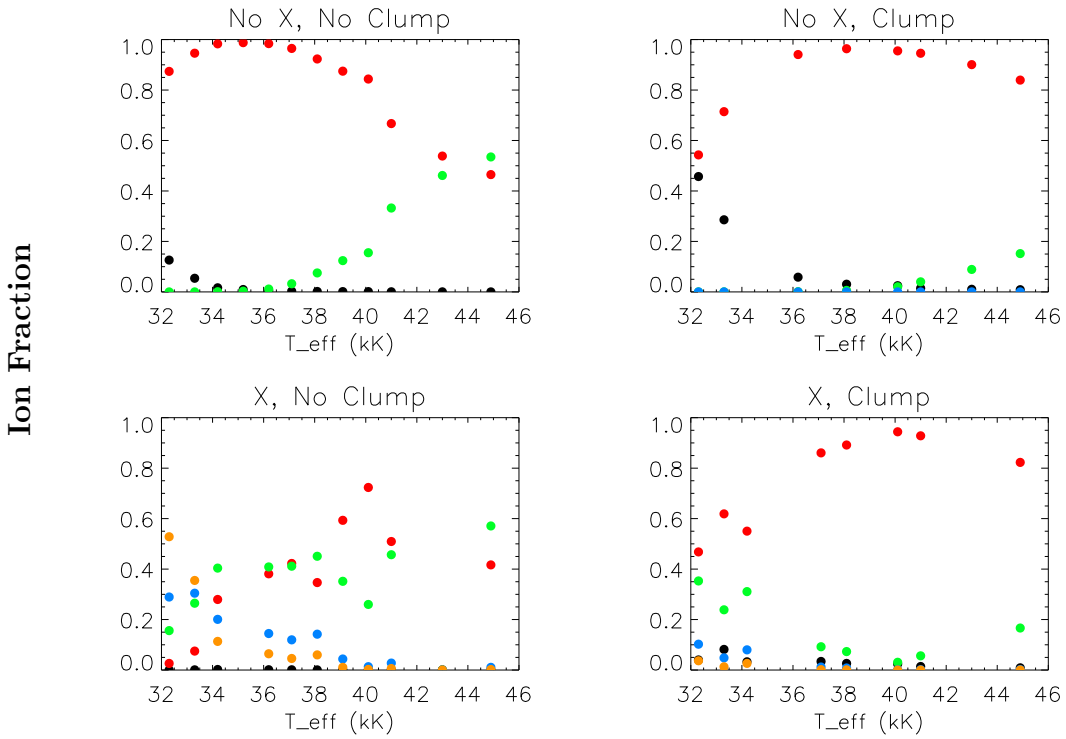


Table 4.3 is a further summary of the range over which an ion accounts for more than 0.75 of the total for *all* scenarios. No version of Table 4.3 is given for dwarfs; there is only one ion under investigation that remains dominant regardless of scenario - $Si^{4+}$ - which is dominant for the whole temperature range for every clumping and X-ray scenario.

Martins et al. (2005*b*) show how X-rays alter the carbon ionization structure with radius, and show that they make the difference between CIV and CV being dominant in the wind. That paper also shows the estimated ion fractions derived from CMFGEN models of CIV for clumped models, and the general trend across the O star range is qualitatively in keeping with that derived here. Bouret et al. (2005) show how O and P ion fractions vary radially, and show that PVI converts to PV with clumping, whilst OV appears to give way to OIV. This second paper does not offer any direct comparison to a scale with $T_{eff}$.

**Figure 4.18.** Dwarf ion fractions in log space for oxygen. Black = $O^{2+}$, red = $O^{3+}$, green = $O^{4+}$, blue = $O^{5+}$, yellow = $O^{6+}$. 'X' stands for X-rays and 'Cl' for clumping factor.

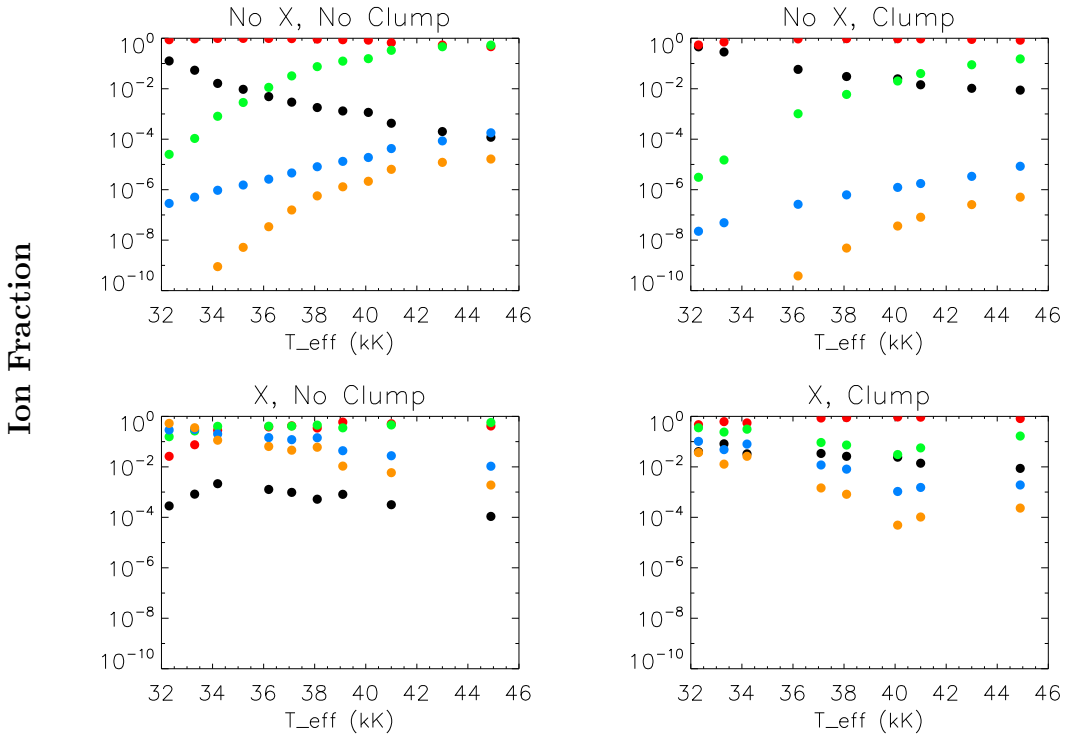

**Figure 4.19.** Dwarf ion fractions for phosphorus. Black = $P^{3+}$, red = $P^{4+}$, green = $P^{5+}$. 'X' stands for X-rays and 'Cl' for clumping factor.

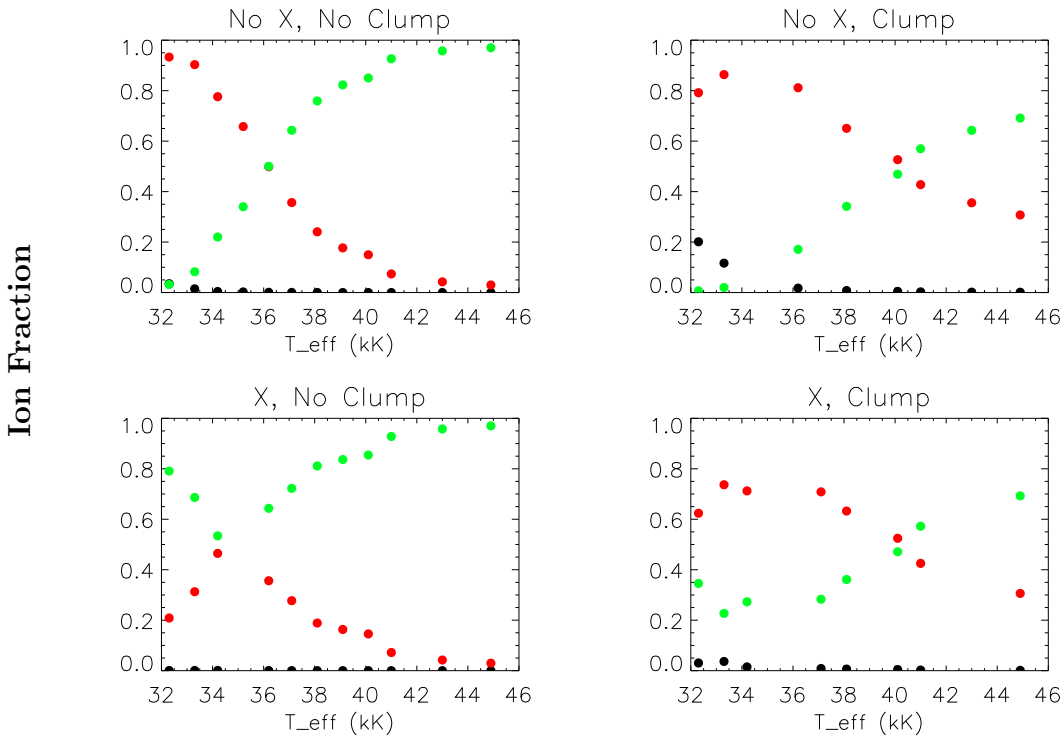

**Figure 4.20.** Dwarf ion fractions in log space for phosphorus. Black = $P^{3+}$, red = $P^{4+}$, green = $P^{5+}$. 'X' stands for X-rays and 'Cl' for clumping factor.

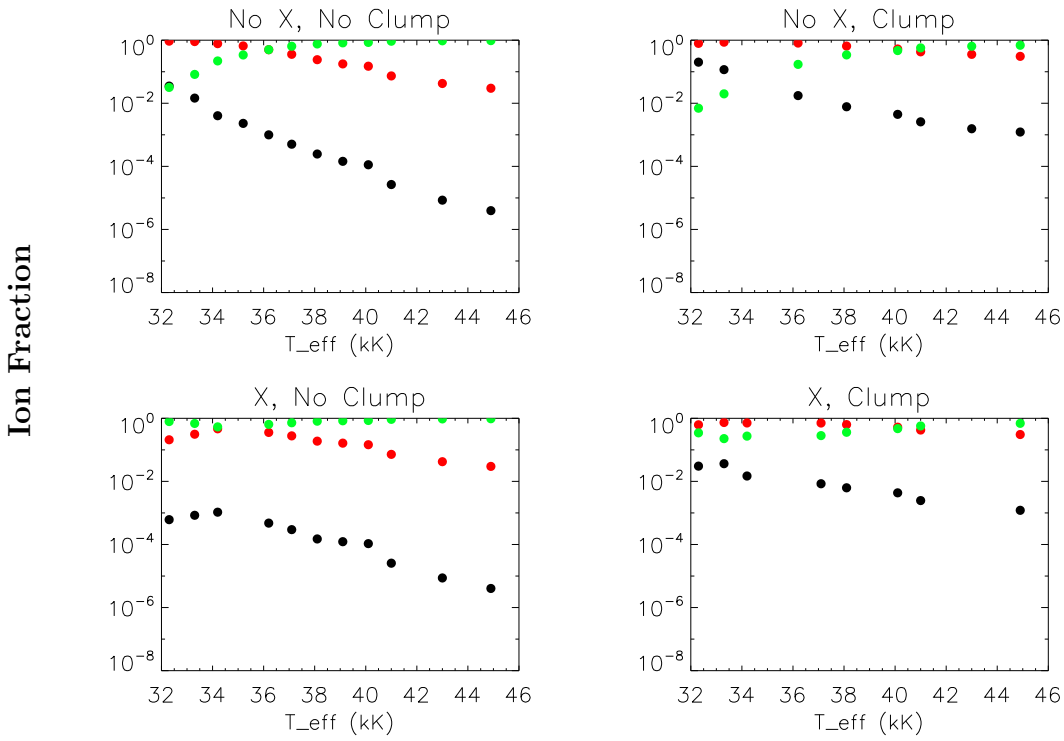

**Figure 4.21.** Dwarf ion fractions for sulphur. Black = $S^{3+}$, red = $S^{4+}$, green = $S^{5+}$, blue = $S^{6+}$. 'X' stands for X-rays and 'Cl' for clumping factor.

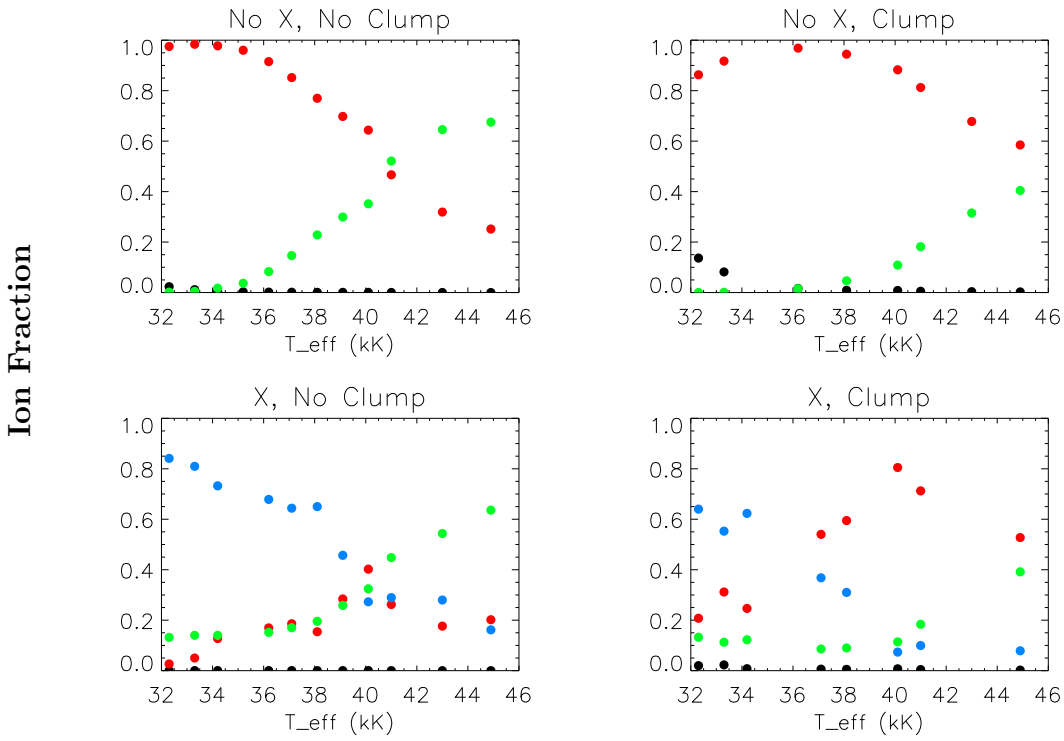

**Figure 4.22.** Dwarf ion fractions in log space for sulphur. Black = $S^{3+}$, red = $S^{4+}$, green = $S^{5+}$, blue = $S^{6+}$. 'X' stands for X-rays and 'Cl' for clumping factor.

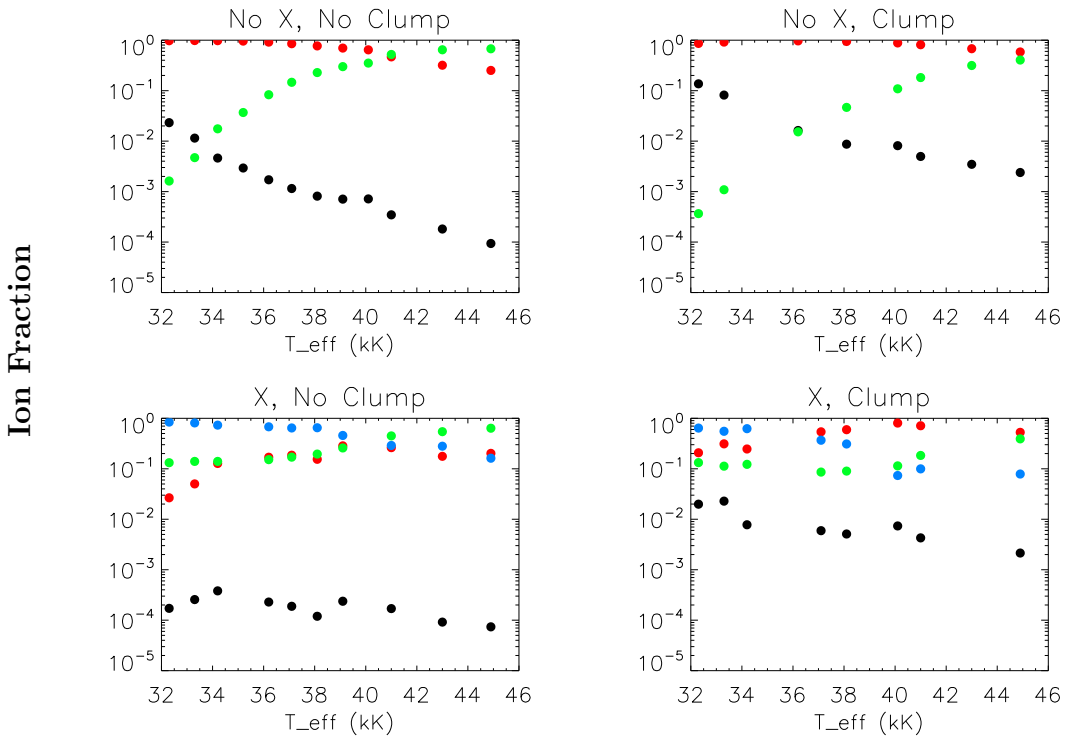

**Figure 4.23.** Dwarf ion fractions for silicon. Black = $Si^{2+}$, red = $Si^{3+}$, green = $Si^{4+}$. 'X' stands for X-rays and 'Cl' for clumping factor.

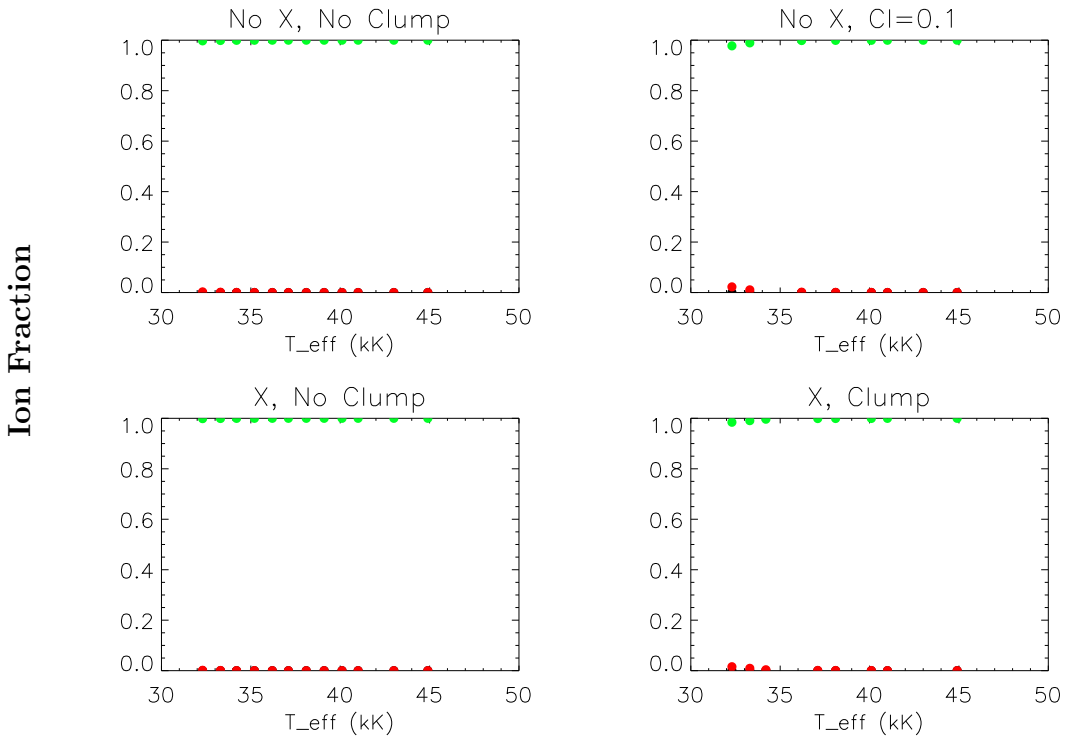

**Table 4.1.** Dominant ions in Supergiants for C, N and O

| Ion | Scenario | Dominant range (≥50%) | Dominant range (≥75%) |
|---|---|---|---|
| $C^{2+}$ | No X, No C | 30-31kK | - |
| | No X, C | 30-31.5kK | 30-31kK |
| | X, No C | - | - |
| | X, C | 30-31.5kK | 30-31kK |
| $C^{3+}$ | No X, No C | 31-40kK | 31.5-37.5kK |
| | No X, C | 31.5-42kK | 34-41kK |
| | X, No C | 31-39kK | 32-36.5kK |
| | X, C | 32-42kK | 34-41kK |
| $C^{4+}$ | No X, No C | - | - |
| | No X, C | - | - |
| | X, No C | 39-42kK | - |
| | X, C | - | - |
| $N^{2+}$ | No X, No C | 30-31kK | - |
| | No X, C | 30-31.5kK | 30-30.5kK |
| | X, No C | - | - |
| | X, C | 30-31.5kK | 30-30.5kK |
| $N^{3+}$ | No X, No C | 31-40kK | 31-42kK |
| | No X, C | 31.5-42kK | 33-42kK |
| | X, No C | 30.5-42kK | 31.5-39kK |
| | X, C | 31.5-42kK | 33-42kK |
| $O^{2+}$ | No X, No C | 30-32kK | 30-31kK |
| | No X, C | 30-35kK | 30-33kK |
| | X, No C | 30-32kK | 30-31kK |
| | X, C | 30-34.5kK | 30-32.5kK |
| $O^{3+}$ | No X, No C | 32-42kK | 35-42kK |
| | No X, C | 35-42kK | 38-42kK |
| | X, No C | 32-42kK | 35-39kK |
| | X, C | 34.5-42kK | 38-42kK |

**Table 4.2.** Dominant ions in Supergiants for P, S and Si

| Ion | Scenario | Dominant range (≥50%) | Dominant range (≥75%) |
|---|---|---|---|
| $P^{3+}$ | No X, No C | 30-31kK | 30-30.5kK |
| | No X, C | 30-33kK | 30-31kK |
| | X, No C | 30-31.5kK | 30-30.5kK |
| | X, C | 30-33kK | 30-31kK |
| $P^{4+}$ | No X, No C | 31-39kK | 33-36kK |
| | No X, C | 33.5-42kK | 36-39kK |
| | X, No C | 31.5-39kK | 32.5-37kK |
| | X, C | 33.5-42kK | 36.5-39kK |
| $P^{5+}$ | No X, No C | - | - |
| | No X, C | - | - |
| | X, No C | 39.5-42kK | - |
| | X, C | - | - |
| $S^{3+}$ | No X, No C | 30-31.5kK | - |
| | No X, C | 30-33kK | 30-31kK |
| | X, No C | 30-31kK | - |
| | X, C | 30-33kK | 30-31kK |
| $S^{4+}$ | No X, No C | 31.5-42kK | 33-39kK |
| | No X, C | 33-42kK | 36.5-42kK |
| | X, No C | 31-38.5kK | 33-35kK |
| | X, C | 33-42kK | 37-42kK |
| $Si^{3+}$ | No X, No C | - | - |
| | No X, C | 30-31kK | 30-30.5kK |
| | X, No C | - | - |
| | X, C | 30-32kK | - |
| $Si^{4+}$ | No X, No C | 31-42kK | 33-39kK |
| | No X, C | 34-42kK | 36-42kK |
| | X, No C | 31.5-38.5kK | 33-35kK |
| | X, C | 33-42kK | 36-42kK |

**Table 4.3.** Dominant ions in Supergiants, regardless of scenario. Ions are only included if their fraction is greater than 75% for all clumping and X-ray scenarios for some temperature range.

| Ion | Dominant range |
|---|---|
| $C^{3+}$ | 34-36.5kK |
| $N^{3+}$ | 33-39kK |
| $O^{2+}$ | 30-31kK |
| $O^{3+}$ | 38-39kK |
| $P^{3+}$ | 30-30.5kK |

**Table 4.4.** Dominant ions in Dwarfs for C, N and O. $O^{6+}$ shows dominance in the unclumped X-ray scenario at $\sim$ 32kK but is not included in this table.

| Ion | Scenario | Dominant range ($\geq$50%) | Dominant range ($\geq$75%) |
|---|---|---|---|
| $C^{3+}$ | No X, No C | 32-35kK | 32-34kK |
| | No X, C | 32-38kK | 32-36kK |
| | X, No C | - | - |
| | X, C | 32-39kK | - |
| $C^{4+}$ | No X, No C | 36-46kK | 37-46kK |
| | No X, C | 41-46kK | - |
| | X, No C | 32-46kK | 32-46kK |
| | X, C | 40-46kK | - |
| $N^{3+}$ | No X, No C | 32-42kK | 32-40kK |
| | No X, C | 32-46kK | 32-45kK |
| | X, No C | $\sim$ 40kK | - |
| | X, C | 33-46kK | 37-42kK |
| $N^{4+}$ | No X, No C | 43-46kK | - |
| | No X, C | - | - |
| | X, No C | 42-46kK | - |
| | X, C | - | - |
| $N^{5+}$ | No X, No C | - | - |
| | No X, C | - | - |
| | X, No C | 32-33kK | $\sim$ 32kK |
| | X, C | - | - |
| $O^{3+}$ | No X, No C | 32-44kK | 32-40kK |
| | No X, C | 32-46kK | 35-46kK |
| | X, No C | $\sim$ 40kK | - |
| | X, C | 33-46kK | 36-46kK |
| $O^{4+}$ | No X, No C | 45-46kK | - |
| | No X, C | - | - |
| | X, No C | 43-46kK | - |
| | X, C | - | - |

**Table 4.5.** Dominant ions in Dwarfs for P, S and Si

| Ion | Scenario | Dominant range (≥50%) | Dominant range (≥75%) |
|---|---|---|---|
| $P^{4+}$ | No X, No C | 32-35kK | 32-34kK |
| | No X, C | 32-40kK | 32-36kK |
| | X, No C | - | - |
| | X, C | 32-40kK | - |
| $P^{5+}$ | No X, No C | 37-46kK | 38-46kK |
| | No X, C | 41-46kK | - |
| | X, No C | 32-46kK | 32kK, 38-46kK |
| | X, C | 41-46kK | - |
| $S^{4+}$ | No X, No C | 32-40kK | 32-38kK |
| | No X, C | 32-46kK | 32-41kK |
| | X, No C | - | - |
| | X, C | 37-46kK | ∼40kK |
| $S^{5+}$ | No X, No C | 41-46kK | - |
| | No X, C | - | - |
| | X, No C | 42-46kK | - |
| | X, C | - | - |
| $S^{6+}$ | No X, No C | - | - |
| | No X, C | - | - |
| | X, No C | 32-28kK | 32-33kK |
| | X, C | 32-34kK | - |
| $Si^{4+}$ | No X, No C | 32-42kK | 32-42kK |
| | No X, C | 32-42kK | 32-42kK |
| | X, No C | 32-42kK | 32-42kK |
| | X, C | 32-42kK | 32-42kK |

The main purpose of this chapter has been to present the ion fractions of C, N, O, S, P and Si from the grid of O stars described in previous chapters, highlighting the specific effects of X-rays and micro-clumping. We see clearly that the injection of X-rays shifts populations to higher stages. The details of this effect are important to consider when implementing X-rays in stellar atmosphere models. There are also some more subtle effects that have been seen in the data. It has been learned that

- Clumping appears to shift the ion balance in dwarfs more than for supergiants
- X-rays affect the low temperature end of the dwarf scale more than at the high temperature end
- When clumping is at a very low level, X-rays affect the balance of ions in dwarfs much more than in supergiants
- Assuming a low level of clumping with X-rays (suggested as possible in the previous chapter), $S^{6+}$ is unexpectedly significant in hotter supergiants.
- $P^{4+}$ is dominant (>50%) in supergiants over a similar temperature range to that suggested by previous studies
- In dwarfs, $C^{4+}$ is dominant over the whole O star range if clumping is low, but $C^{3+}$ has a non-negligible contribution ($\gtrsim$10%) at low to mid temperatures. This has significance to Chapter 5.
- In dwarfs, the fractions of carbon ions in later types can vary a lot between two models with different but observationally permitted X-ray levels.

Clumping has a somewhat stronger effect on the ion balance in dwarfs than in supergiants; the crossing point where dominance shifts from one ion to another is shifted by a larger amount in dwarfs, typically by a few kK, as opposed to just 1000K or so in supergiants. In non-X-ray models there is a clear shift in most ions at the higher and lower temperature end as recombination enhancement causes populations to change. In supergiants, where the grid parameters are well populated enough to include both moderate and strong clumping, it seems that moderate clumping is enough to have a noticeable effect on the ion balance, but there is not much further effect seen by adding more clumping.

There are only a few ions for the supergiant models that can be said with very great certainty to be dominant in all cases, although this is partly down to the rather stringent

condition that the ions be above a fraction of 0.75. We see other patterns emerge if requiring only that the fraction be greater than 0.5; we see that $C^{3+}$, $N^{3+}$, $O^{3+}$, $P^{4+}$, $S^{4+}$ and $Si^{4+}$ are all dominant for some subset of O stars. The assertion that the $P^{4+}$ ion is dominant for some O stars by Fullerton et al. (2006) is consistent with the results here. That investigation claims the ion to be dominant for either O4-7 or O7-9.7 stars depending on whether theory or empirical estimators are used. In the current investigation, since we believe the winds of these objects to be in some way clumped (very mildly clumped according to Chapter 3), and we observe X-rays acting in the winds, we should perhaps favour the models that include both effects. In this case $P^{4+}$ accounts for more than half the phosphorus in O3-O8 supergiants, or roughly O4-O6 supergiants if the more stringent test is used. This is entirely compatible with the Fullerton study. If the clumping is weak enough that the ion fractions are more similar to the unclumped models here, then the range over which $P^{4+}$ is dominant in supergiants is 32.5-37kK, or spectral types O5.5-8.5.

A fundamental caveat to all this is that CMFGEN does not treat porosity (a la Oskinova et al. 2007) nor does it include the general effects of optically thick clumping discussed in Sundqvist et al. (2010). The latter authors claim that only moderate clumping factors are needed to reduce the strength of PV profiles for supergiants. Optically thick clumps would presumably change the ion balance in some way since the effect shields some material from radiation, and so it would remain at a lower ion stage. It is possible that this effect, combined with recombination from enhanced density that comes from any kind of clumping, would leave electrons lying in lower states than in the pure micro-clumping approach.

CMFGEN does not account for possible effects of XUV emission, that Waldron & Cassinelli (2010) claim reduces $q$(PV) significantly. That study also claims there is minimal effect on $q$(SV) from XUV radiation, due to the unique energy distribution of XUV lines - the strong collection of XUV lines that lie around the PV/VI ionization edge lie just *short* of the SV/VI ionization edge. This claim implies that if $S^{4+}$ is found to be dominant it is a real dominance that cannot be altered by XUV effects.

The next steps from here are to apply what has been learned from the way spectra and ion fractions respond to clumping and X-rays. Two such applications are described in the next two chapters; a study of the CIV profiles of O dwarfs, and of sulphur profiles in O supergiants.

This page is intentionally left almost blank

# Chapter 5

# Mass-loss and ionization conditions in the weak-wind regime

*'A great wind is blowing, and that gives you either imagination or a headache. '*

Catherine the Great

In this chapter, the focus turns to the study of weak winds in O stars, accomplished by examining UV line profiles empirically. This is a shift from the approach adopted thus far in this thesis work of using model atmosphere calculations. There are a few reasons for this change: firstly the UV profiles one sees in weak-wind objects are generally full of substructure that is wiped out by the saturation of profiles in say supergiants. CMFGEN is not able to match all this substructure whereas empirical techniques can account for the change in the local optical depth as a function of velocity and hence follow any Narrow Absorption Components (NACs) or other profile sub-troughs. Additionally an empirical estimate of the mass-loss conditions is useful as a check on what model atmospheres predict. It was seen in Chapter 3 that the shape of the CIV resonance doublet is difficult to predict in later type O stars and hence it is highly desirable to have such an outside check. As described in the introduction chapter, there is a discordance

between different spectroscopic mass-loss diagnostics in O supergiants, and very low rates of mass-loss predicted by NLTE modelling in O dwarfs. There is not yet a definitive answer to precisely how low the mass-loss rates in late-type O dwarfs are. We need to understand exactly what the ionization conditions of the winds are, and how ion fraction estimates affect the determination of mass-loss rates. The motivation for wanting this understanding comes from various quarters. The current theory of line-driven winds, described in Chapter 1, does not account for the low wind-momenta estimated for late O dwarfs, and so any thorough mass-loss investigation of this object type also constitutes a test of line-driven wind theory. Additionally weak winds in the Galaxy are a useful proxy for the winds that might be expected in a low metallicity environment, and therefore there is even a cosmological dimension to this area of study. Further, both clumped-wind and unclumped-wind scenarios will be employed in this part of the project and thus wind structure will be probed through yet another line of investigation.

What follows is an introduction to empirical modelling of UV resonance lines, a description of the code used to perform that modelling, and an account of a project to fit CIV (1548,1551Å) and NV (1239,1243Å) doublets in order to determine details about mass-loss and wind ionization in weak-wind O dwarfs.

## 5.1 Definition of a weak wind

To say a star has a weak wind is somewhat subjective without some further objective clarification, since any star with a lower mass-loss rate or terminal wind velocity than another has by comparison a weaker wind. In arguably the first study to discover statistically significant cases of mass-loss rates lower than line-driven wind theory predicts, Chlebowski & Garmany (1991) did not define a weak wind per se, rather they pointed out that some wind densities can be lower than predicted. In this investigation, some criteria that have come about since then have been examined to decide which stars to study. Firstly, the mass-loss rate is an obvious way of classifying a weak wind. Martins et al. (2005*b*) begin by stating that a star with an estimated mass-loss less than $10^{-8} M_{\odot} yr^{-1}$ has a weak wind. The authors then go further and suggest that there is some luminosity cut-off ($\sim \log L/L_{\odot} = 5.2$), below which NLTE models are forced to predict far lower mass-loss rates than those of Vink et al. (2000). Using the mass-loss criterion in conjunction with the parameters of the CMFGEN grid for dwarfs, we could term a weak-winded star as

being of spectral type O8.5 V or later. If we choose a luminosity cut-off then instead we are left with stars of type O7 V or later. Perhaps an even better way to decide what counts as a weak-winded star is to re-examine the WLR relationship discussed in Chapter 1, and reproduced in Figure 5.1. The luminosity at which O dwarfs appear to turn downward in normalised wind-density, taking into account all the diagrams from Chapter 1, is around $\sim \log L/L_{\odot} = 5.3$, corresponding in the model grid to a spectral type O6.5 V. For this reason, O dwarfs of this type and later are investigated in this chapter.

**Figure 5.1.** The Wind-momentum Luminosity Relation from Puls et al. (2008), seen also in Chapter 1. O dwarfs are represented by stars.

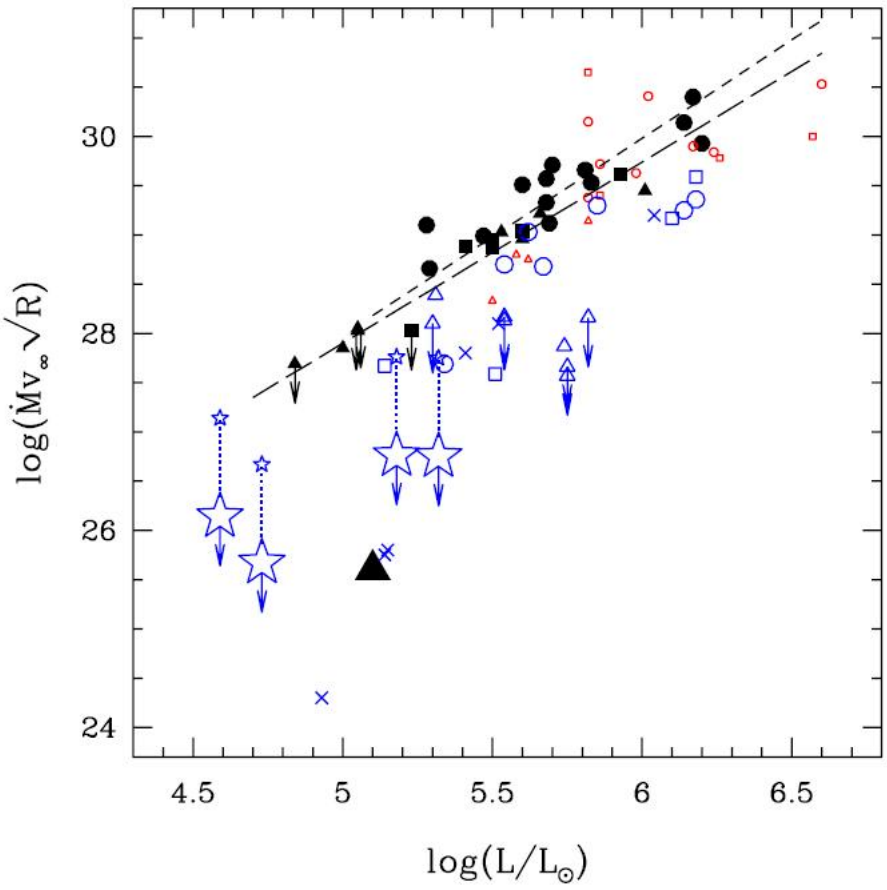


## 5.2 The analysis of ultraviolet resonance lines

P-Cygni profiles formed by resonance scattering contain a wealth of information about stellar winds encoded in their precise size and shape. Resonance scattering is the process

whereby an ion in the ground state absorbs a photon, is photo-excited, and a photon is emitted immediately by a radiative decay of the electron. The new photon has essentially the same energy as the original photon in the rest frame of the scattering ion, but has a new direction. This process happens frequently in a stellar wind because the relatively low density (compared to the star itself, for example) is such that many ions are in the ground state. As a one-body radiative process, UV resonance scattering is proportional to the local density of matter, and a denser local medium will lead to a higher incidence of scattering and so stronger spectral lines. Another way of stating this is that the formation of resonance scattering lines is controlled by the local optical depth of a given line

$$\tau_{rad}(r) = \frac{\pi e^2}{m_e c} \lambda f n(r) \left(\frac{dv}{dr}\right)^{-1} \tag{5.1}$$

where we assume the Sobolev approximation holds, and so $\tau_{rad}(r)$ is a local quantity, $\frac{\pi e^2}{m_e c}$ is the classical absorption cross-section, $\lambda$ the rest wavelength of the transition, $f$ the oscillator strength, and $n(r)$ the occupation number of the lower level of the transition (the ground state for resonance scattering).

As per Olson (1982), one can use mass conservation in spherical geometry to re-write

$$n(r) = \frac{\dot{M} A_E q_i}{4\pi r^2 v(r) \mu m_H} \tag{5.2}$$

where $\dot{M}$ is the mass-loss rate, $A_E$ is the elemental abundance, $q_i$ is the ion fraction, $\mu$ is the mean atomic weight and $m_H$ is the mass of hydrogen. Substituting this into the expression for optical depth yields

$$\tau_{rad}(r) = \frac{\pi e^2}{m_e c} \lambda \frac{\dot{M} A_E q_i}{4\pi \mu m_H} \left(r^2 v(r) \frac{dv}{dr}\right)^{-1}. \tag{5.3}$$

This implies that if you are able to constrain the velocity law correctly then you can derive the mass-loss rate by fitting the resonance lines with a model. The key caveat here though is that the mass-loss rate is entangled with abundance and ion fraction, the latter quantity in particular being crucial to this thesis. For O dwarfs it is relatively safe to assume solar abundances for CNO elements since there shouldn't have been enough time

for the outer layers to be peeled off exposing altered amounts of elements from hydrogen burning (although rotational mixing may possibly play a role). The ion fractions have been addressed in the preceding chapter, and will be re-discussed in light of the empirical aspect of the investigation later in this chapter.

### 5.2.1 Sobolev with Exact Integration

The Sobolev with Exact Integration (SEI) code of Lamers et al. (1987) was based on an idea given by Hamann (1981), who suggested that the systematic deviations of the Sobolev approximation from the Comoving Frame method were due to how the formal integral of radiative transfer was treated, and also how both overlapping doublets and underlying photospheric components were considered. The code calculates line profiles in a spherically expanding outflow in which the wind velocity increases monotonically outwards. The Sobolev approximation is used to evaluate the source function whilst the radiative transfer equation is solved exactly, giving an accurate description of the observed line profile. The code was modified by Haser et al. (1995), who included a radially dependent macroturbulent velocity in the analysis, noting that neglecting this can lead to significant errors in the derived mass-loss rates and ion fractions. The code takes into account the contribution from overlapping doublets and a photospheric contribution, of a form of the user's choosing, and it assumes a smooth wind. (See Chapter 7 for comments about new techniques using SEI to treat a porous wind). Massa et al. (2003) adapted the method so that one can select the optical depth in 21 independent velocity bins, rather than assuming a functional form of this quantity. This permits a much closer fit to observations and allows for large structure to be probed. This is key to the study of later type objects which don't have the saturated and relatively smooth wind profiles that can be adequately matched using the functional form of the optical depth that was included with the older version of the code.

The SEI code as used in this thesis work is that of Massa et al. (2003), and requires the following input parameters to be specified:

- *Terminal Velocity* - must be determined in order to compute the normalised velocity parameter $w \equiv v(r)/v_\infty$.

- *Velocity Law* - a standard $\beta$-type velocity law is assumed, of the form

$$w = w_0 + (1 - w_0)\left(1 - \frac{1}{x}\right)^{\beta} \tag{5.4}$$

where $x = r/R_*$ and $R_*$ is the stellar radius, and $w_0$ is set to 0.01. $\beta$ affects the shape of the line profile since via the equation of mass continuity

$$\dot{M} = 4\pi R_*^2 v_\infty x^2 w(x)\rho(x) \tag{5.5}$$

the velocity law is related to the density distribution. Usually the parameters of the velocity law are determined by a fit to a saturated wind line where one is available. In practice with an unsaturated line it is difficult to derive a value for $\beta$ and one must generally live with whatever emission one gets, concentrating on fitting the absorption trough.

- *Macroturbulent velocity* - the turbulent velocity parameter simulates the effects of macroturbulent velocity fields in the wind, due to such phenomena as shocks. It is characterised by a Gaussian distribution with a $1\sigma$ dispersion parameter $w_D$ and has the effect of smoothing out the distribution of $\tau(w)$ in the wind. The main effects of this parameter are to decrease the sharpness of the absorption trough of the profile near the terminal velocity, to shift the maximum velocity blueward and the emission peak redward.

- *Input photospheric spectrum* - there are essentially three options for including a photospheric contribution in the analysis. The first is to use a spectrum of the same spectral type as that which is to be modelled, but of lower luminosity class such that it contains less or no evidence of a wind. This option is ruled out for these dwarf O stars since even dwarfs have some wind lines, indeed that is why they are being modelled in this investigation. The second option is to use Gaussian distributions for the photospheric lines, where an optical depth is specified. This is a relatively good approximation but does not account for the detail around a given spectral line such as the blanketing effect causing the 'continuum' level to be lower. The

third option, and the one preferred in this study was to use models from the plane-parallel photospheric code TLUSTY (Hubeny & Lanz 1995), using identical stellar parameters to the star in question. The model photospheric spectrum approach is key in this investigation for CIV since the photospheric spectrum is quite strong in that region of wavelength space. NV lies over a weaker photospheric spectrum, and so a Gaussian would probably be sufficient, but since the TLUSTY spectra were already being used for CIV they were also used for NV.

- *Wind optical depth* - the SEI code assumes that the optical depth can be described by the Sobolev optical depth, and that it acts radially. It is basically a free parameter once the velocity law and photospheric contributions have been set, and is modelled in 21 separate velocity bins interactively to fit the profile of the line. Because it is assumed that only material at a velocity less than $w_i + w_D$ contributes to the line profile formation at $w_i$, one practically chooses a fitting value of optical depth at $w = 1$ and proceeds inwards fitting the rest of the absorption trough.

Additional parameters needed to fit the line accurately are the projected rotational velocity and the systemic radial velocity. After the fit has been accomplished, the mass-loss rate is determined through equation 5.3, if it can be disentangled from the ion fraction and the elemental abundance. Assuming the surface abundances are solar, they can be adopted directly from the study of Asplund et al. (2005). The ion fractions are the most difficult quantity to determine, as documented in the previous chapter.

Unsaturated lines are required to give a meaningful set of values for $\tau(w)$, and for $\dot{M}q_i$. A saturated line, whilst useful for determining the velocity parameters such as $\beta$ and $v_\infty$, will only permit a lower limit of $\dot{M}q_i$ to be derived.

## 5.3 Background

The study of Fullerton et al. (2006) introduced a big controversy in the study of mass-loss in O stars. It suggested that for supergiants in the mid O-type range, there was an enormous discordance between mass-loss diagnostics in different wavelength regimes, and potentially very great consequences in the knock-on effect to stellar evolution. The product $\dot{M}q_i$ was derived from the PV far-UV doublet (1118,1128Å) for a sample of O supergiants, and the mass-loss rate was found to be up to 120 times lower than derived

from H$\alpha$ and radio measures, assuming $P^{4+}$ to be dominant for a part of the O star range. The keys to whether this study was reporting true mass-loss rates are whether the ion fraction is near unity or not, and whether the smooth-wind approximation of SEI is valid.

For weak-wind objects, such as late-type O dwarfs, a mass-loss determination is much more difficult than for supergiants. H$\alpha$ is mostly observed in absorption for these objects being only a photospheric profile slightly filled with wind emission. Due to the low density wind, even a reasonably large change in mass-loss rate does not alter the profile much, as seen in Figure 5.2. In addition one needs accurate knowledge of the photospheric spectrum itself in order to deduce the contribution from the wind, and hence the effect of mass-loss. Radio measures for this object type are few and far between, since excess radio flux is at a relatively low level, and can be detected in only the brightest or nearest objects.

**Figure 5.2.** These different H$\alpha$ models from CMFGEN, all for a spectral type O8.5 V, span an order of magnitude in mass-loss. Once rotationally broadened, the minor changes seen in the core of the profile are easily lost in the noise of observations.

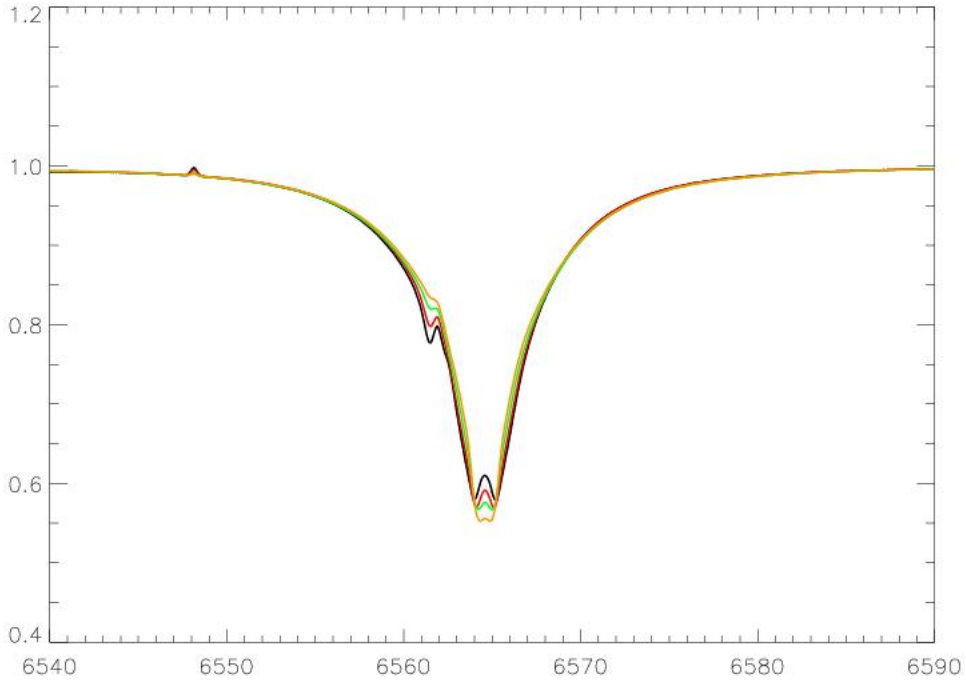


The option of empirical analysis of UV line profiles to assess the mass-loss rate in O dwarfs is very appealing; there is a large body of data at UV wavelengths in existence, and SEI is relatively straightforward to use in performing the analysis. The early CMFGEN grid used for testing suggested that the fraction of $C^{3+}$, corresponding to the CIV resonance

doublet (1548, 1551Å), was dominant for a portion of O stars from spectral type O6.5V through to O8.5V, whilst the full grid that was finally computed seems to suggest the possibility of dominance at later types also, in all scenarios apart from an unclumped wind with X-rays (see Chapter 4). In this range CIV exhibits strong, unsaturated line profiles such that the SEI code can be used to fit them quite unambiguously, rather than merely deriving limits as in the case of saturated lines that are seen at earlier types. This portion of the project uses the SEI code to fit empirical profiles to observations in 43 O dwarfs in the spectral type range O6.5-9.5 V. The product of their mass-loss rate and $C^{3+}$ ion fraction ($\dot{M}q_{CIV}$) is subsequently derived and compared to estimates, both observational and theoretical, of the mass-loss rates of the objects. These are then discussed in light of the ion fractions computed using CMFGEN in previous chapters. In addition, NV profiles are fitted where possible in the same objects, with the aim of further constraining mass-loss and ionization using a different diagnostic line.

## 5.4 The sample

The sample of 44 Galactic O dwarf stars chosen for this investigation are listed in Table 5.1 along with their terminal velocities. These terminal velocities are from Prinja et al. (1990) unless marked with an asterisk, in which case they are those adopted in the fitting process in this study. They are used later to derive the modified wind-momentum of each star's wind, to compare with the WLR in Figure 5.1.

### 5.4.1 Sources of stellar parameters

The stellar parameters necessary to perform the fits and to derive the final product $\dot{M}q_i$ were both gathered from literature, and derived from the CMFGEN grid described in earlier chapters. The following is a brief synopsis of the different sources.

- Terminal velocity (Prinja et al. 1990) - this study derived the terminal wind velocities of many hot stars by measuring the position of the highest 'black' velocity in saturated UV wind profiles, or the position of the narrow absorption component (NAC) in unsaturated profiles. For O stars, the errors are claimed to be $\leq 100 kms^{-1}$.

- Radius - this quantity enters the derivation of $\dot{M}q_i$ and was derived from other stellar parameters ($T_{eff}$, $L_*$) used in the CMFGEN grid. Parameters were matched

**Table 5.1.** Objects in this investigation. Asterisks mark the values of terminal velocity derived through the fitting process, rather than taken from literature.

| HD/CPD | Spectral Type | $v_\infty$ km s$^{-1}$ | $\log L/L_\odot$ | $T_{eff}$ (kK) |
|---|---|---|---|---|
| 5005 | O6.5 V | 2835 | 5.2 | 36.9 |
| 12993 | O6.5 V | 2290 | 5.2 | 36.9 |
| 17505 | O6.5 V((f)) | 2265 | 5.2 | 36.9 |
| 42088 | O6.5 V | 2155 | 5.2 | 36.9 |
| 54662 | O6.5 V | 2395 | 5.2 | 36.9 |
| 93146 | O6.5 V((f)) | 2565 | 5.2 | 36.9 |
| 93161B | O6.5 V((f)) | 3350* | 5.2 | 36.9 |
| 101436 | O6.5 V | 2600 | 5.2 | 36.9 |
| 165052 | O6.5 V(n)((f)) | 2295 | 5.2 | 36.9 |
| 206267 | O6.5 V((f)) | 2680 | 5.2 | 36.9 |
| -59 2603 | O7 V((f)) | 1795 | 5.1 | 35.6 |
| 35619 | O7 V | 1870 | 5.1 | 35.6 |
| 36879 | O7 V(n) | 2170 | 5.1 | 35.6 |
| 44811 | O7 V | 1500* | 5.1 | 35.6 |
| 46485 | O7 Vn(e) | 1780 | 5.1 | 35.6 |
| 47839 | O7 V((f)) | 2055 | 5.1 | 35.6 |
| 48099 | O7 V | 2925 | 5.1 | 35.6 |
| 91824 | O7 V((f)) | 2270 | 5.1 | 35.6 |
| 152623 | O7 V(n)((f)) | 3015 | 5.1 | 35.6 |
| 159176 | O7 V | 2555 | 5.1 | 35.6 |
| 41997 | O7.5 V(n) | 2500* | 5.0 | 34.4 |
| 53975 | O7.5 V | 1795 | 5.0 | 34.4 |
| 152590 | O7.5 V | 1745 | 5.0 | 34.4 |
| 155806 | O7.5 V[n]e | 2390 | 5.0 | 34.4 |
| 14633 | ON8 V | 1690 | 4.9 | 33.3 |
| 41161 | O8 Vn | 2035 | 4.9 | 33.3 |
| 46056 | O8 V(n) | 1305 | 4.9 | 33.3 |
| 46966 | O8 V | 2105 | 4.9 | 33.3 |
| 48279 | O8 V | 1635 | 4.9 | 33.3 |
| 60848 | O8 V:pe var | 1720 | 4.9 | 33.3 |
| 93222 | O8 V | 2645 | 4.9 | 33.3 |
| 100213 | O8 Vn | 1625 | 4.9 | 33.3 |
| 101413 | O8 V | 2230 | 4.9 | 33.3 |
| 46149 | O8.5 V | 1450* | 4.82 | 32.6 |
| 73882 | O8.5 V((n)) | 2315 | 4.82 | 32.6 |
| 216532 | O8.5 V((n)) | 1220* | 4.82 | 32.6 |
| 75759 | O9 Vn | 1245 | 4.8 | 33.3 |
| 193322 | O9 V:((n)) | 1605 | 4.8 | 33.3 |
| 209481 | O9 V: | 1925 | 4.8 | 33.3 |
| 214680 | O9 V | 1120 | 4.8 | 33.3 |
| 34078 | O9.5 V | 1100* | 4.71 | 32.3 |
| 38666 | O9.5 V | 1100* | 4.71 | 32.3 |
| 93027 | O9.5 V | 1130* | 4.71 | 32.3 |
| 149757 | O9.5 Vnn | 1505* | 4.71 | 32.3 |

**Figure 5.3.** Position of programme objects on Hertzsprung-Russell Diagram. Post main-sequence tracks are shown from Schaller et al. (1992). Some points correspond to multiple objects of very similar or the same parameters. There is not enough evidence from this to suggest that these objects have strayed far from the main sequence.

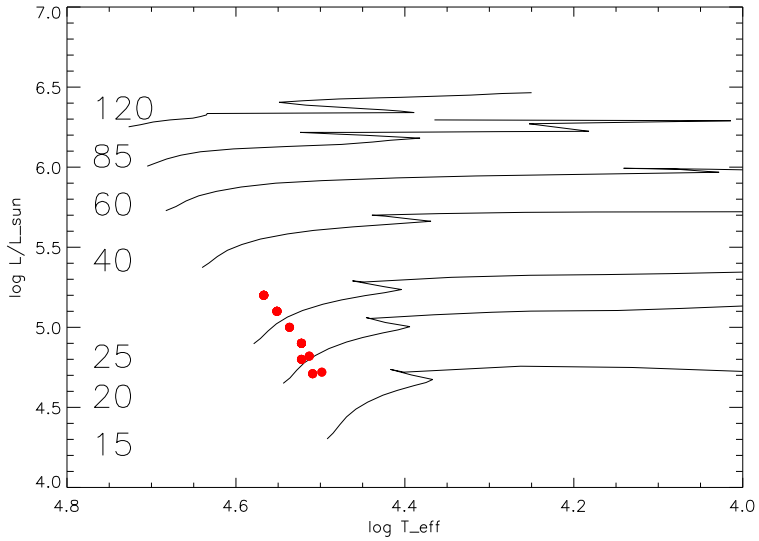


to spectral types and used on that basis.

- Abundances (Asplund et al. 2005) - assumed to be solar due to the relatively unevolved nature of O dwarfs.

- $\beta$ - taken from the same sources as the parameters used to calibrate the CMFGEN grid. Generally in the range 0.8 to 1.2.

- Projected rotational velocity (Penny 1996; Howarth et al. 1997) - an accurate rotationally broadened underlying photospheric profile is necessary to produce accurate fits to the wind line. Penny analysed *IUE* high dispersion spectra, cross-correlating photospheric lines with a narrow-lined O star, HD 34078. The Howarth et al. (1997) catalogue is based on cross-correlations to $\tau$ Sco, and there is generally good agreement between the two catalogues, although the latter is more comprehensive.

- Systemic radial velocity (Wenger et al. 2007) - 'The SIMBAD astronomical database provides basic data, cross-identifications, bibliography and measurements for astronomical objects outside the solar system.' Radial velocities from SIMBAD come from a variety of original sources dating as far back as Wilson (1953).

## 5.5 Empirical fits with SEI

A systematic fitting process was employed for the object sample. Firstly, parameters were gathered from the sources described above. Initially, after the photospheric contribution was set, the terminal velocity from the literature was input, and then adjusted in increments of 10 km $s^{-1}$ until the high velocity portion of the fit appeared by eye to be in the right place. Next $\beta$ was adjusted starting with a value of 1.0, a typical number for O stars, and allowed to vary between ∼0.7 and ∼1.5, although values in the range 0.8-1.2 were preferred since this is the approximate range seen in the literature for O stars. The turbulent velocity was then changed from an initial value of $0.1v_\infty$ in increments of $0.01v_\infty$ until the shape of the blue edge of the profile had been matched. Where literature values of $\beta$ and $v_{turb}$ were available and reliable, these were used as starting values instead. After this the value of $\tau_{rad}(w)$ was varied in 21 velocity bins starting with the outer wind ($w = 1$), and then the fit proceeded inwards interactively until the best possible match had been achieved.

#### UV spectra

The region of the ultraviolet spectrum in which CIV and NV sit has been observed by a few notable space observatories. The *Copernicus* satellite was launched in 1972 and circled the earth until 1981, taking spectra in the near and far UV of around 550 bright objects, mostly bright stars. *IUE* was launched in 1978 and defied all predictions of its lifetime, staying in scientific operation until the mid-1990s, by which time it had taken in excess of 104,000 spectra between 1150 and 3200Å. The *STIS* spectrograph aboard the Hubble Space Telescope has also observed in the ultraviolet, returning high signal-to-noise spectra of many bright objects.

Deciding which spectra to use from which spacecraft was done in the following way. The Galactic O-star Catalogue of Maíz-Apellániz et al. (2004) was consulted for O dwarfs in the range predicted dominant by the original CMFGEN grid, that had reliable spectral type classifications from such sources as Walborn (1972) and Walborn (1982). These were then fed into a search using the Multimission Archive at STScI (MAST) for each of the above missions. It was found that most of them were only available in *IUE* datasets, with CPD -59 2603 and HD 101436 retrieved from *STIS* data. The spectra were retrieved, rebinned at every 0.1Å, and normalised by carefully and interactively fitting a spline curve

as a continuum to divide by. This normalisation was not always easy, mostly due to the noise level in *IUE* spectra. Consistency was ensured by adopting the same 'hinge points' in the spline curve for all spectra, and there can be good confidence in the final normalised spectrum for all of the sample.

**Photospheric contributions**

As discussed above, the most accurate and usable photospheric standards are spectra derived from TLUSTY. In order to make the best use of these, the spectra were broadened using the subroutine ROTIN3, part of the TLUSTY distribution, which convolves a spectrum with both rotational and instrumental profiles in a specified wavelength range. After broadening they were compared with the corresponding observed spectrum, one on top of the other, and scaled such that the photospheric lines on either side of the profile lined up properly, giving confidence that the lines underlying the wind profile would be a correct interpretation of how it would look without a wind. This scaling was generally a multiplication by a constant across the spectrum in the vicinity of the wind line. This is shown in Figure 5.4.

**Figure 5.4.** TLUSTY model spectrum lined up with corresponding observed spectrum of HD 12993 (O6.5 V), showing match for photospheric lines on either side of the wind profile.

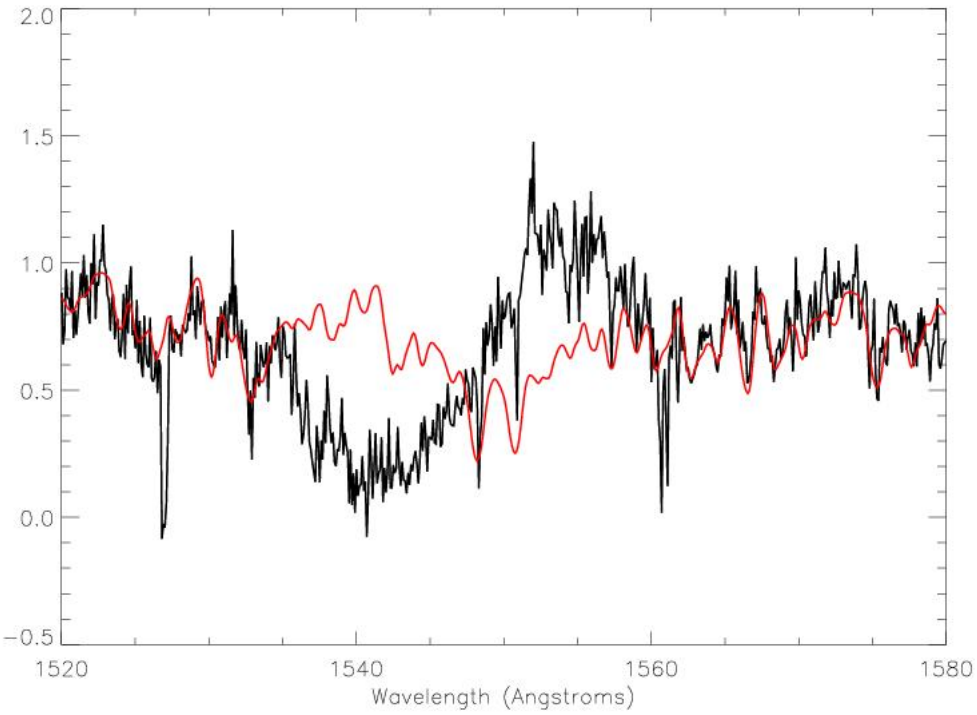

### 5.5.1 CIV Fits

Figures 5.5 to 5.11 show a selection of examples of the fits that were achieved, and the rest are shown in Appendix A. Some difficulties were encountered in producing the best possible fits. The following figures include a breakdown of transmitted and scattered portions of the line profile. Increasing the optical depth at a high velocity to decrease the transmitted flux causes the forward-scattered component at lower velocities in the absorption trough. Eventually a point of saturation is reached at which the forward scattered flux level is higher than the observed profile, and arbitrary large values of $\tau_{rad}$ at those lower velocities cannot reduce the flux level. This meant that it was not always straightforward to produce a good fit at lower velocities, particularly when fitting NV lines (see §5.5.2).

**Figure 5.5.** SEI fit to the CIV line in HD 54662 [O6.5 V]

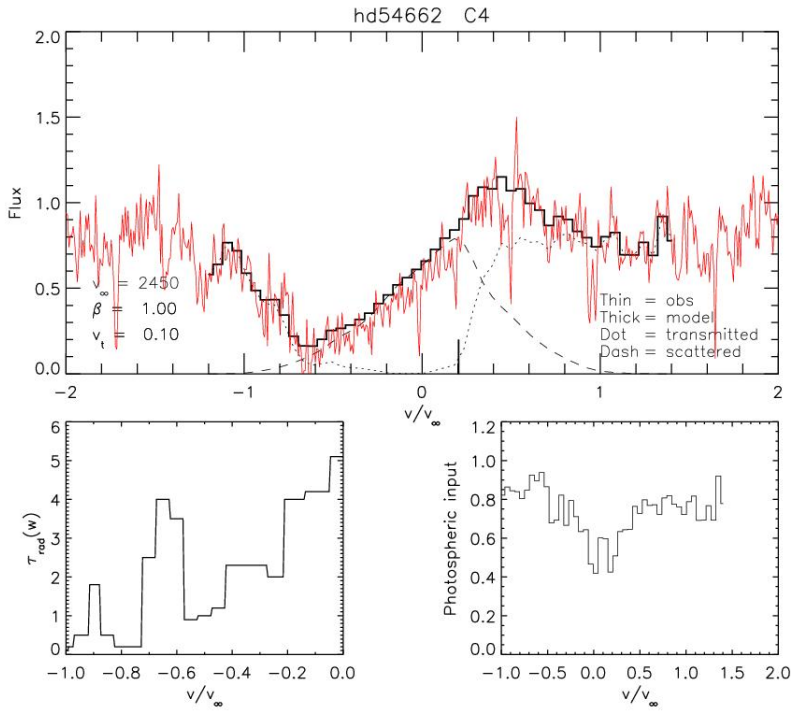


Priority was given to matching the absorption trough, as in some cases the emission component would be under- or over-predicted. Often it was not possible to produce as good a fit to the emission component as to the absorption, even with a variety of values of $\beta$ and $v_{turb}$. This could be the signature of the conditions in the wind - a strong mismatch between the absorption and emission components that cannot be resolved using any of

**Figure 5.6.** SEI fit to the CIV line in HD 35619 [O7 V]

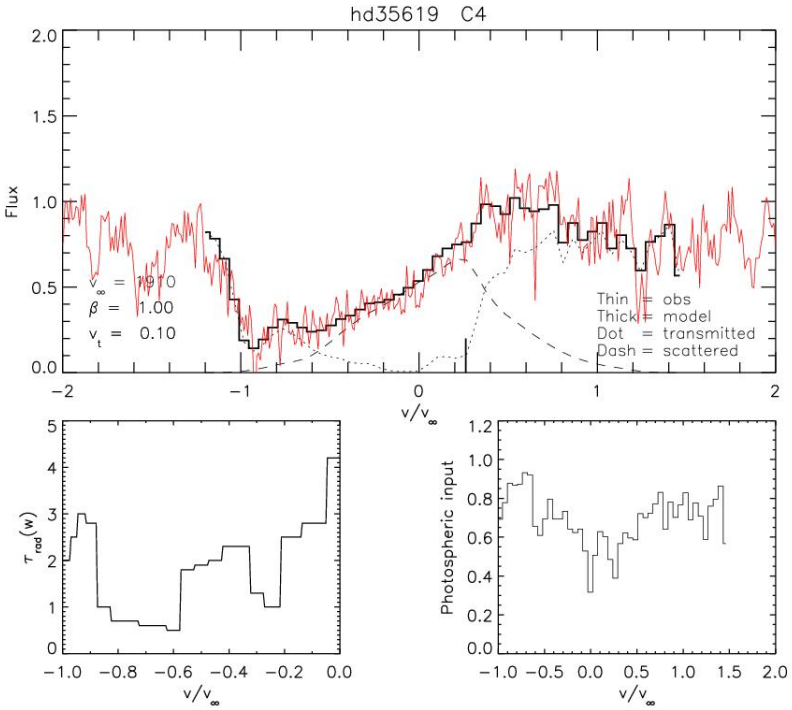


**Figure 5.7.** SEI fit to the CIV line in HD 155806 [O7.5 V[n]e]

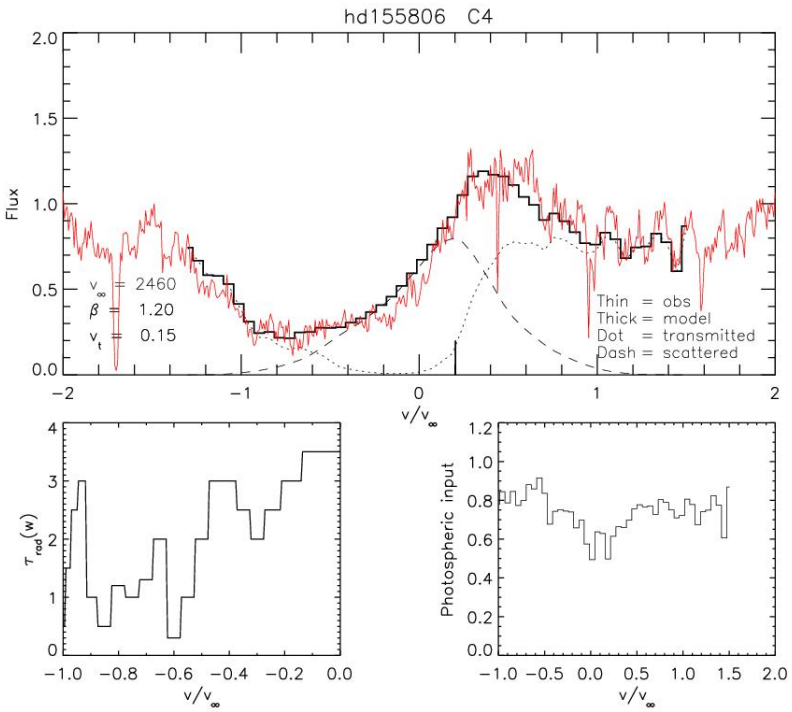

**Figure 5.8.** SEI fit to the CIV line in HD 14633 [ON8 V]

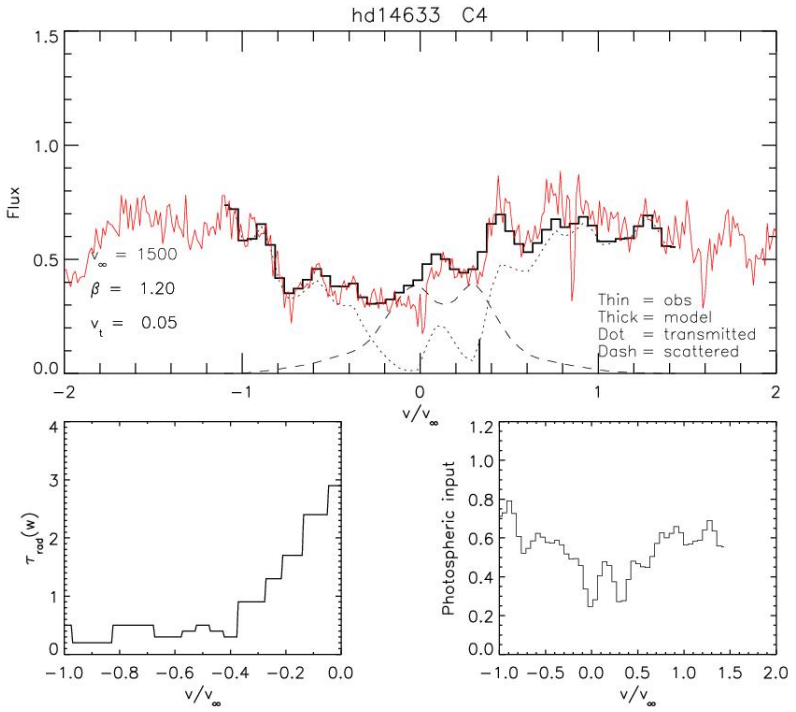


**Figure 5.9.** SEI fit to the CIV line in HD 46149 [O8.5 V]

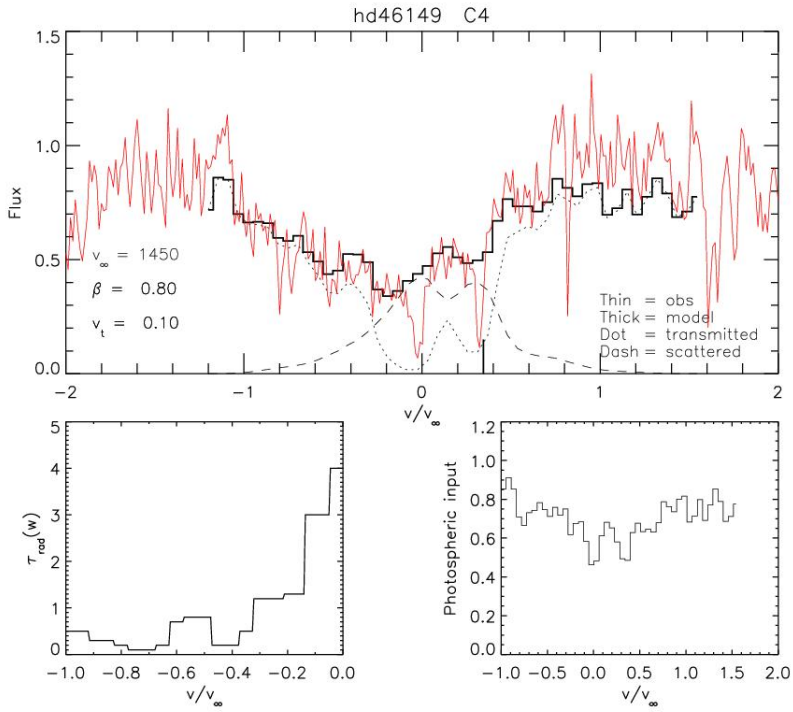

**Figure 5.10.** SEI fit to the CIV line in HD 193322 [O9 V:((n))]

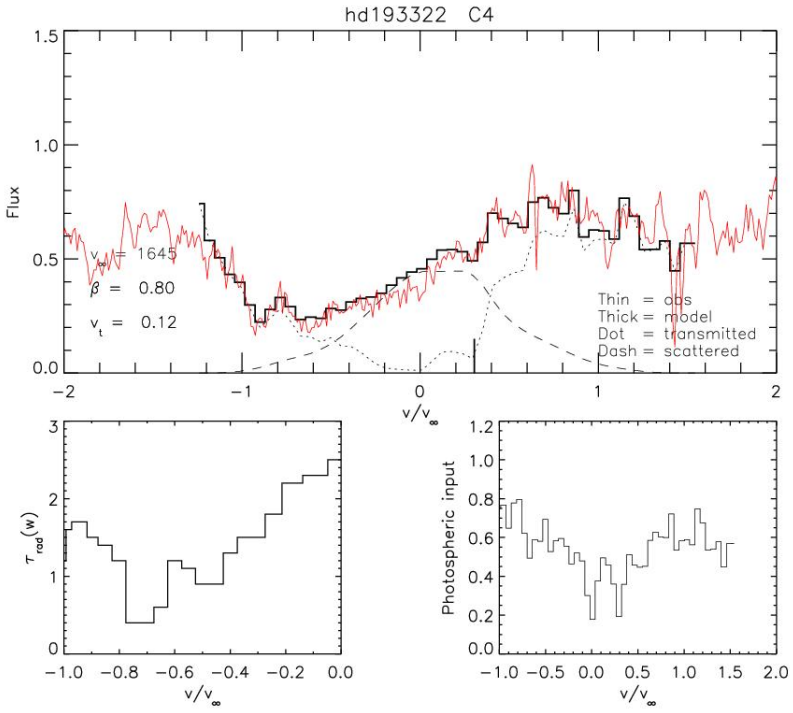


**Figure 5.11.** SEI fit to the CIV line in HD 34078 [O9.5 V]

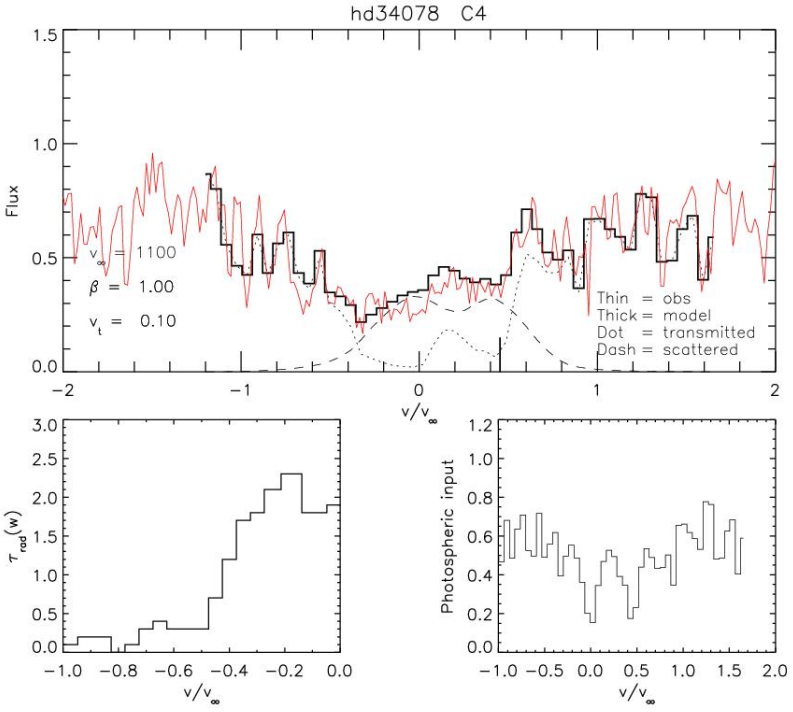

the model parameters may signify a breakdown of one of the model assumptions. In the plots in this chapter the model roughly traces through the emission component in that it passes through the noise, however if there were higher signal to noise data available it might be that this slight inconsistency cannot be ignored, and could demonstrate a break in spherical symmetry of the wind, for example. This conjecture cannot currently be dealt with given the noise of *IUE* observations, but is held as a subject for future work.

The quantity $\dot{M}q_i(w)$ was calculated through an SEI subroutine and, in the same way as in Massa et al. (2003), $q_i$ was integrated and normalised to the range $w = 0.2 - 0.9$ using

$$\langle q_i \rangle \equiv \frac{\int_{0.2}^{0.9} q_i dw}{\int_{0.2}^{0.9} dw} \tag{5.6}$$

to give a value for $\dot{M}q_i$ from across the wind. The low velocity portion is left out of this integral due to the acknowledged difficulties in fitting near the emission part of the spectrum, whilst omitting the highest velocity portion accounts for the variable phenomena that occur there, such as accelerating narrow absorption components (e.g. Prinja & Howarth 1986). The results shown in section 5.6 are hence derived from this normalised region of the wind profile.

### 5.5.2 Nv fits

The Nv resonance line doublet (1239,1243Å) presents quite strong and unsaturated profiles in the spectral type range that has been the subject of investigation for this chapter. This means that it is suitable for modelling with the SEI method and, although it is not predicted to be dominant in the O star range, it is possible it could help offer insight into the ionization conditions in the wind, and perhaps mass-loss too. Conveniently, the Nv doublet lies at 1239, 1243Å, and so is present in the exact same *IUE* spectra as Civ. One further step is required to reduce the observations of Nv due to the blend of the higher velocity portion of Nv with the red wing of the interstellar Lyman $\alpha$ profile. The Ly$\alpha$ line was removed by fitting it with a fully damped synthetic profile, with a particular column density (usually around $10^{21} - 10^{22} cm^{-3}$) and dividing it through. This left the high-velocity portion of the profile with some uncertainty due to dividing by very small numbers (i.e. dividing the saturated portion of the observed Ly$\alpha$ profile by the synthetic

equivalent). The resulting 'noise' was snipped out using the spectral analysis program DIPSO. For different objects the Ly$\alpha$ lies over the blueward extent of the Nv profile by different amounts. A higher interstellar column density gives a larger Ly$\alpha$ profile, and a higher terminal velocity in the star causes the blue part of the wind profile to extend further. This leads to uncertainties in the fit at higher velocities, but is generally negated by assuming the same velocity range as before, between $w = 0.2 - 0.9$.

**Figure 5.12.** SEI fit to the Nv line in HD 42088 [O6.5 V]

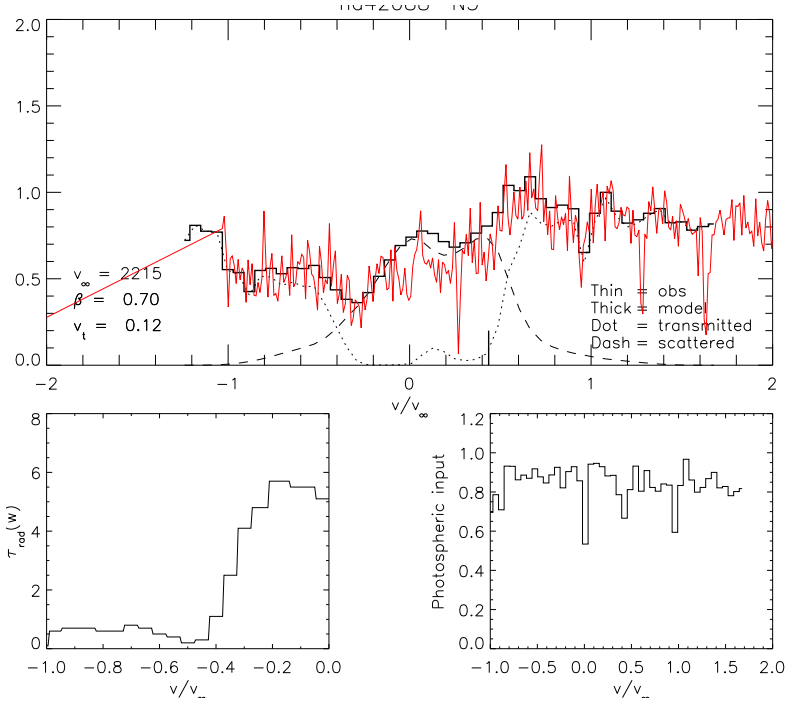


Figures 5.12, 5.13 and 5.14 show some examples of the best fits achieved to observed Nv profiles, and the remainder are included in Appendix A. Not all of the objects in the sample for Civ presented Nv profiles that could be fit. In the later type objects this was because there was no discernable wind profile present (O9V and O9.5V), whilst for some earlier type objects it was impossible to fit them. In some cases this was due to a 'bump' from the emission part of the blue doublet component. It was impossible to force this bump down by increasing the value of $\tau_{rad}$, without forcing another part of the profile down further than the observed line. Some fits retain this feature to some extent, but they are included since the fit to the absorption trough is so good. As before, the match to the absorption component is prioritised since we expect mass-loss effects to exhibit themselves far more obviously in the absorption column than in the emission halo of a stellar wind.

**Figure 5.13.** SEI fit to the Nv line in HD 48099 [O7 V]

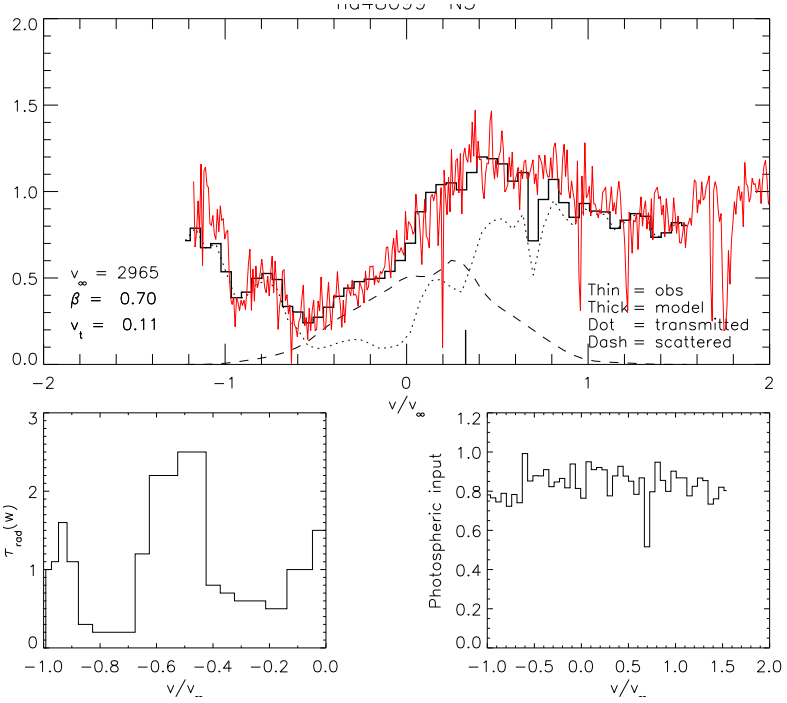


**Figure 5.14.** SEI fit to the Nv line in HD 46966 [O8 V]

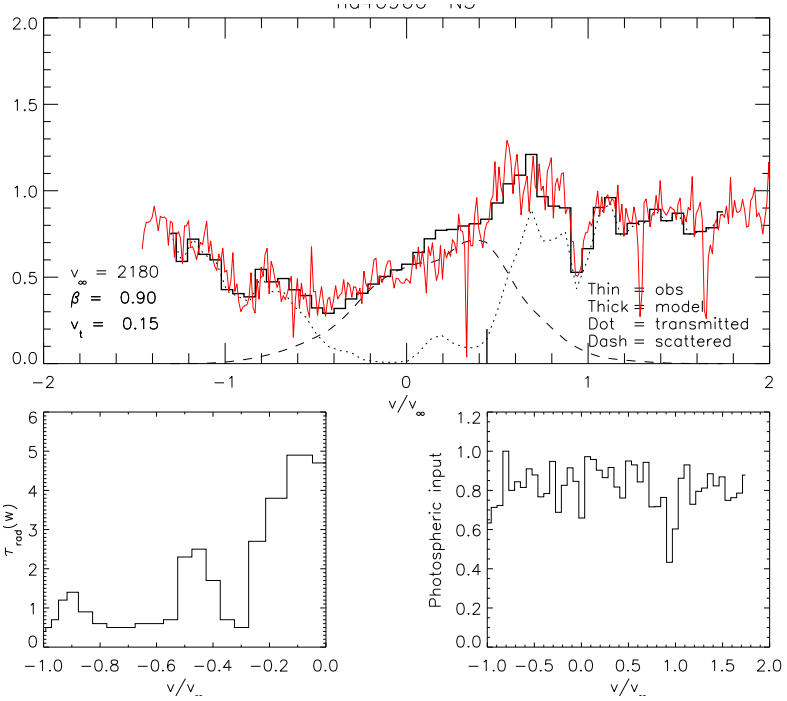

### 5.5.3 Uncertainties

The uncertainties on the derived mass-loss rates are worked out by propagating errors from equation 5.3. The quantities that enter the uncertainty are $\tau_{rad}$, $R_*$, $v_\infty$ and abundance, which in this case is assumed to have negligible uncertainty. It is found that generally the selected $\tau_{rad}$ is correct to within 0.2, although where there is a particularly noisy spectrum it is difficult to find a conclusive level at which to leave the line profile. Errors are increased accordingly in this case. Martins et al. (2005*b*) find errors in derived $R_*$ of 10-20%, and these are adopted here. Generally it is found that uncertainty in terminal velocity as taken from Prinja et al. (1990) is sufficient at a value of $\pm 50$ km s$^{-1}$, but where $v_\infty$ has been altered to achieve a better fit, the error was calculated by increasing and decreasing the value to extremes until it no longer fit. The propagation of these uncertainties leaves an error on the quantity $\dot{M}q_i$ of about 25%, similar to that found by Fullerton et al. (2006).

## 5.6 Results

As the resulting values for $\dot{M}$ and $\dot{M}q_i$ are assessed, comparisons are made with the mass-loss determinations of Vink et al. (2000, 2001), using literature parameters for the stars in his equation for a Galactic O star of solar abundance:

$$\begin{aligned}
\log \dot{M} \;=\;& -\ 6.697\ (\pm 0.061) \\
& +\ 2.194\ (\pm 0.021)\ \log(L_*/10^5) \\
& -\ 1.313\ (\pm 0.046)\ \log(M_*/30) \\
& -\ 1.226\ (\pm 0.037)\ \log\left(\frac{v_\infty/v_{esc}}{2.0}\right) \\
& +\ 0.933\ (\pm 0.064)\ \log(T_{eff}/40000) \\
& -\ 10.92\ (\pm 0.90)\ \{\log(T_{eff}/40000)\}^2 \\
& \text{for } 27\ 500 < T_{eff} \leq 50\ 000\text{K}
\end{aligned} \tag{5.7}$$

which Vink et al. (2000) derived using a linear regression to the parameters. Where parameters are not explicitly derived in the literature, values from the appropriate spectral type in this investigation's CMFGEN grid are used. The derived values for $\dot{M}q_i$ are

**Table 5.2.** Mean ion fractions (normalised over range $w = 0.2 - 0.9$) from models discussed in Chapters 3 and 4, for both smooth and moderately clumped scenarios. Only models with X-rays are used. The precise values for O8 have been interpolated since X-ray models were not completed for this type.

| Spectral Type | $q_{CIV}$ No Clumping | $q_{CIV}$ Clumping | $q_{NV}$ No clumping | $q_{NV}$ Clumping |
|---|---|---|---|---|
| 6.5 | 0.10 | 0.52 | 0.38 | 0.09 |
| 7 | 0.15 | 0.59 | 0.35 | 0.11 |
| 7.5 | 0.19 | 0.69 | 0.35 | 0.07 |
| 8 | 0.23 | 0.70 | 0.35 | 0.20 |
| 8.5 | 0.27 | 0.55 | 0.36 | 0.29 |
| 9 | 0.15 | 0.65 | 0.28 | 0.23 |
| 9.5 | 0.09 | 0.50 | 0.20 | 0.32 |

tabulated in Table 5.3 for CIV and NV.

**Figure 5.15.** Comparison of mass-loss estimates from CIV and NV. Black = no clumping; red = moderate clumping.

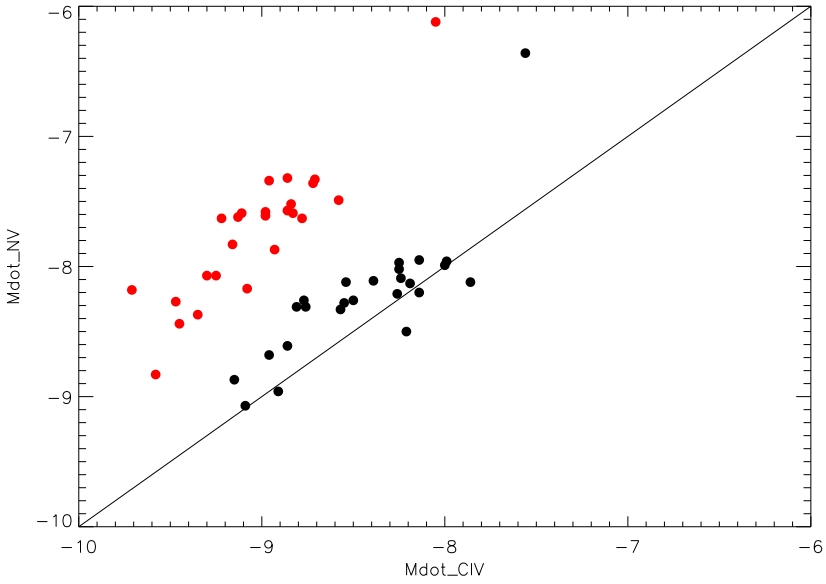


Armed with these values for $\dot{M}q_i$ for both CIV and NV, there are two lines of analysis that can be followed. We can either adopt a mass-loss rate from the literature, leaving us with an ion fraction to compare with those derived in Chapter 4, or we can adopt the ion fractions from Chapter 4, assuming they are reliable and hence deduce a mass-loss rate directly.

Table 5.2 lists the ion fractions for both $C^{3+}$ and $N^{4+}$ from the CMFGEN grid, for

**Table 5.3.** $\dot{M}q_i$ as derived from CIV and NV. Gaps in the NV column indicate that either a satisfactory fit could not be achieved or that the wind is too weak to display a NV wind component.

| HD/CPD | Spectral Type | $log(\dot{M}\langle q_i \rangle)$ $C^{3+}$ | $log(\dot{M}\langle q_i \rangle)$ $N^{4+}$ |
|---|---|---|---|
| 5005 | O6.5 V | -9.25 | -8.39 |
| 12993 | O6.5 V | -9.14 | -8.37 |
| 17505 | O6.5 V | -8.86 | -8.54 |
| 42088 | O6.5 V | -9.26 | -8.63 |
| 54662 | O6.5 V | -9.21 | -8.92 |
| 93146 | O6.5 V | -9.14 | -8.62 |
| 93161B | O6.5 V | -9.04 | |
| 101436 | O6.5 V | -9.00 | -8.41 |
| 165052 | O6.5 V | -9.50 | -8.68 |
| 206267 | O6.5 V | -8.99 | -8.38 |
| -59 2603 | O7 V | -9.96 | |
| 35619 | O7 V | -9.57 | |
| 36879 | O7 V | -9.39 | -8.79 |
| 44811 | O7 V | -9.85 | |
| 46485 | O7 V | -9.17 | |
| 47839 | O7 V | -9.21 | -8.57 |
| 48099 | O7 V | -9.06 | -8.55 |
| 91824 | O7 V | -9.36 | -8.58 |
| 152623 | O7 V | -9.07 | -8.48 |
| 159176 | O7 V | -9.01 | -8.59 |
| 41997 | O7.5 V | -9.07 | |
| 53975 | O7.5 V | -9.87 | -9.33 |
| 152590 | O7.5 V | -9.63 | -9.42 |
| 155806 | O7.5 V | -9.27 | -8.74 |
| 14633 | O8 V | -10.22 | |
| 41161 | O8 V | -9.45 | -8.77 |
| 46056 | O8 V | -9.98 | |
| 46966 | O8 V | -9.40 | -8.77 |
| 48279 | O8 V | -8.20 | -6.82 |
| 60848 | O8 V | -9.60 | -9.14 |
| 93222 | O8 V | -8.99 | |
| 100213 | O8 V | -9.73 | -9.53 |
| 101413 | O8 V | -9.50 | -9.07 |
| 46149 | O8.5 V | -10.31 | |
| 73882 | O8.5 V | -9.34 | -8.71 |
| 216532 | O8.5 V | -10.00 | |
| 75759 | O9 V | -10.14 | |
| 193322 | O9 V | -9.88 | |
| 209481 | O9 V | -9.78 | |
| 214680 | O9 V | -10.37 | |
| 34078 | O9.5 V | -10.51 | |
| 38666 | O9.5 V | -10.36 | |
| 93027 | O9.5 V | -10.24 | |
| 149757 | O9.5 V | -9.91 | |

**Table 5.4.** Mass-loss rates compared with literature. The final column contains values derived using NLTE model fits by Martins et al. (2005*b*) and Marcolino et al. (2009), the latter marked with stars.

| HD/ CPD | Spectral Type | $log\dot{M}_{Civ}$ Cl | $log\dot{M}_{Civ}$ No Cl | $log\dot{M}_{Nv}$ Cl | $log\dot{M}_{Nv}$ No Cl | $log\dot{M}$ (Vink) | $log\dot{M}$ (M05/Ma09) |
|---|---|---|---|---|---|---|---|
| 5005 | O6.5 V | -8.96 | -8.25 | -7.34 | -7.97 | -6.47 | |
| 12993 | O6.5 V | -8.86 | -8.14 | -7.32 | -7.95 | -6.36 | |
| 17505 | O6.5 V | -8.58 | -7.86 | -7.49 | -8.12 | -6.30 | |
| 42088 | O6.5 V | -8.98 | -8.26 | -7.58 | -8.21 | -6.33 | -8.0 |
| 54662 | O6.5 V | -8.93 | -8.21 | -7.87 | -8.50 | -6.30 | |
| 93146 | O6.5 V | -8.86 | -8.14 | -7.57 | -8.20 | -6.42 | -7.25 |
| 93161B | O6.5 V | -8.76 | -8.04 | | | -6.30 | |
| 101436 | O6.5 V | -8.72 | -8.00 | -7.36 | -7.99 | -6.43 | |
| 165052 | O6.5 V | -9.22 | -8.50 | -7.63 | -8.26 | -6.30 | |
| 206267 | O6.5 V | -8.71 | -7.99 | -7.33 | -7.96 | -6.30 | |
| -59 2603 | O7 V | -9.73 | -9.14 | | | -6.43 | |
| 35619 | O7 V | -9.34 | -8.75 | | | -6.46 | |
| 36879 | O7 V | -9.16 | -8.57 | -7.83 | -8.33 | -6.54 | |
| 44811 | O7 V | -9.62 | -9.03 | | | -6.43 | |
| 46485 | O7 V | -8.94 | -8.35 | | | -6.43 | |
| 47839 | O7 V | -8.98 | -8.39 | -7.61 | -8.11 | -6.55 | |
| 48099 | O7 V | -8.83 | -8.24 | -7.59 | -8.09 | -6.43 | |
| 91824 | O7 V | -9.13 | -8.54 | -7.62 | -8.12 | -6.43 | |
| 152623 | O7 V | -8.84 | -8.25 | -7.52 | -8.02 | -7.13 | |
| 159176 | O7 V | -8.78 | -8.19 | -7.63 | -8.13 | -6.62 | |
| 41997 | O7.5 V | -8.91 | -8.35 | | | -6.82 | |
| 53975 | O7.5 V | -9.71 | -9.15 | -8.18 | -8.87 | -6.50 | |
| 152590 | O7.5 V | -9.47 | -8.91 | -8.27 | -8.96 | -6.63 | -7.78 |
| 155806 | O7.5 V | -9.11 | -8.55 | -7.59 | -8.28 | -6.80 | |
| 14633 | O8 V | -10.10 | -9.58 | | | -7.02 | |
| 41161 | O8 V | -9.30 | -8.81 | -8.07 | -8.31 | -6.62 | |
| 46056 | O8 V | -9.83 | -9.34 | | | -6.68 | |
| 46966 | O8 V | -9.25 | -8.76 | -8.07 | -8.31 | -6.94 | |
| 48279 | O8 V | -8.05 | -7.56 | -6.12 | -6.36 | -6.62 | |
| 60848 | O8 V | -9.45 | -8.96 | -8.44 | -8.68 | -7.02 | |
| 93222 | O8 V | -8.84 | -8.35 | | | -6.62 | |
| 100213 | O8 V | -9.58 | -9.09 | -8.83 | -9.07 | -6.62 | |
| 101413 | O8 V | -9.35 | -8.86 | -8.37 | -8.61 | -6.62 | |
| 46149 | O8.5 V | -10.05 | -9.74 | | | -6.86 | |
| 73882 | O8.5 V | -9.08 | -8.77 | -8.17 | -8.26 | -7.36 | |
| 216532 | O8.5 V | -9.74 | -9.43 | | | -6.86 | -9.22* |
| 75759 | O9 V | -9.95 | -9.32 | | | -6.88 | |
| 193322 | O9 V | -9.69 | -9.06 | | | -6.88 | |
| 209481 | O9 V | -9.59 | -8.96 | | | -6.88 | |
| 214680 | O9 V | -10.18 | -9.55 | | | -6.88 | |
| 34078 | O9.5 V | -10.21 | -9.46 | | | -6.69 | -9.5 |
| 38666 | O9.5 V | -10.06 | -9.31 | | | -7.05 | -9.5 |
| 93027 | O9.5 V | -9.94 | -9.19 | | | -7.09 | |
| 149757 | O9.5 V | -9.61 | -8.86 | | | -6.88 | -8.8* |

**Figure 5.16.** Derived mass-loss rates assuming CMFGEN ion fractions in Table 5.2, compared with Vink's mass-loss recipe. Black: $C^{3+}$ with clumping; red: $C^{3+}$ without clumping; green: $N^{4+}$ with clumping; blue: $N^{4+}$ without clumping.

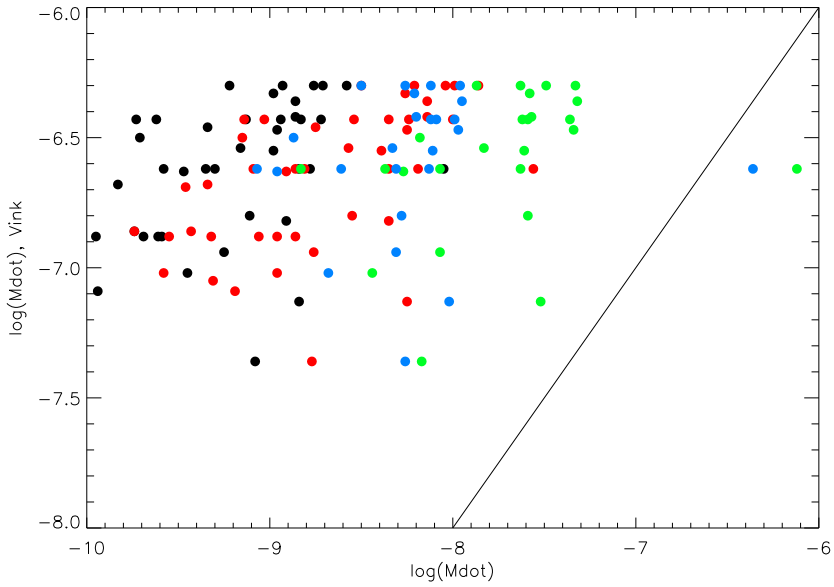


**Figure 5.17.** Plot showing the comparison between mass-loss rate in this investigation for CIV and the Vink mass-loss recipe. The diagonal line represents direct agreement between the two. Four different ion fractions are shown. A value of around 0.001 is required for a good match.

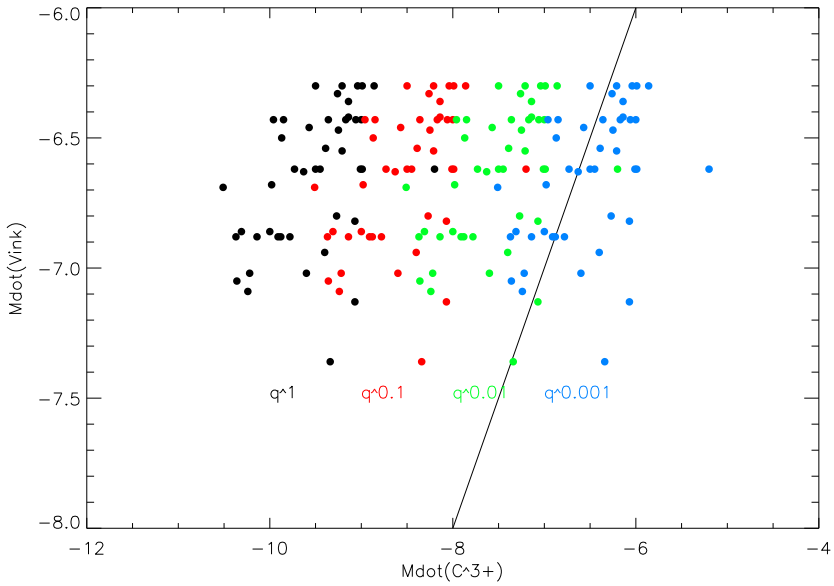

**Figure 5.18.** Plot showing the comparison between mass-loss rate in this investigation for Nv and the Vink mass-loss recipe. The diagonal line represents direct agreement between the two. Four different ion fractions are shown. A value of around 0.01 is required for a good match.

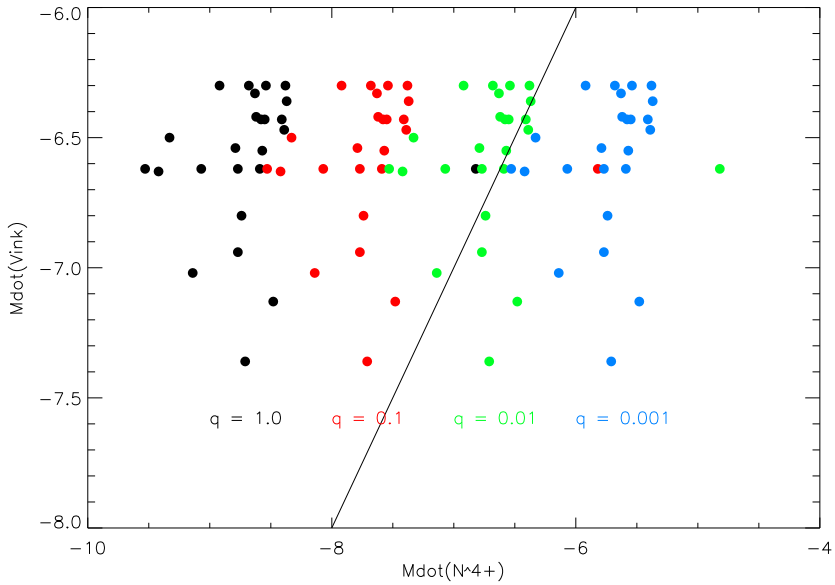


both unclumped and moderately clumped wind scenarios. The value for an O8 dwarf is interpolated from the other values since no models were converged at this spectral type. The confidence we have in these values comes from previous chapters, where it was shown how well the UV and optical spectra compare to observations. A caveat to that is that the strengths of Civ profiles of late O dwarfs in the CMFGEN grid are mildly over-predicted. This will not affect the broad conclusions to this chapter, however, since Chapters 3 and 4 also showed that raising the X-ray input to produce a correct Civ profile did not reduce the corresponding ion fraction by an amount significant to this study. It was shown in Chapters 3 and 4 that for O dwarfs an unclumped model is better than one with moderate or strong clumping, although since we do see structure in O star winds, it is possible that the clumping level is just lower than what is considered moderate here. For this reason, the moderately clumped model ion fractions are included here as an upper limit on the clumping factor. If the CMFGEN ion fractions are used, we obtain values for the mass-loss as tabulated in Table 5.4. These are listed side-by-side with values calculated using the Vink mass-loss recipe, and those from Martins et al. (2005*b*) and Marcolino et al. (2009). Since the luminosities and effective temperatures used to calculate the mass-loss rates in this investigation are slightly different to those used in comparison studies, it is wise to

check the difference a change of luminosity of this factor would make to the final derived value.

Figure 5.15 shows how mass-loss rates derived using CIV compare with those using NV, for both clumped and unclumped scenarios, including only those objects for which NV could be fitted. What is immediately obvious is that when the winds are moderately clumped in the models, the ion fractions cause the mass-loss estimates from different lines to be different by about an order of magnitude, NV predicting a higher mass-loss rate than CIV in the clumped case. As can be seen in Table 5.2 this is because as clumping is implemented, the ion fraction $q_{CIV}$ goes up whilst the fraction $q_{NV}$ goes down. The unclumped winds on the other hand show agreement between diagnostic lines. The underlying physical reason for why the two ion fractions diverge in the presence of clumping is not immediately clear, but if we observe Figure 5.19, a schematic from Massa et al. (2003) we can see why this might be. It shows the range of ionization energies corresponding to the various transitions, and how with extra energy the ionization state changes. In an approximate way clumping, through density enhancement and altered recombination rates, causes the ionization state to move from right to left on that diagram. Any ions corresponding to CV and NV will 'recombine' to CIV and NIV. This explains why the addition of clumping strengthens CIV but weakens NV. The fact that only the unclumped models seem appropriate for both NV and CIV to predict similar mass-loss rates may indicate again that a very weakly clumped wind works best, at least with CMFGEN.

Figure 5.16 shows the different mass-loss estimates compared with those from the Vink mass-loss recipe. They produce a large scatter, covering more than 2 orders of magnitude. The anomalous point to the right in each colour corresponds to HD 48279, which has stronger wind profiles than might be expected of an O dwarf of its spectral type, and is likely down to this object's possible status as an ON star (Sota et al. 2008), having modified abundances. This was only realised after finding this anomalous point. Since the quantity being derived nominally incorporates the elemental abundance, any divergence from solar will result in a different value. HD 14633, also catalogued as an ON star, does not appear as an anomalous point. The points corresponding to models with unclumped winds, i.e. those we believe from previous chapters to be the ones that best reproduce spectra, show a disagreement with the mass-loss recipe of around 2 orders of magnitude, and sometimes almost three. This matches the conclusions of Martins et al. (2005*b*), who also find weak-winded O dwarfs fall about 2 orders of magnitude below 'canonical' values.

**Figure 5.19.** Schematic of ionization energies from Massa et al. (2003).

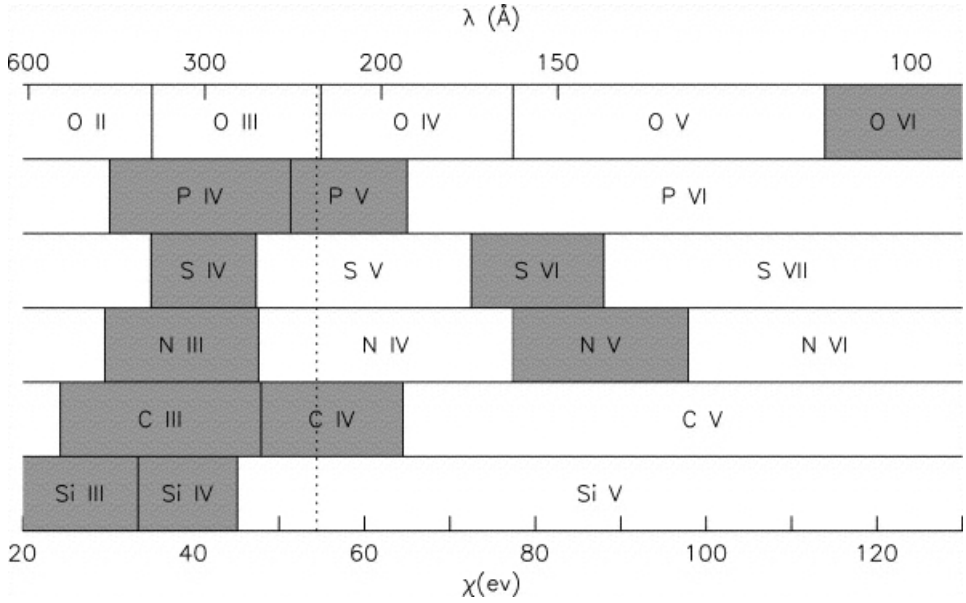


Figures 5.17 and 5.18 show the mass-loss rates based on CIV and NV, with a selection of different ion fractions. $\dot{M}q_i$ for CIV requires an ion fraction of around 0.001 in order to match the mass-loss predicted by the Vink recipe. By comparison, the *lowest* $C^{3+}$ ion fraction predicted by the models at the spectral types in question is 0.09, almost two orders of magnitude higher. For NV an ion fraction of more like 0.01 is required to match the Vink values. The lowest predicted by CMFGEN is 0.07, and that is for the unfavoured clumped models. In the unclumped models, ion fractions of 0.3 are more like what is seen (see Figure 5.20, reproduced from Chapter 4).

Therefore, adopting mass-loss rates from the Vink recipe leaves us with ion fractions that are far too low compared to the CMFGEN models, or alternatively adopting the CMFGEN ion fractions from the outset leaves us with mass-loss rates lower than Vink by orders of magnitude.

In comparing the values of mass-loss rate derived to the few literature values available (Table 5.4), it is noted that Martins et al. (2005*b*) and Marcolino et al. (2009) adopt slightly different values of physical parameters. Given that in the calculation of mass-loss rate in this study,

$$\dot{M} \propto R \propto \frac{L^{0.5}}{T_{eff}^2}, \tag{5.8}$$

**Figure 5.20.** Carbon ion fractions for dwarfs, reproduced from Chapter 4.

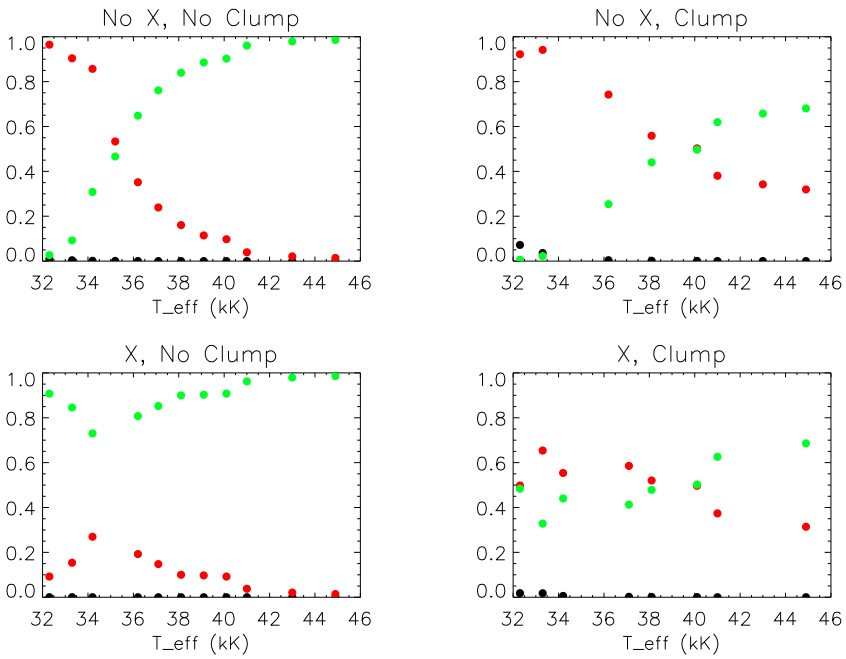


we may scale the relevant quantities to match, thus comparing like with like. For simplicity, the literature value is scaled rather than the other multiple columns in Table 5.4. The only two significant changes are for HD 152590 and HD 149757. In the former case it brings the value closer to the literature one, and in the latter case further away, although not by a significant margin.

Figures 5.21 and 5.22 show where the predicted values of $\dot{M}$ using CMFGEN ion fractions fall in the Wind-momentum Luminosity Relationship, where the radius and luminosity have been adopted from the CMFGEN grid. Regardless of whether clumping

**Table 5.5.** Comparison of adopted parameters, to be used in conjunction with Table 5.4. The scaling of mass-loss rates from this enables more direct comparison. The scaling factor comes from Eq. 5.8.

| HD | $T_{eff}$, L (This Study) | $T_{eff}$, L (Literature) | Scaling factor | Scaled log $\dot{M}$ |
|---|---|---|---|---|
| 42088 | 36.9, 5.20 | 38, 5.23 | 0.97 | -7.93 |
| 93146 | 36.9, 5.20 | 37, 5.22 | 0.99 | -7.25 |
| 152590 | 34.4, 5.00 | 36, 4.79 | 0.71 | -7.93 |
| 216532 | 32.6, 4.82 | 33, 4.79 | 0.94 | -9.25 |
| 34078 | 32.3, 4.71 | 33, 4.77 | 1.03 | -9.49 |
| 38666 | 32.3, 4.71 | 33, 4.66 | 0.91 | -9.54 |
| 149757 | 32.3, 4.71 | 32, 4.86 | 1.22 | -8.71 |

is switched on in the corresponding CMFGEN model or not, the points fall below the relationship expected for O stars by more than 1 dex, and up to around 3 dex. Because of the luminosities adopted from the CMFGEN grid, the points also trace back further down the X-axis than in Figure 5.1, and the value of $\log D_{mom}$ is generally lower than anything in that figure. We should perhaps trust the values for CIV, since the fits achieved are generally better than for NV. These values (from both NV and CIV) appear consistent with those derived in Martins et al. (2005*b*), which fall as low as 24.8. This reinforces potential issues with line-driven wind theory, and will be discussed further in this chapter's final section.

Further information can be gleaned from these results about ionization in the winds of O dwarfs. By plotting out all the values derived for $\dot{M}q_i$ with effective temperature, we can find out whether a peak in this value is predicted for either CIV or NV. Previously this might have been interpreted as a sign of dominance in a particular temperature range, but we have seen that this is not necessarily the case in the unclumped X-ray CMFGEN models, where the peak is well below an ion fraction of 0.5. Instead it is of interest to discover whether any such peak occurs in the empirical datapoints, and whether it coincides with any CMFGEN model scenarios. It is expected that the mass-loss rate would change quite steadily with spectral type for dwarfs, and so the peak, if one is seen, would be in the ion fraction.

The product of mass-loss rate and ion fraction derived using the SEI code is plotted as a function of effective temperature for CIV and NV in Figures 5.23 and 5.24 respectively. Neither of them appears to clearly show a peak at a particular temperature, although there is a mild suggestion of one for NV at around 38 kK. This position does not appear to correspond with any peak in the CMFGEN ion fractions of Chapter 4, so could instead be an artefact of mass-loss. In each plot the outlier, again, is HD 48279, due to it's enhanced abundances. It is likely that any strong peak in the ion fractions is washed out by the scatter in the diagrams. This scatter could originate from a wide range in mass-loss rate, otherwise the only way to get the ion fractions to change by large amounts in the models is to change the clumping scenario. A further avenue of study might be to investigate this scatter more thoroughly, and find out whether it can be put down to clumping, mass-loss rate, or sheer uncertainty.

The general decline in $\dot{M}q_i$ for CIV towards lower temperatures (later spectral types) can likely be attributed to the decline in mass-loss rate, although it is difficult to say this

with too much certainty given how unsure we are about O star mass-loss rates. We can be sure however that there will not be a strong *increase* in mass-loss rate into the B-star regime. If the decline for CIV is mostly down to the mass-loss rate, then the fact that $\dot{M}q_i$ for NV is rather constant over the same range would imply that $N^{4+}$ actually declines as the effective temperature rises. However since the fraction of this ion only changes by around a factor of 2 or 3 in the CMFGEN predictions of Chapter 4, it would again be washed out by the scatter in points.

Figure 5.25 shows the ratio $\dot{M}q_{CIV}/\dot{M}q_{NV}$ compared with CMFGEN's $q_{C^{3+}}/q_{N^{4+}}$ for both clumped and unclumped winds. The unclumped scenario matches SEI's prediction very well, unlike the clumped one. This may not be that surprising since SEI deals only with smooth winds, but perhaps it is further evidence that only very mild clumping is required for O dwarfs to be quite satisfactorily described. It stems again from the CIV and NV ion fractions diverging with the introduction of clumping.

**Figure 5.21.** Derived CIV modified wind-momenta. Black: unclumped; green: clumped. The line represents the 'standard' relation expected for O stars (Kudritzki & Puls 2000).

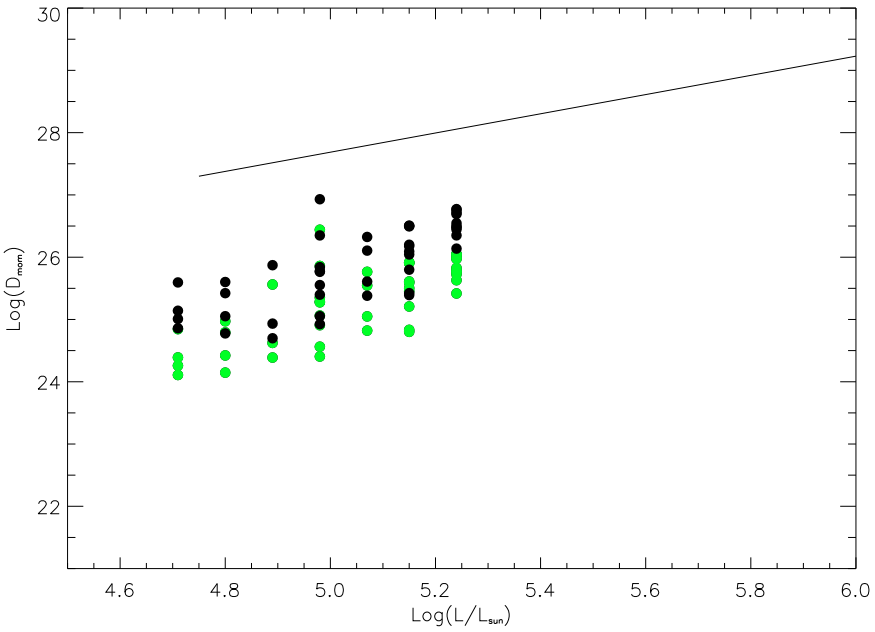

**Figure 5.22.** Derived Nv modified wind-momenta. Black: unclumped; green: clumped. The line represents the 'standard' relation expected for O stars (Kudritzki & Puls 2000).

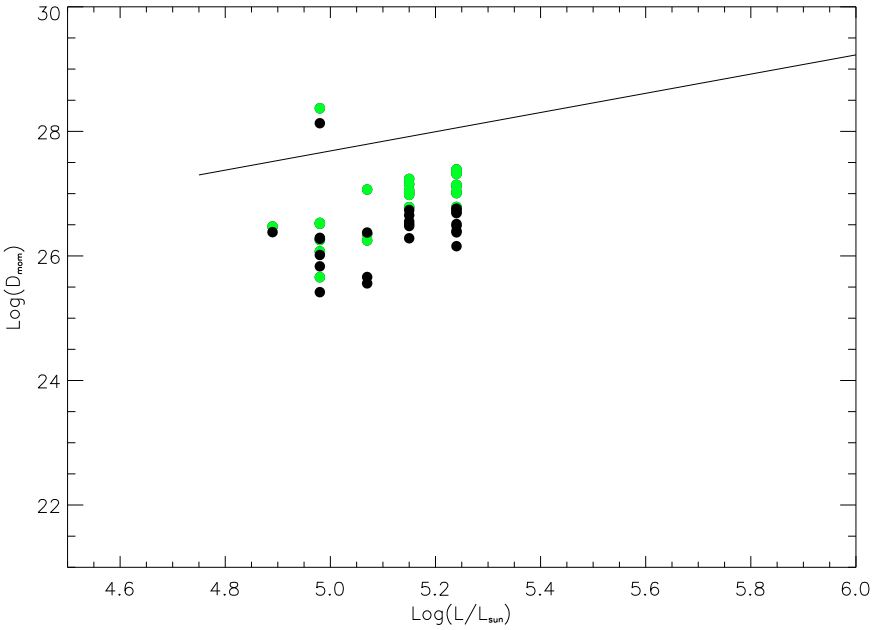


**Figure 5.23.** $\dot{M}q_i$ for Civ, plotted for the whole sample against effective temperature.

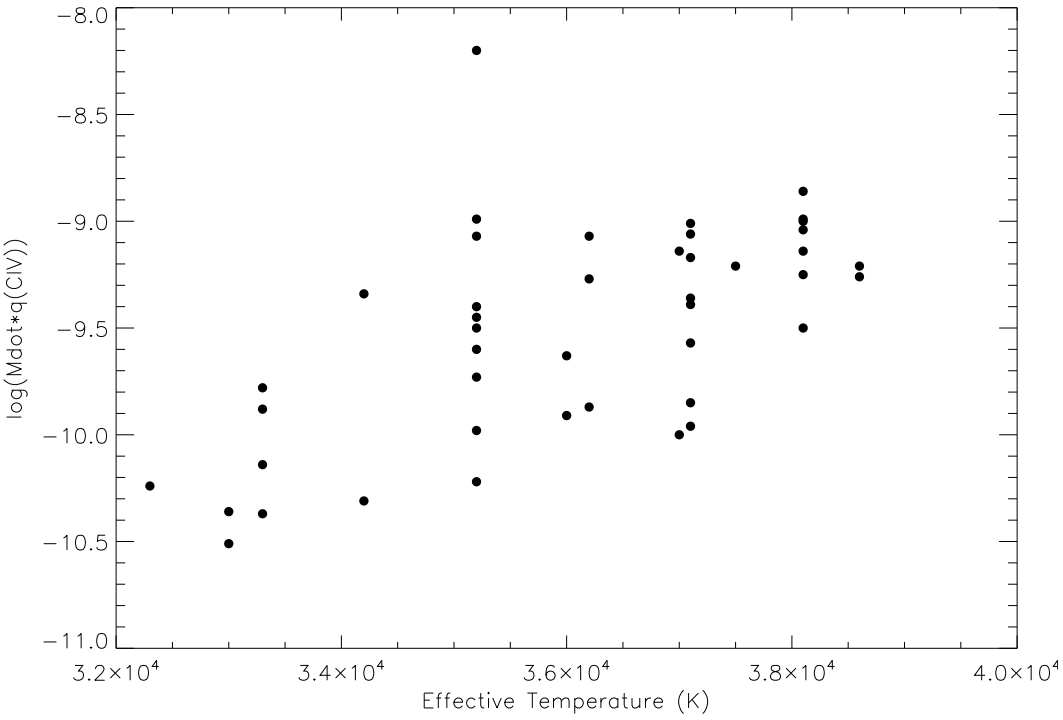

**Figure 5.24.** $\dot{M}q_i$ for Nv, plotted for the whole sample against effective temperature.

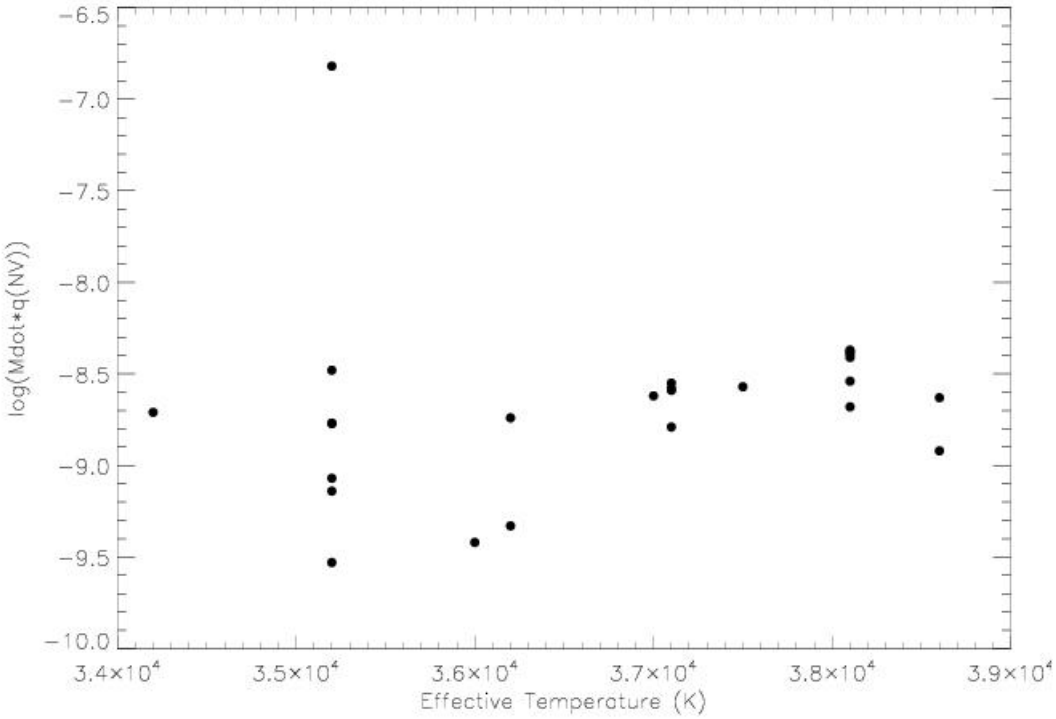


**Figure 5.25.** The ratio of ion fractions from Civ and Nv. Black: derived from CMFGEN models with clumping; red: derived from CMFGEN models without clumping; green: derived by dividing $\dot{M}q_{CIV}$ by $\dot{M}q_{NV}$ from SEI.

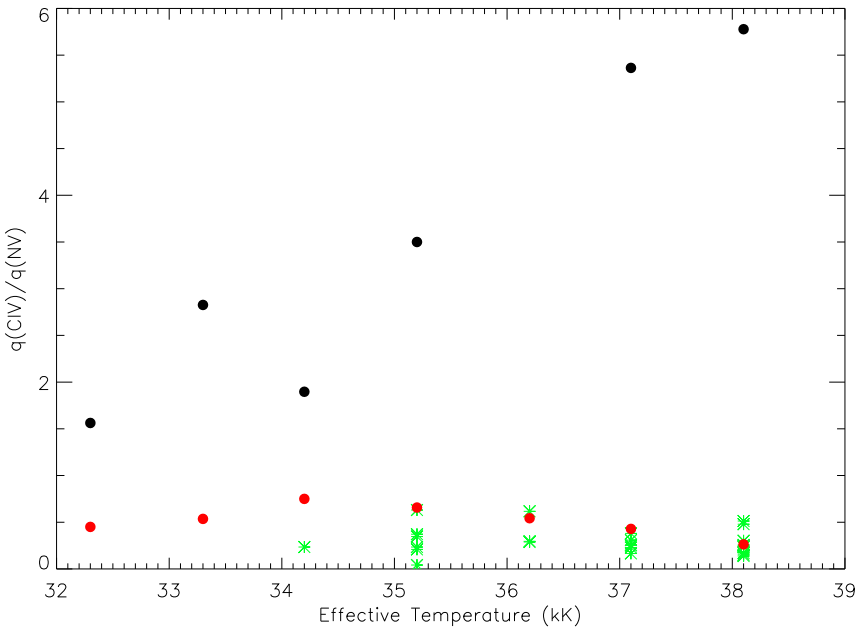

## 5.7 Conclusions

In this chapter, the SEI method has been used to match model profiles to CIV and NV in a sample of 43 Galactic O dwarf stars, with the aim of estimating mass-loss and learning about ionization conditions in the wind of weak winded objects.

Fits were made to CIV in all objects with most of them very well reproduced, and only a few that could not be matched. Any small deviations from a satisfactory fit are unlikely to affect the estimated $\dot{M}q_i$ beyond the given errors. $\dot{M}q_i$ for CIV is found to be systematically between 2 and 3 orders of magnitude below the theoretical predictions from the Vink mass-loss recipe, which itself is comparable to the available radio and H$\alpha$ measures. This implies that either the $C^{3+}$ ion fraction lies in the range 0.001-0.01 for these objects, or there is a major discrepancy in mass-loss estimates. The model predictions of CMFGEN for the ion fractions do not support the idea of values as low as 0.01, although the true effects of X-rays and clumping are still to be fully determined. In addition, the comparison values derived through H$\alpha$ are somewhat questionable due to the line's insensitivity to mass-loss at later O types. The predominant shortcoming of the SEI code is that it assumes the wind to be homogeneous (though the optical depth is somewhat flexible), which means that if the wind is arranged in clumps that fall outside the volume filling factor approximation, then the shape and size of the UV wind profiles could be easily misinterpreted. One way to harness the capabilities of the SEI code to find out about wind 'porosity', and a future avenue of investigation, is to model well-separated doublet components of a line individually, treating them as singlets, and allowing the ratio of the optical depth of the components to vary from what the atomic properties of the gas dictate. This has been done in B supergiants by Prinja & Massa (2010) and will be further discussed as part of the 'Future Work' section of Chapter 7.

### 5.7.1 Discussion

One of the aims of this chapter was to clarify and constrain the mass-loss rates of late-type O dwarf stars; those with 'weak winds'. Referring back again to Figure 5.20, we see that given a wind scenario of moderate micro-clumping and an X-ray flux consistent with observations, then the fraction of $C^{3+}$ is at approximately 50% for all the stars in the sample (O6.5-9.5). Given the consistent X-rays and the large body of evidence for wind structure in literature, this scenario is difficult to ignore. When used to disentangle the

product $\dot{M}q_i$ derived from CIV in this chapter, it leads to mass-loss rates in the range $10^{-9}$-$10^{-10} M_{\odot} yr^{-1}$ (see Table 5.4). That table also shows how the mass-loss rates from this investigation are even lower than those measured by Martins et al. (2005*b*) for the same objects, although that study estimates the mass-loss rate for other late-type O dwarfs as being of order $10^{-10} M_{\odot} yr^{-1}$. Marcolino et al. (2009) also find mass-loss rates as low as $4.5{\times}10^{-10} M_{\odot} yr^{-1}$ for O dwarfs using a CMFGEN analysis. So if we believe the ion fractions predicted by CMFGEN in Chapter 4, whose corresponding synthetic spectra appear reasonable (Chapter 3) then we are left with the very low mass-loss rates seen in Table 5.4, and these agree with recent pure model atmosphere analysis. Alternatively if the clumping factor is actually very low, as some of the models in Chapter 3 suggest, the mass-loss rates derived are still very low, as seen in the adjacent column of Table 5.4, and in fact have better direct agreement with those of Martins et al. (2005*b*). The models with smooth winds predict an ion fraction $C^{3+}$ of between 0.1 and 0.3 for the late O dwarfs.

We see in Figure 5.21 that the value of $D_{mom}$, the modified wind-momentum, lies up to 3 dex below that expected for O stars in general from Kudritzki & Puls (2000). This represents a more comprehensive illustration of the problem as displayed in Figure 5.1. The large scatter in Figure 5.21 has to come from either the mass-loss rate, the terminal velocity or the stellar radius (since $D_{mom} = \dot{M} v_{\infty} R^{0.5}$). The range in terminal velocities for late O dwarfs only spans about a factor of 2 and the stellar radius of a main sequence O star is similarly confined to rather a narrow predicted range, so this scatter must be largely down to the mass-loss rate. Indeed the range of mass-loss rates measured in this study do cover more than an order of magnitude. The important feature of these plots concerning mass-loss rates is that *all* the points fall well below the relation given by Kudritzki & Puls (2000).

These very low mass-loss rates lead us to a few possible conclusions. The first is that there is an intrinsic problem with the theory of line-driven winds, the possibility of which is discussed in the introduction to this thesis. An up-to-date treatment of a thinner wind in which coulomb decoupling occurs might be necessary to see whether it is predicted to have a noticeable effect on the overall mass-loss rate of the star, and indeed whether such an effect can account for the orders of magnitude discrepancy seen. Given how very successful the theory of line-driven winds has been, it is very important to address any such issues, and perhaps the next steps are for model atmosphere and hydrodynamical approaches to converge and attempt to produce a much more realistic model of a hot

star and its wind. Krtička et al. (2010) have made first steps in treating more fully the decoupling of a stellar wind in the context of a low metallicity environment. Any real issue with the theory of line-driving leads to a problem with predictions of evolutionary tracks, which cannot deal with changes in O star mass-loss rates of more than a factor of around 2-4 (Hirschi et al. 2008).

If the understanding of line-driving is not to blame for producing this discordance, then we must instead look to the quantities from which the mass-loss rate has been derived (see Equation 5.3). This means we should question the ion fraction (or the mechanism from which it has been constrained), the elemental abundance and the local radial optical depth.

We can immediately dismiss the elemental abundance $A_E$ as a possible source of discrepancy; the solar carbon abundance is very well constrained and there is no reason to suspect that Galactic O main sequence stars should have a significantly modified set of abundances from the solar values. Indeed Marcolino et al. (2009) performed an explicit abundance analysis on their sample of O dwarfs and found nothing out of the ordinary.

Turning again to the ion fractions, we can question whether we have good reason not to trust those produced by CMFGEN in Chapter 4. In favour of those ion fractions we have the fact that the corresponding spectra are quite representative of typical observed objects' spectra for many cases. The wind profiles fare well in a side-by-side comparison with observations for much of the range over which the grid in earlier chapters runs. The part of that range that brings most difficulties though is the later end of the dwarf range. Modifications to the X-ray flux are required to produce realistic CIV profiles, although it remains within the observed range for O stars. In any case, the predictions of CMFGEN would need to be wrong by some way in order to bring the predicted mass-loss rates in this chapter into line with those of Vink et al. (2000) - the ion fractions would need to change from being of order 0.1 and upwards to being of order 0.001. This is not a reasonable change to expect merely from a set of modified parameters in the code; rather the way the code works and the physics it employs would need to be altered. In the current CMFGEN framework, we have seen how the introduction of extra X-rays to make a profile weaker and hence more realistic (Chapter 3) also changes the ion fraction of $C^{3+}$. It is likely that to reduce it to 0.001 would require an X-ray flux which is too high. The newest incarnation of CMFGEN, XCMFGEN (Zsargo et al. 2009) may have new light to shed on this scenario when it is publicly released, although it's focus is on a correct and thorough treatment of OVI and a tenuous interclump medium.

If the elemental abundance and ion fractions are suitable, we are left with the possibility that $\tau_{rad}$ is not being correctly treated. This is essentially the issue of how the wind is structured but in another form. If the wind is composed of an arrangement of clumps that allow flux to pass through unattenuated (the so-called Venetian-blind model (Oskinova et al. 2007)), then the wind profile will be filled in by this flux. The value of $\tau_{rad}$ will then be underestimated compared to a profile arising from a non-porous wind. Oskinova et al. (2007) argue for such a version of strong clumping, showing how this treatment can produce the correct size of PV profile in the O supergiant $\zeta$ Puppis whilst keeping a 'canonical' mass-loss rate. The model assumes a void inter-clump medium and isotropic clumps which are described by a clump size and a characteristic clump-clump separation. That investigation proposes that there are of order $10^3$ to $10^4$ optically thick clumps in the line-forming region for $\zeta$ Puppis. This model has the advantage that the parametrisation of porosity does not affect the size of H$\alpha$ profiles. However it does not reproduce the shape of PV accurately, and is thus far only 'proven' in early O supergiants. Additionally it is a treatment which is designed to account for a discrepancy much smaller than what is seen in the current analysis.

Further questions arise regarding a 'Venetian-blind' setup, particularly if one is attempting to account for a mass-loss discordance of two orders of magnitude. Such a discordance as predicted in the current study would require the wind to be arranged into even fewer optically thick clumps, separated by even greater distance than that treated by Oskinova et al. (2007). It is not obvious that it is even possible to produce a P-Cygni profile from such a wind. As was seen in Chapter 1 the formation of a P-Cygni profile requires an absorptive column in front of the disc of the star and a 'halo' of material in the rest of the wind following some velocity law. A wind composed of only a handful of clumps might not follow anything like a $\beta$ law, and the absorption from only a few clumps may not produce the characteristic absorption trough seen in observations.

Another problem with a wind composed of relatively few, relatively large optically thick clumps, is that we would expect to see a lot of variability in the wind profiles as these clumps propagate out from the star. Whilst we do see some variability in the profiles such as DACs, these tend to be rotationally modulated. There is no obvious reason why clumps would be rotationally modulated, especially given they are likely to be going through a process of formation and destruction with time. Studies of variability in O dwarf stars by Kaper et al. (1997, 1999) show no such 'random' changes in the wind profiles. If there is

some arrangement of optically thick clumps however, it is possible that very high quality data taken in future could help to constrain the scale of the clumps.

Another way in which a wind could be 'porous', and hence the radial optical depth might be underestimated, is that prescribed by Sundqvist et al. (2010). In that study it is stated that for line formation in the winds of hot stars, the primary effect from optically thick clumping is likely to come from the velocity field rather than from a spatial porosity like that from Oskinova et al. (2007). This velocity-porosity, or 'vorocity' Owocki (2008), has an effect even if a homogeneous velocity field is assumed, according to the authors. Further, they show that only a relatively modest clumping scenario is required to give very clear reductions in profile strength, and so the picture is potentially consistent with the findings of the earlier chapters of this thesis.

As yet however, the work of Sundqvist et al. (2010) has been applied mainly to supergiants in order to address the PV problem, and not to dwarfs. If it's effects are similar in the less luminous regime then it is a real contender to explain the discordance of mass-loss rates, by way of weakening profiles and hence causing $\tau_{rad}$ to be underestimated.

It is highly desirable that new treatments of porosity, vorosity and optically thick clumping be applied directly to O dwarfs, a category of object that according to this thesis does not need a strong clumping scenario to predict realistic spectra, and yet still exhibits a major mass-loss discrepancy.

In conclusion, in this chapter it has been shown that:

- CIV doublets in weak wind O dwarfs can be very well fitted empirically, and the quantity $\dot{M}q_i$ be derived and well determined.
- NV is also well fitted in a high fraction of the same objects, and any uncertainties due to poorly fitted emission peaks or blending with Ly$\alpha$ are resolved by normalising the velocity range in the profile which is considered when computing $\dot{M}q_i$.
- If 'canonical' mass-loss rates are assumed, there is a sizable discordance between the resultant ion fractions and those derived using CMFGEN.
- Similarly, if the CMFGEN ion fractions, which stem from what are believed to be good models, are adopted, then the resulting mass-loss rates are much lower than

those derived using the Vink mass-loss recipe.

- The derived mass-loss rates from NV and CIV agree best when unclumped model ion fractions from CMFGEN are used.
- Taking the ratio of ion fractions for CIV and NV in SEI and comparing to clumped and unclumped cases in CMFGEN, the unclumped case is a far better match.
- There does not appear to be a peak in ion fraction over the narrow effective temperature range in question, for either $C^{3+}$ or $N^{4+}$. If this peak does exist, it would most likely be washed out by the scatter in the data.
- A thorough investigation into the effects of optically thick clumping and associated phenomena is required in this temperature and luminosity regime, although the only thing driving this is that there remains a discrepancy in mass-loss rates or ion fractions, not that there is a difficulty in producing realistic model spectra.

This page is intentionally left almost blank

# Chapter 6

# NLTE fits of Sulphur wind lines

*'I have had my results for a long time: but I do not yet know how I am to arrive at them. '*

Karl Friedrich Gauss

Sulphur in early O supergiants has three consecutive ion stages with corresponding wind lines in (F)UV observations. Additionally, these three stages ($S^{3+}$, $S^{4+}$ and $S^{5+}$) are predicted by the CMFGEN models computed in this thesis work (Chapters 2, 3 and 4) to account for almost all the sulphur in the wind, in most clumping and X-ray scenarios. It is only in the smooth wind model with X-rays that $S^{6+}$ also becomes significant (see Figure 6.1). This presents an opportunity to perform an exploratory study on these sulphur lines, and to try and determine mass-loss properties of the early supergiants.

A second very important reason to explore mass-loss according to the excited Sv line at 1502Å in particular is that discussed by Waldron & Cassinelli (2010). In that work it is claimed that whilst the effects of extreme-UV (XUV) radiation change the interpretation of Pv profiles regarding mass-loss, Sv is immune to those effects. This comes through the fractional abundance of $P^{4+}$ being reduced by XUV radiation. A mass-loss determination from Sv ought to be more robust than the somewhat controversial Pv (Fullerton et al. 2006). The SEI code (see Chapter 5) was originally built to deal with resonance lines only, and the Sv line is an excited line. New and ongoing work is seeking to introduce a

**Figure 6.1.** CMFGEN fractions of sulphur ions, reproduced from Chapter 4. Black = $S^{3+}$, red = $S^{4+}$, green = $S^{5+}$, blue = $S^{6+}$.

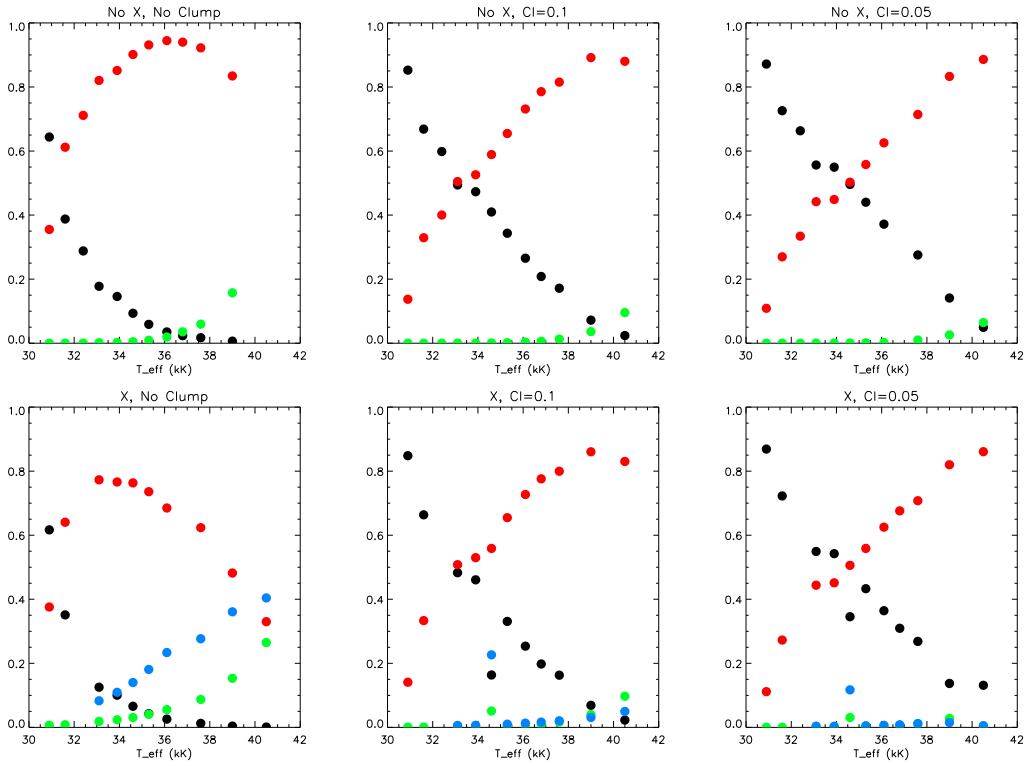


more complex source function to model the Sv excited line using SEI. This requires the populations of sulphur ions to be correctly estimated, and highlights the importance of ab initio NLTE calculations such as those with CMFGEN for estimating these populations.

A further final reason to use sulphur lines is that it is a non-CNO element, and as such it is expected to remain at solar abundance in Galactic objects, having not been processed as C, N and O are. This puts it ahead of oxygen, which also has three successive ion stages with observable wind lines.

In this chapter, a pilot study using sulphur lines is performed as a check on the current mass-loss estimates that exist. A small sample of Galactic early O type supergiants with spectral types O4 or O5 I are modelled using CMFGEN, utilising grid models described in Chapter 2 as starting points. A fit to Sv is prioritised, and Siv and Svi are also addressed. The best-fitting mass-loss rate for each object is determined and this is compared to current best estimates in the literature. Finally ion fractions are read from the best fitting models such that $\dot{M}q_i$ can be derived; a quantity which has been used in the preceding chapter, and is key to any future empirical mass-loss studies that may utilise sulphur lines.

## 6.1 The sample

We expect to see SiV (1063,1073Å, $3s^2 3p - 3s3p^2$) and SVI (933,945Å, $2p^6 3s - 2p^6 3p$) wind lines over much of the O star range, particularly in supergiants, as is evidenced by all the model spectra in Chapter 3. SiV appears in all the supergiant models whilst SVI has weakened to photospheric between O6.5 and O9. SV (1502Å, $3s3p - 3p^2$) however is usually much weaker because it forms from an excited transition rather than being a resonance line, as the others are. CMFGEN appears to suggest that $S^{4+}$ is actually that dominant stage for much of the temperature range of O supergiants, subject to the effects of X-rays and clumping as discussed in Chapter 4. For any scenario this ion is at least an important contributor to the total sulphur population in the wind, as seen in Figure 6.1. The analysis of mass-loss depending on sulphur must be done using objects where the SV line exhibits the effects of a wind, i.e. a relatively strong, asymmetric profile. An examination of archival UV data (from *IUE*) of various O subtypes shows that for Galactic objects only the earlier types of supergiants have a clear SV wind profile, and it is much smaller than those exhibited by CIV and NV, for example. This is unsurprising due to the excited nature of the transition and the lower cosmic abundance of sulphur ($1.38 \times 10^{-5}$H) compared to C, N, O.

With this in mind, the objects listed in Table 6.1 were chosen to be fitted using CMFGEN. Their spectra, shown in Figure 6.2 demonstrate the slightly windy nature of the lines, compared to spectra of other objects which have only a photospheric component to the line. Since TLUSTY models (Hubeny & Lanz 1995) are used as lower boundaries for CMFGEN models, they help to show up wind lines when plotted over observations. HD 210839 is a borderline case where there is a slight asymmetry, but it was decided that only the very clear wind profiles would be modelled in this project due to the time and computing constraints present. Additionally since the SV line is only sampling a portion of the wind (generally out to approximately $0.4v_\infty$), it is more informative to measure mass-loss rates from objects with the stronger wind profiles (i.e. those that probe further out in the wind). Spectra were sourced from the Multimission Archive at STScI (MAST), resampled at every 0.1Å and normalised. There were *IUE* spectra available for all five objects listed in Table 6.1, and *FUSE* data for HD 14947 and HD 190429A. Spectra were prepared in a similar fashion to those discussed in Chapter 3 §1.

Each of the objects' spectral type was confirmed through the Galactic O star catalogue

**Table 6.1.** The sample. References for temperature and luminosity are Repolust et al. (2004) (R), Markova et al. (2004) (M), Bouret et al. (2005) (B), Martins et al. (2005*a*) (Ma) and Oskinova et al. (2007) (O). Where possible the most recent measure was used. Not all parameters were found for HD 15570 in the literature, but this is irrelevant since the object was later ejected from the sample, as discussed in the text. All terminal velocities are lifted from Prinja et al. (1990) except for HD 16691, which was set during the fitting process. Other parameter sources are discussed in the text. References for spectral type are Walborn (1972) (W72) and Walborn (1973) (W73).

| HD | Spectral Type | $v_\infty$ $(kms^{-1})$ | $v_{rad}$ $(kms^{-1})$ | $v \sin i$ $(kms^{-1})$ | $T_{eff}$ (kK) | $\log \frac{L}{L_\odot}$ |
|---|---|---|---|---|---|---|
| 14947 | O5 I (W73) | 1885 | -54 | 133 | 37.5 (R) | 5.70 (R) |
| 15570 | O4 I (W72) | 2605 | -15 | - | 39.0 | 5.83 |
| 16691 | O4 I (W73) | 2475* | -41 | - | 39.2 (M) | 5.92 (M) |
| 190429A | O4 I (W73) | 1880 | -16 | 135 | 39.0 (B) | 5.90 (B) |
| $\zeta$ Pup | O4 I (W72) | 2485 | -24 | 203 | 40.0 (Ma) | 5.90 (O) |

(Maíz-Apellániz et al. 2004), which itself draws from various literature. The original spectral classification references are included in Table 6.1.

## 6.2 Method

Fundamental physical parameters such as effective temperatures were adopted from the most recent investigations where they were deduced spectroscopically. These parameters were used to define new CMFGEN models, which were constructed using O4 and O5 I models from the grid described in Chapter 2 as starting points. Only the models including X-rays were used because it was shown in Chapter 3 that X-rays are required to produce the most realistic spectra. The initial mass-loss rates used were those from the appropriate corresponding spectral type model in the CMFGEN grid in Chapter 2 (rounded to the nearest $0.5\times10^{-6} M_\odot yr^{-1}$), and then models were produced with different mass-loss rates depending on the output from the initial model. If the Sv profile was weaker or stronger than in the observation, the subsequent model was adjusted accordingly. When several models had been accumulated, they were plotted over the observed spectrum to deduce the best fit. The use of a $\chi^2$ test was considered, but rejected in this instance due to the relatively noisy observations. Stray points in the profile due to the noise could lead to an incorrect conclusion about the best fit. As a consistency check the models were

**Figure 6.2.** Sv (marked in dotted line) weakens from early to mid type O supergiants. In O4 and O5 it is relatively strong and asymmetric, whereas by O7 it has become almost entirely photospheric. The relative strength of Civ can be seen on the right of the figure.

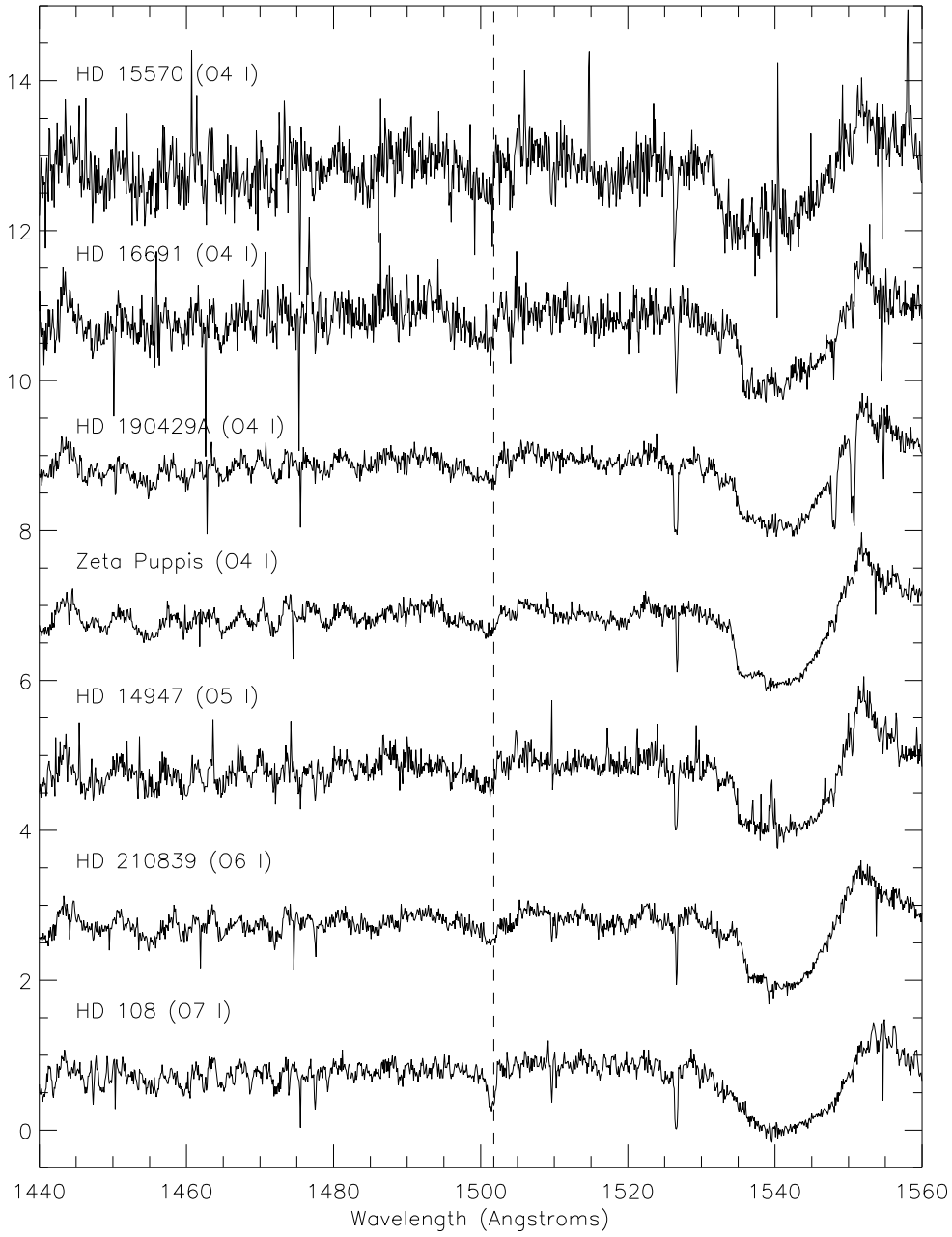

also plotted over the observed spectrum of the excited NIV line at 1720Å. This line is generally much stronger than SV and helps to show whether the model is accurate across the spectrum, for different elements.

Solar abundances according to Asplund et al. (2005) were used, bypassing an explicit abundance analysis. Such an analysis could be implemented in a more in-depth study in future, although we do not expect the abundance of sulphur to be much changed from the solar value anyway. Projected rotational velocities were adopted directly from Penny (1996), terminal velocities from Prinja et al. (1990) and radial velocities taken from SIMBAD and references therein.

The continuum level was checked against the model spectrum on either side of the wind line being modelled. If there was a clear discrepancy between model and observation, the model was used as a guide and the observed spectrum multiplied by an appropriate factor to bring them into line.

Previous chapters have shown that it is possible to regard the clumping factor as close to unity for some objects, however we know from a host of literature sources that there is wind structure of some kind present (see Chapter 1). For this reason, models were run for both the smooth wind and moderately clumped wind scenarios, and the most appropriate mass-loss rate for each case was deduced. Chapter 3 showed that for early type supergiants, the SV line is slightly sensitive to the clumping factor when X-rays are present, and that SIV is very sensitive to it. This is another reason to ensure all likely possibilities are covered regarding clumping - it is possible that the clumping factor lies somewhere between the smooth and moderately clumped cases.

It is difficult to achieve a good fit to both the absorption and emission components of the SV wind profile. Priority was given to fitting the absorption since the absorptive column is more sensitive to changes in the mass-loss rate.

Where far-UV observations were available from the archive (i.e. for HD 14947 and HD 190429A), the SIV doublet was used as a secondary check on the mass-loss rate. In most data from Galactic O stars it is difficult to precisely determine the shape of the SIV doublet against the overlying interstellar profiles. Given the contrasting shapes of interstellar lines and the absorption components of resonance wind lines however, it is possible to trace the depth and shape of the wind line in an approximate way.

It is impossible to fit SVI lines in the stars in this sample, since the interstellar extinction, interstellar lines and sheer noise make the spectrum shortward of 1000Å very difficult

to interpret and normalise (see Fig 6.3). It is possible to fit this line also in LMC or SMC stars, and indeed this has begun to be done by some authors, but a lower metallicity makes SV more difficult to observe in some LMC/SMC objects.

**Figure 6.3.** The *FUSE* spectrum shortward of 1000Å, resampled at 0.1Å. A CMFGEN model is scaled and shown in red, showing how much of the expected spectrum is wiped out by interstellar lines, extinction and noise. The dotted lines show the rest wavelengths of the SVI doublet.

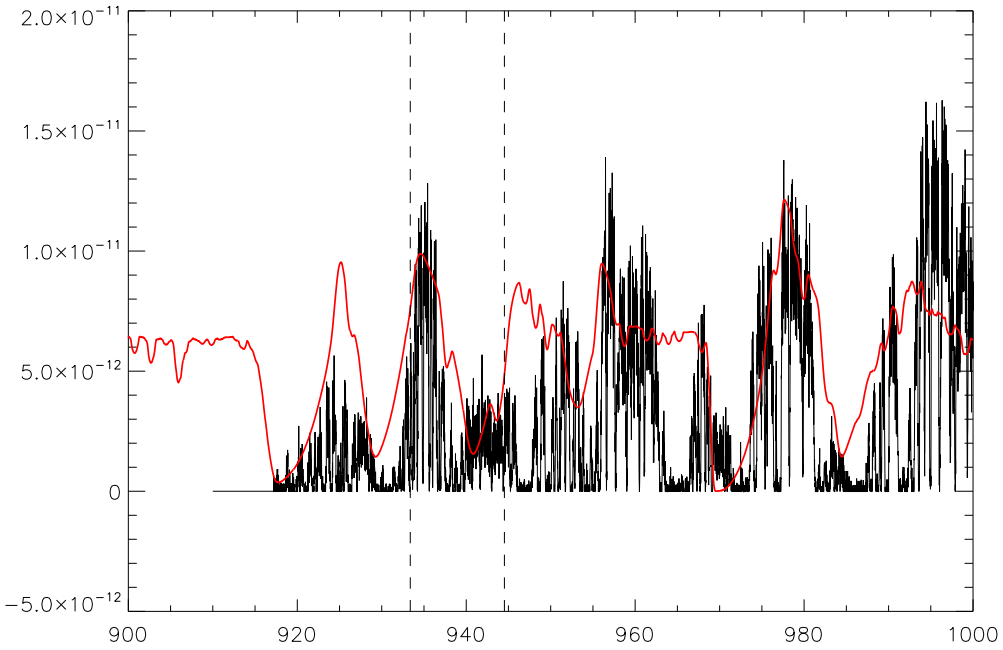


## 6.3 Fits

HD 15570 has a much larger noise level in *IUE* archival observations than other sample objects, and moreover there is only one observation on the archive, so an average cannot be taken. Three models fitted using temperature and luminosity parameters from the CMFGEN grid discussed in Chapter 2 are plotted over the sole observation in Figure 6.4. Because of this high level of noise the object was ejected from the sample and no further models were run.

Fits for the other four sample objects are shown in Figures 6.5 to 6.24. SV is fitted in all objects for both clumped and unclumped scenarios. SIV is also fitted in HD 14947 and HD190429A, the objects where *FUSE* data is available. All figures for sulphur lines are

shown with the same axis scale - this highlights the difference in strength between the SV and SIV lines.

**Figure 6.4.** The noise level in the sole archival observation of HD15570 was too high for further analysis. The three models (in this case with clumped winds) have mass-loss rates of 4, 5 and $6\times10^{-6}M_{\odot}yr^{-1}$ (red, green and blue respectively). This shows that the mass-loss rate is approximately $5\times10^{-6}M_{\odot}yr^{-1}$, but due to the excessive noise a tight constraint cannot be gained.

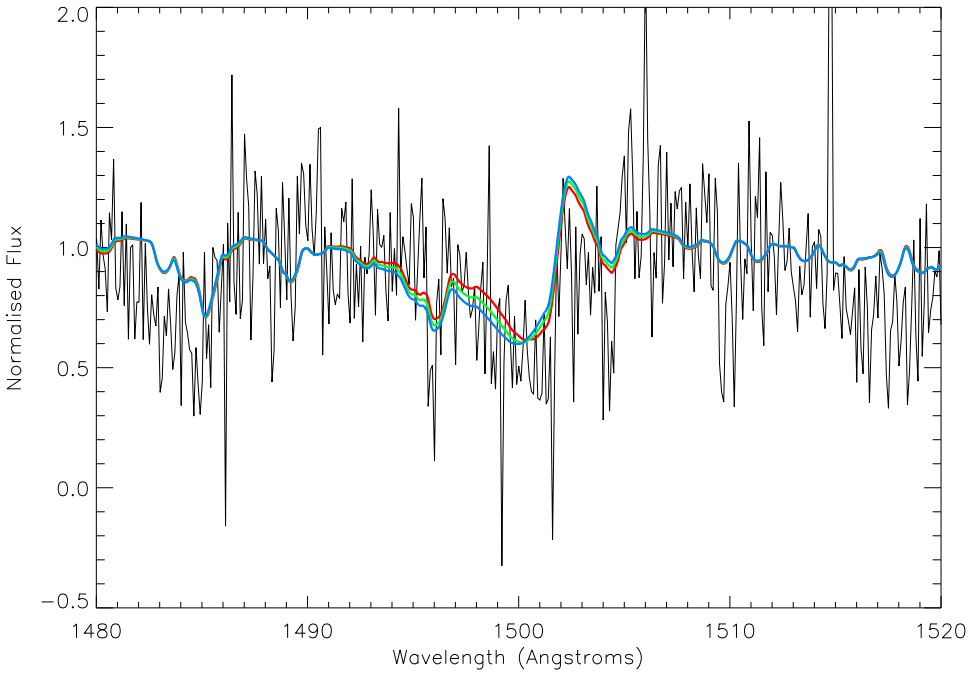


### 6.3.1 Comments on the fits

#### HD 14947

Figure 6.5 shows the fits derived for a clumped wind scenario in HD 14947. With priority given to fitting the absorption column, the best fit from the models gives a mass-loss rate of $1\times10^{-6}M_{\odot}yr^{-1}$. The models on either side which have mass-loss rates of 0.5 and $1.5\times10^{-6}M_{\odot}yr^{-1}$ appear to be good constraints and thus the uncertainties have upper limits of $0.5\times10^{-6}M_{\odot}yr^{-1}$. The level of the continuum seems to be set appropriately as the models pass through the parts of the observed spectrum on either side of the wind line.

Figure 6.6 shows model fits to HD 14947 but with an unclumped wind scenario. The best fitting model here also has a mass-loss rate of $1\times10^{-6}M_{\odot}yr^{-1}$, with upper and lower

**Figure 6.5.** Clumped model fits to Sv for HD 14947. Red = $0.5\times10^{-6}M_{\odot}yr^{-1}$, green: $1\times10^{-6}M_{\odot}yr^{-1}$, blue: $1.5\times10^{-6}M_{\odot}yr^{-1}$

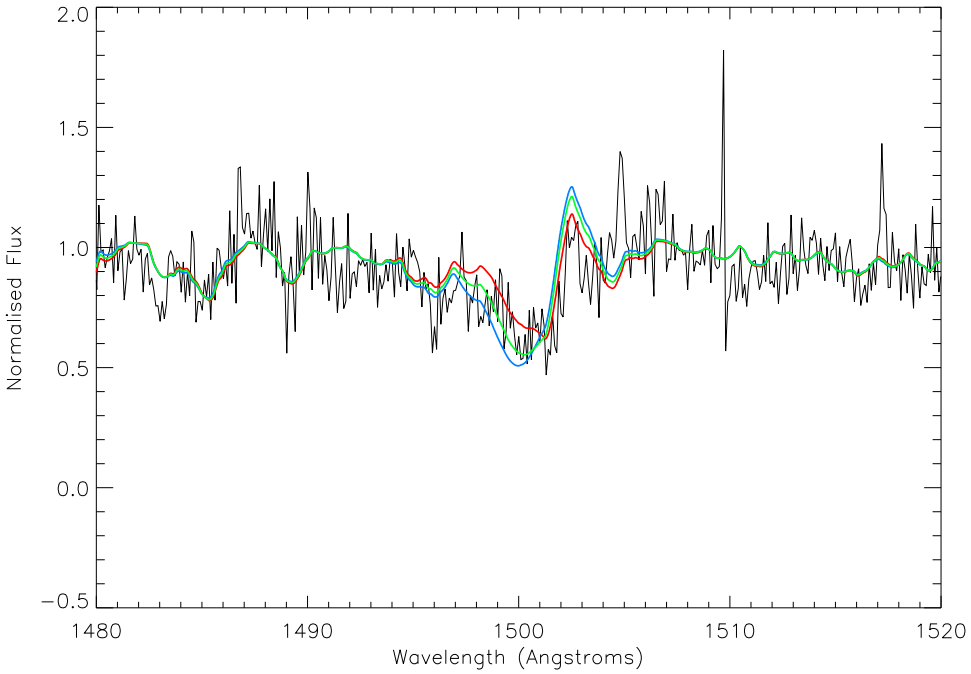


**Figure 6.6.** Unclumped model fits to Sv for HD 14947. Red: $0.5\times10^{-6}M_{\odot}yr^{-1}$, green: $1\times10^{-6}M_{\odot}yr^{-1}$, blue: $2\times10^{-6}M_{\odot}yr^{-1}$

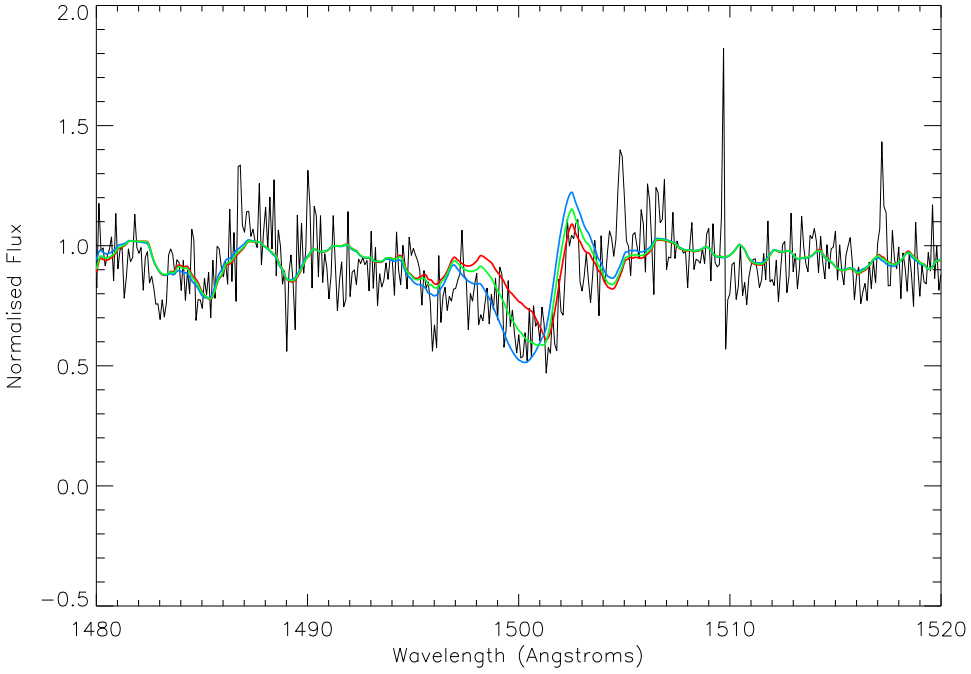

limits of 2 and $0.5\times10^{-6}M_{\odot}yr^{-1}$ respectively. These are conservative uncertainties since the models at the outer limits only just pass through the observed spectrum.

**Figure 6.7.** Clumped model fits to SiV for HD 14947. Red = $0.5\times10^{-6}M_{\odot}yr^{-1}$, green: $1\times10^{-6}M_{\odot}yr^{-1}$, blue: $1.5\times10^{-6}M_{\odot}yr^{-1}$

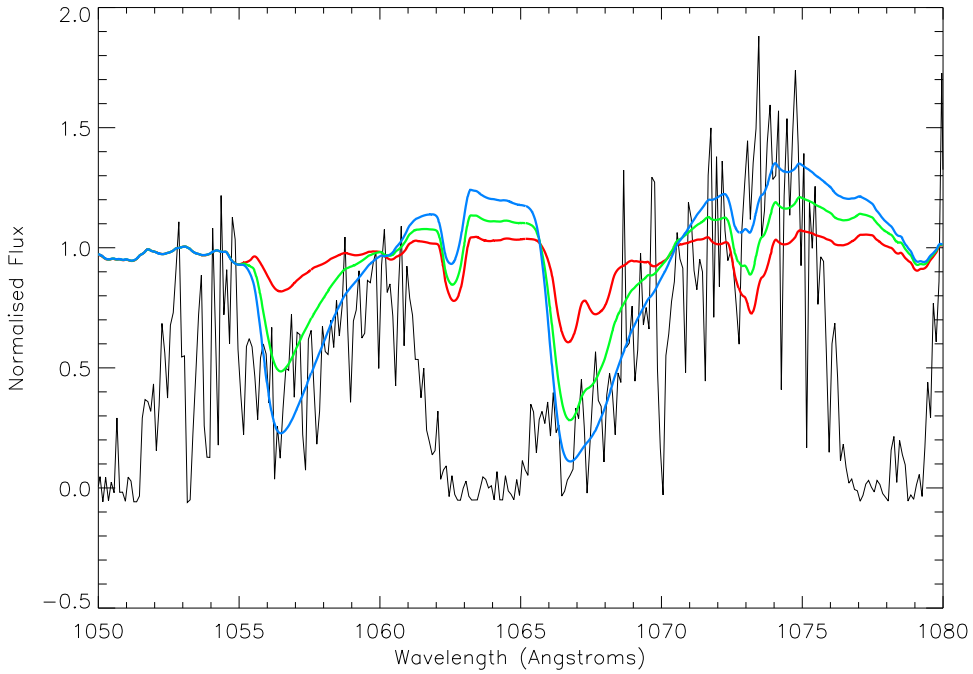


Figures 6.7 and 6.8 show the same models but at the wavelength range of SiV, plotted over *FUSE* observations. For the clumped case a mass-loss rate of $1\times10^{-6}M_{\odot}yr^{-1}$ appears to come up a little short, and $1.5\times10^{-6}M_{\odot}yr^{-1}$ seems more appropriate. This could be partly due to the difficulty in setting a continuum level in the observations of the far-UV due to interstellar line pollution. In general the clumped wind fits confirm a mass-loss rate in the range 1-1.5$\times10^{-6}M_{\odot}yr^{-1}$. The unclumped models on the other hand do not fit very well at all, and the model that fits the SV line best has SiV profiles which are too weak. As is shown in Figure 6.8 it takes a mass-loss rate of $4\times10^{-6}M_{\odot}yr^{-1}$ to get close to fitting the observed profile. This could constitute evidence that clumped models from CMFGEN are more appropriate in the far-UV.

Figures 6.9 and 6.10 show a range of models plotted for NiV (1718.6Å), used as a consistency check on the results derived from sulphur. For the clumped case the best fitting model has a mass-loss rate of $1.5\times10^{-6}M_{\odot}yr^{-1}$, and there is a suggestion that even a slightly higher value might be a better fit. This is a larger value than was derived

**Figure 6.8.** Unclumped model fits to SiV for HD 14947. Red: $0.5\times10^{-6}M_{\odot}yr^{-1}$, green: $1\times10^{-6}M_{\odot}yr^{-1}$, blue: $2\times10^{-6}M_{\odot}yr^{-1}$, yellow: $4\times10^{-6}M_{\odot}yr^{-1}$

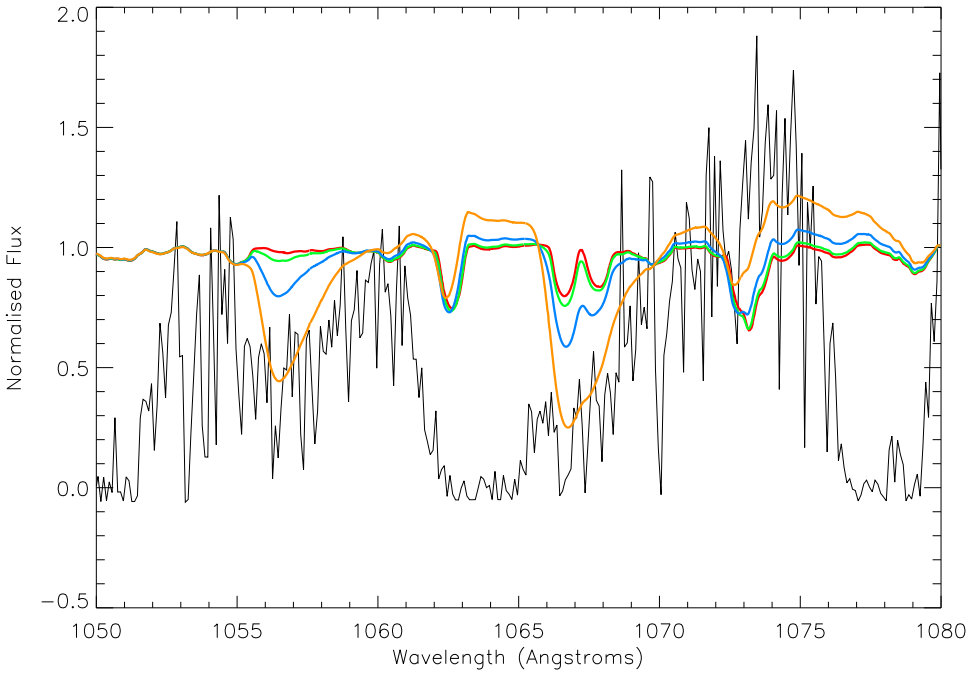


**Figure 6.9.** Clumped model fits to NiV for HD 14947. Red $= 0.5\times10^{-6}M_{\odot}yr^{-1}$, green: $1\times10^{-6}M_{\odot}yr^{-1}$, blue: $1.5\times10^{-6}M_{\odot}yr^{-1}$

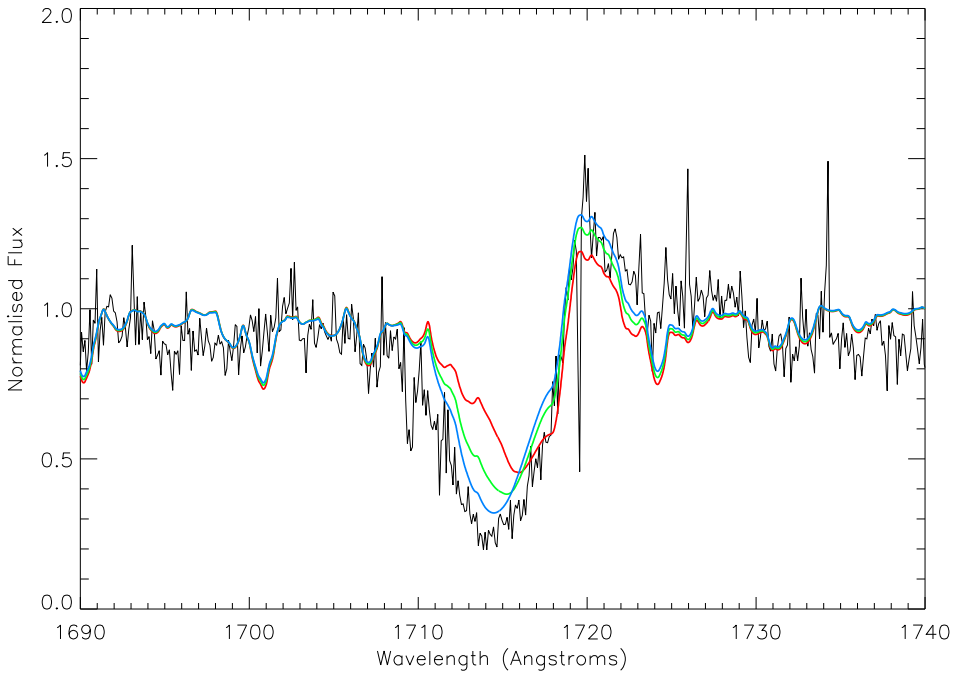

**Figure 6.10.** Unclumped model fits to NIV for HD 14947. Red = $0.5\times10^{-6}M_{\odot}yr^{-1}$, green: $1\times10^{-6}M_{\odot}yr^{-1}$, blue: $2\times10^{-6}M_{\odot}yr^{-1}$, yellow: $4\times10^{-6}M_{\odot}yr^{-1}$

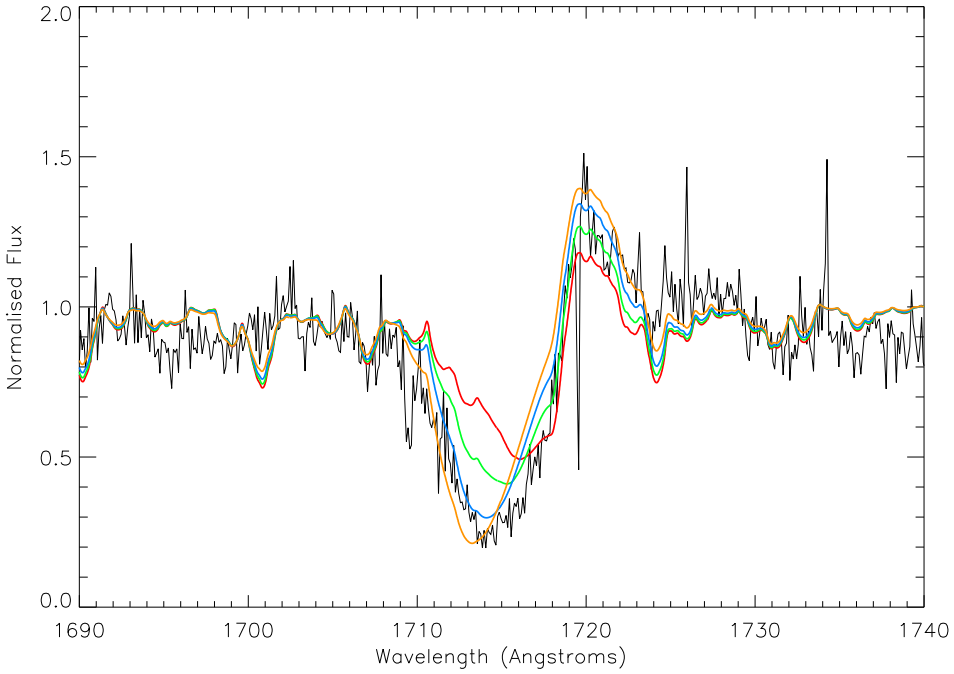


using SV, but is close enough to give confidence in a rate of around 1-2$\times10^{-6}M_{\odot}yr^{-1}$, accounting for all diagnostics treated here. The unclumped case for NIV has a best fit value between 2 and $4\times10^{-6}M_{\odot}yr^{-1}$. Again this value is higher than derived from just SV, and perhaps gives reason for the uncertainties to be increased.

### HD 16691

Figure 6.11 shows the clumped model fits to the observed spectrum of HD 16691 around SV. This observed spectrum is rather noisy, but not nearly as noisy as that of HD 15570. A patch of the spectrum to the left of SV makes it difficult to gauge the continuum level with very good accuracy, although the rest of the spectrum at this wavelength regime seems to suggest that the continuum level chosen is correct. Models with mass-loss rates of 0.8 and $4\times10^{-6}M_{\odot}yr^{-1}$ are at the absolute limits of the profile, and represent very conservative uncertainties. The mass-loss rate that fits best is in the range 1.5-2$\times10^{-6}M_{\odot}yr^{-1}$. A nominal rate of $1.75\times10^{-6}M_{\odot}yr^{-1}$ is adopted, although there is no explicit model for this.

Figure 6.12 shows some unclumped models plotted with the observed spectrum. The

**Figure 6.11.** Clumped model fits to Sv for HD 16691. Red: $0.8{\times}10^{-6} M_{\odot} yr^{-1}$, green: $1.5{\times}10^{-6} M_{\odot} yr^{-1}$, blue: $2{\times}10^{-6} M_{\odot} yr^{-1}$, yellow: $4{\times}10^{-6} M_{\odot} yr^{-1}$

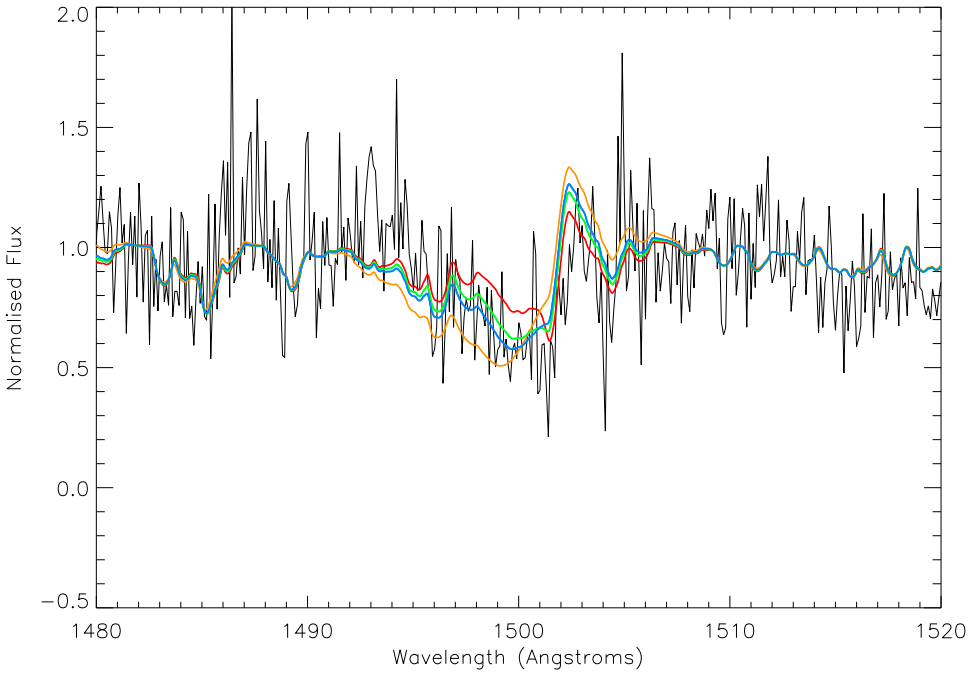


**Figure 6.12.** Unclumped model fits to Sv for HD 16691. Red: $3{\times}10^{-6} M_{\odot} yr^{-1}$, green: $4{\times}10^{-6} M_{\odot} yr^{-1}$, blue: $5{\times}10^{-6} M_{\odot} yr^{-1}$

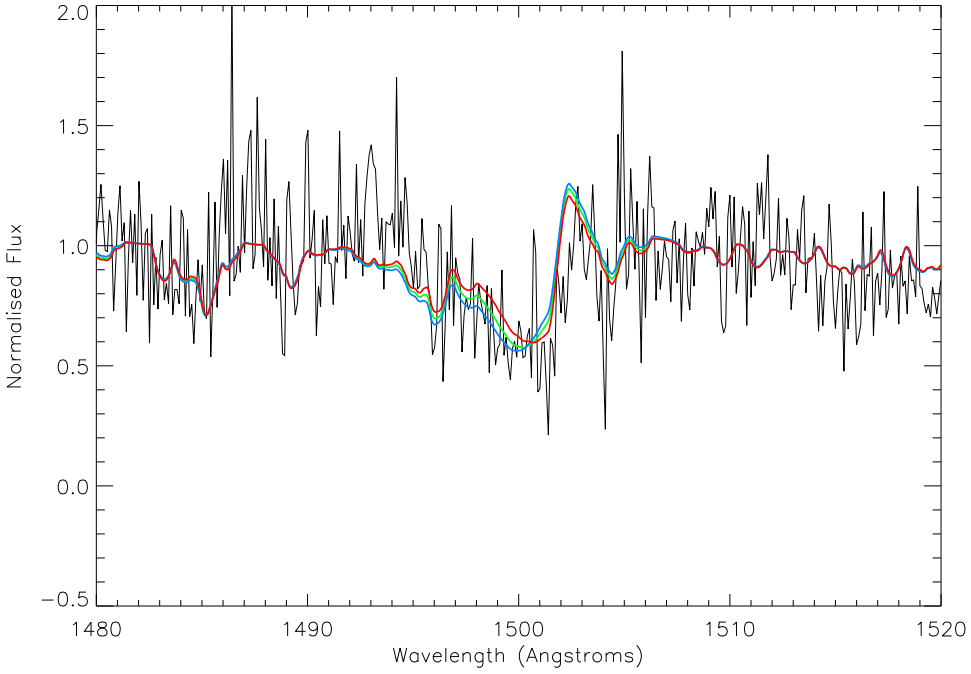

mass-loss rate alterations make less difference than for the clumped case. The models offer an informative constraint on the mass-loss rate of $4\pm1\times10^{-6}M_{\odot}yr^{-1}$. This value differs from that gained from the clumped models by around a factor of 2.

**Figure 6.13.** Clumped model fits to NIV for HD 16691. Red: $0.8\times10^{-6}M_{\odot}yr^{-1}$, green: $1.5\times10^{-6}M_{\odot}yr^{-1}$, blue: $2\times10^{-6}M_{\odot}yr^{-1}$, yellow: $4\times10^{-6}M_{\odot}yr^{-1}$

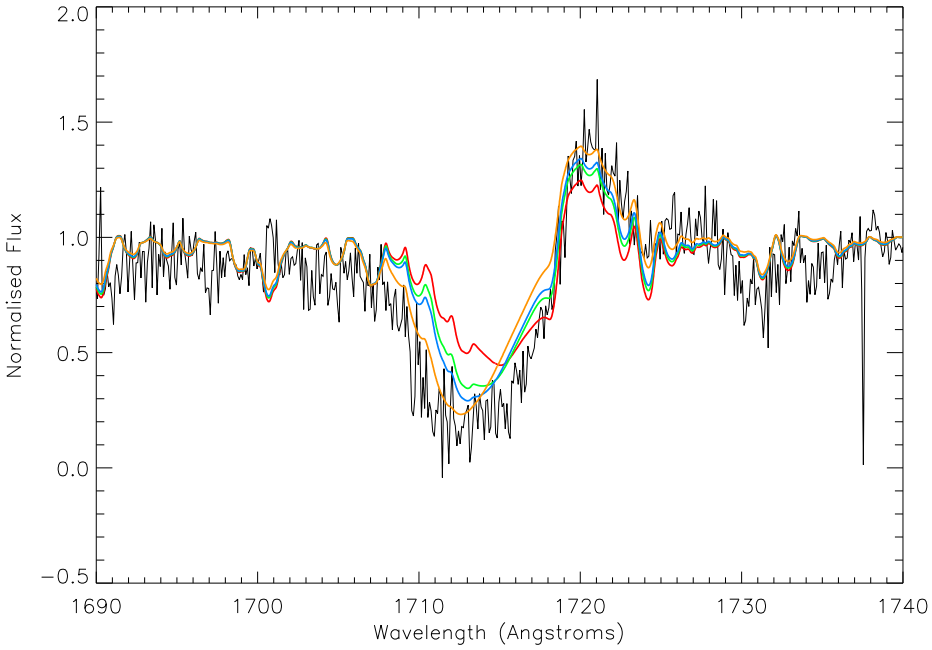


Figures 6.13 and 6.13 show the NIV fits for HD 16691. In the case of a clumped wind the best fitting model has a mass-loss rate of $4\times10^{-6}M_{\odot}yr^{-1}$, which is at the upper boundary of uncertainty obtained by modelling SV. In the unclumped case, the fits to NIV confirm with some confidence the mass-loss rate obtained using SV.

### HD 190429A

Figure 6.15 shows model fits to HD 190429A for a clumped wind. The observed spectrum is much cleaner where noise is concerned than other objects discussed before, and the continuum level can be in little doubt. The upper and lower limits shown in Figure 6.15 are just outside the observed data in the absorption part of the profile, and so are very conservative limits. They represent uncertainties of $1\times10^{-6}M_{\odot}yr^{-1}$. With some very simple visual interpolating it is likely that the mass loss with tighter uncertainties would be $1.5\pm0.5\times10^{-6}M_{\odot}yr^{-1}$.

**Figure 6.14.** Unclumped model fits to NIV for HD 16691. Red: $3\times10^{-6}M_{\odot}yr^{-1}$, green: $4\times10^{-6}M_{\odot}yr^{-1}$, blue: $5\times10^{-6}M_{\odot}yr^{-1}$.

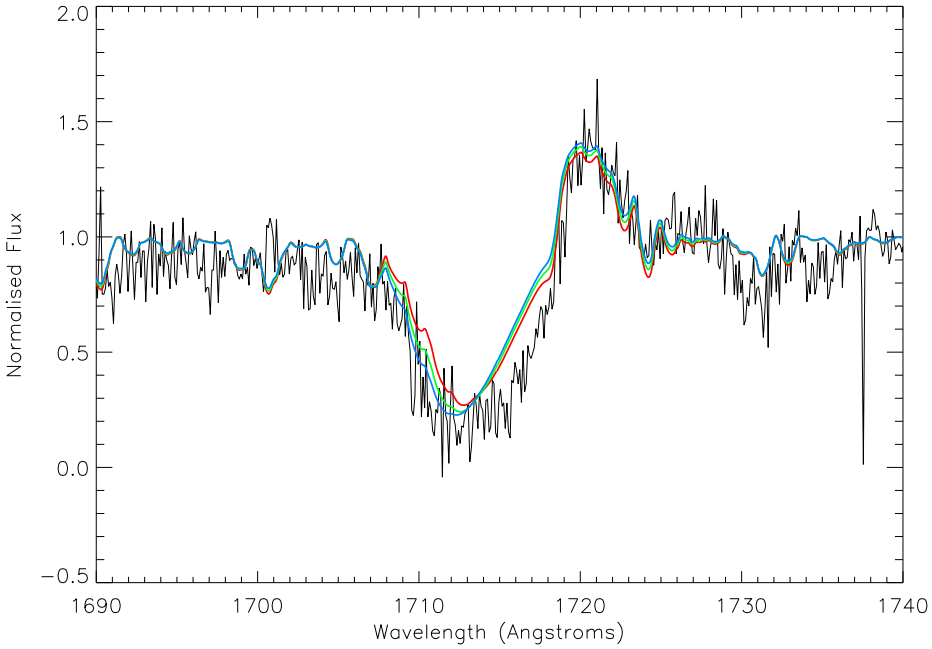


**Figure 6.15.** Clumped model fits to SV for HD 190429A. Red: $0.5\times10^{-6}M_{\odot}yr^{-1}$, green: $1.5\times10^{-6}M_{\odot}yr^{-1}$, blue: $2.5\times10^{-6}M_{\odot}yr^{-1}$

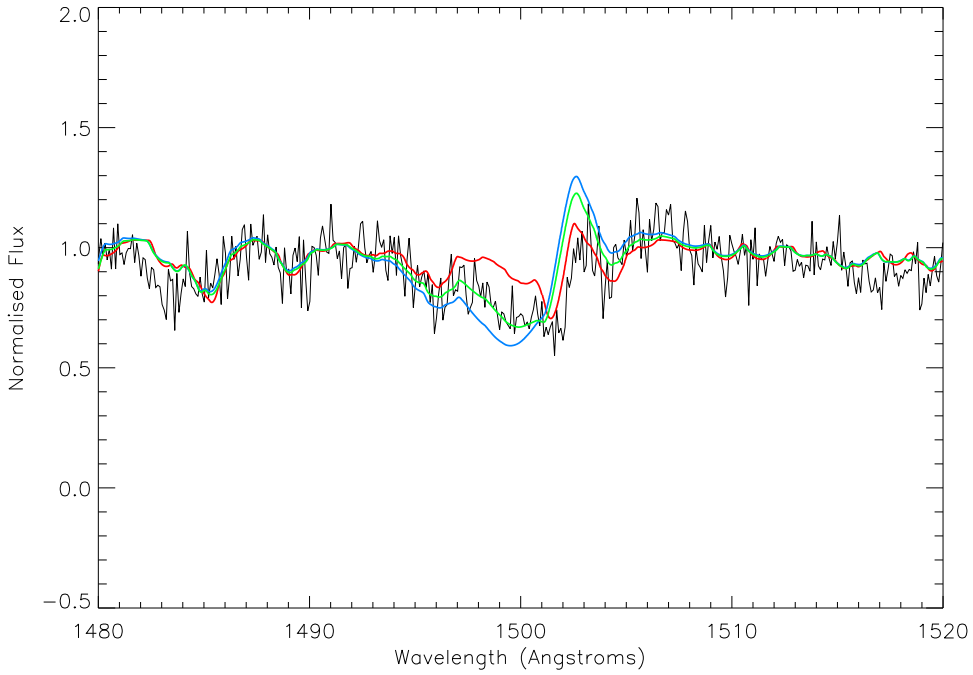

**Figure 6.16.** Unclumped model fits to SV for HD 190429A. Red: $0.5\times10^{-6}M_{\odot}yr^{-1}$, green: $1.5\times10^{-6}M_{\odot}yr^{-1}$, blue: $2\times10^{-6}M_{\odot}yr^{-1}$, yellow: $2.5\times10^{-6}M_{\odot}yr^{-1}$

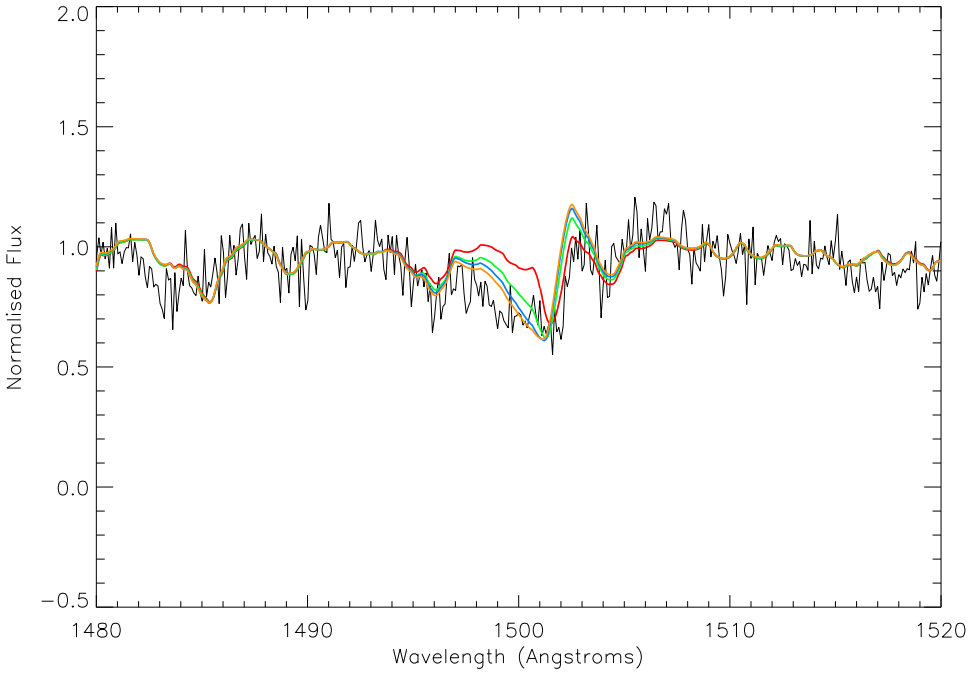


Figure 6.16 shows the unclumped model fits. $0.5\times10^{-6}M_{\odot}yr^{-1}$ is clearly too low to match the profile, but the absorption component does not vary significantly over the range 1.5 to $2.5\times10^{-6}M_{\odot}yr^{-1}$. The redward portion of the absorption component cannot be perfectly matched by any model, but the best is probably that with a mass-loss rate of $1.5\times10^{-6}M_{\odot}yr^{-1}$. The blueward component is not matched by any model, and so there is a problem with reproducing the shape of the profile. Despite this, it is clear that a mass-loss rate of the order 2-3$\times10^{-6}M_{\odot}yr^{-1}$ achieves the correct size of profile. A mass-loss rate of $2.5\times10^{-6}M_{\odot}yr^{-1}$ is adopted, but without a clear upper limit in uncertainty due to a lack of appropriate models. The lower limit of $1.5\times10^{-6}M_{\odot}yr^{-1}$ is appropriate given the model's position near the top of the data in the observed spectrum.

Figure 6.17 shows the clumped model fits to the SIV doublet in HD 190429A. The best fit lies between the models with 1.5 and $2.5\times10^{-6}M_{\odot}yr^{-1}$, which matches the SV estimate within the errors. As there was for HD 14947 there is some uncertainty related to where the continuum level is chosen for HD 190429A due to interstellar lines. For this reason the SIV fits offer only a mild constraint on the mass-loss rate.

Figure 6.18 shows the unclumped models and observation of the SIV doublet. A large

**Figure 6.17.** Clumped model fits to SiV for HD 190429A. Red: $0.5\times10^{-6}M_{\odot}yr^{-1}$, green: $1.5\times10^{-6}M_{\odot}yr^{-1}$, blue: $2.5\times10^{-6}M_{\odot}yr^{-1}$

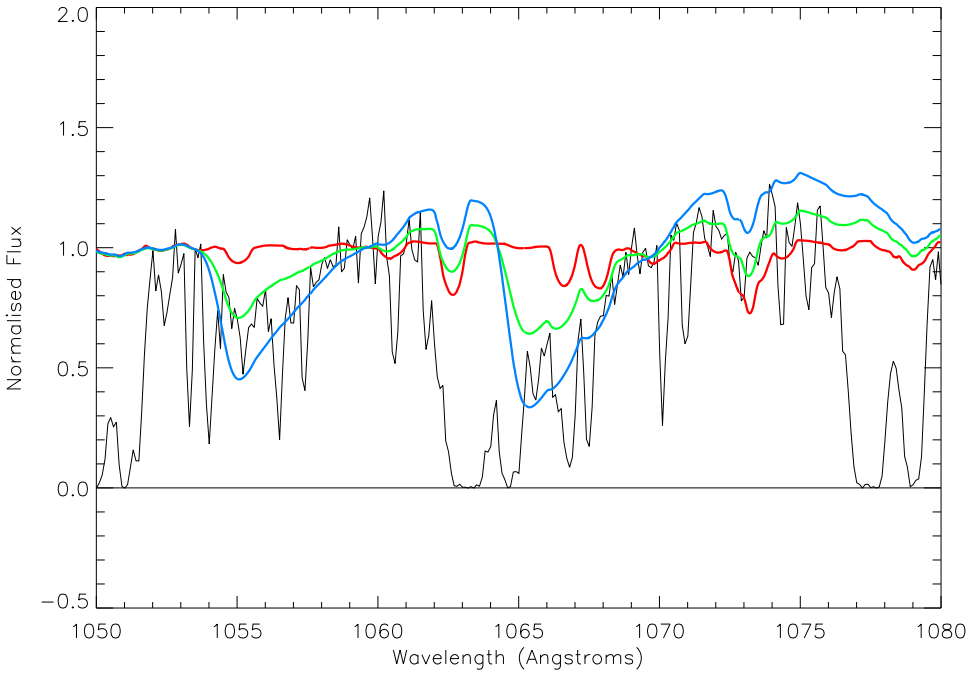


**Figure 6.18.** Unclumped model fits to SiV for HD 190429A. Changing the mass-loss rate from 0.5 all the way to 4.0 makes very little difference to the model.

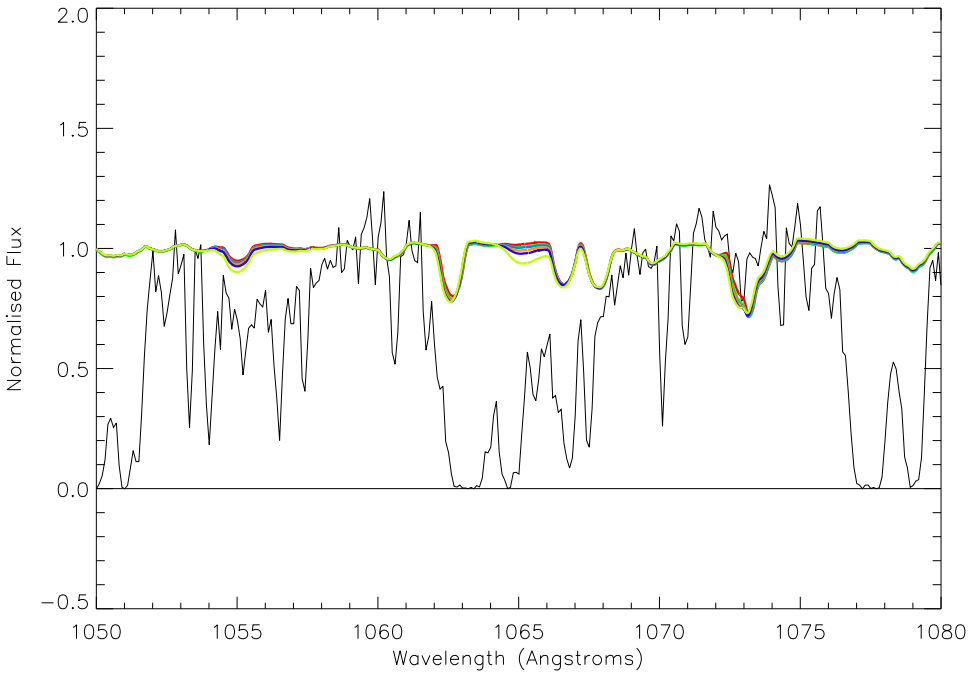

variation in the mass-loss rate, from 0.5 to $4\times10^{-6}M_{\odot}yr^{-1}$ barely changes the profiles at all, and the model doublet is far too weak compared to the observed spectrum. A far higher mass-loss rate is needed to match the profile, and this might lead to a SV profile which is unrealistically strong in the same model. It is very striking how different the fits are for clumped and unclumped scenarios, and it appears in this case that the line is very sensitive to clumping. One would expect this to be due to a major shift in the population levels, but Figure 6.1 shows that clumping does not change the population of $S^{3+}$ drastically at hotter temperatures. All this may imply that only clumped-wind models can consistently reproduce the sulphur spectrum of O supergiants.

**Figure 6.19.** Clumped model fits to NIV for HD 190429A. Red: $0.5\times10^{-6}M_{\odot}yr^{-1}$, green: $1.5\times10^{-6}M_{\odot}yr^{-1}$, blue: $2.5\times10^{-6}M_{\odot}yr^{-1}$

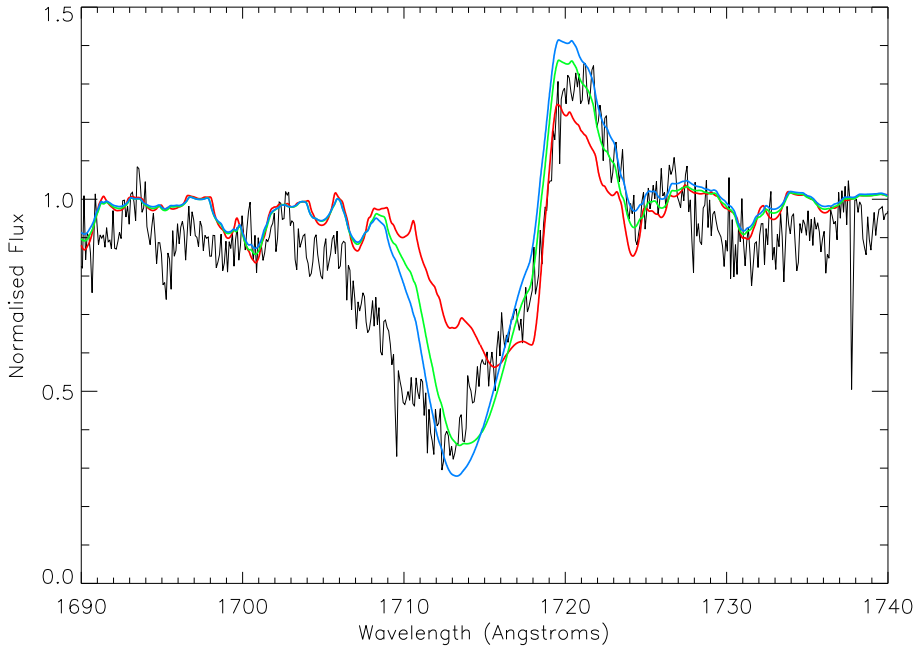


Figures 6.19 and 6.19 show the fits to NIV for HD 190429A. The profile is not well matched in either case at higher velocities, however the mass-loss rates for the best fitting profiles are $1.5\times10^{-6}M_{\odot}yr^{-1}$ and $2\times10^{-6}M_{\odot}yr^{-1}$ for the clumped and unclumped cases respectively. Due to this problem with profile fitting the HeII wind line (1640.4Å) was also used for consistency (as shown in Figures 6.21 and 6.22). For the clumped case a mass-loss rate of $1.5\times10^{-6}M_{\odot}yr^{-1}$ fits the absorption trough best, although only that with $2.5\times10^{-6}M_{\odot}yr^{-1}$ can reproduce the emission. In the unclumped case none of the

**Figure 6.20.** Unclumped model fits to NIV for HD 190429A. Red: $0.5\times10^{-6}M_{\odot}yr^{-1}$, green: $1.5\times10^{-6}M_{\odot}yr^{-1}$, blue: $2\times10^{-6}M_{\odot}yr^{-1}$, yellow: $2.5\times10^{-6}M_{\odot}yr^{-1}$

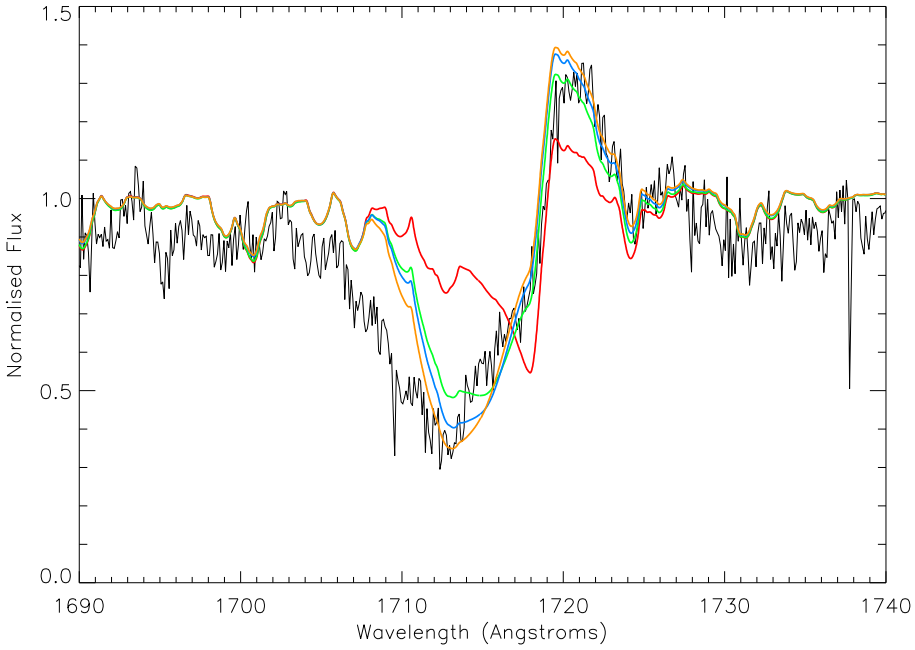


**Figure 6.21.** Clumped model fits to HeII for HD 190429A. Red: $0.5\times10^{-6}M_{\odot}yr^{-1}$, green: $1.5\times10^{-6}M_{\odot}yr^{-1}$, blue: $2.5\times10^{-6}M_{\odot}yr^{-1}$

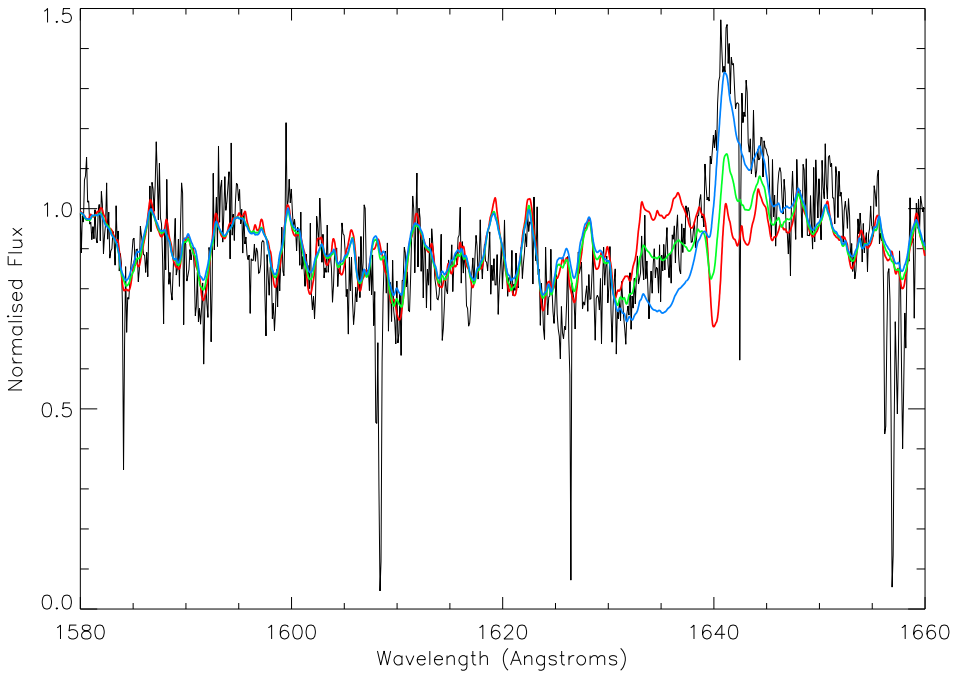

**Figure 6.22.** Unclumped model fits to HeII for HD 190429A. Red: $0.5\times10^{-6}M_{\odot}yr^{-1}$, green: $1.5\times10^{-6}M_{\odot}yr^{-1}$, blue: $2\times10^{-6}M_{\odot}yr^{-1}$, yellow: $2.5\times10^{-6}M_{\odot}yr^{-1}$, navy: $3\times10^{-6}M_{\odot}yr^{-1}$, lime: $4\times10^{-6}M_{\odot}yr^{-1}$

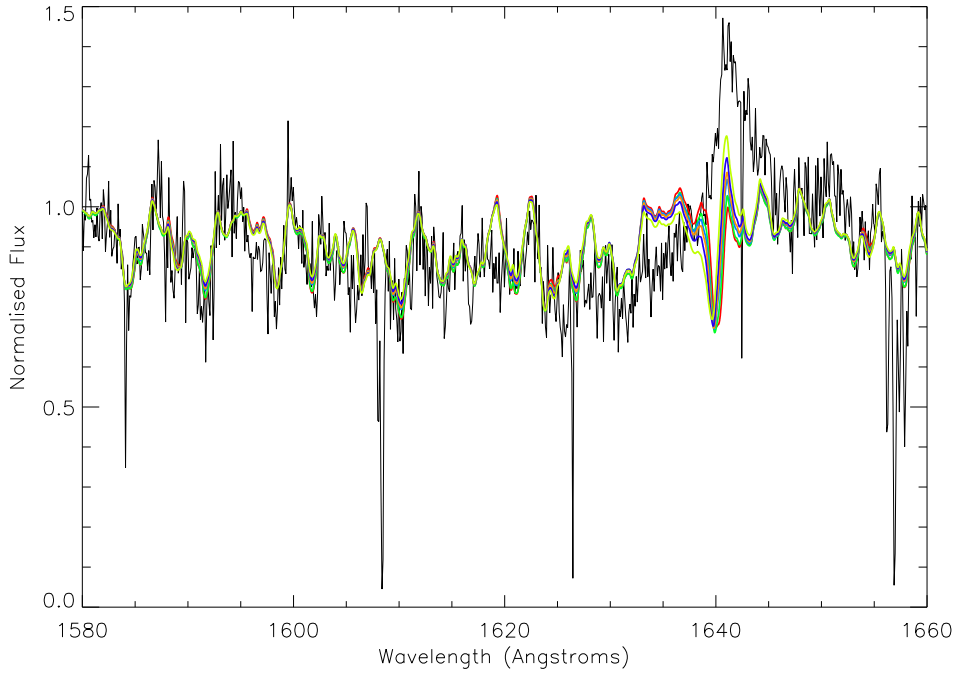


range of completed models can produce the HeII profile, as was the case for the SiV doublet. This anomaly may be an indication that within the confines of CMFGEN model atmospheres, clumping is required for this object. Generally the best fitting mass-loss rates from 'consistency' lines is in agreement with that derived from SV.

### $\zeta$ Puppis

Figure 6.23 shows clumped model fits to the observed SV spectrum of $\zeta$ Puppis. The best fit to the absorption part of the profile comes from the model with a mass-loss rate of $2.5\times10^{-6}M_{\odot}yr^{-1}$. The other models run that were intended to be limits are actually too far from the data, setting the mass-loss rate well within the range 1 to $5\times10^{-6}M_{\odot}yr^{-1}$. Extra models run at a later stage may achieve better constraints. In the light of the investigation of Fullerton et al. (2006), this result is enough to show that the mass-loss rate is of the order $10^{-6}M_{\odot}yr^{-1}$, and is somewhat closer to H$\alpha$, radio and X-ray measures than to that from PV (see Table 6.2).

Figure 6.24 shows the fits for the unclumped models for $\zeta$ Puppis. The model that best fits the absorption component is that with a mass-loss rate of $7.5\times10^{-6}M_{\odot}yr^{-1}$,

**Figure 6.23.** Clumped model fits to Sv for $\zeta$ Puppis. Red: $1{\times}10^{-6} M_{\odot} yr^{-1}$, green: $2.5{\times}10^{-6} M_{\odot} yr^{-1}$, blue: $5{\times}10^{-6} M_{\odot} yr^{-1}$

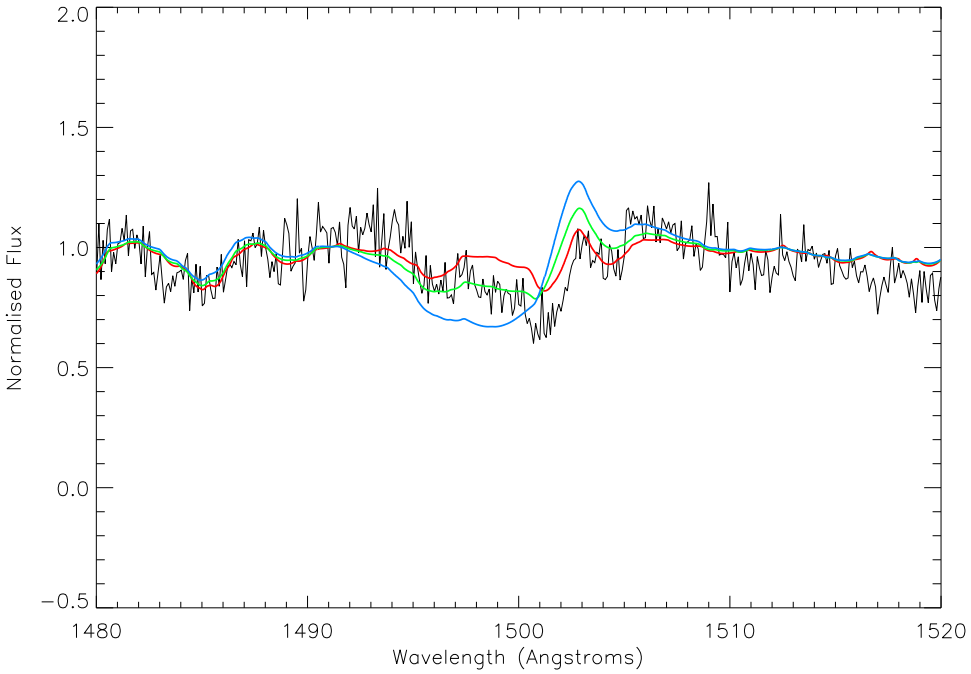


**Figure 6.24.** Unclumped model fits to Sv for $\zeta$ Puppis. Red: $2.5{\times}10^{-6} M_{\odot} yr^{-1}$, green: $5{\times}10^{-6} M_{\odot} yr^{-1}$, blue: $7.5{\times}10^{-6} M_{\odot} yr^{-1}$

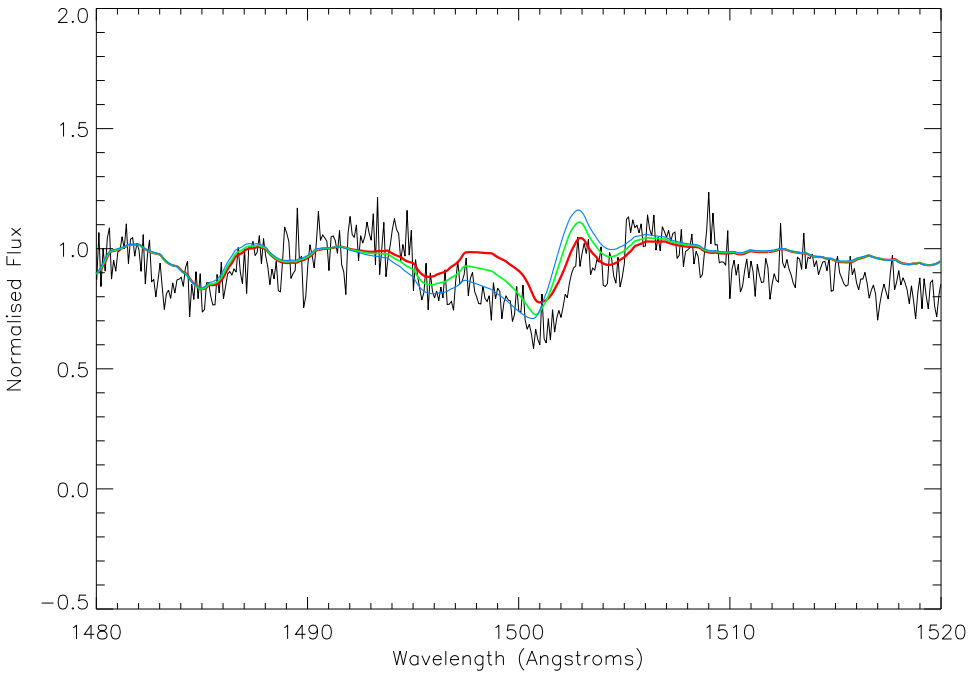

with a good lower limit of $5{\times}10^{-6} M_{\odot} yr^{-1}$. Not enough models were run to establish an upper limit, but a rough extrapolation might suggest a value of around $10^{-5} M_{\odot} yr^{-1}$. This is very high and not at all consistent with other measures, and so may be rather too conservative an uncertainty. For both the clumped and unclumped cases the profile shapes do not match particularly well, demonstrating the shortcomings of the CMFGEN modelling approach in this case.

No adequate archival data is available for use for $\zeta$ Puppis in the far-UV, however Figure 6.25 shows the comparison of models to a SiV spectrum from Morton & Underhill (1977). In the clumped case the closest match appears to be that with a mass-loss rate of 5-7.5$\times 10^{-6} M_{\odot} yr^{-1}$, which is in agreement with the upper limit derived from SV. In the unclumped case however there is no agreement at all, even for the highest mass-loss rate.

Figures 6.26 and 6.27 show fits to the NIV wind line in $\zeta$ Puppis. In the clumped case the best matching profile corresponds to a mass-loss rate of $1{\times}10^{-6} M_{\odot} yr^{-1}$, which is in agreement with the lower limit of uncertainty from SV. In the unclumped case the model with a mass-loss rate of $2.5{\times}10^{-6} M_{\odot} yr^{-1}$ is of the right size to match the profile, but is somewhat displaced. A further consistency check is employed in HeII, seen in Figure 6.28, which gives a best fitting mass-loss rate of $7.5{\times}10^{-6} M_{\odot} yr^{-1}$. This is in agreement with that derived from SV.

### 6.3.2 Comparison with literature estimates

Table 6.2 gives the derived mass-loss rates from this investigation alongside estimates according to H$\alpha$, radio and X-ray observations where they are available. Additionally the values of $\dot{M} q_i$ from Fullerton et al. (2006) are given. Table 6.4 gives the fraction of $S^{4+}$ according to the CMFGEN model that best matches the observed profile.

An important note to accompany Table 6.2 is that the literature comparison mass-loss rates are derived using a variety of different assumptions to those in the current investigation, and using different methods. Specifically, slightly different fundamental parameters may be assumed. Different distances to the star are adopted, which are tied in to the values of stellar luminosity and effective temperature (through absolute magnitude and stellar radius). For this reason, Table 6.3 is presented here with the values of stellar luminosity and effective temperature adopted for the sample objects, both for this investigation and for the sources of comparison. The radio mass-loss rates can be easily scaled to a new

**Figure 6.25.** No archival data in the far-UV was usable for ζ Puppis, however the Copernicus spectrum is displayed in Morton & Underhill (1977) and reproduced in the top panel, below. The middle panel shows a series of clumped models, and the bottom panel shows a series of unclumped models. The colours are as for Figures 6.23 and 6.24.

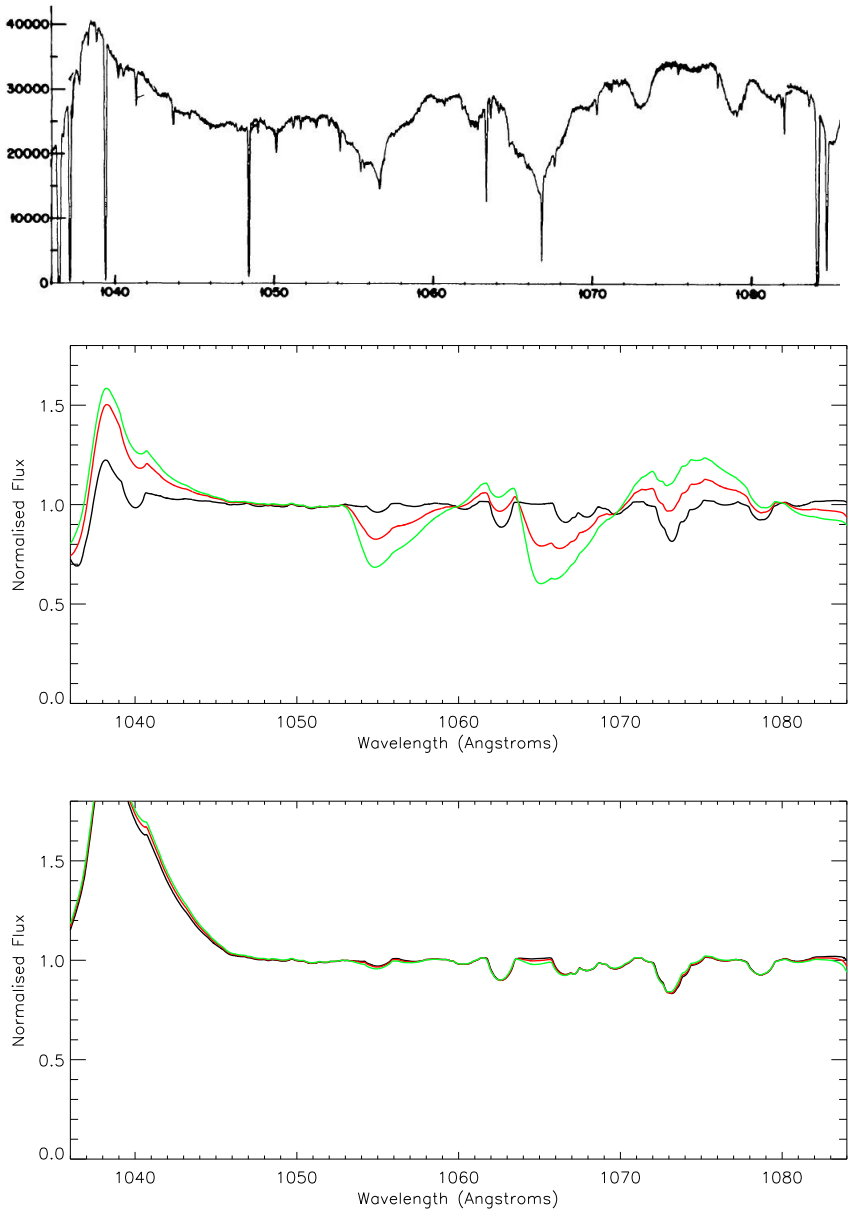

**Figure 6.26.** Clumped model fits to NIV for $\zeta$ Puppis. Red: $1{\times}10^{-6} M_{\odot} yr^{-1}$, green: $2.5{\times}10^{-6} M_{\odot} yr^{-1}$

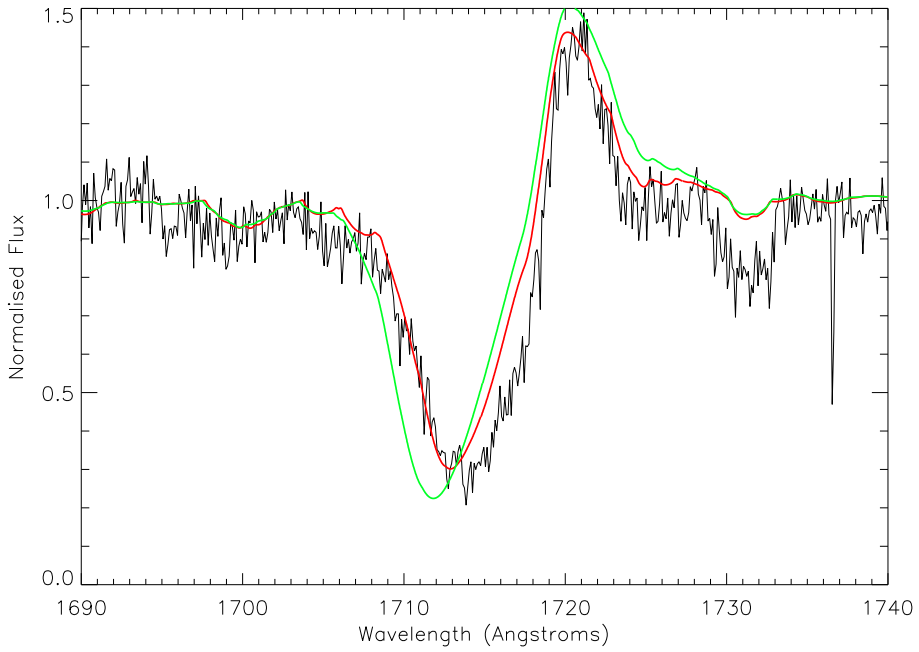


**Figure 6.27.** Unclumped model fits to NIV for $\zeta$ Puppis. Red: $2.5{\times}10^{-6} M_{\odot} yr^{-1}$

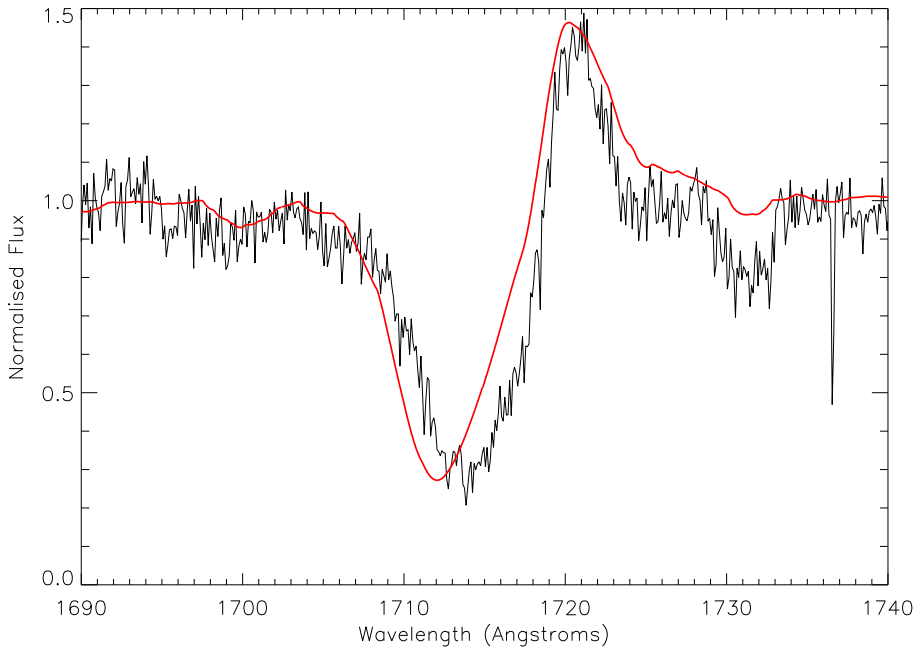

**Figure 6.28.** Unclumped model fits to HeII for $\zeta$ Puppis. Red: $2.5{\times}10^{-6} M_{\odot} yr^{-1}$, green: $5{\times}10^{-6} M_{\odot} yr^{-1}$, blue: $7.5{\times}10^{-6} M_{\odot} yr^{-1}$

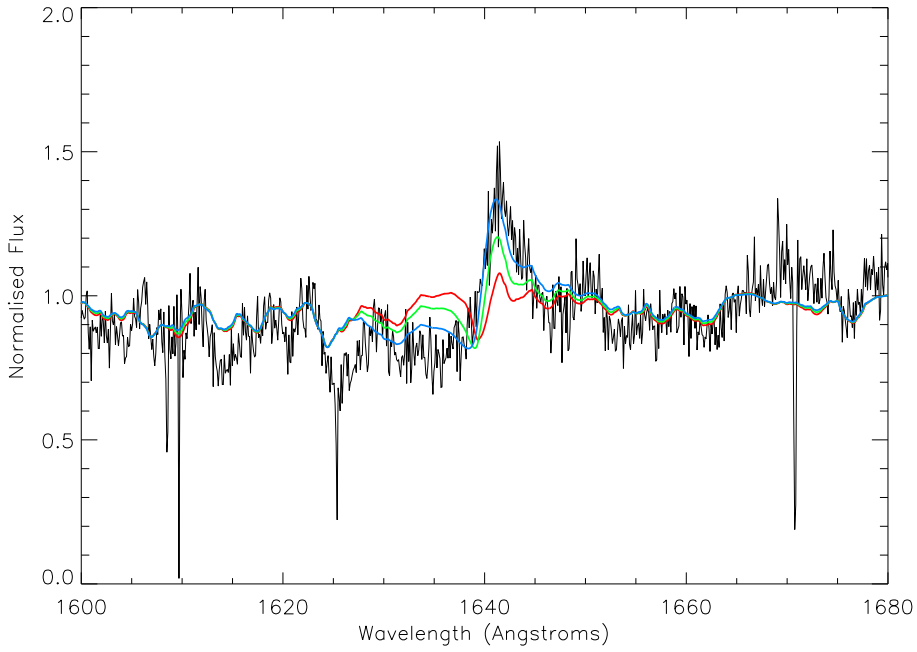


**Table 6.2.** Mass-loss rates derived in this investigation from SV compared with other (unclumped) estimates in the literature. All mass-loss rates are given in units of $10^{-6} M_{\odot} yr^{-1}$. Literature references are: [1]Repolust et al. (2004), [2]Markova et al. (2004), [3]Scuderi et al. (1998), [4]Lamers & Leitherer (1993), [5]Cohen et al. (2010). All values of $\dot{M}q_i$ derived from PV are from Fullerton et al. (2006).

| Star | $\dot{M}$ (this study, clumped/unclumped) | $\dot{M}$ (H$\alpha$) | $\dot{M}$ (Radio) | $\dot{M}$ (X-rays) | $\dot{M}q_i$ (PV) |
|---|---|---|---|---|---|
| HD 14947 | $1.0{\pm}0.5/1.0^{+1}_{-0.5}$ | $8.5^{1}/16^{2}$ | $3.0^{3}$ | - | 0.26 |
| HD 16691 | $1.75^{+2.25}_{-0.95}/4.0{\pm}1$ | $12.5^{2}$ | - | - | - |
| HD 190429A | $1.5{\pm}0.5/2.5^{+?}_{-1}$ | $14.1^{2}$ | $6.9^{3}$ | - | 0.44 |
| $\zeta$ Pup | $2.5^{+2.5}_{-1.5}/7.5{\pm}2.5$ | $8.7^{1}/6.4^{2}$ | $4.1^{4}$ | $3.5^{5}$ | 0.44 |

luminosity using the $\dot{M}$-$L$ scaling relation of Scuderi et al. (1998):

$$\log \dot{M} = (1.25 \pm 0.30) \log L, \tag{6.1}$$

where $\dot{M}$ is in $M_{\odot} yr^{-1}$ and $L$ is in $L_{\odot}$. The differences in adopted luminosity between radio mass-loss rates and those from the current investigation are very small and fall within the uncertainties given. For H$\alpha$ results, it is only the luminosities of Markova et al. (2004) that differ significantly from those used here. As an indicator of how the H$\alpha$ mass-loss rates may differ if the adopted luminosities were scaled to those used here, the relation found my Prinja et al. (1990) can be used. For HD 14947, the difference in luminosity would bring the Markova et al. (2004) mass-loss rate down to $3.7{\times}10^{-6}\dot{M}yr^{-1}$. The value for HD 190429A would come down from 14.1 to $10.7{\times}10^{-6}\dot{M}yr^{-1}$, and that for *zeta* Pup up from 6.4 to $8.7{\times}10^{-6}\dot{M}yr^{-1}$.

In order to scale the results from Fullerton et al. (2006) appropriately, it is noted that in the calculation of the mass-loss rate (multiplied by the ionization fraction) in that work, the mass-loss rate

$$\dot{M} \propto \frac{L^{0.5}}{T_{eff}^{2}}. \tag{6.2}$$

For HD 14947, the difference in adopted parameters is negligible. For HD 190429A the above scaling factor reduces the mass-loss rate of Fullerton et al. (2006) slightly to $0.42{\times}10^{-6}\dot{M}yr^{-1}$, and that of $\zeta$ Pup is increased to $0.46{\times}10^{-6}\dot{M}yr^{-1}$.

For the X-ray mass-loss rate for $\zeta$ Pup, the luminosity and effective temperature are similar enough to those used by Cohen et al. (2010) that any scaled mass-loss rate would be found within the uncertainties. However a larger terminal velocity was used in the current investigation than in the X-ray study. Using the terminal velocity in the current study, the X-ray value of mass-loss rate would be lowered by around 30%.

**HD 14947**

Both the clumped and unclumped models suggest a mass-loss rate of $1{\times}10^{-6}M_{\odot}yr^{-1}$, which is about an order of magnitude lower than H$\alpha$ measures and slightly smaller than radio flux levels suggest, but higher than the value of $\dot{M}q_i$ from PV by almost an order

**Table 6.3.** Comparisons of parameters important for deriving mass-loss rate - the effective temperature and luminosity. Each column gives these values in units of kK and $L_{\odot}$ respectively. Sources are Repolust et al. (2004) (R04), Markova et al. (2004) (M04), Scuderi et al. (1998) (S98),Lamers & Leitherer (1993) (L93), Cohen et al. (2010) (C10) and Fullerton et al. (2006) (F06).

| Star | This thesis | R04 | M04 | S98 | L93 | C10 | F06 |
|---|---|---|---|---|---|---|---|
| HD 14947 | 37.5, 5.70 | 37.5, 5.70 | 37.7, 6.08 | 40.3, 5.72 | | | 37.5, 5.69 |
| HD 16691 | 39.2, 5.92 | | 39.2, 5.92 | | | | |
| HD 190429A | 39.0, 5.90 | | 39.2, 5.97 | 42.4, 5.92 | | | 39.2, 5.96 |
| $\zeta$ Pup | 40.0, 5.90 | 39.0, 5.90 | 39.2, 5.82 | | 42.4, 5.9 | 39.0, 5.85 | 39.0, 5.89 |

of magnitude. The uncertainties claimed for both H$\alpha$ and radio estimates are around $0.1{\times}10^{-6} M_{\odot} yr^{-1}$, and for $\dot{M}q_i$ are $0.65{\times}10^{-7} M_{\odot} yr^{-1}$. This means that none of the existing estimates match those in this study. If some clumping were included in the radio measure it might reduce the corresponding mass-loss rate to a similar value derived here; it would be reduced by the square-root of the clumping factor. Moderate clumping ($f = 0.1$) would bring them almost perfectly in to agreement.

**HD 16691**

The only available estimate for comparison is from H$\alpha$, and is out of agreement with this study. The clumped case is nearly an order of magnitude lower, and the unclumped case is about a factor of 3 smaller. If moderate clumping were included in the H$\alpha$ analysis the mass-loss rate estimated would be around $4{\times}10^{-6} M_{\odot} yr^{-1}$, just into agreement with the clumped case in this study, within the uncertainties.

**HD 190429A**

The mass-loss rates derived for both clumped and unclumped cases are in agreement with each other within uncertainties. For the H$\alpha$ measure to agree it would require a rather strong clumping factor (filling factor $f \simeq 0.01$). The radio flux estimate however could be reduced adequately using a filling factor $f \simeq 0.08$. The estimate using PV is around a factor of 4-5 smaller than in this study.

**$\zeta$ Puppis**

The most recent estimate of the mass-loss rate of $\zeta$ Puppis is that of Cohen et al. (2010). In that study it is claimed that no special treatment of optically thick clumping is required to derive a reliable result. It also claims a statistical uncertainty of about 10%, but an uncertainty based on uncertain continuum opacity as a factor of 2. This puts it in agreement with the values derived in this study, and also with radio measures. The current study's estimate with clumping is too small compared to the H$\alpha$ value, but they would surely agree if a modest clumping scenario were employed in the H$\alpha$ measure. $\dot{M}q_i$ from PV is again smaller by almost an order of magnitude.

**Table 6.4.** Sv ion fractions from models.

| Star | q(Sv) (clumped) | q(Sv) (unclumped) |
|---|---|---|
| HD 14947 | 0.90 | 0.52 |
| HD 16691 | 0.85 | 0.41 |
| HD 190429A | 0.86 | 0.28 |
| $\zeta$ Pup | 0.66 | 0.24 |

## 6.4 Discussion and Chapter Conclusions

In this chapter CMFGEN model atmospheres have been used to fit the observable sulphur wind lines in a sample of early O supergiants in order to estimate their mass-loss rates. HD 15570 was ejected from the sample due to the high noise level in the observed spectrum, leaving HD 14947, HD 16691, HD 190429A and $\zeta$ Puppis. The Sv excited line at 1502Å was available in *IUE* data for all four objects, and *FUSE* data of the Siv resonance line at 1063/1073Å were available for HD 14947 and HD 190429A. Both moderately clumped and unclumped winds were considered.

It is found that the absorption components of the Sv lines in each object can be fit reasonably well, but better for HD 14947 and HD 16691 than the other two objects. The mass-loss rate can generally be constrained to within a factor of 2. This leaves it in agreement with radio flux measures *if* a moderate clumping factor is used for both. The mass-loss rates in this study are generally smaller than H$\alpha$ estimates by larger amounts, and the latter need larger clumping factors to match the clumped case from Sv, and even then the clumping factor would not be consistent between H$\alpha$ and a CMFGEN model. The estimates from Fullerton et al. (2006) are far smaller than other estimates. The fits to Siv where available are shown to be in good agreement with Sv when the wind is clumped in the models, but less so if they are not.

$S^{4+}$ is shown to account for around 90% of the wind material if the wind is clumped, and around 50-65% if it is not. For subsequent studies of sulphur lines it is useful to know whether all of these useful adjacent stages that have observable transitions are trace ions or close to dominance. This has been treated generally in Chapter 4, but here the total $S^{3+}$ + $S^{4+}$ + $S^{5+}$ is derived from the models that represent specific objects, and shown in Table 6.5. As can be seen the clumping factor makes significant differences to how important different ions are. In all clumped cases the Sv line represents an ion that

is the dominant form of sulphur in the wind, but only accounts for more than 50% of sulphur in HD 14947 for the unclumped cases. In the clumped case $S^{6+}$ accounts for a very small fraction of the sulphur in the wind but when there is no clumping it becomes very important.

In essence we see that any study employing all three consecutive transitions that are observable will be tracing more than 90% of the sulphur in the wind if there is moderate clumping, but only about 50-65% of it in a smooth-wind scenario.

Overall it has been found in this study that moderately clumped-wind CMFGEN models of Sv predict very similar mass-loss rates to radio measures once the clumping factor has been applied to the latter. There is also good agreement with the latest X-ray measure which does not rely upon optically thick clumping effects. The measures are a good deal higher than those given by Fullerton et al. (2006), implying that the ion fraction for Pv is around 0.1; not dominant as suggested both by that study and by the calculations in this thesis (Chapter 4). This gives some weight to the argument of Waldron & Cassinelli (2010), at least in as much as the Pv not being dominant and it being due to a process not implemented in standard analysis. There is still a fundamental problem in dealing with Pv in model atmosphere analysis, given the suggestion here of a mass-loss rate that requires $q_{PV}$ to be low, whilst it is still predicted dominant (>50%) by models. Additionally a caveat to the mass-loss rates derived from fitting Sv is that the line does not sample the whole wind since it does not extend to the full terminal velocity. It is therefore possible that there are factors affecting the observed mass-loss rate in the outer wind that are not being traced by this line.

**Table 6.5.** Sulphur ion fractions in models. The fraction of $S^{3+}$ for the unclumped models for HD 190429A and $\zeta$ Puppis is negligible (less than 0.001).

| Star | Clumped | | | Total | Unclumped | | | | Total |
|---|---|---|---|---|---|---|---|---|---|
| HD/Name | $S^{3+}$ | $S^{4+}$ | $S^{5+}$ | | $S^{3+}$ | $S^{4+}$ | $S^{5+}$ | ($S^{6+}$) | (no $S^{6+}$) |
| 14947 | 0.04 | 0.9 | 0.03 | 0.97 | 0.003 | 0.52 | 0.13 | (0.34) | 0.65 |
| 16691 | 0.02 | 0.86 | 0.07 | 0.95 | 0.002 | 0.41 | 0.18 | (0.40) | 0.59 |
| 190429A | 0.02 | 0.86 | 0.07 | 0.95 | neg. | 0.28 | 0.23 | (0.49) | 0.51 |
| $\zeta$ Pup | 0.004 | 0.66 | 0.26 | 0.92 | neg. | 0.24 | 0.33 | (0.43) | 0.57 |

This page is intentionally left almost blank

# Chapter 7

# Conclusions and future work

*'I have made this letter longer than usual, only because I have not had the time to make it shorter. '*

Blaise Pascal

This thesis has sought to provide answers and insights regarding the winds of Galactic O type stars, with particular attention paid to the effects of wind-clumping and X-rays on mass-loss and ion fractions.

The specific questions posed as part of Chapter 1 pertain to the effects of these phenomena on spectra and on ion fractions, and to how discordant new mass-loss estimates are with those previously constrained. In addition it was asked whether spectral lines corresponding to successive ion stages of sulphur can be used to more reliably predict mass-loss rates, and whether we are close to knowing with certainty the true rates of mass-loss for any O stars.

In Chapter 3, the spectra of the CMFGEN grid described in Chapter 2 were examined. They compare well with observations in UV, FUV and optical wavelength ranges. It was shown that X-rays must be included in model atmosphere calculations if NV and OVI resonance doublets are to be correctly predicted, but that in the current setup of models it is difficult to constrain the exact level of X-rays required from these lines alone. CIV was shown to be particularly sensitive to X-rays in later spectral type O dwarfs, and

that X-rays can actually have a greater effect on the wind profile than either changes in the clumping scenario or in the mass-loss rate. Several wind lines were shown to be sensitive to clumping, particularly in the FUV. This is due to the ion stage population changes that occur through altered recombination rates. Although some profiles could not be satisfactorily predicted at all (most notably PV), the scenario that produced the best, most realistic spectra was often the smooth-wind one. Given the CMFGEN models, this implies that the actual level of clumping in many Galactic O star winds may be lower than that with a filling factor 0.1 ('moderate' clumping). The specific detail of the profiles will most likely be resolved as models grow to include more detailed physics, and as observations are taken with higher signal-to-noise and of more objects.

In Chapter 4, ion fractions from the CMFGEN grid were presented for different X-ray and clumping scenarios. It was shown that ion populations shift to a higher ionization balance with the introduction of X-rays, and that the density enhancement from clumping parametrisation causes a somewhat inverse effect whereby recombination is more favoured. Clumping was shown to have a greater effect in dwarfs than in supergiants, and X-rays were shown to have an apparently stronger effect upon the later type dwarfs than those at early type. Some ions were dominant (>50%) for a certain sub-range of O stars, but very few were very dominant (>75%) for any portion of the O stars range regardless of the X-ray and clumping scenarios. $C^{3+}$ was shown to be an important contributor to the total amount of carbon in the wind, which was essential in the interpretation of results in Chapter 5.

In Chapter 5, the product of mass-loss rate and ion fraction was derived for a sample of mid to late type O dwarfs, from both CIV and NV resonance doublets. It was found that if CMFGEN ion fractions are assumed then the mass-loss rates are estimated to be at least an order of magnitude lower than canonical values, and conversely if canonical mass-loss rates are used then the CMFGEN ion fractions are shown to be incorrect. It remains unclear exactly whether it is the ion fractions that are to blame, and hence the models need to be addressed, or that the optical depths used are wrong due to the effects of optically thick clumping. The latter has some support in the literature, although the former is possibly true to some extent, and more sophisticated models will eventually be required.

In Chapter 6, the SV wind profiles of a small sample of early O supergiants were fitted using CMFGEN models, and objects' SIV lines were also fitted for two cases. The mass-loss

rates of these objects was constrained to within about a factor of 2 for both a smooth wind and a moderately clumped scenario. It was found that the mass-loss estimates derived were in good agreement with radio flux measures if a moderate clumping factor is used. The rate determined for $\zeta$ Puppis was shown to be in agreement with the most recent literature value, an X-ray measure that requires no optically thick clumping effects. The results are only brought into question by the inability to fit the full profile in some cases, and it is likely that an improvement in the modelling is needed. The key result is that the mass-loss rates were much more in agreement with radio and X-ray measures than with those derived from empirical modelling of the Pv resonance doublet in the far-UV.

In general this thesis has shown support for a mass-loss rate for O supergiants that is in line with other current estimates, whilst for O dwarfs a mass-loss rate far smaller than previously accepted values is supported. So while the Pv problem does not seem to be too big an issue anymore, particularly with the independent Sv measures here and the work of Sundqvist et al. (2010), there now exists a strong demonstration of a discordance in the weak wind regime. Clumping as treated in the 'micro' formalism seems to only be required at a low level in both predicting spectral morphologies and in producing consistent mass-loss rates from different techniques.

## 7.1 Future work

There are several lines of investigation that should be pursued in future that follow on directly from what has been found in this thesis.

One well-known issue in analysing spectra was that observations of Galactic O stars in the far-UV can be severely hampered by interstellar effects. In addition observations from newer instruments across wavebands are sparse for Galactic observations, because as instrumentation improves, local bright point sources are generally not favoured except for calibration purposes. Both these factors can be overcome by observing objects in the Magellanic Clouds instead. The interstellar column density is far lower and the O stars are less likely to saturate the sensors of newer observatories. It also offers the opportunity to extend the current study of X-rays and wind-clumping into a lower metallicity environment. This will require a new grid of CMFGEN models to be computed, including the calibration of different parameters.

In the longer term it is important that models of hot star winds improve. The current

study begins to stretch the model atmosphere approach, and hydrodynamic models do not yet have a completely accurate picture of wind structure. Important work has been started in the studies of Runacres & Owocki (2002) and Dessart & Owocki (2005) regarding hydrodynamical modelling of wind structure, and Cantiello et al. (2009) have shown the possibility that clumps could be seeded by convective zones near the photosphere. Perhaps moving to fully 3-dimensional calculations that include a fuller treatment of wind clumps will help to solve the mass-loss discordance and the nature of wind structure, and will be possible with the improvement of computing facilities. In terms of spectral line synthesis, the biggest steps forward recently have been those taken by Sundqvist et al. (2010) in computing the line force whilst taking into account the effects of optically thick clumping. It has also shown that a spatial porosity has an effect on the blueward portion of resonance line profiles. Next steps in this area could be to apply the findings to a larger set of object types (i.e. to dwarfs) and to address the difficulties in producing the exact line profile shapes.

As observational facilities improve we should also see more 'direct' spectroscopic detection of small structures in the winds of O stars. As the resolution and signal-to-noise get better, it should be possible to detect smaller sub structures in wind profiles in time-series data. Additionally with the advent of improved interferometric techniques, direct imaging of structure may soon be possible near the radio photosphere of the nearer, larger massive stars (e.g. Rigel). There are other observational avenues to be followed in order to learn more about mass-loss and wind clumping. One such avenue has already been investigated by Prinja & Massa (2010). In resonance doublets the ratio

$$\frac{\tau_{blue}}{\tau red} = \frac{\lambda_{blue} f_{blue}}{\lambda_{red} f_{red}} \tag{7.1}$$

has a certain value (approximately 2 in the case of CIV), assuming the medium to be smooth, where $f$ is the oscillator strength, $\tau$ is the optical depth in the line and $\lambda$ is the transition wavelength of the doublet component. If the wind is not smooth however, then this can be changed in the SEI models to a value that lies between 1 and 2. It would be close to 1 if most flux was passing through unattenuated. If a particular portion of the observed disk of the star is covered by optically thick wind material at the wavelength in question, and other parts are left essentially 'bare' then the ratio of doublet components is

likely to diverge from 2. The case of B-type supergiants is the easiest to pursue first, since they have relatively strong winds but with low terminal velocities, so finding separated doublets is easier. This method is one way of tracking the 'porosity' of the wind of a hot star.

Further observational campaigns include one being undertaken using ESO/VLT-CRIRES to take spectra of the Brackett-$\alpha$ line in the near infrared. Puls et al. (2008) have already shown using models that it is expected to respond strongly to changes in mass-loss rate in late O type dwarfs, unlike H$\alpha$ which becomes insensitive. Spectra of a small sub-sample of those objects addressed in Chapter 5 will be available for analysis during 2011. Additionally the advent of new millimetre and sub-mm facilities will help bring about constraints on wind clumping. Puls et al. (2008) give a clear indication that these wavelength regimes are expected to display the highest clumping factors and hence the best observability. In this respect ALMA, a new (sub-)mm array, will offer better observations at this wavelength than anything previously has.

Finally, the e-MERLIN radio array is becoming fully operational and the enhanced sensitivity (30 times more than it's predecessor) will allow more O stars to be observed. The legacy project COBRaS (http://www.ucl.ac.uk/star/research/stars_galaxies/cobras) will measure the radio fluxes of a host of new objects in order to better constrain the mass-loss rates and clumping scenarios.

This page is intentionally left almost blank

# Appendix A

# SEI Plots

This appendix contains all the plots of fits to CIV and NV wind line profiles, corresponding to Chapter 5. Also included are some of the NV fits that were not used due to the poor quality of the fit.

**Figure A.1.** CIV fit for HD 5005 (O6.5 V)

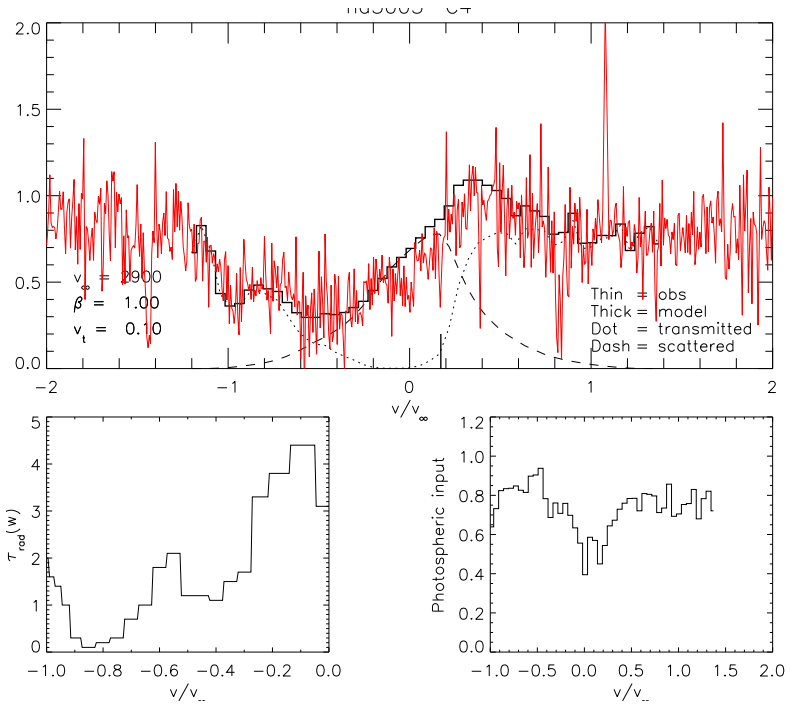

**Figure A.2.** Nv fit for HD 5005 (O6.5 V)

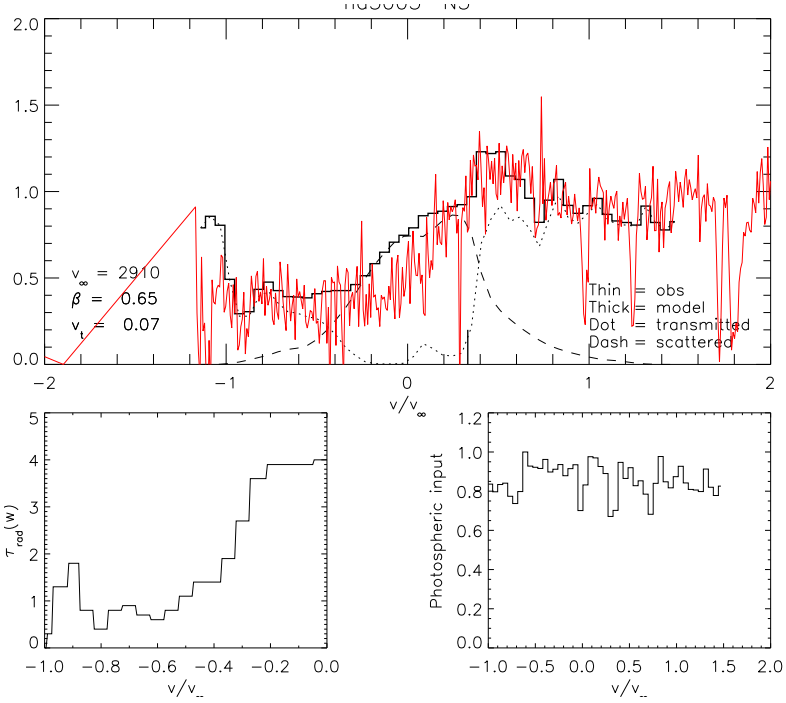


**Figure A.3.** Civ fit for HD 12993 (O6.5 V)

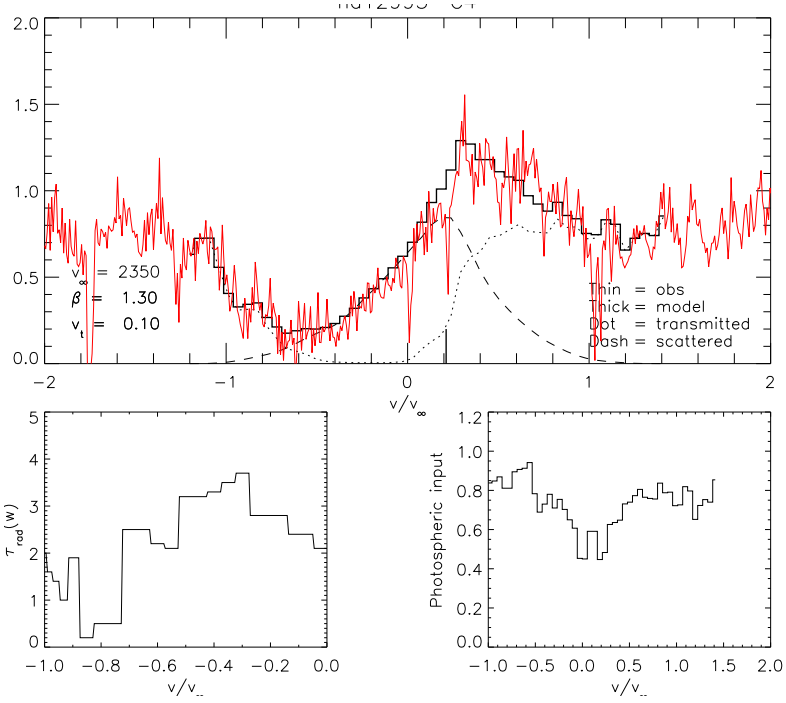

**Figure A.4.** Nv fit for HD 12993 (O6.5 V)

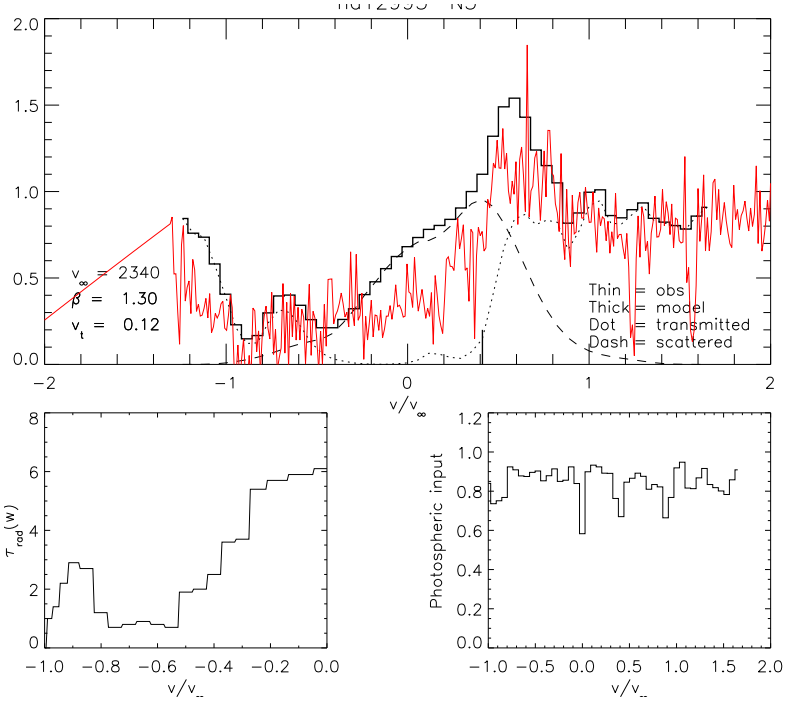


**Figure A.5.** Civ fit for HD 17505 (O6.5 V)

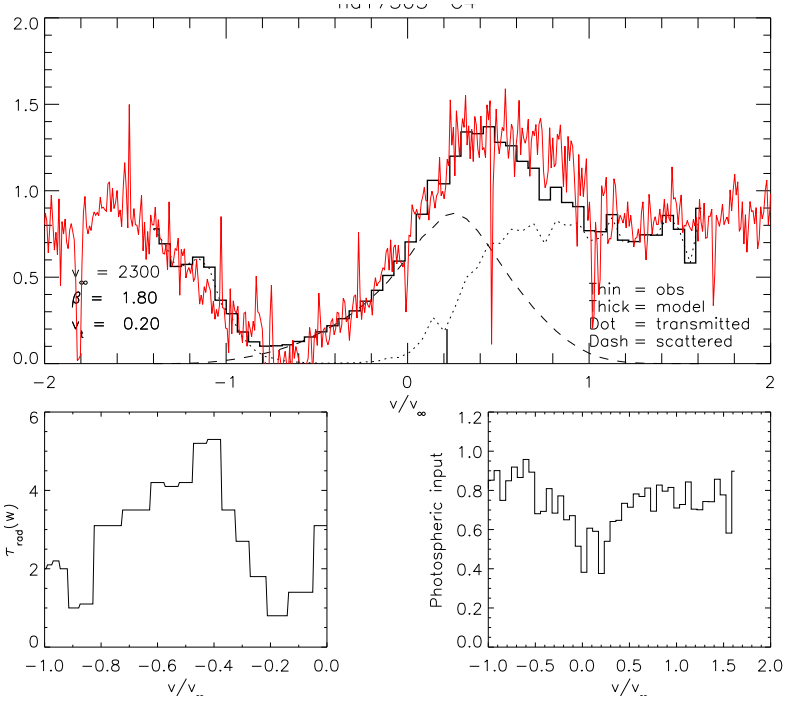

**Figure A.6.** Nv fit for HD 17505 (O6.5 V)

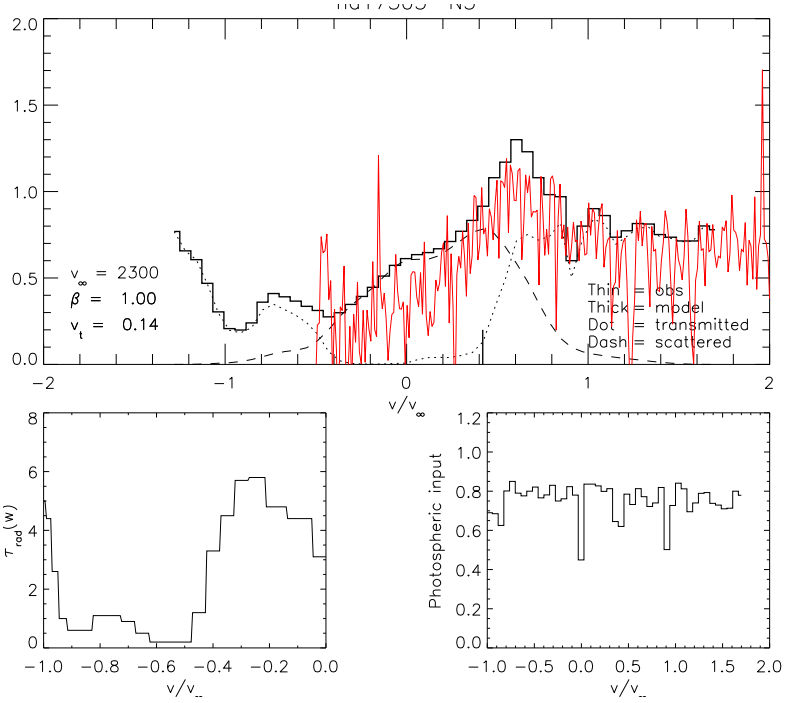


**Figure A.7.** Civ fit for HD 42088 (O6.5 V)

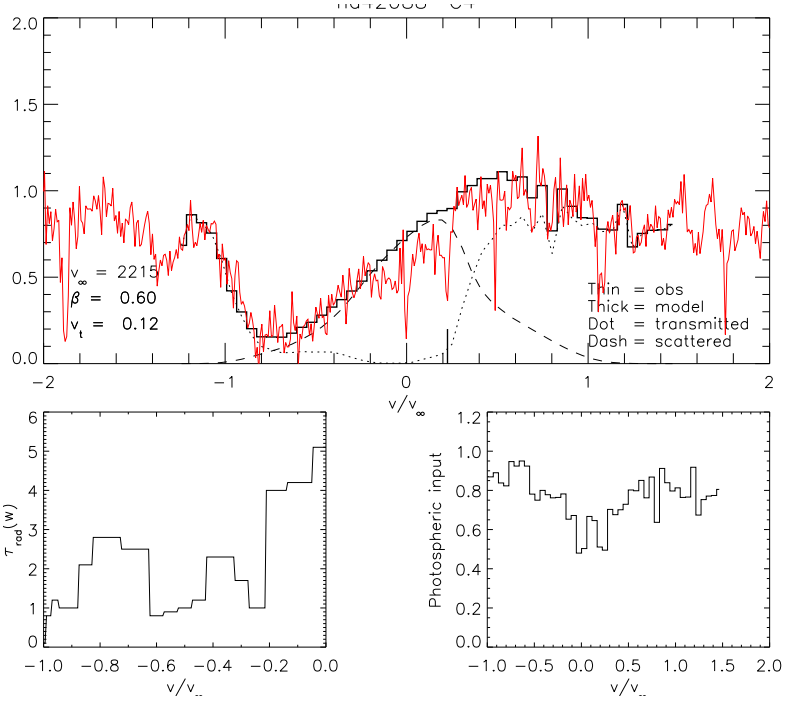

**Figure A.8.** Nv fit for HD 42088 (O6.5 V)

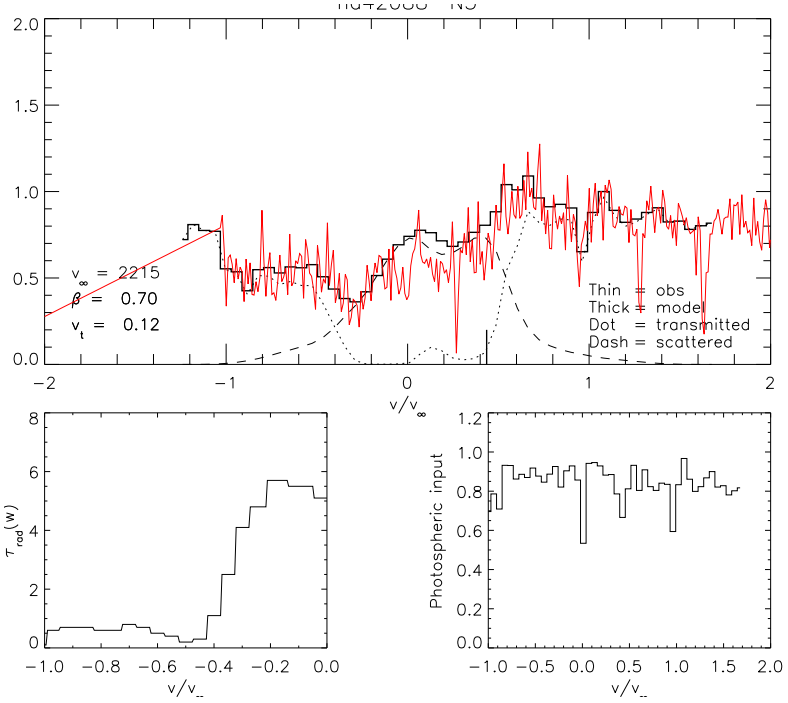


**Figure A.9.** Civ fit for HD 54662 (O6.5 V)

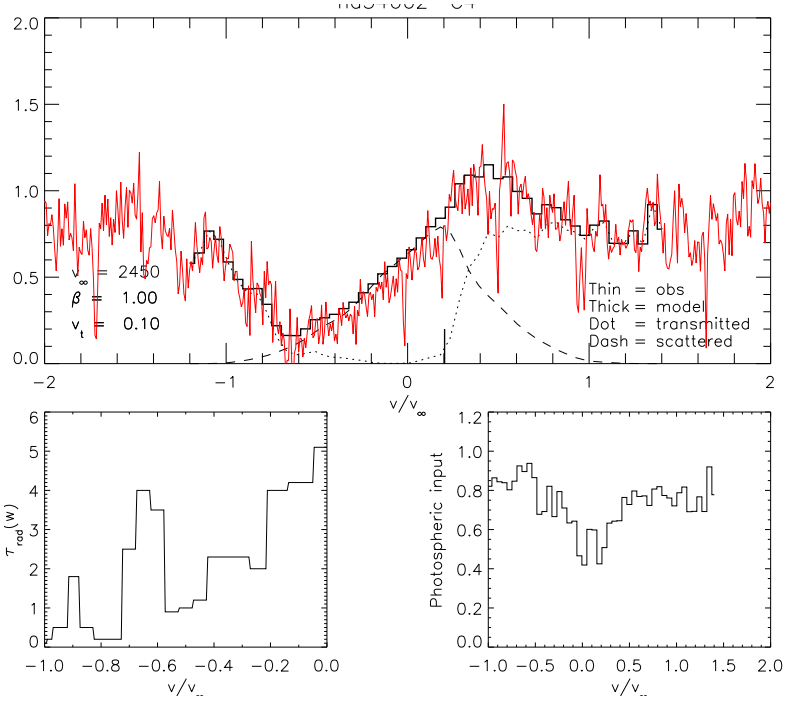

**Figure A.10.** Nv fit for HD 54662 (O6.5 V)

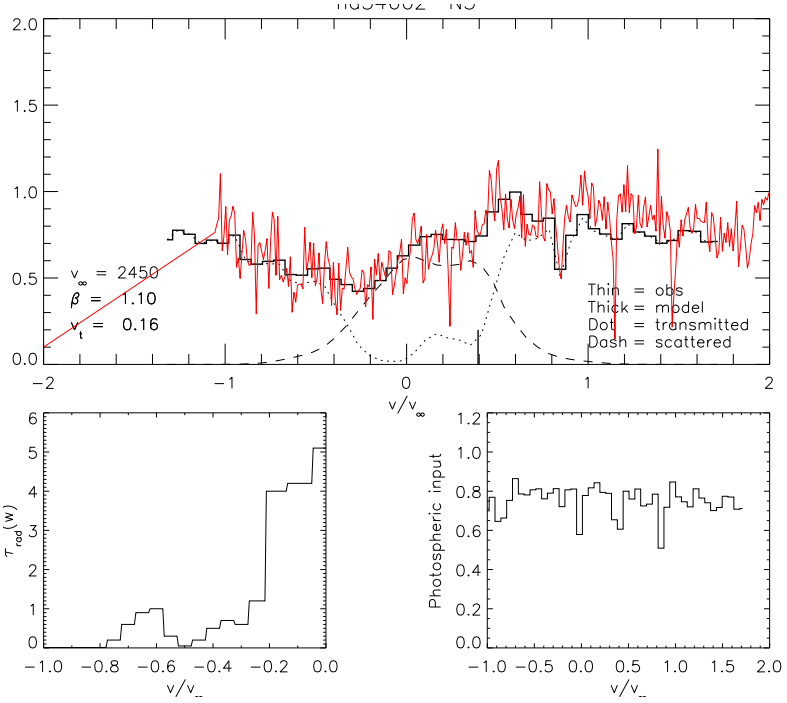


**Figure A.11.** Civ fit for HD 93146 (O6.5 V)

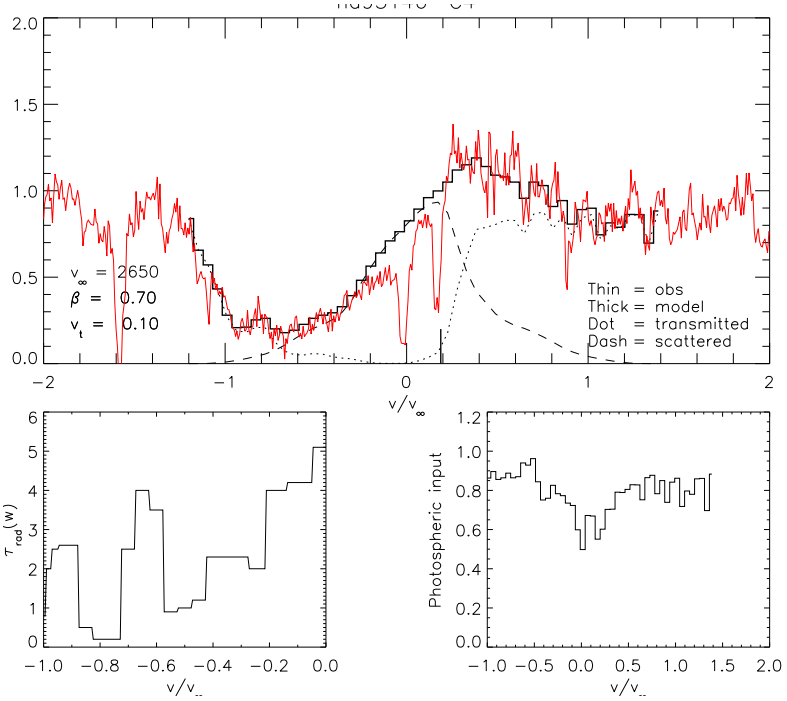

**Figure A.12.** Nv fit for HD 93146 (O6.5 V)

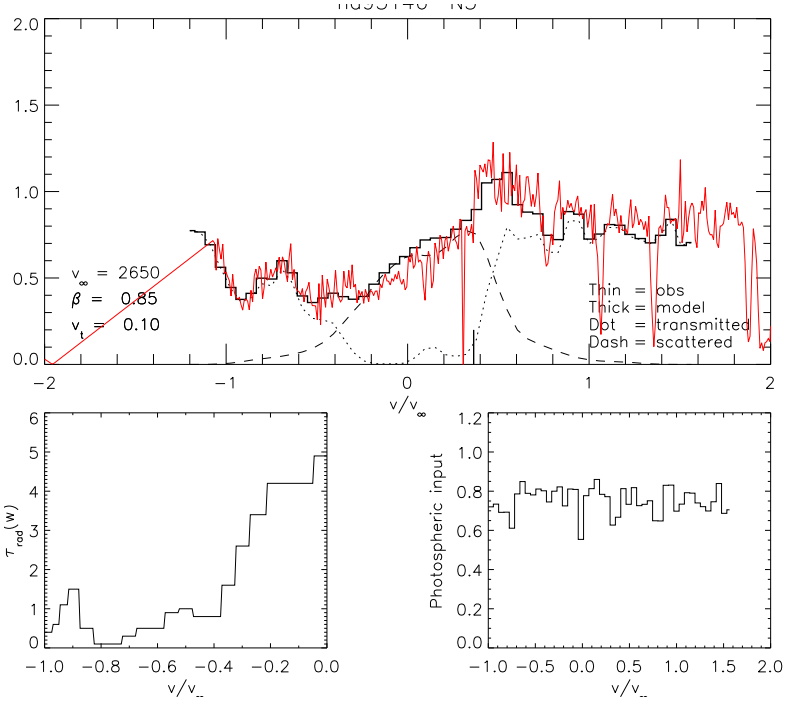


**Figure A.13.** Civ fit for HD 93161B (O6.5 V)

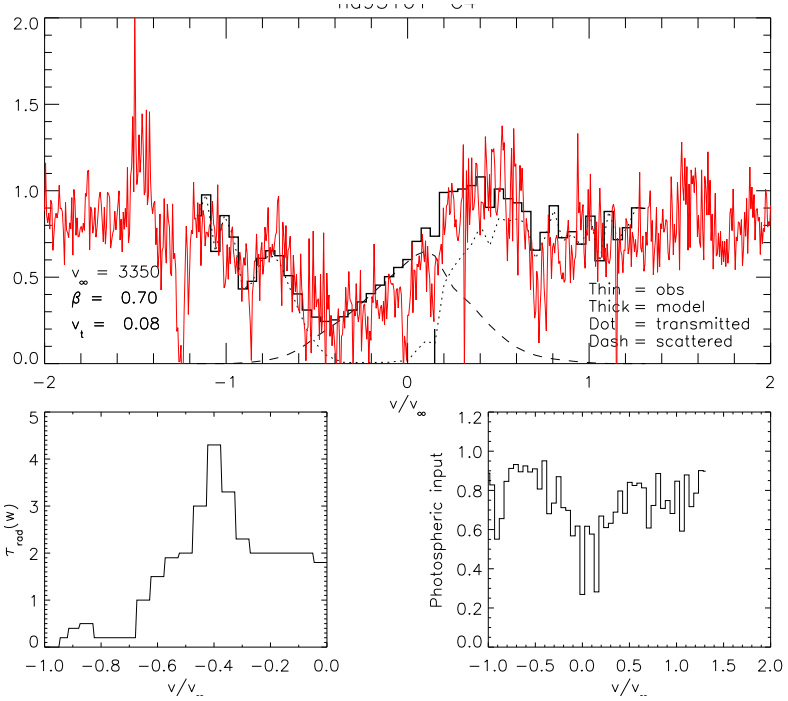

**Figure A.14.** CIV fit for HD 101436 (O6.5 V)

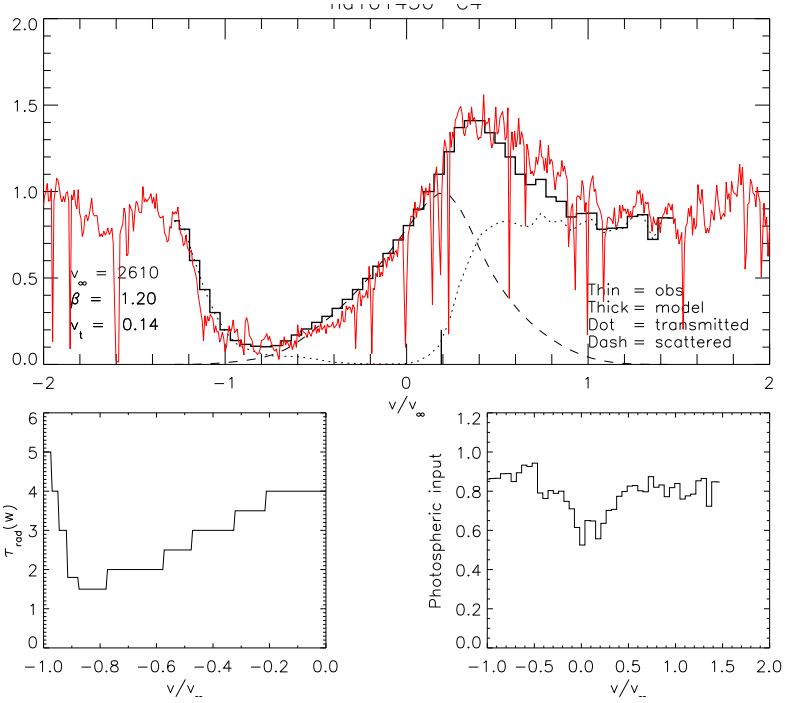


**Figure A.15.** NV fit for HD 101436 (O6.5 V)

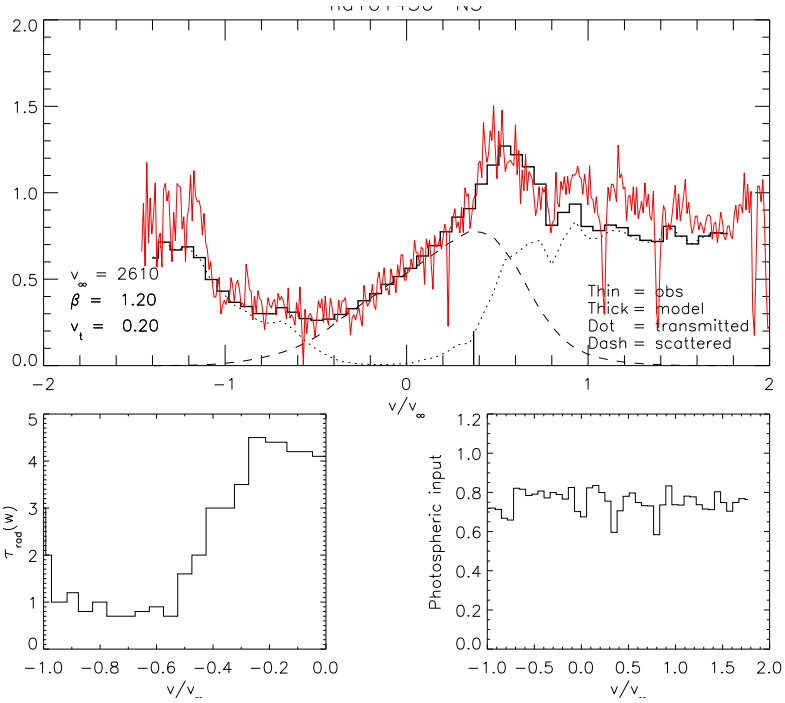

**Figure A.16.** CIV fit for HD 165052 (O6.5 V)

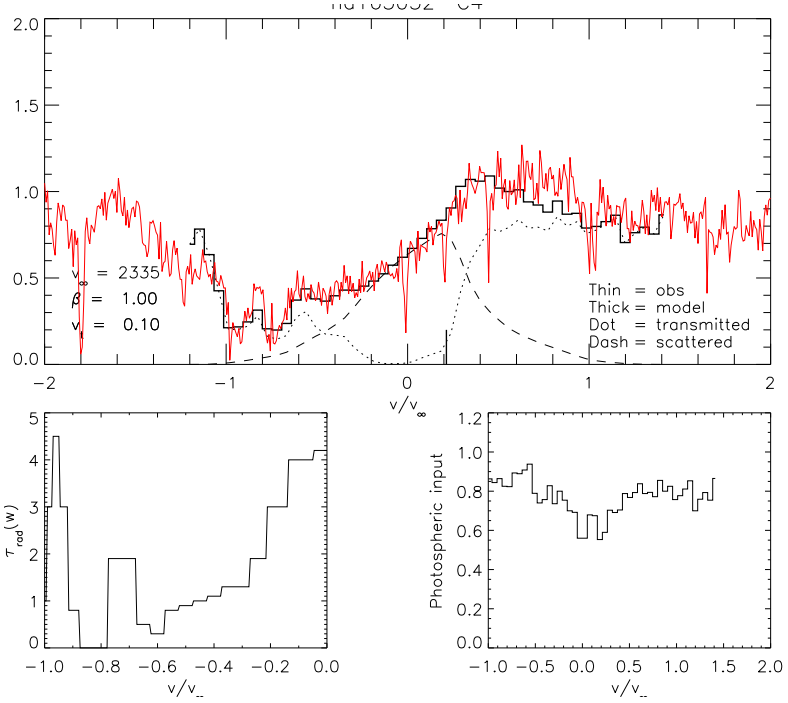


**Figure A.17.** NV fit for HD 165052 (O6.5 V)

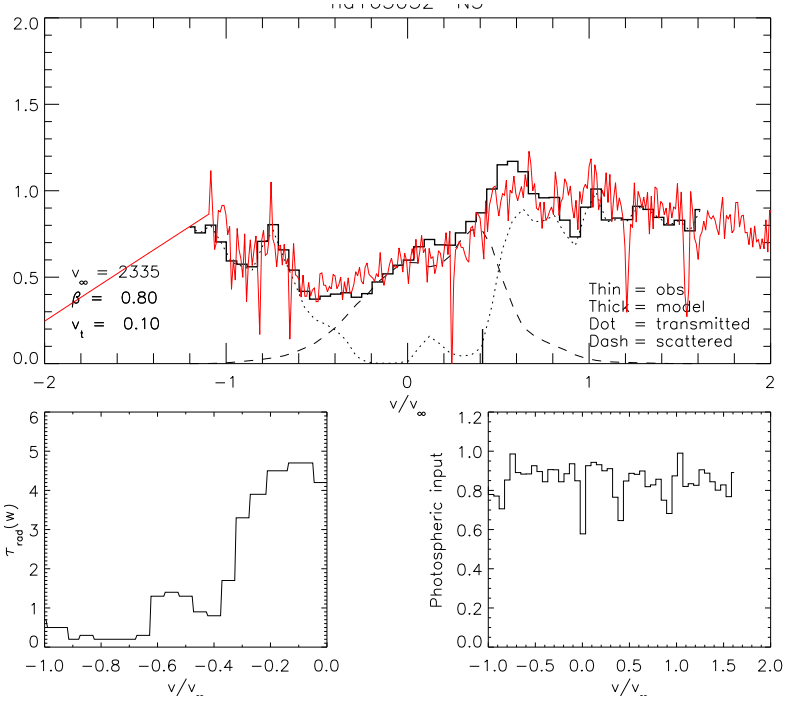

**Figure A.18.** CIV fit for HD 206267 (O6.5 V)

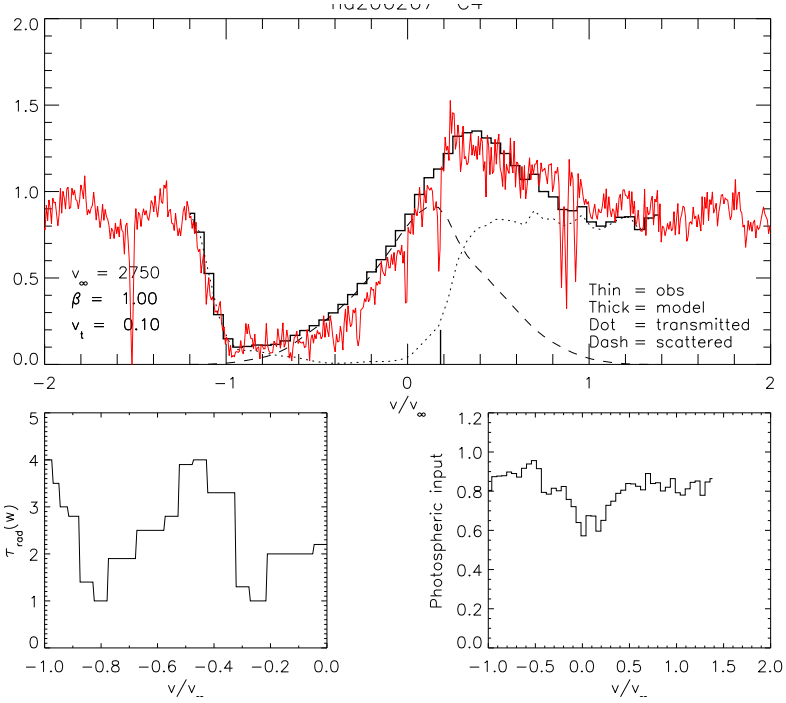


**Figure A.19.** NV fit for HD 206267 (O6.5 V)

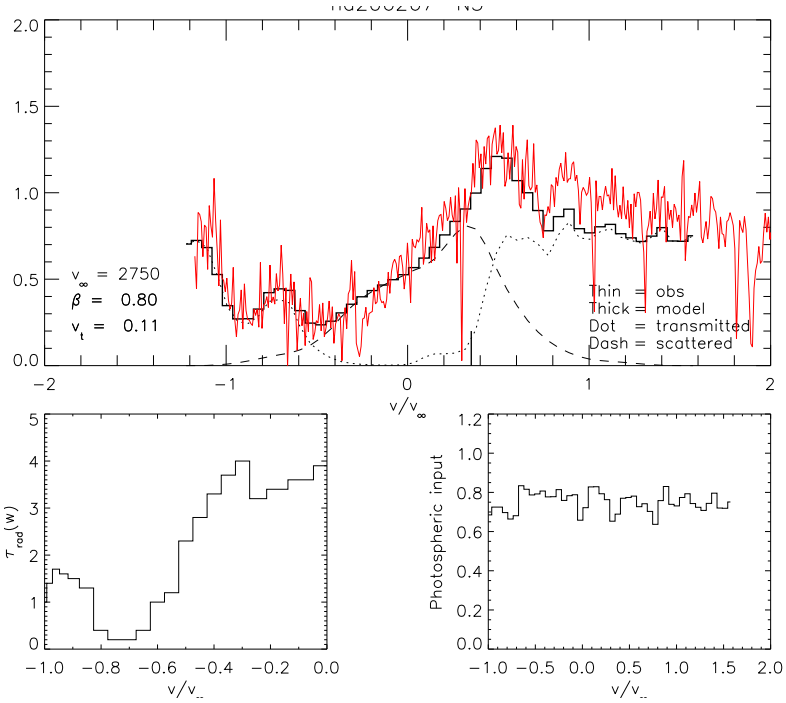

**Figure A.20.** CIV fit for CPD -59 2603 (O7 V)

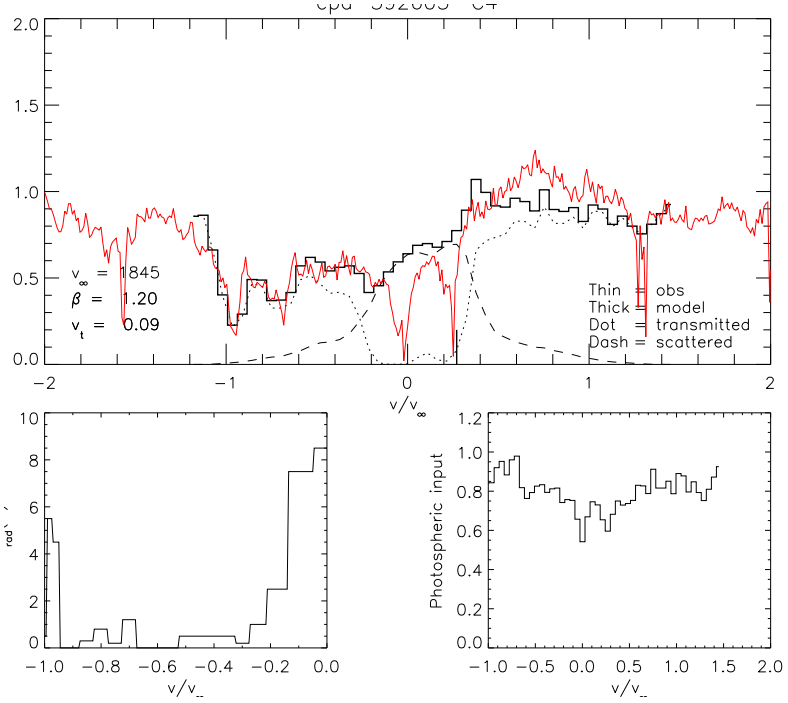


**Figure A.21.** CIV fit for HD 35619 (O7 V)

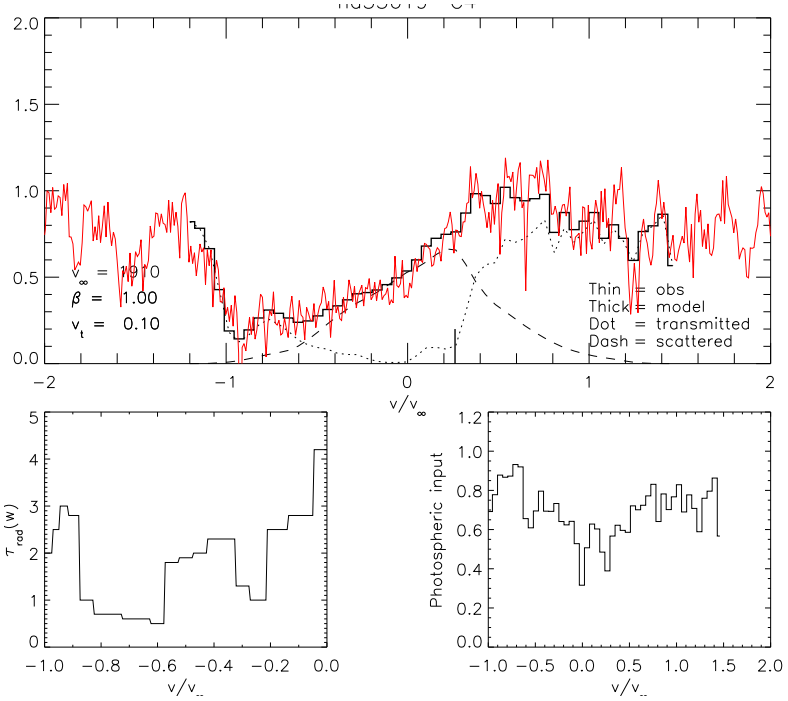

**Figure A.22.** Nv fit for HD 35619 (O7 V). Not used.

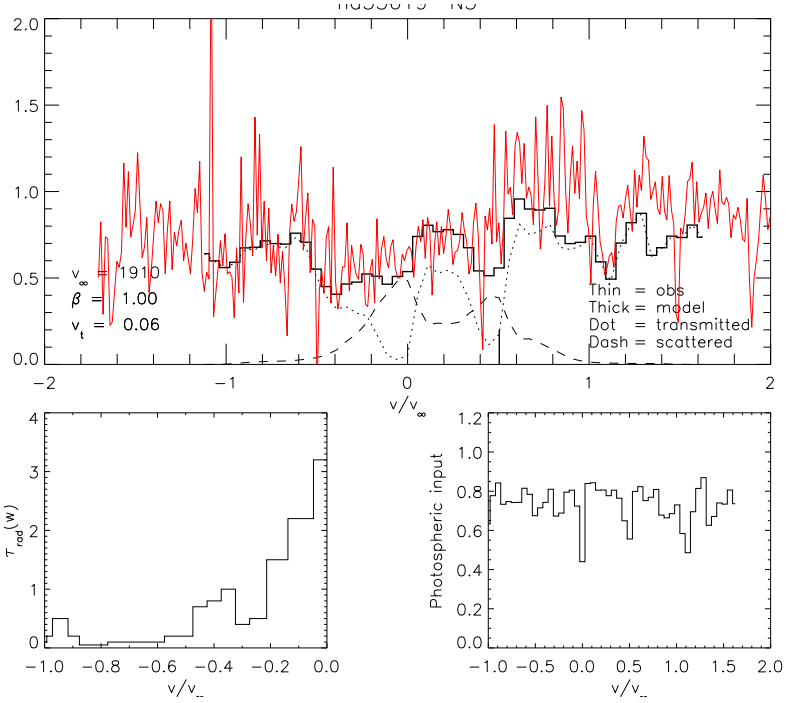


**Figure A.23.** Civ fit for HD 36879 (O7 V)

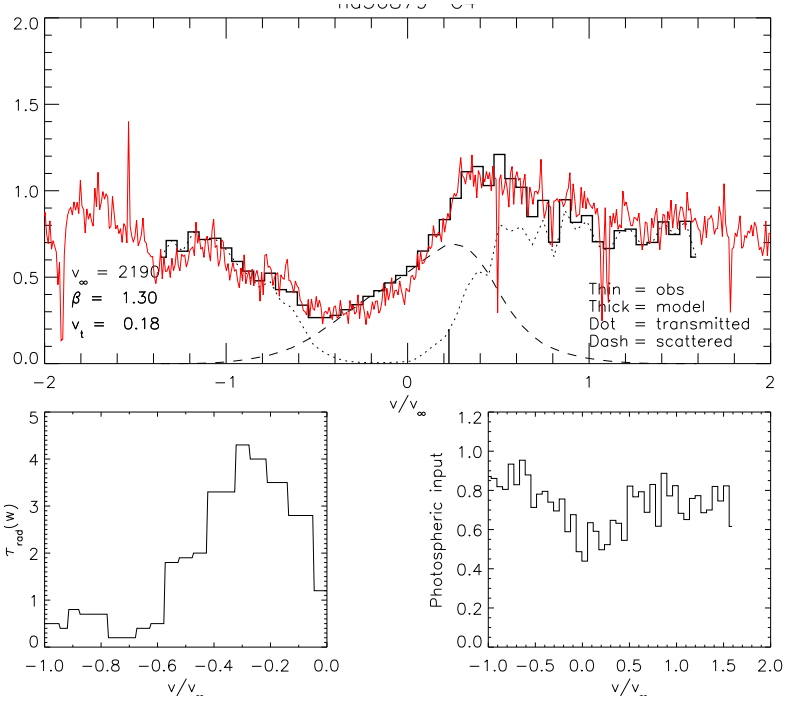

**Figure A.24.** Nv fit for HD 36879 (O7 V)

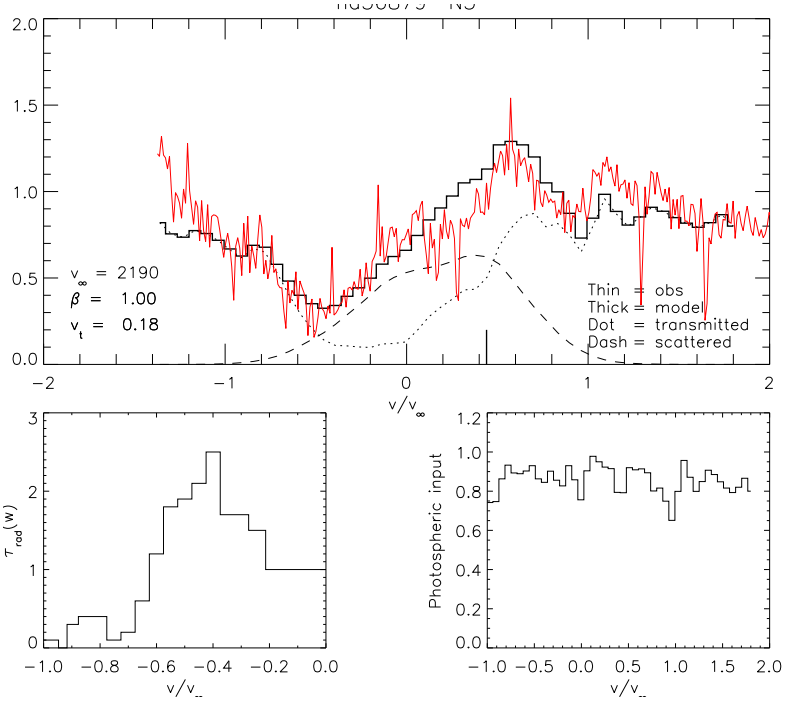


**Figure A.25.** Civ fit for HD 44811 (O7 V)

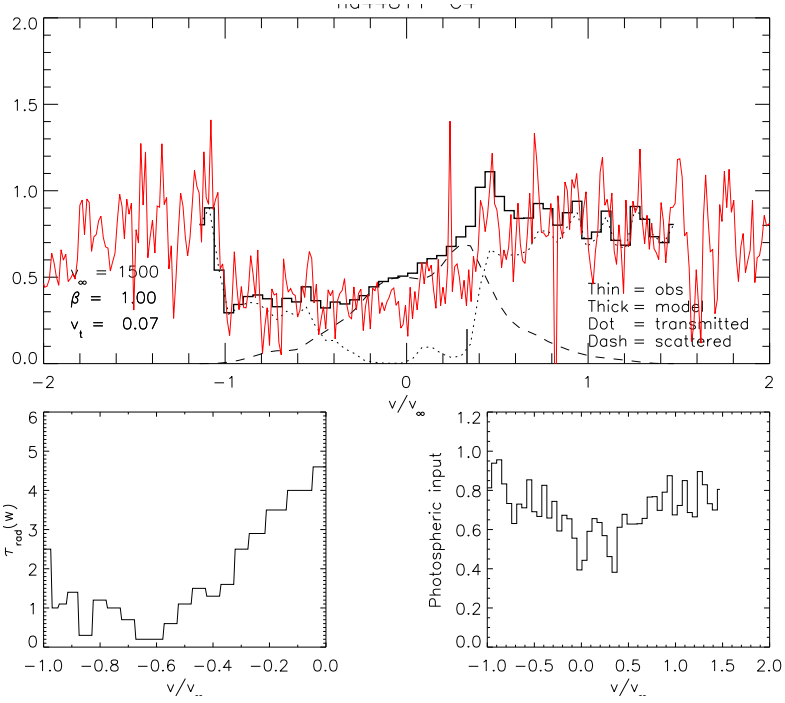

**Figure A.26.** Nv fit for HD 44811 (O7 V). Not used.

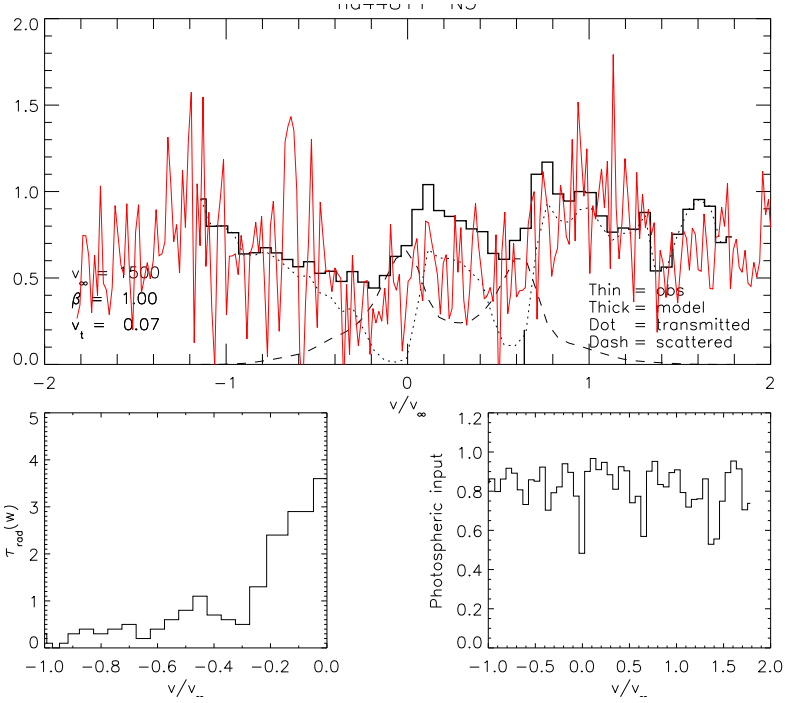


**Figure A.27.** Civ fit for HD 46485 (O7 V)

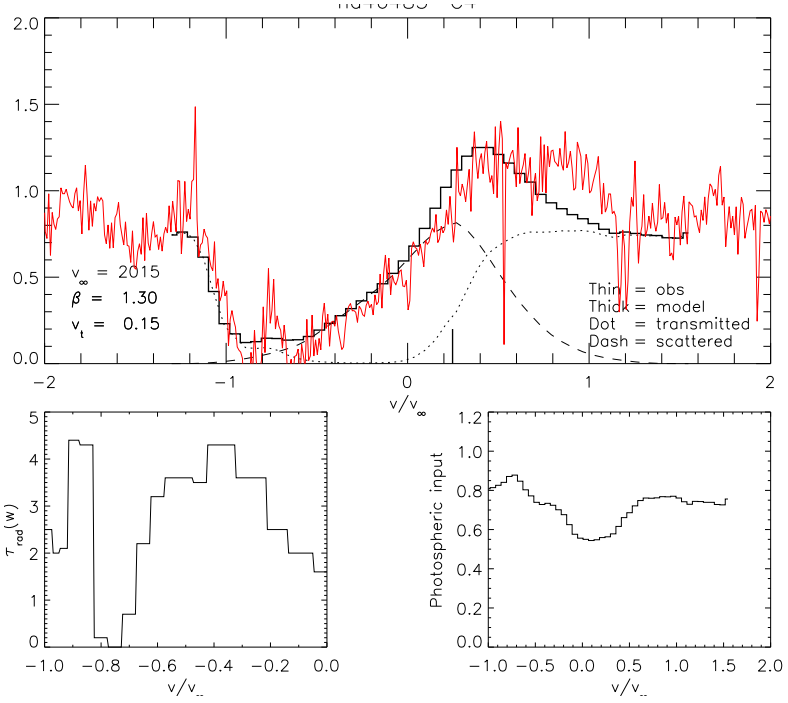

**Figure A.28.** CIV fit for HD 47839 (O7 V)

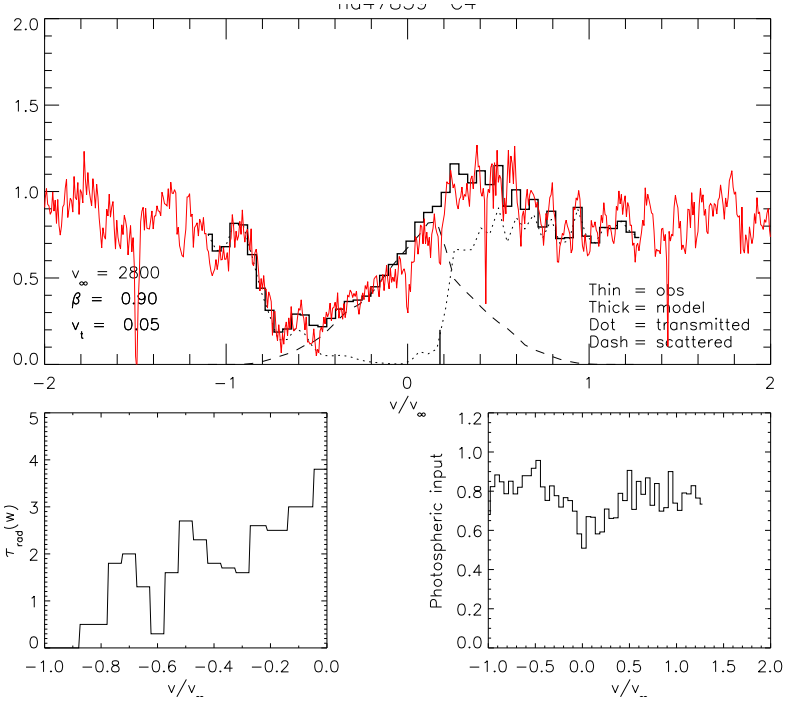


**Figure A.29.** NV fit for HD 47839 (O7 V)

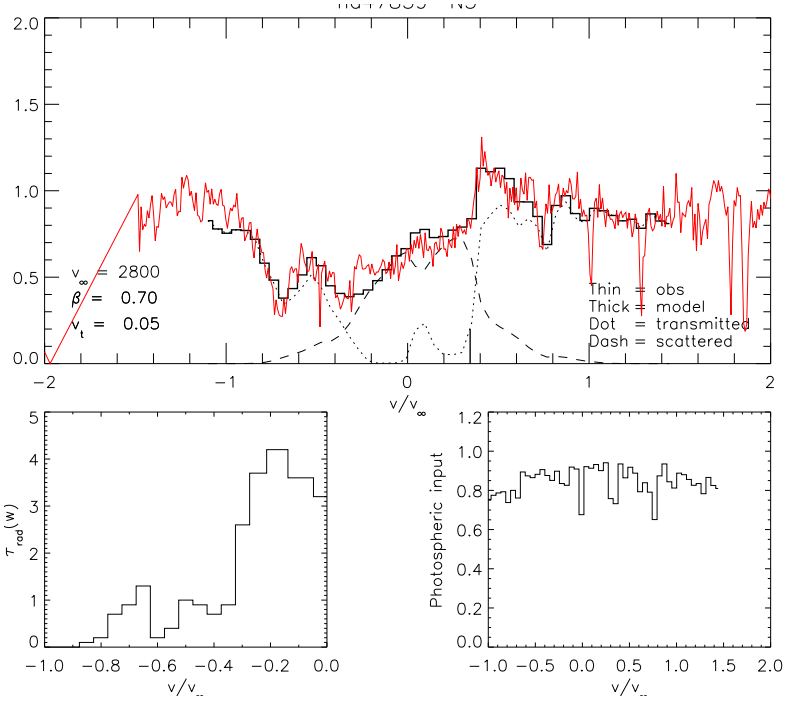

**Figure A.30.** CIV fit for HD 48099 (O7 V)

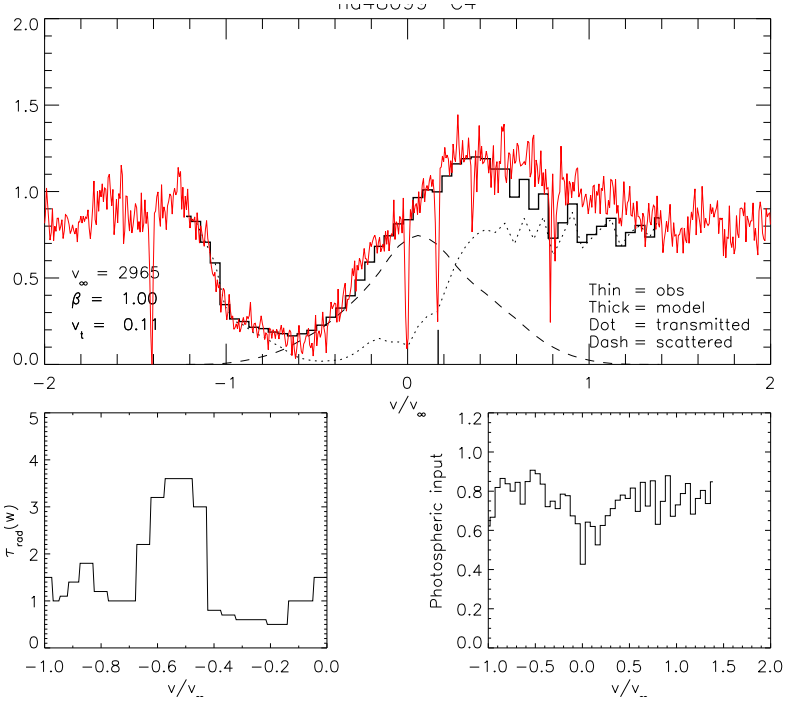


**Figure A.31.** NV fit for HD 48099 (O7 V)

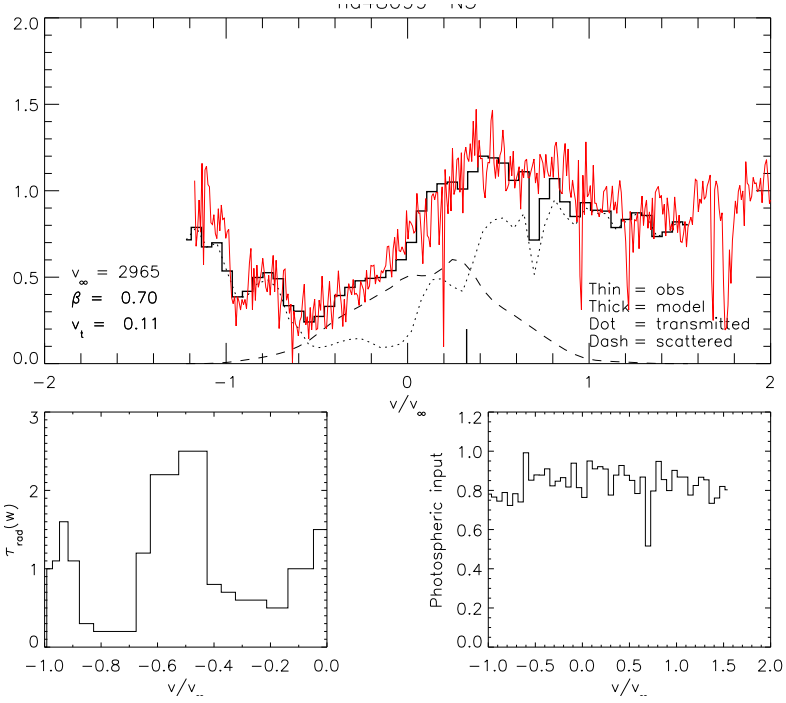

**Figure A.32.** CIV fit for HD 91824 (O7 V)

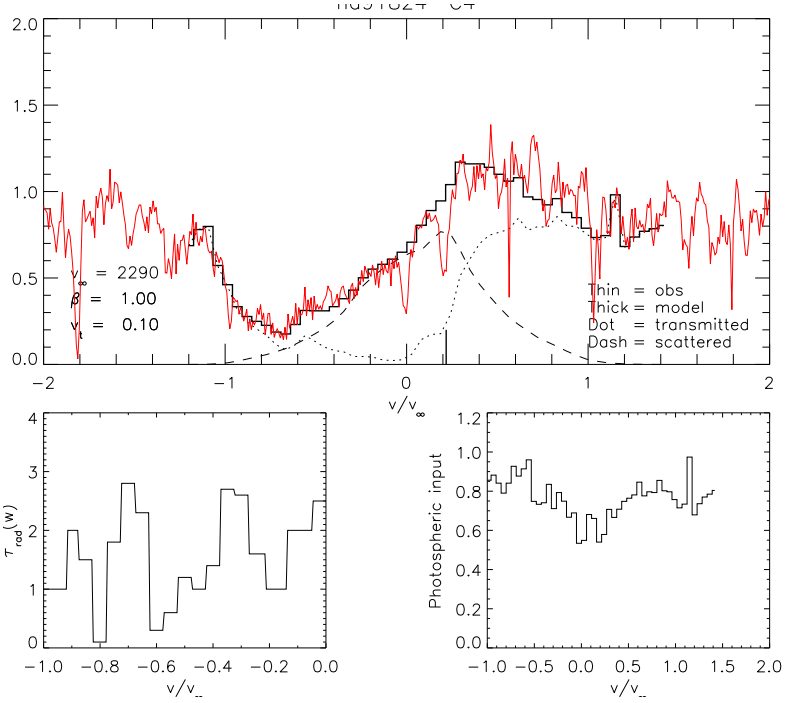


**Figure A.33.** NV fit for HD 91824 (O7 V)

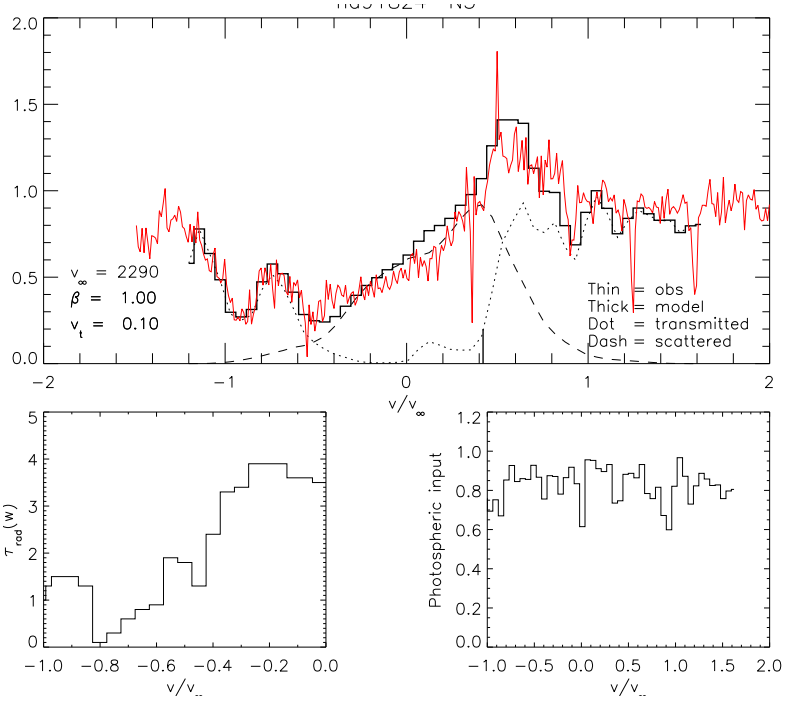

**Figure A.34.** CIV fit for HD 152623 (O7 V)

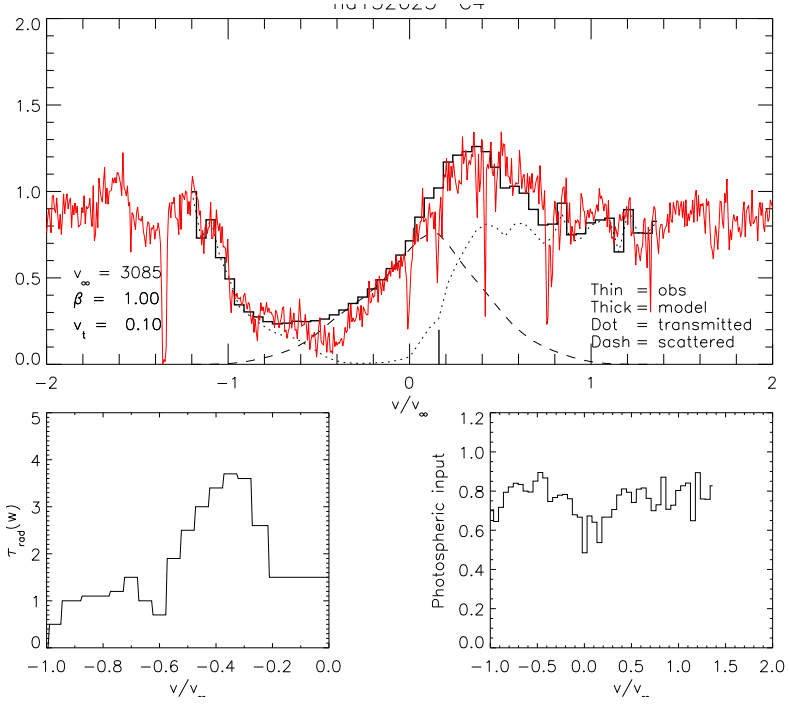

**Figure A.35.** Nv fit for HD 152623 (O7 V)

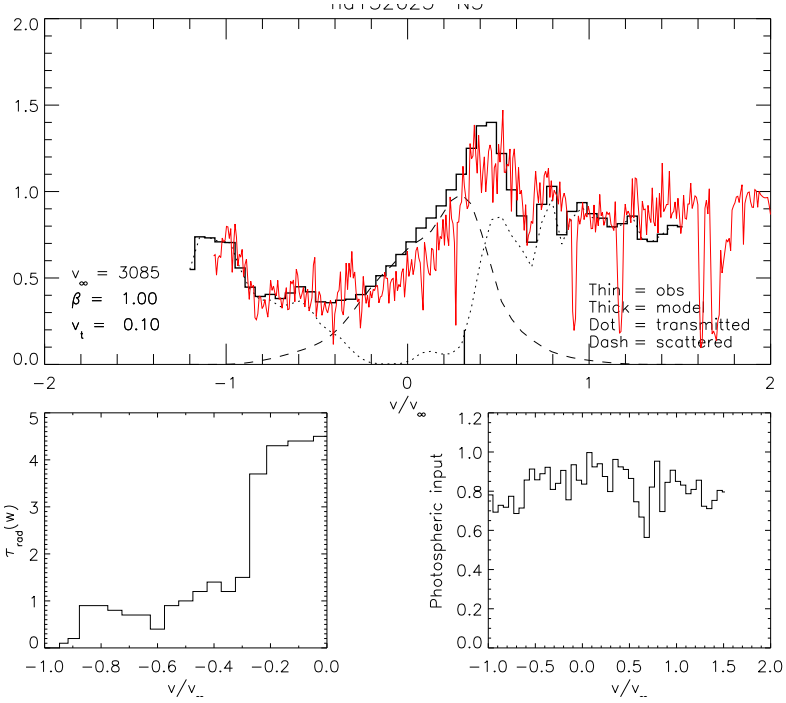


**Figure A.36.** Civ fit for HD 159176 (O7 V)

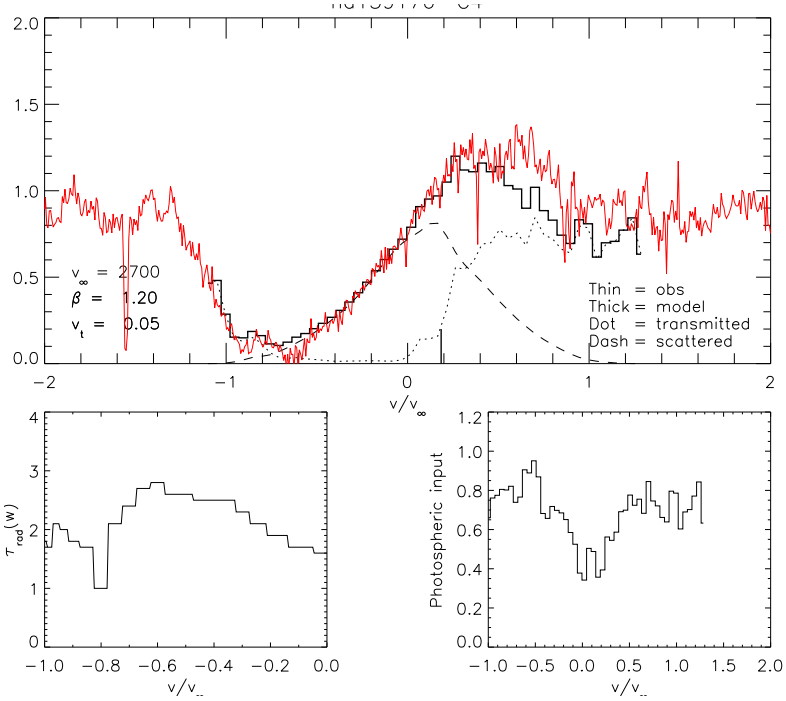

**Figure A.37.** Nv fit for HD 159176 (O7 V)

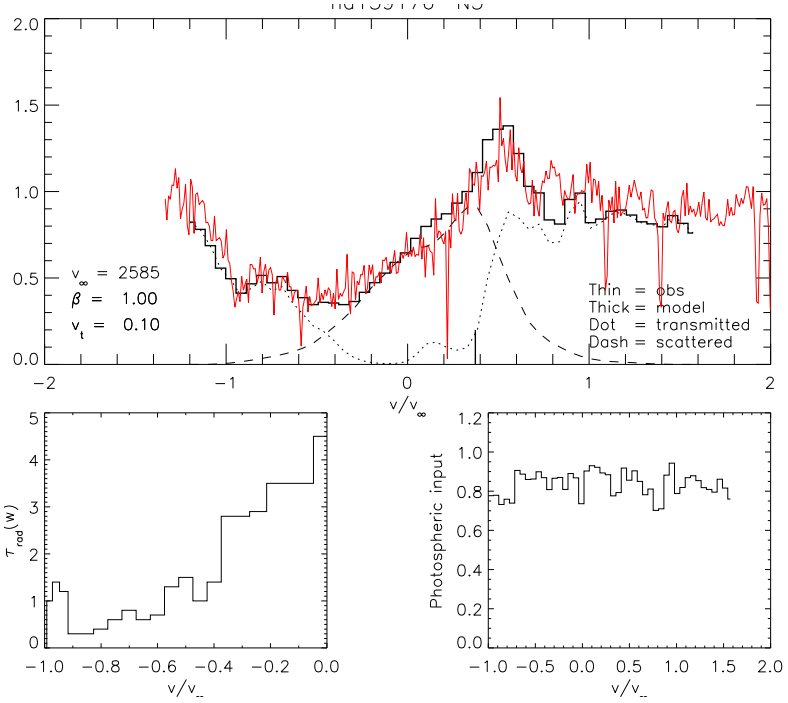


**Figure A.38.** Civ fit for HD 41997 (O7.5 V)

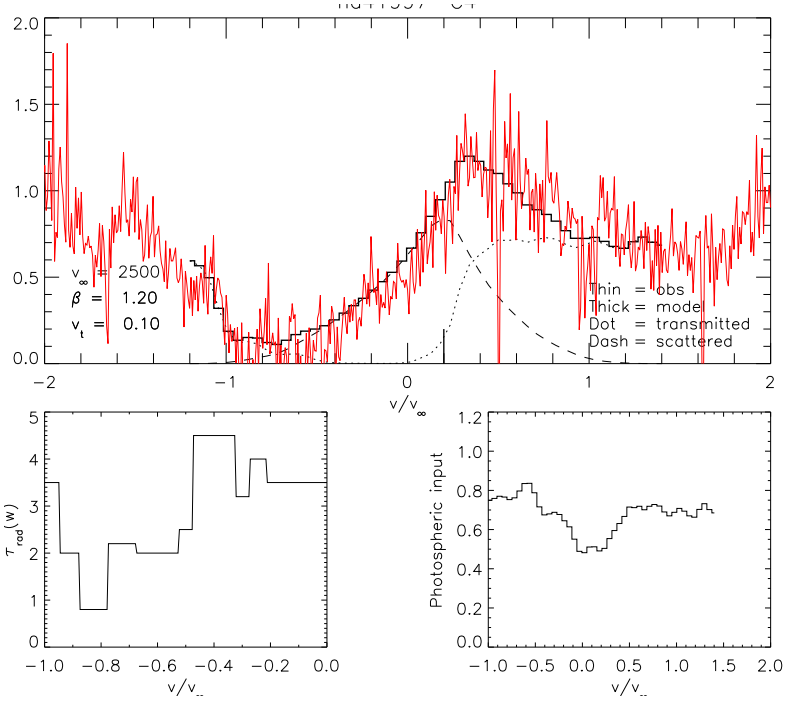

**Figure A.39.** CIV fit for HD 53975 (O7.5 V)

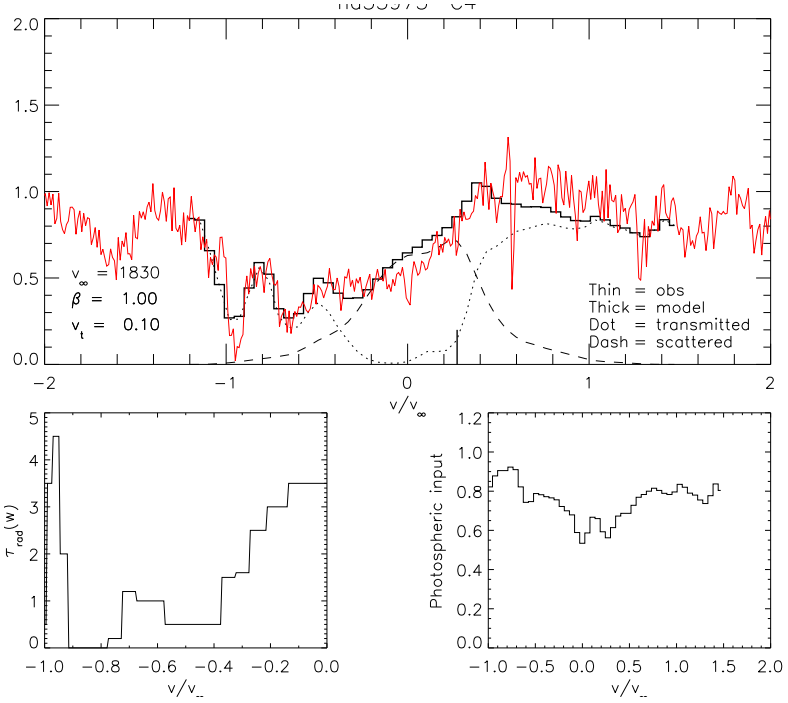


**Figure A.40.** NV fit for HD 53975 (O7.5 V)

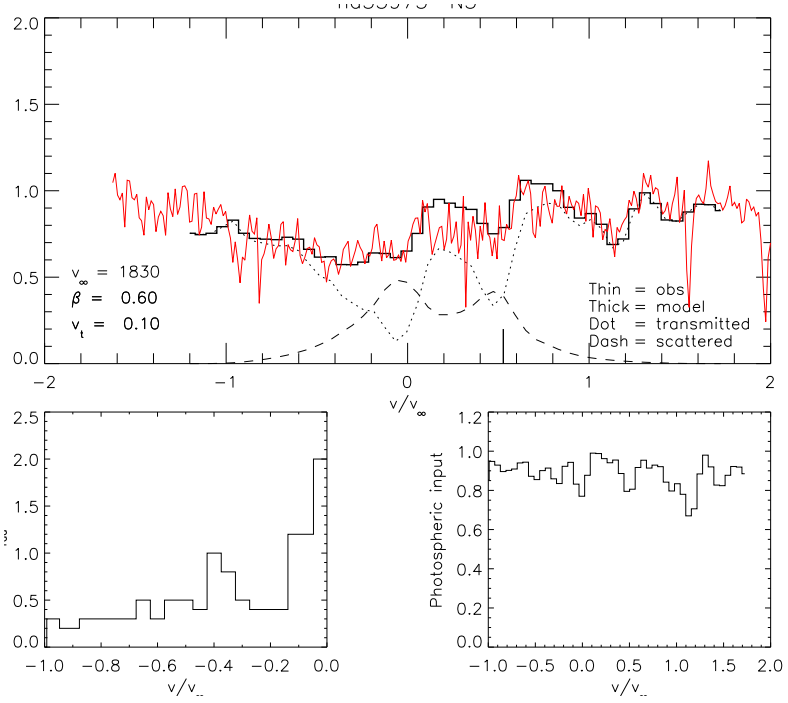

**Figure A.41.** CIV fit for HD 152590 (O7.5 V)

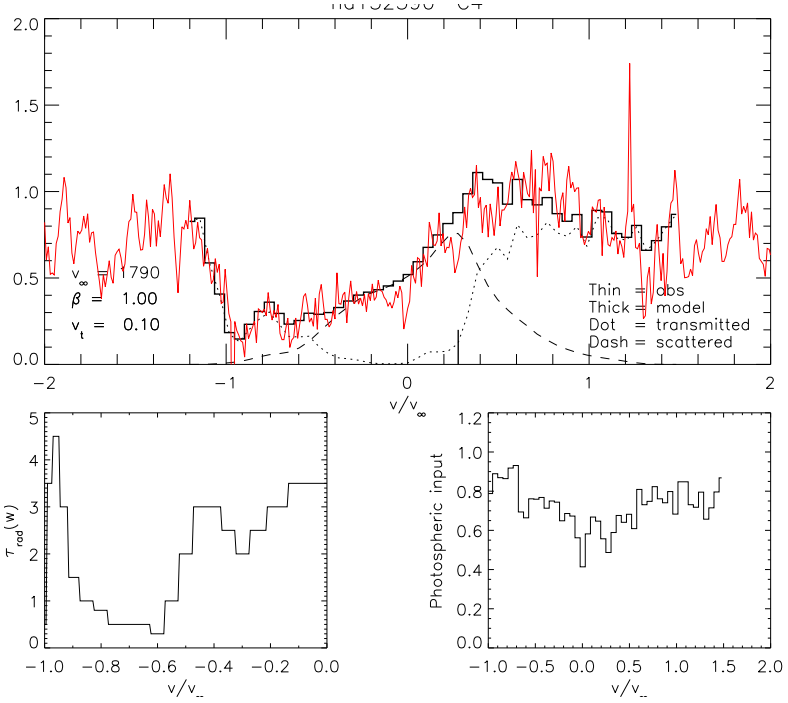


**Figure A.42.** NV fit for HD 152590 (O7.5 V)

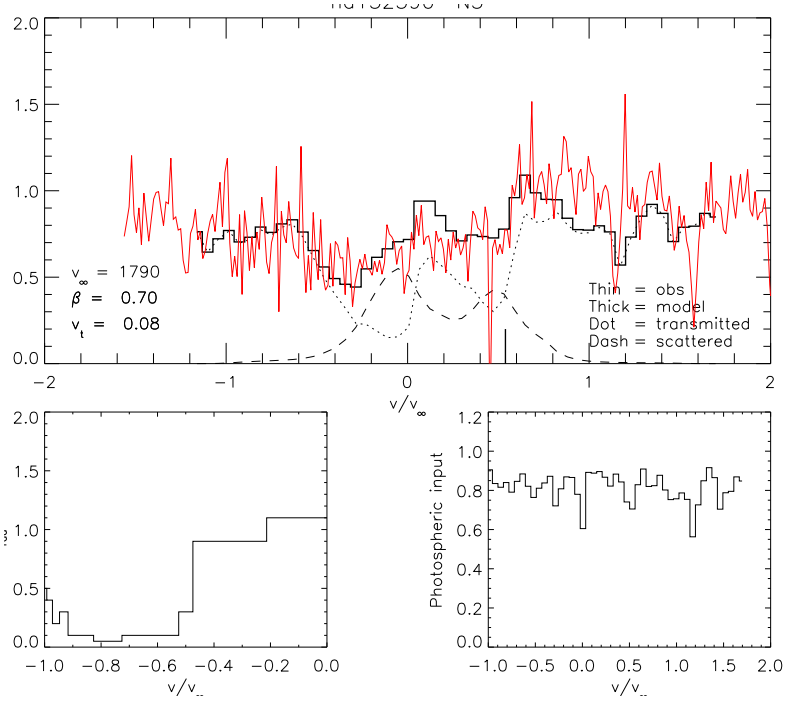

**Figure A.43.** CIV fit for HD 155806 (O7.5 V)

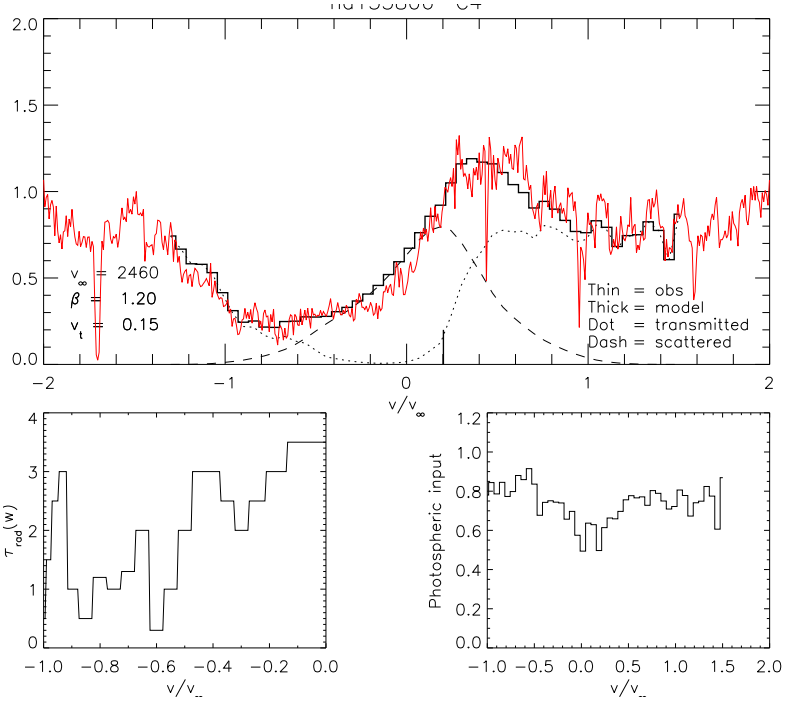


**Figure A.44.** NV fit for HD 155806 (O7.5 V)

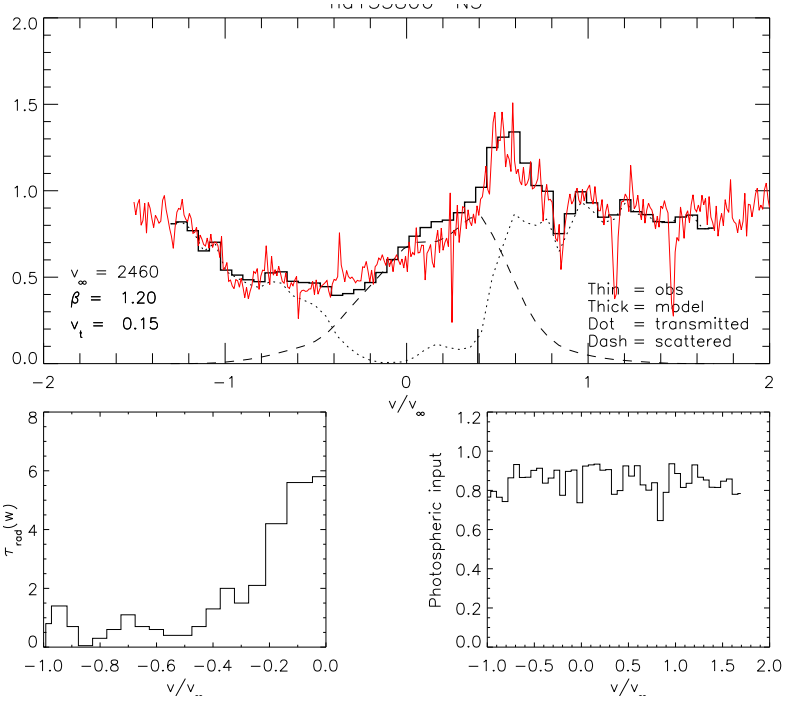

**Figure A.45.** CIV fit for HD 14633 (O8 V)

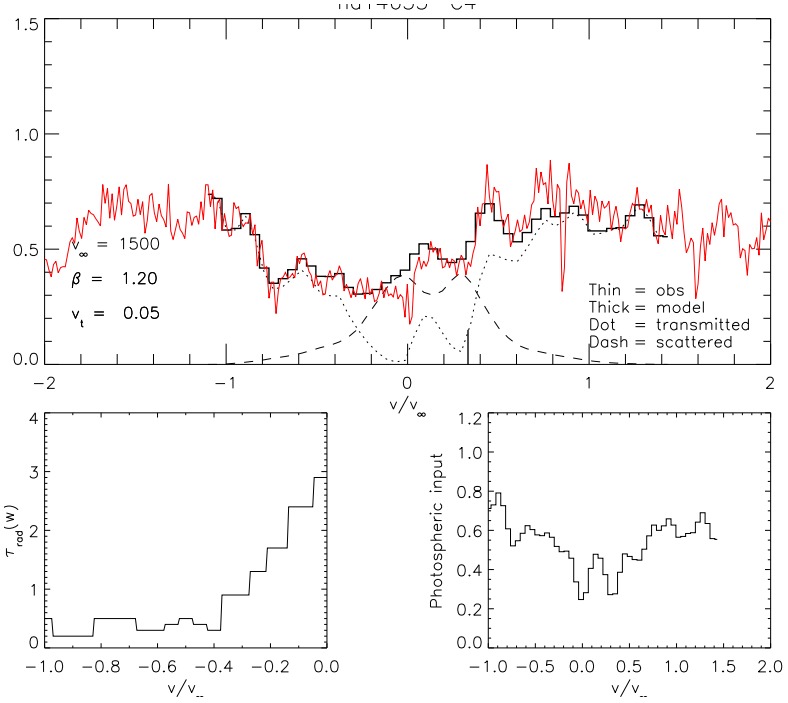


**Figure A.46.** CIV fit for HD 41161 (O8 V)

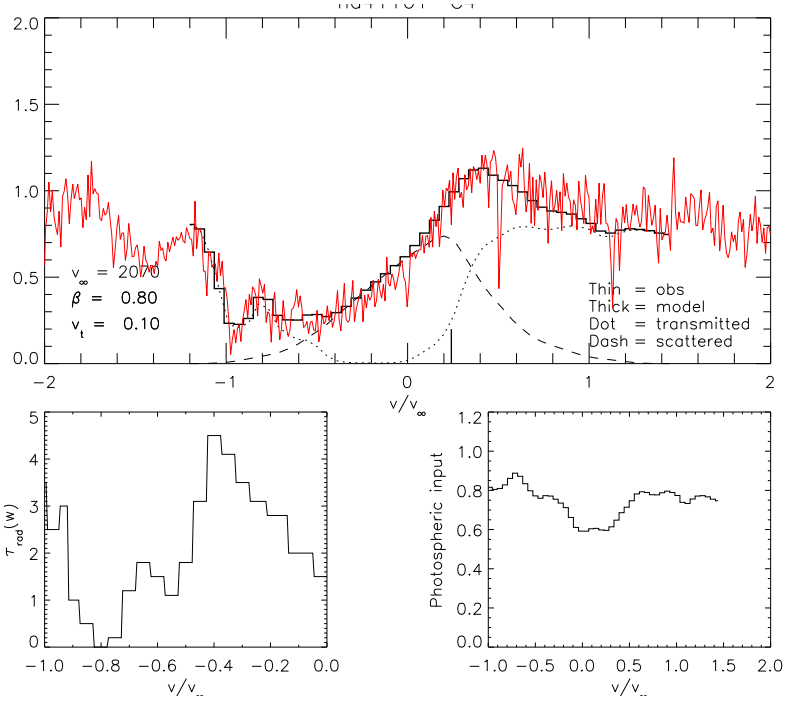

**Figure A.47.** Nv fit for HD 41161 (O8 V)

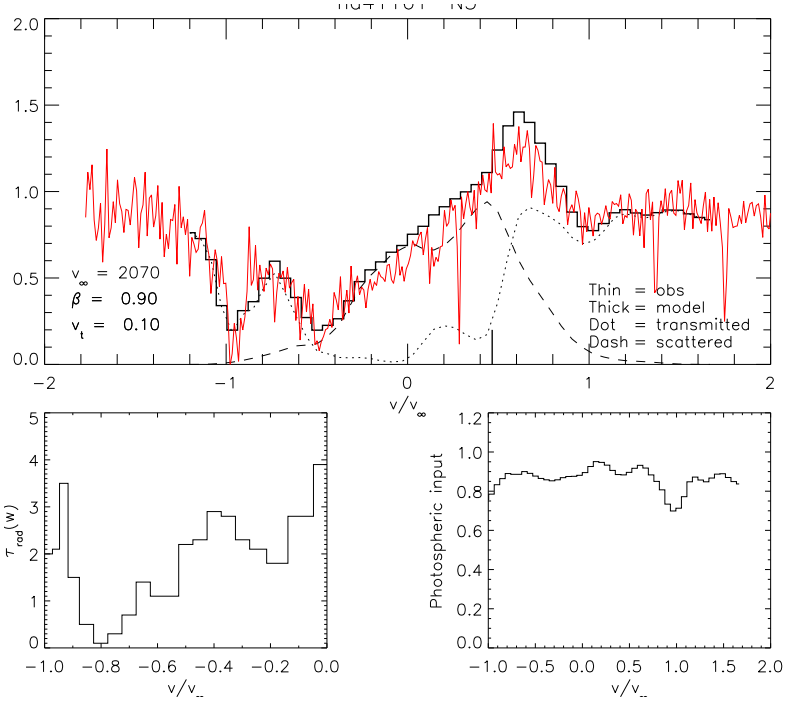


**Figure A.48.** Civ fit for HD 46056 (O8 V)

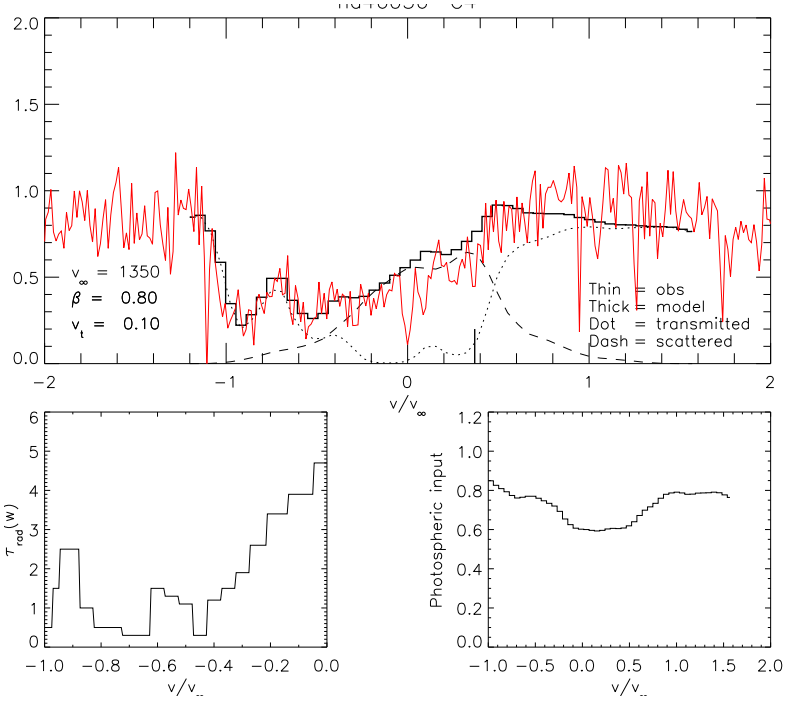

**Figure A.49.** CIV fit for HD 46966 (O8 V)

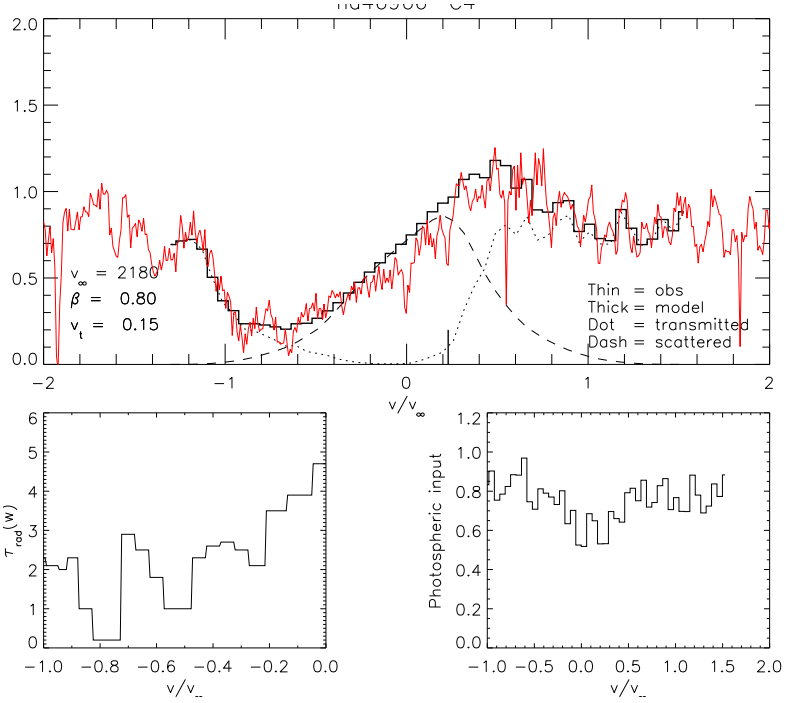


**Figure A.50.** NV fit for HD 46966 (O8 V)

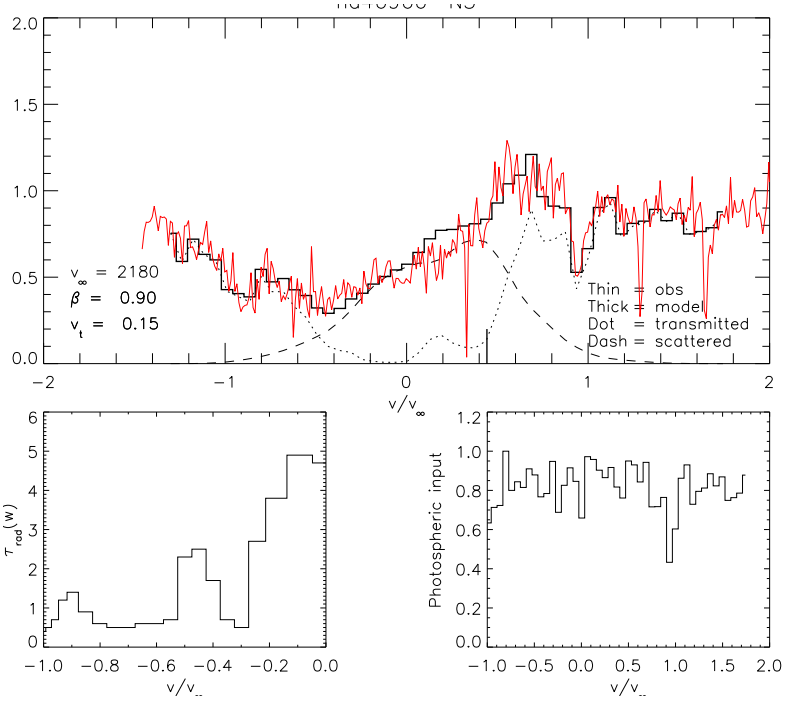

**Figure A.51.** CIV fit for HD 48279 (O8 V)

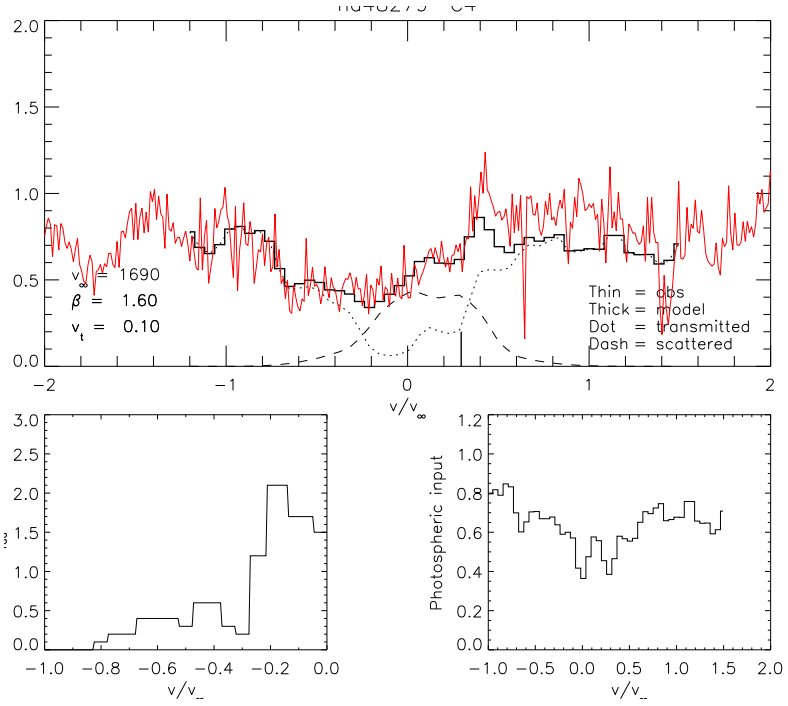

**Figure A.52.** Nv fit for HD 48279 (O8 V)

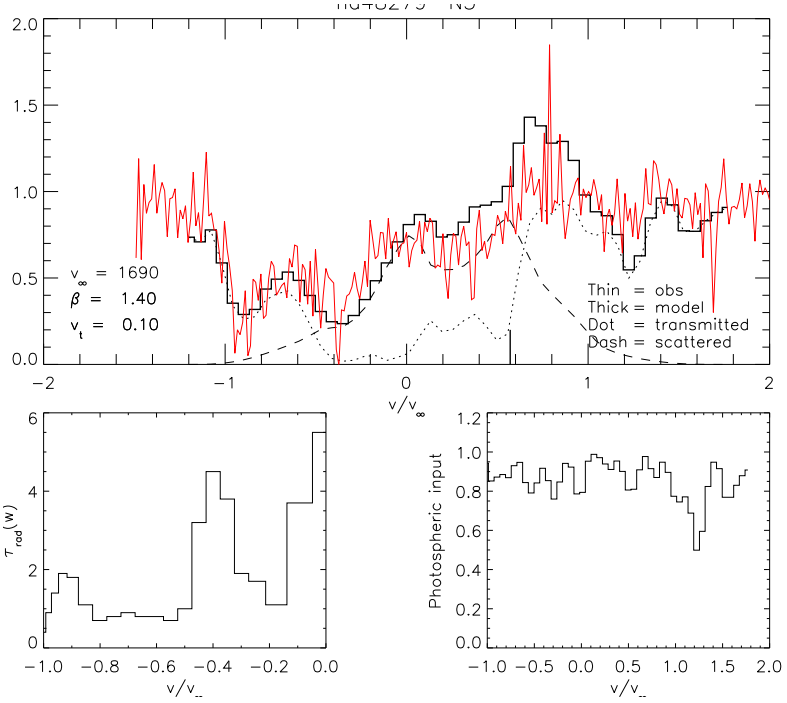


**Figure A.53.** Civ fit for HD 60848 (O8 V)

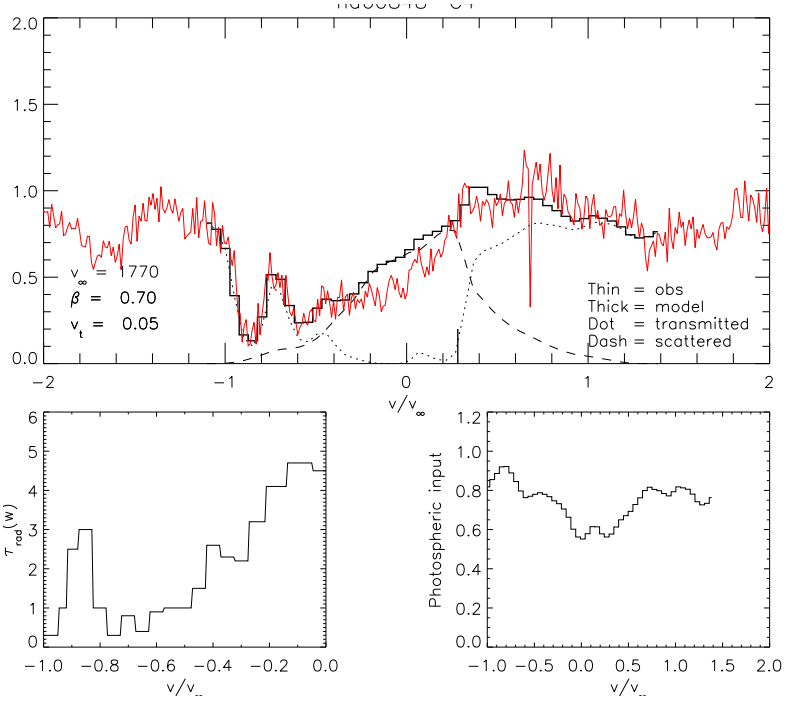

**Figure A.54.** Nv fit for HD 60848 (O8 V)

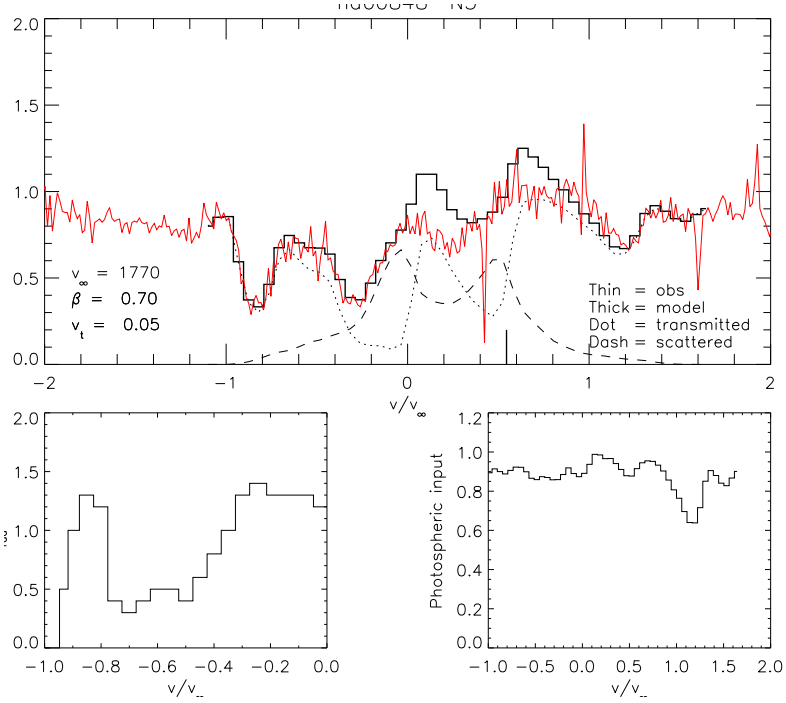


**Figure A.55.** Civ fit for HD 93222 (O8 V)

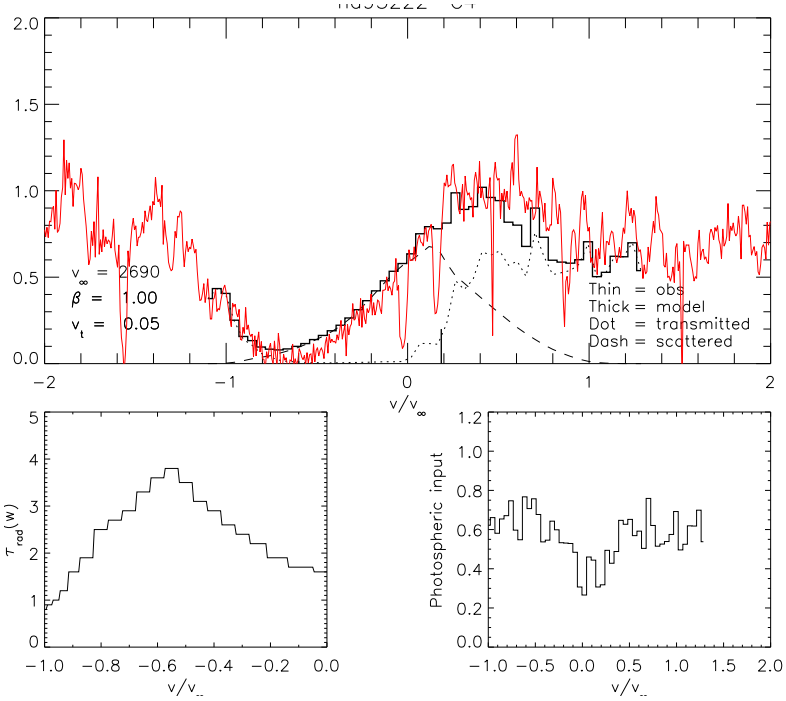

**Figure A.56.** CIV fit for HD 100213 (O8 V)

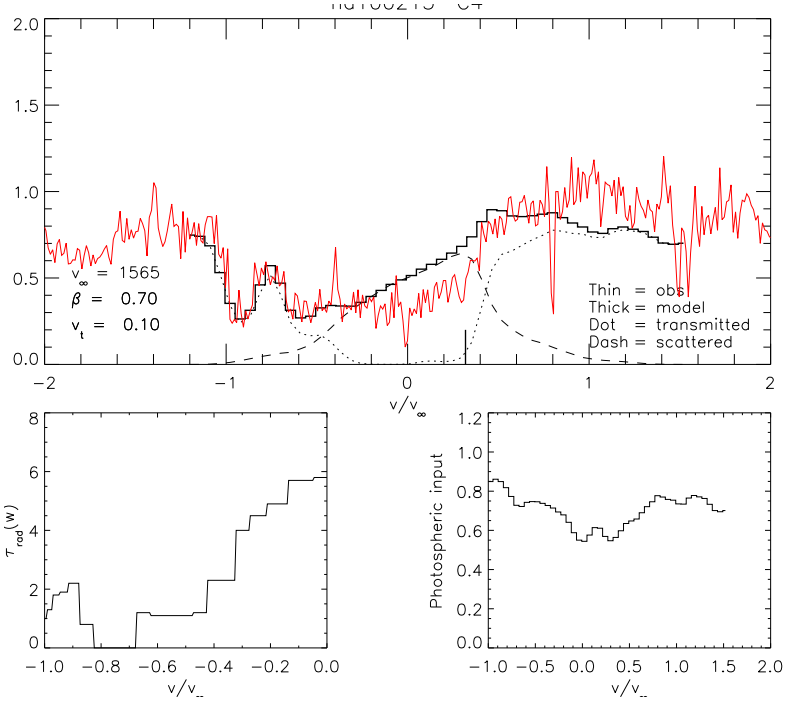


**Figure A.57.** NV fit for HD 100213 (O8 V)

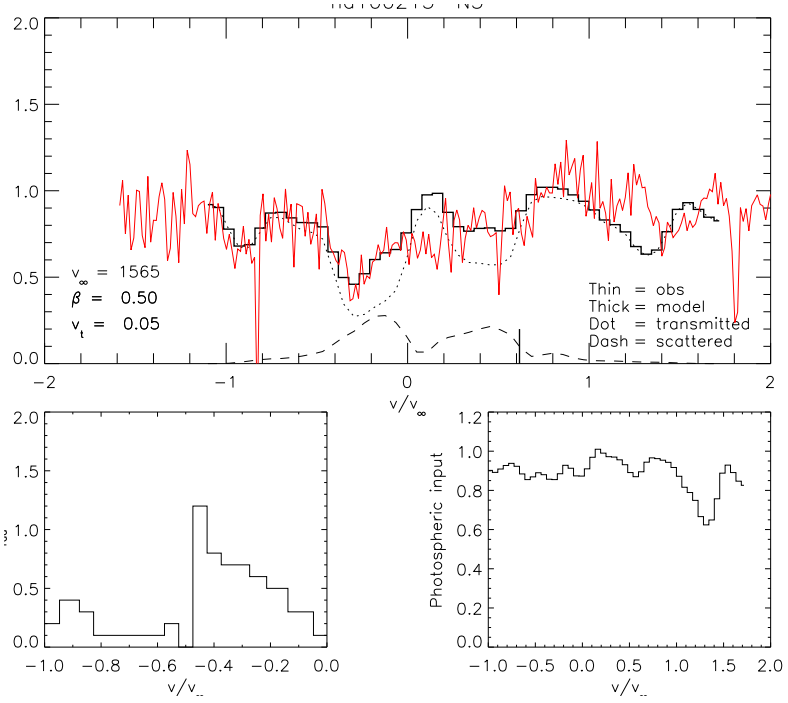

**Figure A.58.** CIV fit for HD 101413 (O8 V)

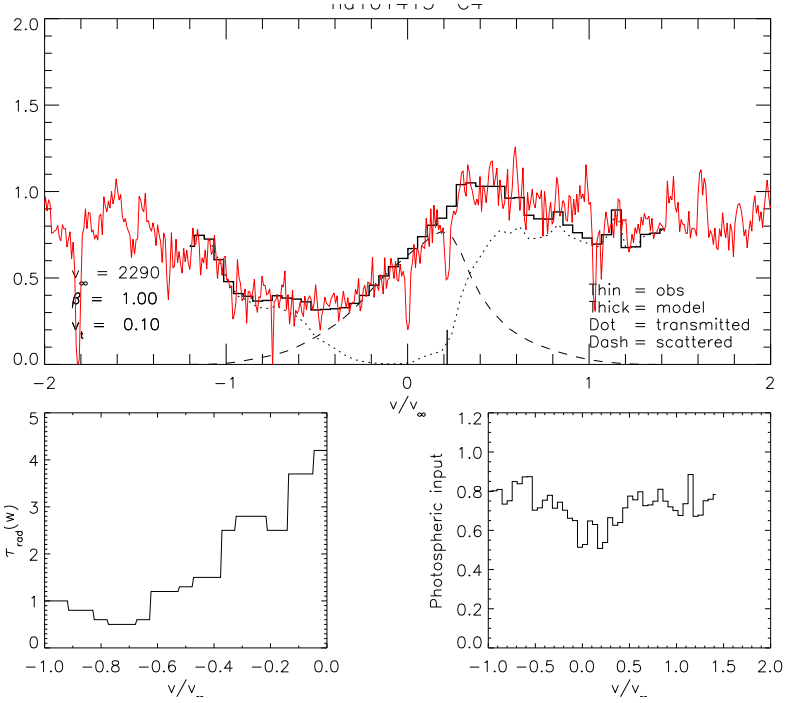


**Figure A.59.** NV fit for HD 101413 (O8 V)

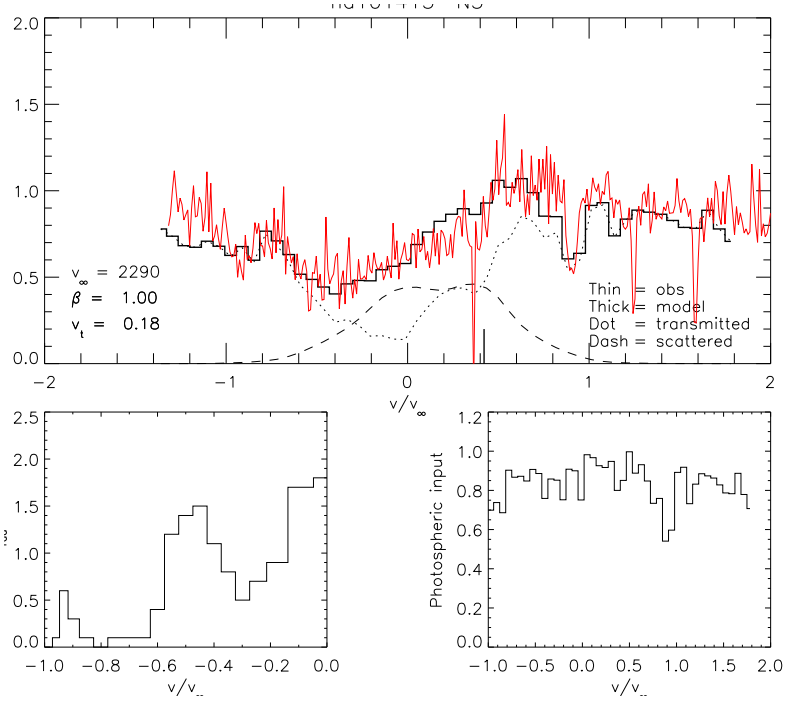

**Figure A.60.** CIV fit for HD 46149 (O8.5 V)

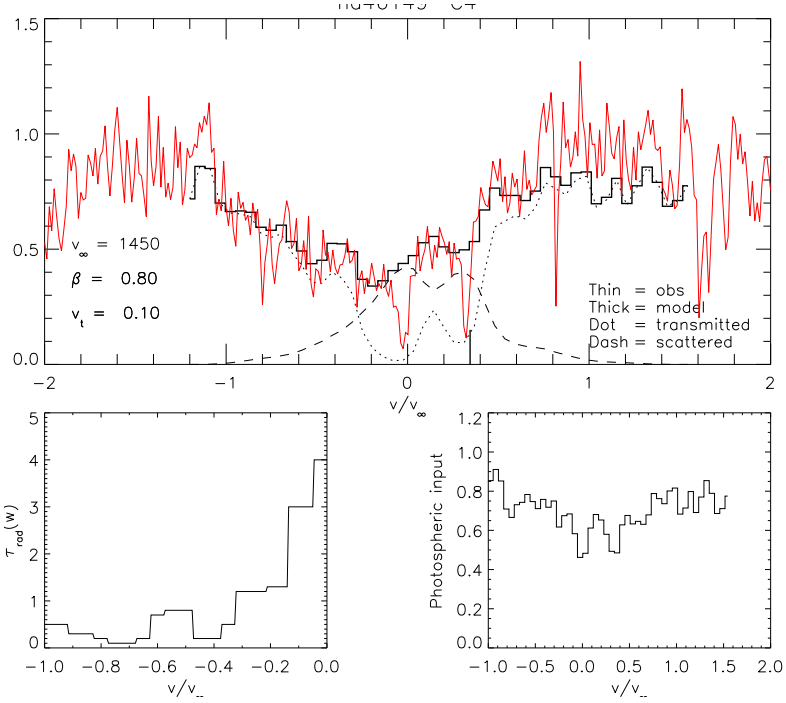


**Figure A.61.** CIV fit for HD 73882 (O8.5 V)

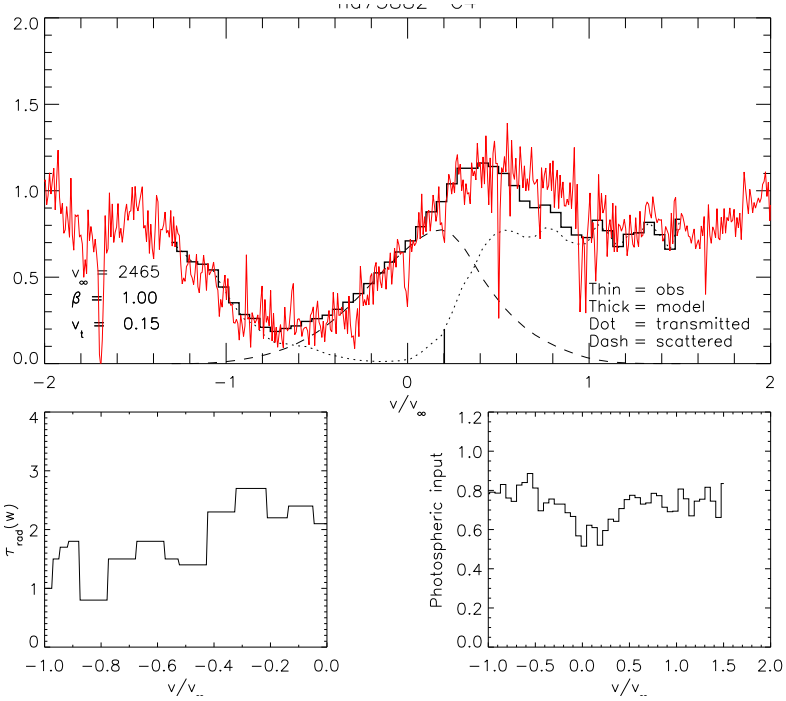

**Figure A.62.** Nv fit for HD 73882 (O8.5 V)

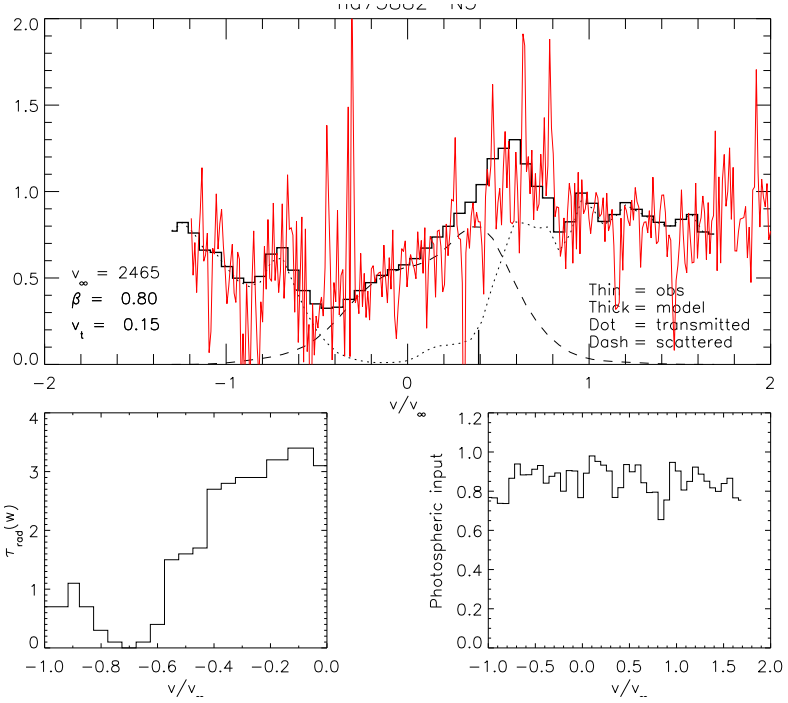


**Figure A.63.** Civ fit for HD 216532 (O8.5 V)

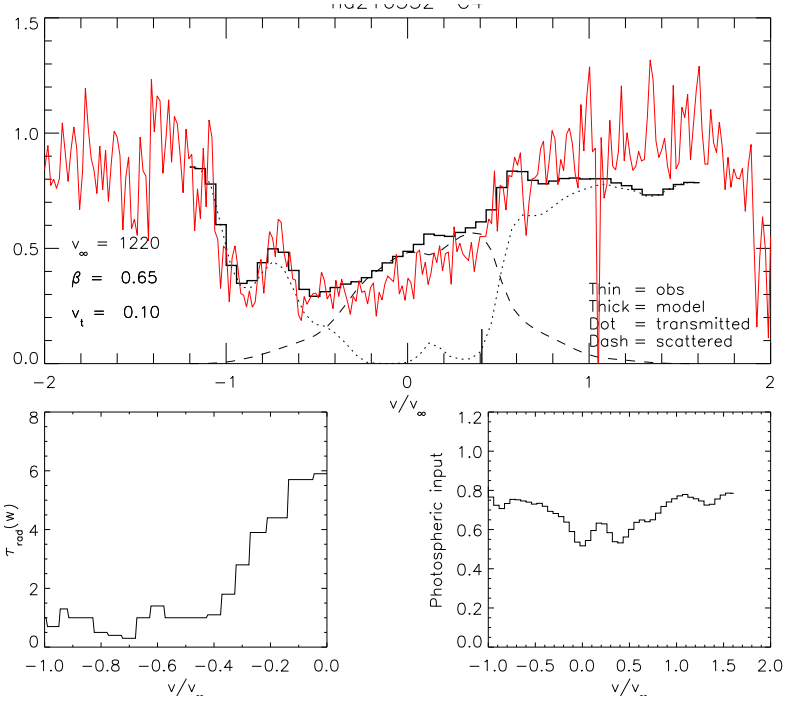

**Figure A.64.** CIV fit for HD 75759 (O9 V)

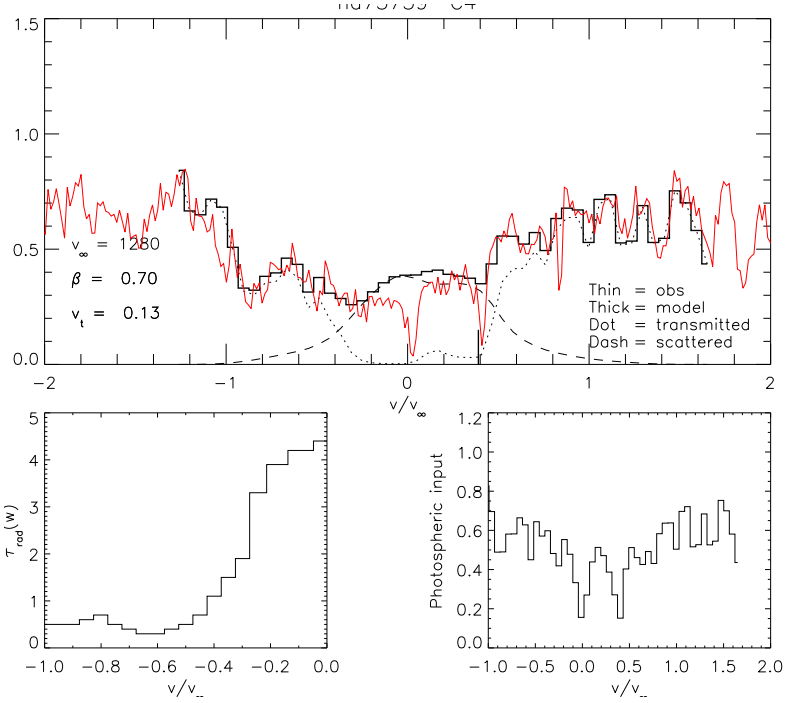


**Figure A.65.** CIV fit for HD 193322 (O9 V)

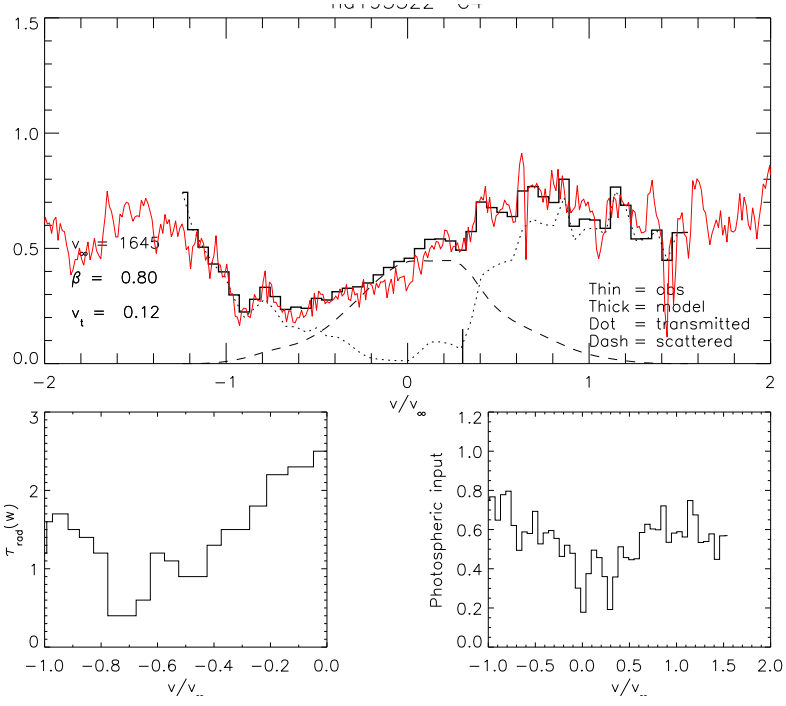

**Figure A.66.** CIV fit for HD 209481 (O9 V)

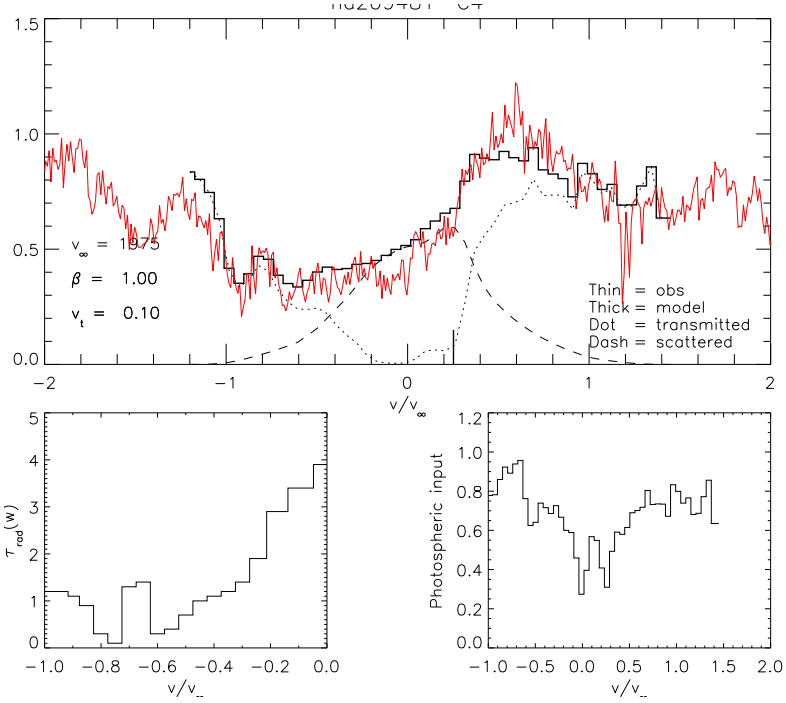


**Figure A.67.** NV fit for HD 209481 (O9 V). Not used.

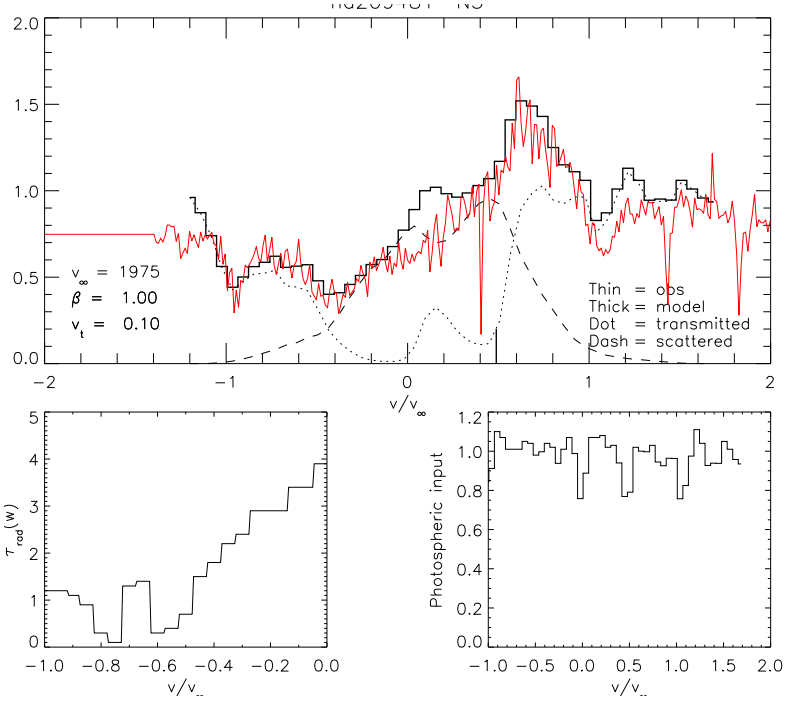

**Figure A.68.** CIV fit for HD 214680 (O9 V)

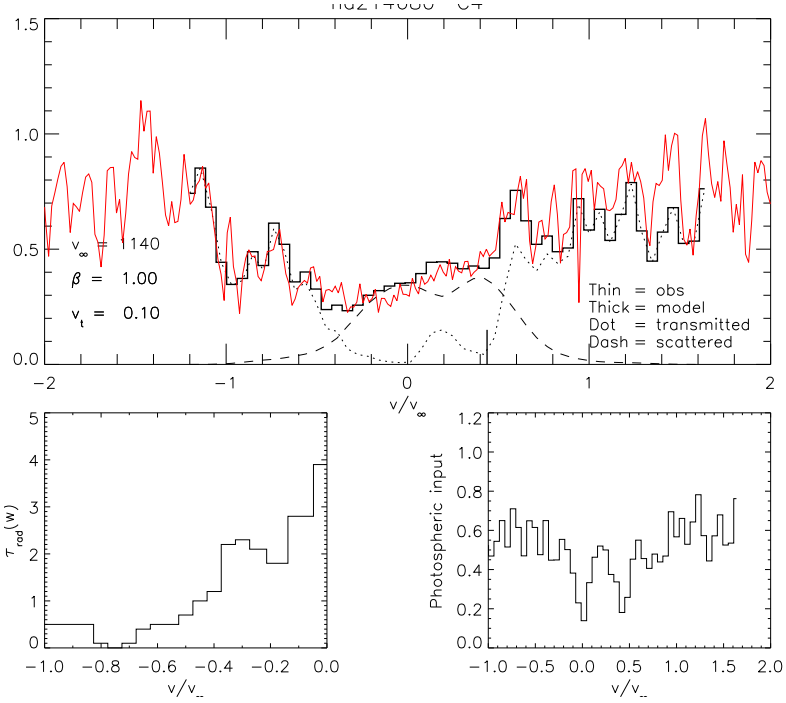


**Figure A.69.** CIV fit for HD 34078 (O9.5 V)

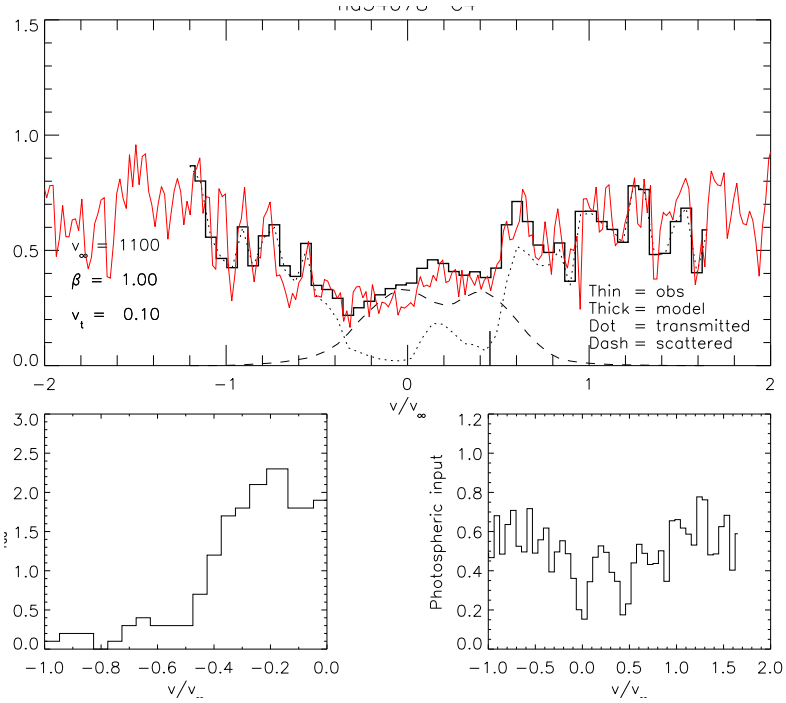

**Figure A.70.** CIV fit for HD 38666 (O9.5 V)

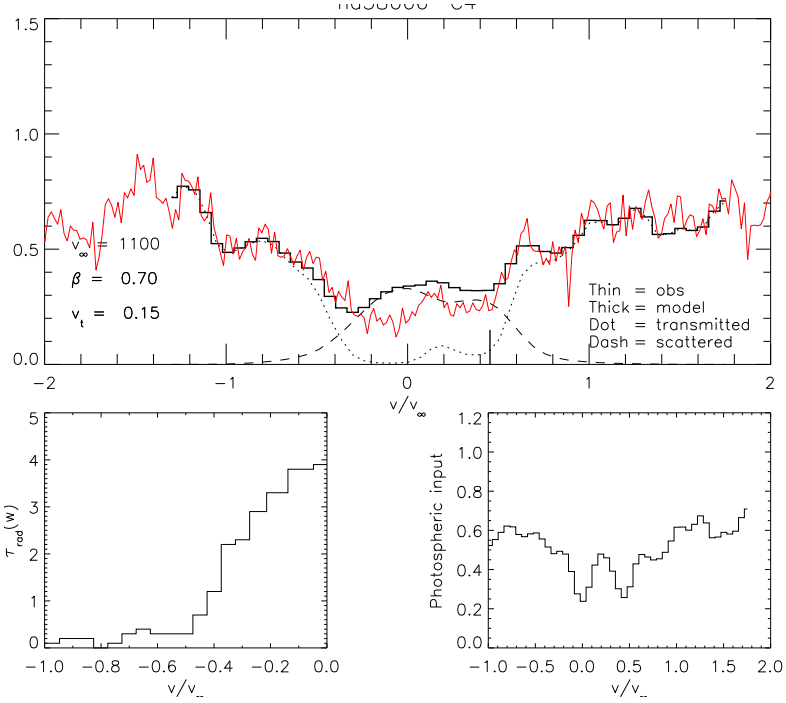


**Figure A.71.** CIV fit for HD 93027 (O9.5 V)

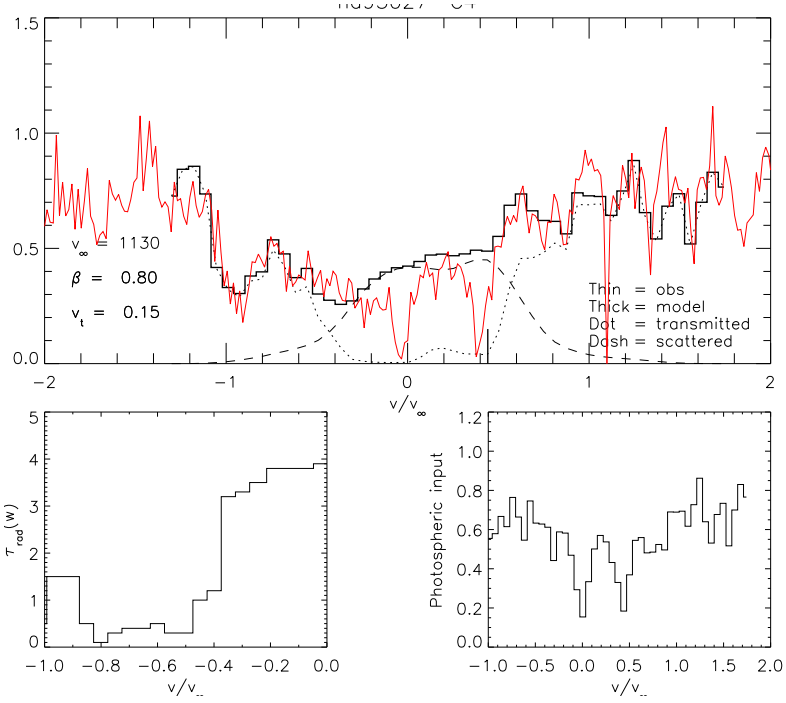

**Figure A.72.** CIV fit for HD 149757 (O9.5 V)

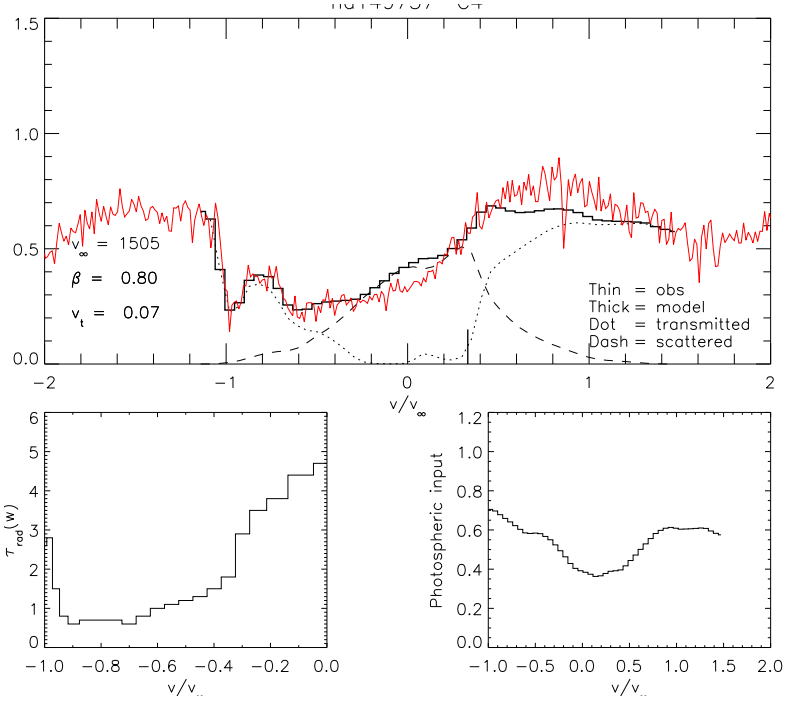

# Bibliography


Abbott, D. C., Bieging, J. H. & Churchwell, E., 1981, *ApJ*, **250**, 645 1.4, 1.5

Abbott, D. C., Bieging, J. H., Churchwell, E. & Cassinelli, J. P., 1980, *ApJ*, **238**, 196 1.4

Anderson, L. S., 1989, *ApJ*, **339**, 558 2.1.2

Asplund, M., Grevesse, N. & Sauval, A. J., 2005, in T. G. Barnes III & F. N. Bash (ed.), *Cosmic Abundances as Records of Stellar Evolution and Nucleosynthesis*, volume 336 of *Astronomical Society of the Pacific Conference Series*, pp. 25–+ 2.4, 5.2.1, 5.4.1, 6.2

Auer, L. H. & Mihalas, D., 1969, *ApJ*, **158**, 641 2.1.1

Auer, L. H. & Mihalas, D., 1972, *ApJSS*, **24**, 193 1.2.1, 1.4

Babel, J., 1995, *A&A*, **301**, 823 1.5

Babel, J., 1996, *A&A*, **309**, 867 1.5

Bouret, J., Lanz, T. & Hillier, D. J., 2005, *A&A*, **438**, 301 1.5, 2.4, 2.2, 2.4.2, 2.4.3, 3.3, 4.3, 6.1

Cantiello, M., Langer, N., Brott, I., de Koter, A., Shore, S. N., Vink, J. S., Voegler, A., Lennon, D. J. & Yoon, S., 2009, *A&A*, **499**, 279 7.1

Castor, J. I., Abbott, D. C. & Klein, R. I., 1975, *ApJ*, **195**, 157 1.3, 1.3.2

Chlebowski, T. & Garmany, C. D., 1991, *ApJ*, **368**, 241 1.5, 5.1

Cohen, D. H., Leutenegger, M. A., Wollman, E. E., Zsargó, J., Hillier, D. J., Townsend, R. H. D. & Owocki, S. P., 2010, *MNRAS*, **405**, 2391 1.4, 1.5, 2.1.4, 3.2.1, 3.5, 6.2, 6.3.2, 6.3, 6.3.2

Conti, P. S. & Alschuler, W. R., 1971, *ApJ*, **170**, 325 1.2, 2.5

Conti, P. S. & Frost, S. A., 1977, *ApJ*, **212**, 728 2.5

Crowther, P. A., 2007, *Ann. Rev. Astr. Astrophys.*, **45**, 177 1.1.2

Crowther, P. A., Dessart, L., Hillier, D. J., Abbott, J. B. & Fullerton, A. W., 2002, *A&A*, **392**, 653 3.5

Davies, B., Oudmaijer, R. D. & Vink, J. S., 2005, *A&A*, **439**, 1107 1.5

Dessart, L. & Owocki, S. P., 2005, *A&A*, **437**, 657 1.5, 1.12, 7.1

Drew, J. E., 1990, *ApJ*, **357**, 573 1.4

Drew, J. E., Hoare, M. G. & Denby, M., 1994, *MNRAS*, **266**, 917 1.5

Eversberg, T., Lepine, S. & Moffat, A. F. J., 1998, *ApJ*, **494**, 799 1.5

Feldmeier, A., Puls, J. & Pauldrach, A. W. A., 1997, *A&A*, **322**, 878 1.5

Friend, D. B. & Abbott, D. C., 1986, *ApJ*, **311**, 701 1.3

Fullerton, A. W., Massa, D. L. & Prinja, R. K., 2006, *ApJ*, **637**, 1025 1.5, 1.13, 1.5, 2.4.2, 3.3, 4.2.1, 4.2.2, 4.3, 5.3, 5.5.3, 6, 6.3.1, 6.3.2, 6.2, 6.3.2, 6.3.2, 6.3, 6.4, 6.4

Hamann, W., 1981, *A&A*, **93**, 353 1.5, 5.2.1

Hamann, W. & Gräfener, G., 2003, *A&A*, **410**, 993 1.2.1

Harnden, Jr., F. R., Branduardi, G., Gorenstein, P., Grindlay, J., Rosner, R., Topka, K., Elvis, M., Pye, J. P. & Vaiana, G. S., 1979, *ApJL*, **234**, L51 1.5

Haser, S. M., Lennon, D. J., Kudritzki, R., Puls, J., Pauldrach, A. W. A., Bianchi, L. & Hutchings, J. B., 1995, *A&A*, **295**, 136 5.2.1

Hillier, D. J., 1990, *A&A*, **231**, 116 1.3

Hillier, D. J., 1991, *A&A*, **247**, 455 1.5

Hillier, D. J., Kudritzki, R. P., Pauldrach, A. W., Baade, D., Cassinelli, J. P., Puls, J. & Schmitt, J. H. M. M., 1993, *A&A*, **276**, 117 2.1.4

Hillier, D. J., Lanz, T., Heap, S. R., Hubeny, I., Smith, L. J., Evans, C. J., Lennon, D. J. & Bouret, J. C., 2003, *ApJ*, **588**, 1039 3.5

Hillier, D. J. & Miller, D. L., 1995, in *Bulletin of the American Astronomical Society*, volume 27 of *Bulletin of the American Astronomical Society*, pp. 839–+ 1.3

Hillier, D. J. & Miller, D. L., 1998, *ApJ*, **496**, 407 1.2.1, 1.3, 2, 2.1.2, 2.2.1

Hillier, D. J. & Miller, D. L., 1999, *ApJ*, **519**, 354 2.1.4

Hirschi, R., Frischknecht, U., Thielemann, F., Pignatari, M., Chiappini, C., Ekström, S., Meynet, G. & Maeder, A., 2008, in L. K. Hunt, S. Madden, & R. Schneider (ed.), *IAU Symposium*, volume 255 of *IAU Symposium*, pp. 297–304 1.1.2, 5.7.1

Howarth, I. D., Prinja, R. K. & Massa, D., 1995, *ApJL*, **452**, L65+ 1.5

Howarth, I. D., Siebert, K. W., Hussain, G. A. J. & Prinja, R. K., 1997, *VizieR Online Data Catalog*, **728**, 40265 2.4, 5.4.1

Hubeny, I. & Lanz, T., 1995, *ApJ*, **439**, 875 1.2.1, 2.1.3, 5.2.1, 6.1

Hundhausen, A. J., 1972, *NASA Special Publication*, **308**, 393 1.5, 1.10

Kaper, L., Henrichs, H. F., Fullerton, A. W., Ando, H., Bjorkman, K. S., Gies, D. R., Hirata, R., Kambe, E., McDavid, D. & Nichols, J. S., 1997, *A&A*, **327**, 281 1.5, 5.7.1

Kaper, L., Henrichs, H. F., Nichols, J. S. & Telting, J. H., 1999, *A&A*, **344**, 231 1.5, 5.7.1

Klein, R. I. & Castor, J. I., 1978, *ApJ*, **220**, 902 1.4

Krtička, J., Votruba, V. & Kubát, J., 2010, *A&A*, **516**, A100+ 5.7.1

Kudritzki, R., Lennon, D. J. & Puls, J., 1995, in J. R. Walsh & I. J. Danziger (ed.), *Science with the VLT*, pp. 246–+ 1.1.1, 1.5

Kudritzki, R. & Puls, J., 2000, *Ann. Rev. Astr. Astrophys.*, **38**, 613 1.8, 5.21, 5.22, 5.7.1

Kudritzki, R. P., Puls, J., Gabler, R. & Schmitt, J. H. M. M., 1991, in R. F. Malina & S. Bowyer (ed.), *Extreme Ultraviolet Astronomy*, pp. 130–+ 1.5

Kurucz, R. & Bell, B., 1995, *Atomic Line Data (R.L. Kurucz and B. Bell) Kurucz CD-ROM No. 23. Cambridge, Mass.: Smithsonian Astrophysical Observatory, 1995.*, **23** 2.2.1

Lamers, H. J. G. L. M. & Cassinelli, J. P., 1999, *Introduction to Stellar Winds* 1.3, 1.5, 1.7

Lamers, H. J. G. L. M., Cerruti-Sola, M. & Perinotto, M., 1987, *ApJ*, **314**, 726 1.4, 5.2.1

Lamers, H. J. G. L. M. & Leitherer, C., 1993, *ApJ*, **412**, 771 6.2, 6.3

Lamers, H. J. G. L. M. & Waters, L. B. F. M., 1984*a*, *A&A*, **136**, 37 1.4

Lamers, H. J. G. L. M. & Waters, L. B. F. M., 1984*b*, *A&A*, **138**, 25 1.4

Lee, H. & Chen, W. P., 2007, *ApJ*, **657**, 884 1.1.1

Leitherer, C., 1988, *ApJ*, **326**, 356 1.4

Lépine, S. & Moffat, A. F. J., 2008, *AJ*, **136**, 548 1.5

Lobel, A. & Blomme, R., 2008, *ApJ*, **678**, 408 1.5, 1.10

Lucy, L. B., 1982, *ApJ*, **255**, 278 1.5

Lucy, L. B., 1983, *ApJ*, **274**, 372 1.5

Lucy, L. B. & Solomon, P. M., 1970, *ApJ*, **159**, 879 1.3, 1.3.2, 1.5

Macfarlane, J. J., Waldron, W. L., Corcoran, M. F., Wolff, M. J., Wang, P. & Cassinelli, J. P., 1993, *ApJ*, **419**, 813 2.1.4

Maíz-Apellániz, J., Walborn, N. R., Galué, H. Á. & Wei, L. H., 2004, *ApJSS*, **151**, 103 1.1, 3.1, 5.5, 6.1

Marcolino, W. L. F., Bouret, J., Martins, F., Hillier, D. J., Lanz, T. & Escolano, C., 2009, *A&A*, **498**, 837 5.4, 5.6, 5.6, 5.7.1

Markova, N., Puls, J., Repolust, T. & Markov, H., 2004, *A&A*, **413**, 693 1.5, 2.4, 2.5, 2.14, 2.4.3, 3.10, 3.2.3, 3.15, 3.23, 6.1, 6.2, 6.3.2, 6.3

Martins, F., Schaerer, D. & Hillier, D. J., 2002, *A&A*, **382**, 999 1.2, 2.1.2

Martins, F., Schaerer, D. & Hillier, D. J., 2005*a*, *A&A*, **436**, 1049 1.2, 2.3, 2.4, 2.5, 2.9, 2.4.3, 3.2.1, 3.2.6, 3.26, 6.1

Martins, F., Schaerer, D., Hillier, D. J., Meynadier, F., Heydari-Malayeri, M. & Walborn, N. R., 2005*b*, *A&A*, **441**, 735 1.5, 2.4, 2.2, 2.7, 2.4.3, 4.3, 5.1, 5.5.3, 5.4, 5.6, 5.6, 5.6, 5.6, 5.7.1

Massa, D., Fullerton, A. W., Nichols, J. S., Owocki, S. P., Prinja, R. K., St-Louis, N., Willis, A. J., Altner, B., Bolton, C. T., Cassinelli, J. P., Cohen, D., Cooper, R. G., Feldmeier, A., Gayley, K. G., Harries, T., Heap, S. R., Henriksen, R. N., Howarth, I. D., Hubeny, I., Kambe, E., Kaper, L., Koenigsberger, G., Marchenko, S., McCandliss, S. R., Moffat, A. F. J., Nugis, T., Puls, J., Robert, C., Schulte-Ladbeck, R. E., Smith, L. J., Smith, M. A., Waldron, W. L. & White, R. L., 1995, *ApJL*, **452**, L53+ 1.5

Massa, D., Fullerton, A. W., Sonneborn, G. & Hutchings, J. B., 2003, *ApJ*, **586**, 996 4.2.1, 5.2.1, 5.5.1, 5.6, 5.19

Massey, P., Puls, J., Pauldrach, A. W. A., Bresolin, F., Kudritzki, R. P. & Simon, T., 2005, *ApJ*, **627**, 477 1.2

Mihalas, D., Kunasz, P. B. & Hummer, D. G., 1976, *ApJ*, **210**, 419 2.1

Milne, E. A., 1926, *MNRAS*, **86**, 459 1.3

Morgan, W. W., Keenan, P. C. & Kellman, E., 1943, *An atlas of stellar spectra, with an outline of spectral classification* 1.1

Morton, D. C., 1967, *ApJ*, **147**, 1017 1.3

Morton, D. C. & Underhill, A. B., 1977, *ApJSS*, **33**, 83 6.3.1, 6.25

Mullan, D. J., 1984, *ApJ*, **283**, 303 1.5

Mullan, D. J., 1986, *A&A*, **165**, 157 1.5

Najarro, F., Puls, J., Herrero, A., Hanson, M. M., Martín-Pintado, J. & Hillier, D. J., 2008, in W.-R. Hamann, A. Feldmeier, & L. M. Oskinova (ed.), *Clumping in Hot-Star Winds*, pp. 43–+ 1.5, 2.1.4

Nazé, Y., 2009, *A&A*, **506**, 1055 1.5

Nugis, T., Crowther, P. A. & Willis, A. J., 1998, *A&A*, **333**, 956 1.5

Nussbaumer, H. & Storey, P. J., 1983, *A&A*, **126**, 75 2.2.1

Olson, G. L., 1982, *ApJ*, **255**, 267 5.2

Olson, G. L., Auer, L. H. & Buchler, J. R., 1986, *Journal of Quantitative Spectroscopy and Radiative Transfer*, **35**, 431 2.1.1

Oskinova, L. M., Feldmeier, A. & Hamann, W., 2004, *A&A*, **422**, 675 1.5

Oskinova, L. M., Hamann, W. & Feldmeier, A., 2007, *A&A*, **476**, 1331 1.5, 1.5, 3.2.1, 3.3, 4.3, 5.7.1, 6.1

Osterbrock, D. & Flather, E., 1959, *ApJ*, **129**, 26 1.5

Owocki, S. P., 2008, in W.-R. Hamann, A. Feldmeier, & L. M. Oskinova (ed.), *Clumping in Hot-Star Winds*, pp. 121–+ 1.5, 5.7.1

Owocki, S. P., Castor, J. I. & Rybicki, G. B., 1988, *ApJ*, **335**, 914 1.5

Owocki, S. P. & Puls, J., 1999, *ApJ*, **510**, 355 1.5

Panagia, N. & Felli, M., 1975, *A&A*, **39**, 1 1.4

Pauldrach, A., 1987, *A&A*, **183**, 295 1.3

Pauldrach, A., Puls, J. & Kudritzki, R. P., 1986, *A&A*, **164**, 86 1.3

Pauldrach, A. W. A., Kudritzki, R. P., Puls, J., Butler, K. & Hunsinger, J., 1994, *A&A*, **283**, 525 1.3

Pauldrach, A. W. A., Lennon, M., Hoffmann, T. L., Sellmaier, F., Kudritzki, R. & Puls, J., 1998, in I. Howarth (ed.), *Properties of Hot Luminous Stars*, volume 131 of *Astronomical Society of the Pacific Conference Series*, pp. 258–+ 1.2.1

Pellerin, A., Fullerton, A. W., Robert, C., Howk, J. C., Hutchings, J. B., Walborn, N. R., Bianchi, L., Crowther, P. A. & Sonneborn, G., 2002, *ApJSS*, **143**, 159 3.3, 3.29, 3.30, 3.31

Penny, L. R., 1996, *ApJ*, **463**, 737 2.4, 5.4.1, 6.2

Pradhan, A. K., Zhang, H. L., Nahar, S. N., Romano, P. & Bautista, M. A., 1996, in *Bulletin of the American Astronomical Society*, volume 28 of *Bulletin of the American Astronomical Society*, pp. 1367–+ 2.2.1

Prinja, R. K., Barlow, M. J. & Howarth, I. D., 1990, *ApJ*, **361**, 607 1.4, 2.4.1, 2.4, 5.4, 5.4.1, 5.5.3, 6.1, 6.2, 6.3.2

Prinja, R. K. & Howarth, I. D., 1986, *ApJSS*, **61**, 357 1.5, 5.5.1

Prinja, R. K., Howarth, I. D. & Henrichs, H. F., 1987, *ApJ*, **317**, 389 1.5

Prinja, R. K. & Massa, D. L., 2010, *A&A*, **521**, L55+ 5.7, 7.1

Puls, J., 2008, in F. Bresolin, P. A. Crowther, & J. Puls (ed.), *IAU Symposium*, volume 250 of *IAU Symposium*, pp. 25–38 2.1

Puls, J., Kudritzki, R., Herrero, A., Pauldrach, A. W. A., Haser, S. M., Lennon, D. J., Gabler, R., Voels, S. A., Vilchez, J. M., Wachter, S. & Feldmeier, A., 1996, *A&A*, **305**, 171 1.2.1, 1.4, 1.5, 2.4.3, 3.5, 3.2.1, 3.20

Puls, J., Kudritzki, R., Santolaya-Rey, A. E., Herrero, A., Owocki, S. P. & McCarthy, J. K., 1998, in I. Howarth (ed.), *Properties of Hot Luminous Stars*, volume 131 of *Astronomical Society of the Pacific Conference Series*, pp. 245–+ 1.5

Puls, J., Markova, N., Scuderi, S., Stanghellini, C., Taranova, O. G., Burnley, A. W. & Howarth, I. D., 2006, *A&A*, **454**, 625 1.5

Puls, J., Urbaneja, M. A., Venero, R., Repolust, T., Springmann, U., Jokuthy, A. & Mokiem, M. R., 2005, *A&A*, **435**, 669 2.4

Puls, J., Vink, J. S. & Najarro, F., 2008, *A&AR*, **16**, 209 1.8, 1.9, 5.1, 7.1

Ralchenko, Y., 2005, *Memorie della Societa Astronomica Italiana Supplementi*, **8**, 96 4.2.1

Repolust, T., Puls, J. & Herrero, A., 2004, *A&A*, **415**, 349 1.5, 2.4, 2.2, 2.5, 2.16, 2.4.3, 3.2.1, 6.1, 6.2, 6.3

Runacres, M. C. & Owocki, S. P., 2002, *A&A*, **381**, 1015 1.5, 1.11, 1.5, 7.1

Runacres, M. C. & Owocki, S. P., 2005, *A&A*, **429**, 323 1.5

Sana, H., Rauw, G., Nazé, Y., Gosset, E. & Vreux, J., 2006, *MNRAS*, **372**, 661 1.5

Santolaya-Rey, A. E., Puls, J. & Herrero, A., 1997, *A&A*, **323**, 488 2.4

Schaller, G., Schaerer, D., Meynet, G. & Maeder, A., 1992, *A&AS*, **96**, 269 1.2, 5.3

Scharmer, G. B., 1981, *ApJ*, **249**, 720 2.1.1

Scuderi, S., Panagia, N., Stanghellini, C., Trigilio, C. & Umana, G., 1998, *A&A*, **332**, 251 6.2, 6.3.2, 6.3

Seaton, M. J., 1995, *The opacity project* 2.2.1

Smartt, S. J., 2009, *Ann. Rev. Astr. Astrophys.*, **47**, 63 1.1.2

Sobolev, V. V., 1960, *Moving envelopes of stars* 1.3.1

Sota, A., Maíz-Apellániz, J., Walborn, N. R. & Shida, R. Y., 2008, in *Revista Mexicana de Astronomia y Astrofisica Conference Series*, volume 33 of *Revista Mexicana de Astronomia y Astrofisica Conference Series*, pp. 56–56 1.1, 3.1, 5.6

Springmann, U. W. E. & Pauldrach, A. W. A., 1992, *A&A*, **262**, 515 1.5

Sundqvist, J. O., Puls, J. & Feldmeier, A., 2010, *A&A*, **510**, A11+ 1.5, 3.5, 4.3, 5.7.1, 7, 7.1

Vacca, W. D., Garmany, C. D. & Shull, J. M., 1996, *ApJ*, **460**, 914 2.1.2

Vink, J. S., de Koter, A. & Lamers, H. J. G. L. M., 2000, *A&A*, **362**, 295 1.1.2, 1.5, 2.4, 2.14, 2.16, 5.1, 5.6, 5.6, 5.7.1

Vink, J. S., de Koter, A. & Lamers, H. J. G. L. M., 2001, *A&A*, **369**, 574 2.4, 5.6

Walborn, N. R., 1972, *AJ*, **77**, 312 5.5, 6.1

Walborn, N. R., 1973, *AJ*, **78**, 1067 6.1

Walborn, N. R., 1982, *AJ*, **87**, 1300 5.5

Walborn, N. R., 1990, in C. D. Garmany (ed.), *Properties of Hot Luminous Stars*, volume 7 of *Astronomical Society of the Pacific Conference Series*, pp. 23–29 1.1

Walborn, N. R. & Fitzpatrick, E. L., 1990, *PASP*, **102**, 379 1.2

Walborn, N. R. & Fitzpatrick, E. L., 2000, *PASP*, **112**, 50 1.1

Walborn, N. R., Nichols-Bohlin, J. & Panek, R. J., 1985, *NASA Reference Publication*, **1155** 3

Walborn, N. R. & Panek, R. J., 1984*a*, *ApJL*, **280**, L27 3

Walborn, N. R. & Panek, R. J., 1984*b*, *ApJ*, **286**, 718 3

Walborn, N. R. & Panek, R. J., 1985, *ApJ*, **291**, 806 3

Waldron, W. L. & Cassinelli, J. P., 2010, *ApJL*, **711**, L30 4.3, 6, 6.4

Wenger, M., Oberto, A., Bonnarel, F., Brouty, M., Bruneau, C., Brunet, C., Cambresy, L., Dubois, P., Eisele, A., Fernique, P., Genova, F., Laloë, S., Lesteven, S., Loup, C., Ochsenbein, F., Vannier, P. J., Vollmer, B., Vonflie, P., Wagner, M. J., Woelfel, F., Borde, S., Beyneix, A., Chassagnard, G., Jasniewicz, G. & Davoust, E., 2007, in S. Ricketts, C. Birdie, & E. Isaksson (ed.), *Library and Information Services in Astronomy V*, volume 377 of *Astronomical Society of the Pacific Conference Series*, pp. 197–+ 5.4.1

Westmoquette, M. S., Gallagher, III, J. S. & Smith, L. J., 2005, in R. de Grijs & R. M. González Delgado (ed.), *Starbursts: From 30 Doradus to Lyman Break Galaxies*, volume 329 of *Astrophysics and Space Science Library*, pp. 85P–+ 1.1.1

Wilson, R. E., 1953, *Carnegie Institute Washington D.C. Publication*, 0 5.4.1

Wright, A. E. & Barlow, M. J., 1975, *MNRAS*, **170**, 41 1.4

Zsargo, J., Hillier, J. D., Bouret, J. C., Lanz, T., Leutenegger, M. A. & Cohen, D. H., 2009, in *American Astronomical Society Meeting Abstracts*, volume 213 of *American Astronomical Society Meeting Abstracts*, pp. 408.15–+ 2.1.4, 3.5, 5.7.1

*“ What a totally amazing excellent discovery. NOT!”*

Wayne Campbell, ‘Wayne’s World’